TESLA-Report 1997-08

Study of Electromagnetic and Hadronic Background in the Interaction Region of the TESLA Collider

Dissertation
zur Erlangung des Doktorgrades
des Fachbereichs Physik
der Universität Hamburg

vorgelegt von
Daniel Schulte
aus Hamburg

Hamburg

1996

Abstract

Future electron-positron experiments at high centre of mass energies require the use of linear colliders. The beam-beam effects in the interaction region lead to the emitting of photons, the so called beamstrahlung, which can pose a hazard to the collider. It also increases the background in the detector due to creation of electron-positron pairs and soft hadronic events and influences experiment by smearing the luminosity spectrum.

A program was developed to simulate the beam-beam effect and the production of background. The possibility to cope with the beamstrahlung in the collider was investigated. With a simple detector simulation the possible reduction of the impact of the background on the detector, in particular the vertex detector , was investigated.

Ideas to measure beam parameters using beam-beam effects are presented, as well as the possibility to collide electrons with electrons or energetic photons with photons.

Top quark production at threshold was used as an example to study the effect of beamstrahlung and background for different colliders.

Zusammenfassung

Zukünftige Elektron-Positron Experimente bei hohen Schwerpunktsenergien erfordern den Einsatz von Linearbeschleunigern. Die Wechselwirkung der Strahlen im Detektor führt in diesen zur Emittierung von Photonen, der sogenannten Beamstrahlung, deren hohe Leistung zur Gefährdung des Beschleunigers führen kann. Sie erhöht zudem den Untergrund im Detektor durch Produktion von Elektron-Positron Paaren sowie durch niederenergetische hadronische Ereignisse, und kann durch Verschmieren des Luminositätsspektrums Experimente beeinflussen.

Es wurde ein Programm entwickelt, um die Strahl-Strahl Wechselwirkung sowie die Erzeugung des Untergrundes zu simulieren. Mit diesem konnte die Möglichkeit, den Beschleuniger vor der Beamstrahlung zu schützen untersucht werden. Mit einer einfachen Detektorsimulation konnte die Wirkung des Untergrundes auf den Detektor, inbesondere den Vertexdetektor, untersucht und eine Maske entworfen werden, diese weitgehend zu reduzieren.

Einige Ideen zur Messung der Strahlparameter mithilfe der Strahl-Strahl Effekte wurden untersucht, ebenso wie die Möglichkeit Elektronen mit Elektronen sowie hochenergetische Photonen miteinander kollidieren zu lassen.

Die Erzeugung von Topquarks an der Produktionsschwelle wird als Beispiel für die Wirkung von Untergrund und Beamstrahlung auf ein Experiment untersucht.

Acknowledgements

I would like to thank B. H. Wiik for being my Doktorvater, P. Schmüser for helpful discussion and M. Leenen for his advice and for making it possible for me to attend a number of workshops where I had the opportunity to meet all the experts.

From R. Brinkmann and also N. Holtkamp and the other experts from DESY I learned a lot about accelerators.

From the ZEUS and H1 experiments I would like to thank a number of people among them U. Schneekloth, E. Elsen, U. Koetz, V. Korbel, J. Gayler and J. Meyer for useful discussions, and J.-E. Olssen for his help to find a copy of the Vermaseren Monte-Carlo.

I also would like to thank O. Napoly and R. Settles for their very helpful discussion on different topics, as well as Chr. Damerell, T. Tauchi, D. Miller, M. Jatzbeck, P. Colas, D. Walz, H. Dinter, A. Koski, P. Pierini and a number of others. With R. Miguel, R. Frey and J. Jaros I had interesting discussion about the top quark, with P. Zerwas about the Higgs.

H. Anlauf (together with T. Ohl) found a bug in GUINEA-PIG (which is now fixed).

Also with M. Seidel, S. Schreiber, A. Drozhdin and K. Hanke I had frequent helpful discussions.

Contents

Chapter 1

Introduction

Electron-positron colliders with a centre of mass energy of 500 GeV or more allow for interesting physics investigations complementary to hadron colliders. They have the potential to discover a medium mass Higgs and possible supersymmetric gauginos and leptons and to perform precise investigations of the Higgs and the top quark.

Since in high energy circular e^+e^--machines the beam particles emit synchrotron radiation with considerable power it will be necessary to use linear colliders instead. The bunches in these machines can be used only once and must therefore have extremely small cross sections in order to achieve a sufficient luminosity and event rates. Compared to existing machines the luminosity has to be increased because of the tendency of the cross sections to fall as $1/s$, where s is the centre of mass energy squared.

This thesis considers background that is produced in the detector and affects the detector itself or the collider components close to it. The main focus is on one of the proposed machine designs, namely TESLA[1]. Beamstrahlung is a limiting factor for the luminosity and a direct background source for the collider. Secondary background exists due to production of lepton pairs and hadrons. The main effects of these backgrounds on the detector, especially the vertex detector and the low angle tagger, are discussed. Some ideas on how to measure the beam sizes at the interaction point are presented. Possible high energy options, an e^-e^- and a $\gamma\gamma$ option are considered. Finally the effect of the beam-beam interaction on the top threshold scan is investigated.

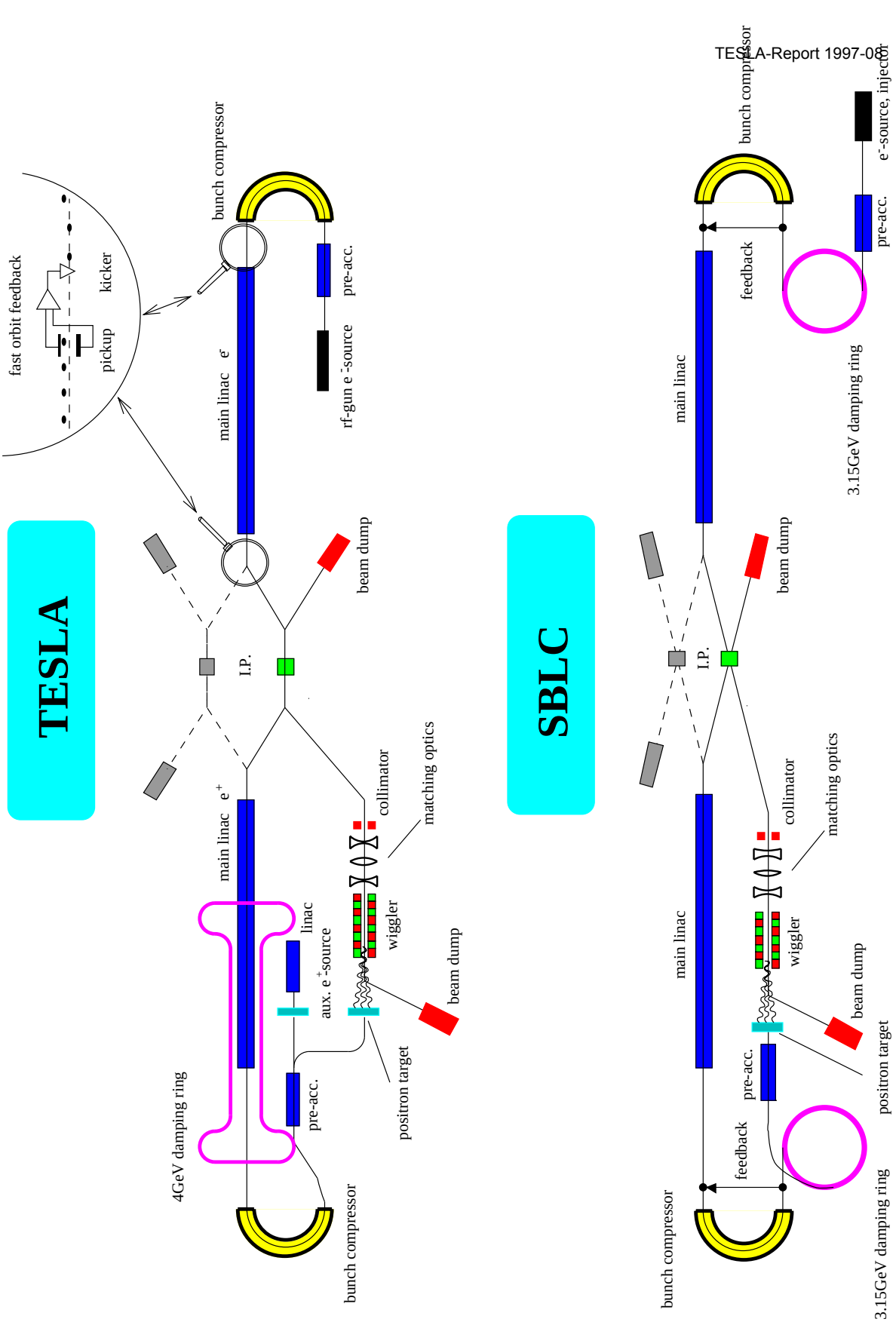

Figure 1.1: Schematic possible layouts of TESLA and SBLC. It should be noted that currently only one detector and interaction point is foreseen, differently from the sketches.

Parameter	unit	SBLC	TESLA	NLC	JLC-S	JLC-C	JLC-X	CLIC	VLEPP
E_{cm}	[GeV]	500	500	500	500	500	500	500	500
L_0	$[10^{33}\mathrm{cm}^{-2}\mathrm{s}^{-1}]$	3.17	3.73	5.09	4.68	4.2	5.41	5.25	12.2
f_{rep}	[Hz]	50	10	180	50	100	150	700	300
N_b		333	1135	90	50	72	85	20	1
t_b	[ns]	6	707	1.4	5.6	2.8	1.4	0.67	$3.3 \cdot 10^6$
N	$[10^{10}]$	1.1	3.63	0.75	1.44	1.0	0.65	0.8	20
$\gamma\epsilon_x/\gamma\epsilon_y$	[μm]	5.0/0.25	14.0/0.25	4.0/0.09	3.3/0.045	3.3/0.045	3.3/0.045	3.4/0.1	20.0/0.08
β_x/β_y	[mm]	11.0/0.45	25.0/0.7	10.0/0.15	10.0/0.1	15.0/0.2	10.0/0.1	10.0/0.13	100.0/0.1
σ_x/σ_y	[nm]	335/15.1	845/18.9	286/5.3	260/3.0	318/4.3	260/3.0	264/5.15	2000/3.9
σ_z	[μm]	300	700	125	120	200	90	160	750
θ_{cross}	[m radian]	(6)	0	(20)	6.4	(8.0)	6.1	(20)	(6)
P_B	[MW]	7.3	8.25	4.8	1.43	3.2	3.2	4.5	2.6
L	$[10^{33}\mathrm{cm}^{-2}\mathrm{s}^{-1}]$	5.3	6.0	6.8	4.6	6.3	5.1	6.4	9.7
L_C	$[10^{29}\mathrm{cm}^{-2}]$	3.1	10.7	4.2	18.2	8.6	4.0	4.6	323
δ	[%]	2.8	2.5	3.2	8.2	3.4	3.1	3.6	10.0
n_γ		1.4	2.0	1.1	1.8	1.3	0.9	1.3	4.7
$\langle E_\gamma \rangle$	[GeV]	4.7	3.1	7.3	11.3	6.3	8.6	7.0	5.3
$L_{e\gamma}$	$[10^{33}\mathrm{cm}^{-2}\mathrm{s}^{-1}]$	3.2	4.2	3.1	3.4	3.0	2.2	3.2	9.9
$L_{\gamma\gamma}$	$[10^{33}\mathrm{cm}^{-2}\mathrm{s}^{-1}]$	2.2	3.7	1.6	3.0	1.7	1.0	1.9	16
N_P	$[10^3]$	26	102	26	150	54	21	30	3980
E_P	$[10^3\,\mathrm{GeV}]$	53	159	78	705	147	76	89	10310
$N_\perp$		7.1/6.0	31.0/28.3	7.0/6.0	37/32	15.8/13.2	6.0/4.9	8.4/6.9	1220/1080
N_{Hadr}		0.04	0.13	0.045	0.48	0.95	0.055	0.055	11
N_{MJ}	$[10^{-2}]$	0.1/0.12	0.3/0.37	0.14/0.17	1.4/1.9	0.27/0.33	0.14/0.18	0.15/0.19	28/32

E_{cm}: Centre of mass energy, f_{rep}: repetition frequency, N_b: number of bunches per tain, σ: bunch dimensions at IP
N: number of particles per bunch, t_b: time between bunches, θ_c: crossing angle (in brackets crab crossing),
L_0: nominal luminosity, L: actual luminosity, β: Beta functions at IP, $\gamma\epsilon$: normalised emittances,
L_C: integrated luminosity per bunch crossing, $L_{e\gamma}, L_{\gamma\gamma}$: $e\gamma$, $\gamma\gamma$ luminosities δ: Average energy loss,
n_γ: number of photons per beam particle, $\langle E_\gamma \rangle$: average photon energy,
P_B: beam power, N_P: Number of pair particles, E_P: Total energy of pair particles,
$N_\perp$: Number of particles with $p_\perp > 20\,\mathrm{MeV}, \pi - 0.15 > \theta > 0.15$,
N_P: Number of pair particles, M_{Hadr}: Hadronic events, M_{MJ}: Minijet events $p_\perp > 3.2\,\mathrm{GeV/c}$.

Table 1.1: Parameters for different proposed linear colliders [1]. All background numbers are per bunch crossing, for $N_\perp$ the first number does not take the external field into account, the second does. For the number of minijets the GRV- and DG-parametrisations are used for the first and second value, respectively.[2]

1.1 Different designs

Several designs for such a linear accelerator are under investigation. Table 1.1[2] on page 7 lists some of their main parameters that are of interest for the detector and interaction region. Two possible designs are investigated at DESY—TESLA and SBLC[3] [2]—for which a schematic design is shown in Figure 1.1. The latter is based on well known technology which is used in the only high energy linear collider built so far, the SLC, which is running at $\sqrt{s} \approx 91\,\mathrm{GeV}$. In many aspects improvements of the technology are necessary nevertheless to reach a centre of mass energy of 500 GeV. The other design considered at DESY—TESLA—is based on superconducting cavities. For this design significant improvements of the gradient achievable with these cavities are required as well as substantial cost reductions. The benefit of this design would be the considerably relaxed tolerances for the machine, the high efficiency for turning electric power into beam power and the excellent time structure for the experiment.

A short overview of the accelerator may be helpful. The main difference between the normal conducting designs SBLC, NLC and the JLC is given by the choice of the operation frequency. The higher frequencies of X-band (about 11 GHz) machines as NLC and JLC-X lead in general to smaller accelerating structures with a higher gradient but tighter tolerances in comparison with the lower frequencies of the S-band (3 GHz) designs SBLC and JLC-S. The C-Band lies in between the other two. The acceleration frequency of TESLA is 1.3 GHz (called L-band) and thus much lower than for the rest. The CLIC design differs from all the others since it uses a second beam to accelerate the main one. This allows for very high gradients but poses problems for the efficiency as well as the emittance increase in the linac.

Each side of these colliders consists of three main parts. The electron (or positron) source, the damping ring and the bunch compressor provide the bunches with the required properties. In the main linac the bunches are accelerated to the required energy. In the interaction region possible tails are removed and the bunch is focused to a small cross section to achieve high luminosity.

The operation frequency of the cavities which accelerate the beam governs the time structure of the beam. This has significant impact on the experiment. In the normal conducting machines like NLC and SBLC a number of bunches is accelerated with a short distance of typically a few nanoseconds between them. Several of these bunch trains can be accelerated with a repetition frequency of some tens per second. This scheme is necessary to achieve a good ratio between the power

[1] The name is an abbreviation of TeV Energy Superconducting Linear Accelerator.

[2] For VLEPP a so called travelling focus scheme is employed to avoid the luminosity loss due to the hourglass effect. The simulation is in this case sensitive to small fluctuations in the macro particle distribution. For CLIC the longitudinal charge distribution is not Gaussian, which is not taken into account here.

[3] SBLC stands for S-Band Linear Collider, refering to the operation frequency.

consumption of the accelerator and the beam power. The length of these trains and the repetition frequency depend on the frequency of the accelerating fields.

While most of the colliders are roughly comparable as far as the timing is concerned with only factors of a few difference there are three exceptions. The first, TESLA, accelerates bunch trains which contain a total charge that is larger by a factor of about eleven than in SBLC for example. The total length of the pulse is three orders of magnitude longer than in the normal conducting machines. This is possible since the superconducting cavities have almost no losses except for the power going into the beam bunch. This in turn allows for a long distance between bunches of about one microsecond. The repetition frequency of this machine is low since the total energy necessary to fill the cavities to achieve the required gradient is lost once per bunch train.

In VLEPP single bunches are accelerated with a comparatively large charge. In CLIC the bunch trains are very short and the spacing between them is even smaller than in the X-band machines NLC and JLC-X. This machine has thus more or less the characteristics of a single bunch machine.

If one compares the beam parameters at the interaction point in Table 1.1 one finds that the emittances and spot dimensions for TESLA are relatively large. This means that the requirements on the machine are relaxed. A vertical spot size of about 70 nm has already been achieved in the Final Focus Test Beam (FFTB) experiment at SLC [3]. The luminosity is comparable with the other designs since the total bunch current is large. This can be done with reasonable low power consumption of the machine since the efficiency of the superconducting cavities is high.

The SBLC bunches are slightly smaller but still large compared to the X-band designs.

1.2 The interaction region

The interaction region consists of four sections. The first after the linac is the collimation region where the tails of the beam are scraped off. This is followed by a big bend which lowers the background going from the machine into the detector. In the case of SBLC and TESLA such a bend is not not foreseen at present, since the background is expected to be small. After the bend comes the final focus system which compresses the beams to the required size at the interaction point in the detector, the final component[4].

For the collimator region, preliminary layouts exist for TESLA as well as for

[4]It may be useful to have two detectors following different design ideas. One could for example aim for higher precision or for more robustness. Using the machine as a high energy photon-photon collider for example also require a detector design different from the for e^+e^- physics. One could switch very fast from one detector to the other if two experimentation halls and final focus systems exist. The big bend would then separate the two beam lines.

SBLC [4]. For TESLA some more detailed investigations were done. The system will consist of two steps to achieve a high efficiency. In addition to usual reduction of background an aim of the collimation system is to protect the elements downstream from an accidentally missteered beam. A beam dump will be placed in front of the collimation region. In case of an abnormal offset of the beam to the beam line the collimators will have to be able to stop ten bunches before the beam dump is switched on. This gives a time of seven microseconds. A realistic collimation section is studied in reference [4].

Even so a big bend is not forseen at present a preliminary design exists [5].

For the final focus system detailed studies have been performed [6]. They include a analysis of the stability of the system. Two main differences to other final focus systems exist. In order to get rid of the spent beam also an outgoing beam line is necessary in TESLA. The main separation is done immediately behind the detector with a separator combining a magnetic and an electric field. The two forces cancel for particles going into the detector, for those leaving it they however will add. It should be noted that this does not rely on the different charges of the incoming and outgoing particles it would work with an e^-e^- collider as well. The second speciality in TESLA is that a collimator for the radiation from the detector is needed. This will be explained in more detail below.

1.3 Overview of the different backgrounds

Here a short overview over the different sources of background will be given including those not covered in this thesis which nevertheless may give constrains on the layout of the interaction region.

1.3.1 Expected event rate

For a centre of mass energy $\sqrt{s} = 500\,\mathrm{GeV}$ the total cross section for the process $e^+e^- \to Z^*/\gamma$ is about 18 pb. The main contribution arises from the so called radiative return to the Z^0 peak. Due to initial state radiation the particles can emit photons. Therefore the effective centre of mass energy of the colliding particles can be close to the Z^0 mass with a small probability. On the other hand the cross section at $\sqrt{s} \approx m_{Z^0}$ is very much larger than at 500 GeV leading to a significant rate. Without initial state radiation the cross section would be about 6 pb. For a luminosity of $6 \cdot 10^{33}\,\mathrm{cm}^{-2}\mathrm{s}^{-1}$ the resulting event rate is about 0.1 Hz. Overlap of two events will thus not be a problem.

1.3.2 Synchrotron radiation in the final doublet

Beam particles emit synchrotron radiation in any magnetic field along the beam line. For the detector, photons emitted in the final doublet are dangerous since

they can not be collimated in front of the detector. So it has to be ensured that they will leave the detector through the aperture of the magnets on the other side. One requires that no photon hits even the second quadrupole on the other side. This can be achieved if one collimates the beam such that no particles exist with an offset to the reference trajectory of more than $12\,\sigma_x$ in x- and $48\,\sigma_y$ in y-direction [4]. This will be done in the collimation region. The collimators are at $8\sigma_x$ and $32\sigma_y$ in x- and y-direction respectively. This is necessary since particles can change their phase during the transport from the collimation section to the interaction point. Not to tighten these requirements the apertures in the detector should allow the synchrotron radiation photons to pass.

The extension of the beam tails in TESLA is not known. The contribution from the damping ring as well as from the bunch compressor can be suppressed by carefully collimating at low energies. The wakefield effects are very small and will thus not populate the tails much. The vacuum will be very good since the machine is superconducting resulting in a small contribution from Coulomb scattering. The main contribution may thus come from dark currents accelerated in the linac. Even if the tails are very small the collimation is needed to protect the final focus and the detector in case of an accidentally missteered beam.

1.3.3 Muon background

The collimation of the high energy beam particles produces secondaries. Among these especially the muons can be a severe background in the detector as found in SLC. The big bend after the collimation region can lower this background significantly. If this proves not to be sufficient then additional spoilers made of magnetised iron can be used. These spoilers have to fill the tunnel and are several meters thick. Since it is not known whether the beams will have significant tails it seems to be reasonable to foresee the space for the spoilers but to build them only if experience shows that they are necessary.

The muon background is studied by M. Sachwitz and H. J. Schreiber in reference [7] and seems to be well under control as long as the beam tails are reasonable in size.

1.3.4 Synchrotron radiation in the final focus system

Photons emitted within the final focus system can form a background in the detector as well. These photons should be collimated before they reach the detector to ensure the remaining can pass without producing any hit. It is important to make sure that these collimators can not be hit by beam particles since this would lead to the production of high energy secondaries. In addition there is an intense photon radiation coming from the detector which the collimators either have to avoid or must be able to withstand.

1.3.5 Beamstrahlung

At the interaction point beam-beam effects cause production of beamstrahlung. This radiation is very intense and collimated in a small cone around the beam axis. Since its power is in the order of a few hundred kilowatts it can be dangerous for the accelerator. If we do not have a crossing angle in the detector the beamstrahlung will go directly into the beam pipe of the opposing final focus system. It has then to be collimated inside the beam pipe. Calculations show that it may be possible. The beamstrahlung itself does not form a background in the detector but secondaries produced by it do.

1.3.6 Pair creation

The beamstrahlung will increase the amount of background due to two-photon processes at the interaction point itself. Here one has to consider the production of low energy electrons and positrons via pair creation. The number of these particles is of the order 10^5 per bunch crossing with an average energy in the GeV range.

1.3.7 Hadronic background

Another process is the production of hadrons. The major part of this background goes into small angles as well, but with some probability high transverse momentum jets can be produced, the so called minijets. This background can only be lowered by reducing the beamstrahlung. Since it depends on the hadronic properties of the photon its study is of some interest.

1.3.8 Losses of the spent beam

The spent beam has a large spread in energy and angular distribution of the particles. The elements that are needed to separate it from the incoming beam can therefore be exposed to an enormous power. These losses are investigated by A. Drozhdin [8].

Chapter 2

Pinch Effect and Beamstrahlung

The two bunches focus each other at the interaction point, a process called pinch effect. Since the particle trajectories are bent due to the pinch effect they emit a radiation called beamstrahlung. This leads to an energy loss of the electrons and positrons. For the colliders under study the photons have energies in the range of a few GeV. The centre of mass energy for the collisions will hence vary more than expected from the energy spread of the incoming beams and the initial state radiation. Since the pinch effect reduces the effective beam cross sections the luminosity is enhanced compared to the nominal one by the luminosity enhancement factor H_D. While this seems to be advantages one has to keep in mind that the geometric dimensions of the beams are given by the allowed average energy loss of the beam particles. This gives an upper limit on the luminosity. The pinch effect is difficult to calculate analytically, so different Monte-Carlo programs were developed for simulation.

2.1 Luminosity

The luminosity of a collider is given in first approximation by

$$L_0 = \frac{N^2}{4\pi\sigma_x\sigma_y} f_r n_b = \frac{N}{4\pi\sigma_x\sigma_y}\eta P_{AC}/E_{cm}. \tag{2.1}$$

N is the number of particles per bunch and $\sigma_{x,y}$ are the transverse dimensions of the beams at the plane $z = 0$ which are assumed to be normal distributed. $f_r n_b$ is the number of bunch crossings per second with n_b the number of bunches per train and f_r the number of trains per second. The repetition frequency is limited for a fixed bunch charge by the available total power P_{AC} times the efficiency η with which this power is transformed into beam power. It is possible to increase the luminosity by either increasing the bunch charge or by decreasing the bunch cross section.

The vertical and horizontal beam dimensions can not be chosen arbitrarily. The transverse sizes of the bunch are given by $\sigma_{x,y} = \sqrt{\beta_{x,y}\epsilon_{x,y}}$. The emittances

$\epsilon_{x,y}$ are properties of the beam and $\gamma\epsilon$ is not changed during the beam transport in first order. The beta functions $\beta_{x,y}$ can be thought of as a property of the beamline lattice, although this is not strictly true since it depends on the particle energy. It can be varied within certain limits. Two important lower limits exist. The first is given by the bunch length. If one of the beta functions is significantly smaller than the bunch length the luminosity will be reduced due to the so called hourglass effect. This simply results from the fact that to achieve the small spot size the angles of the particle trajectories with respect to the beam line, which are given by $\sqrt{\epsilon/\beta}$, have to be rather large. The cross section of the beam will thus vary significantly over its length.

The second lower limit is the Oide limit [9]. The particles emit synchrotron radiation in the last magnets. This changes their energy and accordingly they are focused differently.

While the above limits result in a minimal achievable beam cross section an upper limit on the number of particles per bunch for a given bunch size arises from the beamstrahlung. It is necessary to go into some detail.

2.2 Simplified equation of motion

The electric and magnetic fields of a bunch of ultra relativistic particles are almost transverse to the direction of motion. An ultra relativistic particle passing through the fields of the bunch in opposite direction will feel two forces. If its charge has the opposite sign as that of the bunch particles the electric as well as the magnetic force will bend its trajectory towards the centre of the bunch. If it has the same charge its trajectory will be bend outwards. If it moves into the same direction as the bunch the magnetic and electric forces will cancel each other with an accuracy of $1/\gamma^2$.

For a round beam with Gaussian charge distribution the transverse acceleration can be calculated using:

$$\begin{aligned}\frac{\mathrm{d}^2 r}{\mathrm{d}z^2} &= \frac{1}{\gamma m}\frac{2e}{2\pi\epsilon_0 c^2 r}\int_0^r f(z)\frac{-Ne}{2\pi\sigma_r^2}\exp\left(-\frac{r'^2}{2\sigma_r}\right)2\pi r' dr' \\ &= \frac{-4Nr_e}{\gamma r}\left(1-\exp\left(-\frac{r^2}{2\sigma_r^2}\right)\right)f(z)\end{aligned}$$

where the direction of motion of the bunch is along the z-axis. r_e is the classical electron radius and $f(z)$ the normalised longitudinal charge density. For small distances to the beam axis the force is approximately linear. For a longitudinally homogeneous beam $f(z) = 1/(2\sqrt{3}\sigma_z)$ can be used. Assuming no transverse motion at the beginning of the interaction the equation of motion can then be written as:

$$r(z) = r_0 \cos\left(\sqrt{\frac{2Nr_e}{\gamma\sigma_r^2 2\sqrt{3}\sigma_z}}(z-z_0)\right) \tag{2.2}$$

where (r_0, z_0) are the coordinates of the particle when it reaches the head of the bunch. It is convenient to define the so called disruption parameter:

$$D = \frac{N r_e \sigma_z}{\gamma \sigma^2}$$

For $D \ll 1$ the bunch acts as a thin lens with a focal length $f = \sigma_z / D$ since one can approximate the sine in

$$\frac{\mathrm{d}r}{\mathrm{d}z} = r_0 \sqrt{\frac{N r_e}{\gamma \sigma_r^2 \sqrt{3} \sigma_z}} \sin\left(\sqrt{\frac{N r_e}{\gamma \sigma_r^2 \sqrt{3} \sigma_z}} (z - z_0) \right)$$

by its argument. The velocity at the end of the interaction is then given by:

$$\left| \frac{\mathrm{d}r}{\mathrm{d}z} \right| = \frac{D r_0}{\sigma_z}.$$

It should be noted that the relative velocity of the two bunches is $2c$ so one has to integrate from z_0 to $z_0 + \sqrt{3}\sigma_z$. For $D \gg 1$ one obtains for the maximal angle

$$\left| \frac{\mathrm{d}r}{\mathrm{d}z} \right| \approx \left| \frac{r_0}{\sigma_z} \right| \sqrt{\frac{D}{\sqrt{3}}}$$

If the transverse dimensions of the beam are different in x and y one can define two disruption parameters

$$D_x = \frac{2 N r_e \sigma_z}{\gamma \sigma_x (\sigma_x + \sigma_y)} \quad D_y = \frac{2 N r_e \sigma_z}{\gamma \sigma_y (\sigma_x + \sigma_y)}$$

It is common practise to use x for the larger transverse dimension. The luminosity enhancement due to the pinch effect can be described analytically only for small disruption parameters. However a parametrisation of simulation results is available [10]. One defines two variables

$$H_{D_x,y} = 1 + D_{x,y}^{\frac{1}{4}} \frac{D_{x,y}^3}{1 + D_{x,y}^3} \left(\ln(1 + \sqrt{D_{x,y}}) + \ln \frac{\sigma_z}{0.8 \beta_{x,y}} \right) \tag{2.3}$$

and from these the effective beam sizes are estimated using

$$\begin{aligned} \bar{\sigma}_x &= \sigma_x H_{D_x}^{\frac{-1}{2}} \\ \bar{\sigma}_y &= \sigma_y H_{D_y}^{f(\sigma_x/\sigma_y)} \end{aligned} \tag{2.4}$$

with $f(r) = -(1 + 2r^3)/(6r^3)$. These formulae are not generally valid but usually give good results for sensible values of the parameters.

For all proposed linear colliders $D_x < 1$ and $D_y \gg 1$ are valid. This can be easily understood if one considers the energy loss of the particles.

2.3 Beamstrahlung

The trajectories of the particles can be approximated piecewise by circular arcs. A charged particle travelling on a circular trajectory in an external magnetic field emits synchrotron radiation. Since the trajectories of the particles in the bunches are bent they also emit radiation called beamstrahlung, whose spectrum is the same as that of synchrotron radiation. This may be appear surprising since the field seen by a particle varies rapidly. Assuming the typical opening angle of the field of a particle with respect to the plane perpendicular to its motion to be $1/\gamma$ one finds that a particle at a distance r from the beam axis will see the field produced by about $rN/l\gamma$ particles. For TESLA at a distance $r = \sigma_y$ this would be of the order of one. The emission of synchrotron radiation depends on the coherent field so one has to compare the coherence length to the average longitudinal distance of two particles. The coherence length is the part of the trajectory during which a very distant point is in the opening cone of the light emitted by the electron. The opening angle of this cone is about $1/\gamma$ while the typical bending radius is of the order of meters. The number of coherence lengths η a bunch represents can be approximately calculated using

$$\eta = \gamma\theta_x = D_x\frac{\sigma_x}{\sigma_z}\gamma = \frac{2Nr_e}{\sigma_x + \sigma_y}. \tag{2.5}$$

For the proposed colliders the coherence lengths are in the order of μm and are much larger than the average particle distance of some pm. The spectrum will therefore be similar to that of synchrotron radiation. For $\eta < 1$ the average energy loss would remain the same but the spectrum would change, as for a short magnet [11]. A quantitative comparison of the synchrotron radiation formula with the calculation using individual charges can be found in reference [12].

A useful parameter to describe the beamstrahlung is the critical energy [13]:

$$\omega_c = \frac{3}{2}\frac{\gamma^3 c}{\rho} \tag{2.6}$$

where ρ is the bending radius of the particles trajectory. Often the beamstrahlung parameter Υ is used instead:

$$\Upsilon = \frac{2}{3}\frac{\hbar\omega_c}{E_0}. \tag{2.7}$$

For beams with Gaussian charge distribution one can estimate an average value of this parameter [10]:

$$\langle\Upsilon\rangle = \frac{5}{6}\frac{Nr_e^2\gamma}{\alpha(\sigma_x + \sigma_y)\sigma_z} \tag{2.8}$$

with the electromagnetic coupling constant α.

The spectrum of the emitted photons is given by the Sokolov-Ternov formula [14]:

$$\frac{\mathrm{d}\,\dot{w}}{\mathrm{d}\,\omega} = \frac{\alpha}{\sqrt{3}\pi\gamma^2}\left[\int_x^\infty \mathrm{K}_{\frac{5}{3}}(x')\mathrm{d}x' + \frac{\hbar\omega}{E}\frac{\hbar\omega}{E-\hbar\omega}\mathrm{K}_{\frac{2}{3}}(x)\right] \tag{2.9}$$

where $x = \frac{\omega}{\omega_c}\frac{E}{E-\hbar\omega}$ and $K_{5/3}$ and $K_{2/3}$ are the modified Bessel functions. In the limit $\Upsilon \ll 1$ the power of the photon radiation of a particle is proportional to Υ^2:

$$P = \frac{e^2}{6\pi\epsilon_0}\frac{c}{\rho^2}\gamma^4 = \frac{2}{3}\frac{r_e c}{\lambda_c^2}mc^2\Upsilon^2 \tag{2.10}$$

with $\lambda_c = \hbar/(mc)$.

2.4 Choice of parameters

The average energy loss of a particle due to beamstrahlung is in first approximation proportional to $\Upsilon^2\sigma_z$. Using the approximate average value

$$\Upsilon \propto \frac{N\gamma}{(\sigma_x+\sigma_y)\sigma_z}$$

one finds the average relative energy loss δ

$$\delta \propto \frac{\Upsilon^2\sigma_z}{E} \propto \frac{N^2\gamma}{\sigma_x^2\sigma_z}$$

for $\sigma_y \ll \sigma_x$. Using $\beta_y \propto \sigma_z$ (to achieve the same hourglass effect) one can write

$$\delta \propto \frac{N^2\epsilon_y}{\sigma_x^2\sigma_y^2}.$$

Inserting this expression into the formula for the luminosity leads to

$$L \propto \sqrt{\frac{\delta}{\epsilon_y}}\eta P_{AC}. \tag{2.11}$$

where η is the efficiency for turning total power consumption of the linac P_{AC} into beam power. The luminosity is thus almost independent of the number of particles in one bunch since for a fixed allowed average energy loss the horizontal bunch size has to be proportional to its charge.

The parameters are mainly given by the properties of the accelerator. A small vertical emittance is not easily obtained and hard to preserve during the acceleration. The power consumption should be kept to a reasonable level as well as the average energy loss δ. A high efficiency allows thus for relaxed requirements on the vertical emittance to achieve a reasonable luminosity. This allows looser

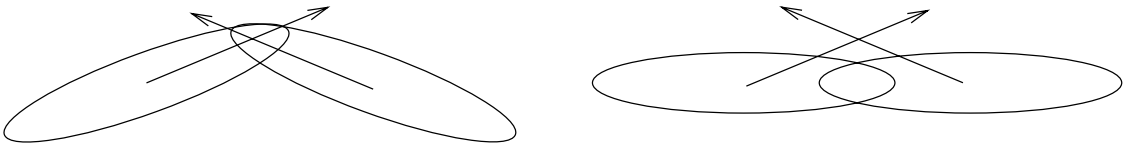

Figure 2.1: The crab crossing scheme on the right versus the normal scheme on the left.

tolerances in the linac. A low efficiency on the other hand requires a small vertical emittance and thus tight tolerances to achieve the same luminosity. The total charge per bunch train and the length of the train are determined by efficiency considerations and available clystrons. The number of bunches into which the total charge can be split is given by the damping rings and the wakefields. A large number of bunches requires a large damping ring. For TESLA with about 1135 bunches in a train a ring of the size of HERA or possibly only of PETRA is needed [15]. A large ring of course means larger costs. Another approach is the use of a damping ring which consists of two straight sections in the same tunnel as the main accelerator with only two small round section on the ends, the so called dog bone design[16]. This would allow for many bunches without the need of much extra tunnel. A high bunch charge on the other hand leads to stronger single bunch wakefields since they scale with N^2.

For TESLA the bunch population is chosen to be $3.63 \cdot 10^{10}$ particles per bunch. The bunch length is 0.7 mm. The vertical emittance was assumed to be $\gamma\epsilon_y = 0.25 \cdot 10^{-6}$ m while the less important horizontal emittance was assumed to be $\gamma\epsilon_x = 14 \cdot 10^{-6}$ m. A further reduction in vertical emittance would allow to enhance the luminosity. The vertical beta function is chosen to be equal to the bunch length but changes up to about 50 % do not affect the luminosity very much as can be found in section 8. The horizontal beta function is set to 25 mm leading to $\sigma_x = 845$ nm and an average energy loss of about 2.5 %.

For SBLC the parameters are $\sigma_x = 335$ nm, $\sigma_y = 15.1$ nm, $\sigma_z = 300\,\mu$m, $N = 1.1 \cdot 10^{10}$, $\gamma\epsilon_x = 5 \cdot 10^{-6}$ m and $\gamma\epsilon_y = 0.25 \cdot 10^{-6}$ m. Both parameter sets are thus relatively conservative compared to others.

One should keep in mind that it is possible to change the parameters to accommodate requirements of the experiment on the luminosity spectrum by giving up part of the luminosity.

2.5 Crossing angle

In order to avoid near encounters of in- and outgoing bunches, it is necessary to introduce a crossing angle between the two beam lines in the designs with a small inter bunch spacing. This is for example the case for SBLC where the next incoming and the outgoing bunch meet at a distance of 0.9 m from the interaction

point. The crossing angles are usually of the order of a few mrad. This would lead to a significant loss in luminosity. For beams without pinch effect the luminosity for a crossing angle α is given by [17]:

$$\frac{L}{L_0} = \frac{1}{\sqrt{1 + \left(\frac{\sigma_z}{\sigma_x} \tan\frac{\alpha}{2}\right)^2}} \tag{2.12}$$

This reduction can however be almost totally avoided by using the so-called crab crossing scheme where the bunches are rotated with respect to the direction of motion as shown in Figure 2.1. This case can be treated as if no crossing angle were present. For TESLA this distance is about 100 m and therefore a crossing angle is not needed.

2.6 Simulation of the pinch effect

The simulation of the pinch effect is mainly based on methods used in plasma physics. The beam particles are replaced by a smaller number of macro-particles (typically a few ten thousand). Since the fields of the particles are transverse one can divide the two beams into slices. Only the two slices of the beams which are at the same z-position can interact with each other. A particle is affected only by the fields of the other beam. After this interaction they are moved forward to interact with the next slice. The interaction within a slice can be treated as a two dimensional problem of line charges. To avoid the computational noise produced by near encounters of two macro-particles one can use either the particle- or clouds-in-cells method. In these methods the slices are divided transversely into cells by a grid. In the first step the charges are distributed over this grid. If the macro-particles are taken to be point-like and thus contribute only to the charge in one cell it is a particle-in-cells method, in the case that they have a finite size and contribute to the charge of several cells it is a clouds-in-cells method. In the second step the fields at the grid points are computed. Using clouds instead of point-like particles helps to suppress high frequency components that are an artifact of the finite resolution of the grid [18]. In the third step the forces on each particle are calculated and the particles are moved.

To compute the potentials at the grid points one can choose between a variety of methods. They can be classified as methods that use a Green function and those which use the Poisson equation. The simplest example for the first type is the direct method where the potential at one point is calculated by summing over the charges of all other grid points times the appropriate Green function. In two dimensions this is:

$$G(x, y) = \frac{\ln(x^2 + y^2)}{4\pi\epsilon_0}$$

If the charge is placed in the centre of the cell this leads to

$$\Phi_{i_0,j_0} = \sum_{i,j\neq i_0,j_0} \frac{Q_{i,j}}{\Delta z} \frac{\ln(((i-i_0)\Delta x)^2 + ((j-j_0)\Delta y)^2)}{4\pi\epsilon_0}.$$

Δx, Δy and Δz are the dimension of a cell, $Q_{i,j}$ is the charge in the cell. If the charges are homogeneously distributed over the cell one has to use:

$$\begin{aligned}\Phi_{i_0,j_0} = \sum_{i,j\neq i_0,j_0} \frac{Q_{i,j}}{\Delta x\Delta y\Delta z} \Big[& F\left(\left(i-i_0+\frac{1}{2}\right)\Delta x, \left(j-j_0+\frac{1}{2}\right)\Delta y\right) \\ & -F\left(\left(i-i_0-\frac{1}{2}\right)\Delta x, \left(j-j_0+\frac{1}{2}\right)\Delta y\right) \\ & -F\left(\left(i-i_0+\frac{1}{2}\right)\Delta x, \left(j-j_0-\frac{1}{2}\right)\Delta y\right) \\ & +F\left(\left(i-i_0-\frac{1}{2}\right)\Delta x, \left(j-j_0-\frac{1}{2}\right)\Delta y\right)\Big]\end{aligned}$$

with

$$F(x,y) = \frac{1}{4\pi\epsilon_0}\int\int \ln(x'^2+y'^2)\mathrm{d}x'\mathrm{d}y' \tag{2.13}$$

$$= \frac{1}{4\pi\epsilon_0}\left[xy\ln(x^2+y^2) + x^2\mathrm{atan}\frac{\mathrm{y}}{\mathrm{x}} + \mathrm{y}^2\mathrm{atan}\frac{\mathrm{x}}{\mathrm{y}} - 3\mathrm{xy}\right] \tag{2.14}$$

It is obvious that this method requires $O(n_x^2 n_y^2)$ operations for a $n_x \cdot n_y$-grid, since any of the $n_x n_y$ cells of a slice contribute to the potential in each of the $n_x n_y$ cells of the slice of the other bunch. A faster method is the use of the fast Fourier transformation, see reference [19], which results only in $O(n_x n_y \ln(n_x n_y))$ operations. The periodicity assumed in the Fourier transformation requires that the grid is twice as large in each dimension as the actually used part.

The second method is to use the Poisson equation

$$\frac{\Phi_{i+1,j} - 2\Phi_{i,j} + \Phi_{i-1,j}}{(\Delta x)^2} + \frac{\Phi_{i,j+1} - 2\Phi_{i,j} + \Phi_{i,j-1}}{(\Delta y)^2} = -\frac{4\pi\epsilon_0 Q_{i,j}}{\Delta x\ \Delta y\ \Delta z}.$$

This leads to a sparse system of linear equations. Several methods exist to solve such a system efficiently. Examples of algorithms can be found in reference [20].

2.7 Generation of beamstrahlung

A useful method to generate beamstrahlung photons is given in reference [21]. The spectrum is expressed in terms of the dimensionless variable v, which is defined via:

$$x = \frac{v^3}{1-v^3} \tag{2.15}$$

where the photon energy is given by $x\hbar\omega_c E/(E+x\hbar\omega_c)$. Using

$$\frac{\mathrm{d}\omega}{\mathrm{d}v} = \frac{3v^2\omega_c}{\left[1-\left(1-\frac{\hbar\omega_c}{E}\right)v^3\right]^2}. \tag{2.16}$$

equation (2.9) can be rewritten as:

$$\frac{\mathrm{d}\dot{w}}{\mathrm{d}v} = A\cdot G\left(v,\frac{\hbar\omega_c}{E}\right)$$

with the constant A

$$A = \frac{4^{1/3}\alpha\gamma c}{\Gamma\left(\frac{4}{3}\right)\rho}.$$

The function G is always smaller than 1:

$$\begin{aligned} G\left(v,\frac{\hbar\omega_c}{E}\right) &= \frac{v^2}{\left[1-\left(1-\frac{\hbar\omega_c}{E}\right)v^3\right]^2}\left[G_1(x)+\frac{\hbar\omega}{E}\frac{\hbar\omega}{E-\hbar\omega}G_2(x)\right] \\ G_1(x) &= \frac{\sqrt{3}\Gamma\left(\frac{1}{3}\right)}{32^{1/3}\pi}\int_x^\infty K_{\frac{5}{3}}(x')\mathrm{d}x' \\ G_2(x) &= \frac{\sqrt{3}\Gamma\left(\frac{1}{3}\right)}{32^{1/3}\pi}K_{\frac{2}{3}}(x). \end{aligned}$$

Since G is close to 1 almost everywhere for small x one can employ a rejection method to generate the photons. First a value v is chosen in the interval $[0,1]$. If a second random number is smaller than $G\left(v,\frac{\hbar\omega_c}{E}\right)$ a photon is emitted with an energy

$$\hbar\omega = \hbar\omega_c\frac{v^3}{1-\left(1-\frac{\hbar\omega_c}{E}\right)v^3}.$$

For the functions G_1 and G_2 a parametrisation can be used.

2.8 Simulation codes

The program ABEL [21] containing the pinch effect and pair creation was written by P. Chen, T. Tauchi and K. Yokoya. It allows for several options to calculate the fields.

Another simulation named GUINEA-PIG[1] was written by the author. It includes pinch effect, beamstrahlung, pair creation and calculation of hadronic backgrounds. It can compute the fields with the direct method, fast Fourier transformation and a Poisson solver. A description of the program and its input as well as output files can be found in appendix A.

[1]This is an abbreviation for Generator of Unwanted Interactions for Numerical Experiment Analysis—Program Interfaced to Geant.

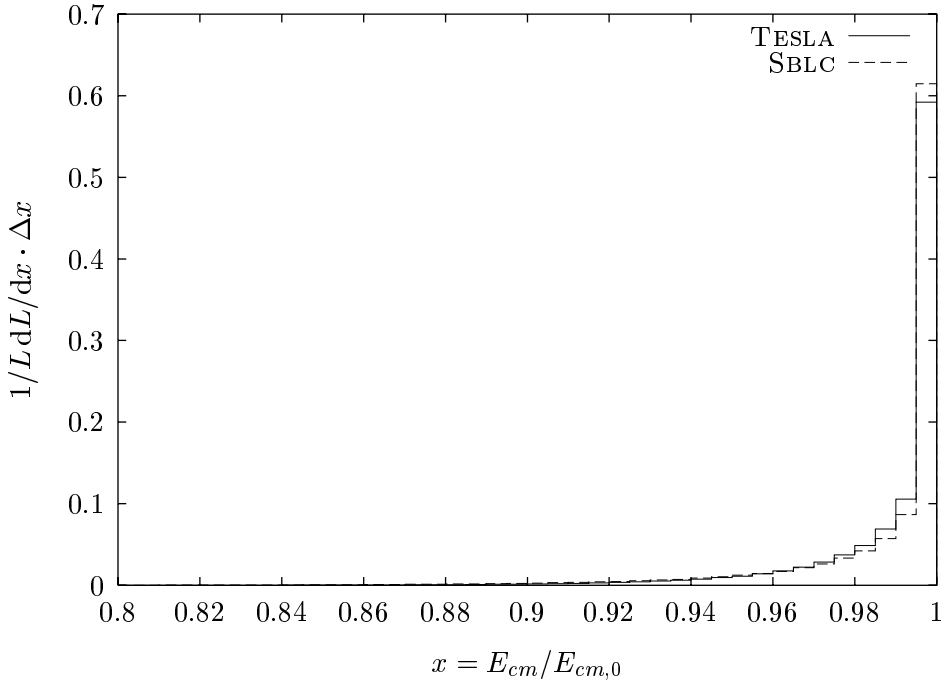

Figure 2.2: The luminosity spectrum resulting from the beamstrahlung only, for TESLA and SBLC. The bins have a width of $\Delta x = 0.5\%$.

2.9 Results

From simulations with GUINEA-PIG one obtains a mean energy loss $\delta \approx 2.5\%$ for TESLA. The luminosity enhancement is $H_D \approx 1.6$. For SBLC one finds $\delta \approx 2.9\%$ and $H_D \approx 1.7$, see Table 1.1. The differential luminosity spectra are shown in Figure 2.2. One can see that they are still nicely peaked at the nominal centre of mass energy. In Figure 2.3 the luminosity spectrum due to initial state radiation is shown for comparison. For the calculation of initial state radiation the formula [22]

$$\begin{aligned} f_e^e(x,Q^2) &= \frac{\beta}{2}(1-x)^{\frac{\beta}{2}-1}\left(1+\frac{3}{8}\beta\right) - \frac{\beta}{4}(1+x) \qquad (2.17) \\ \beta &= \frac{2\alpha}{\pi}\left(\ln\frac{Q^2}{m^2}-1\right) \end{aligned}$$

was used. $f_e^e(x,Q^2)$ is the probability that the electron has an energy xE_0 after initial state radiation. It is obvious that the spectrum due to initial state radiation is peaked more sharply at the nominal centre of mass energy than the one from beamstrahlung, but shows a longer tail towards lower energies. This tail is responsible for the average loss of 5% of the nominal centre of mass energy which is more than from the beamstrahlung. Figure 2.4 shows the low energy

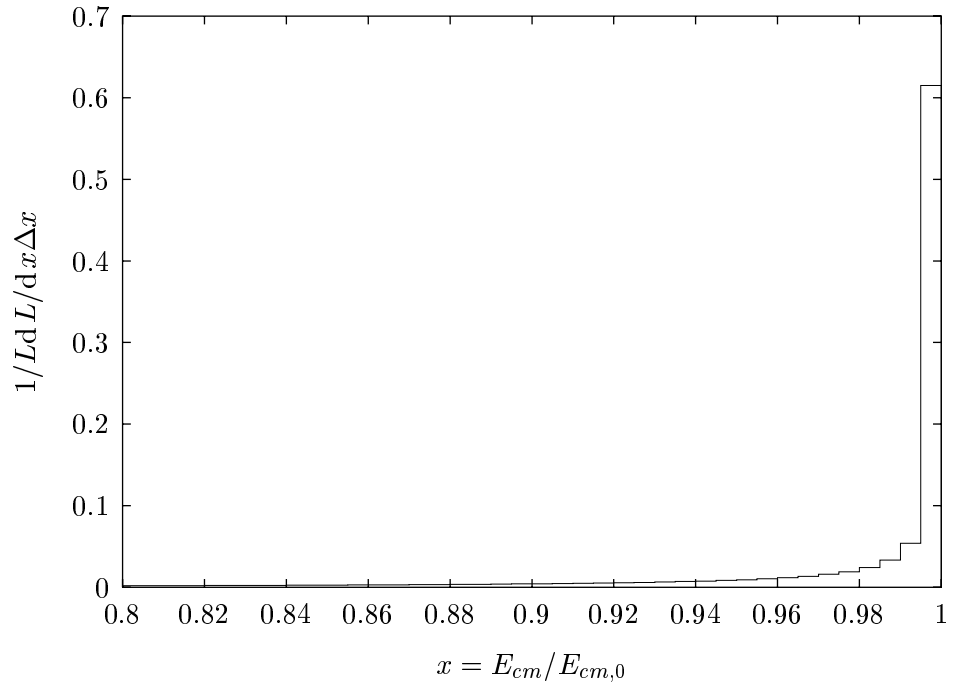

Figure 2.3: The luminosity spectrum due initial state radiation only. As a scale $Q^2 = s$ was taken.

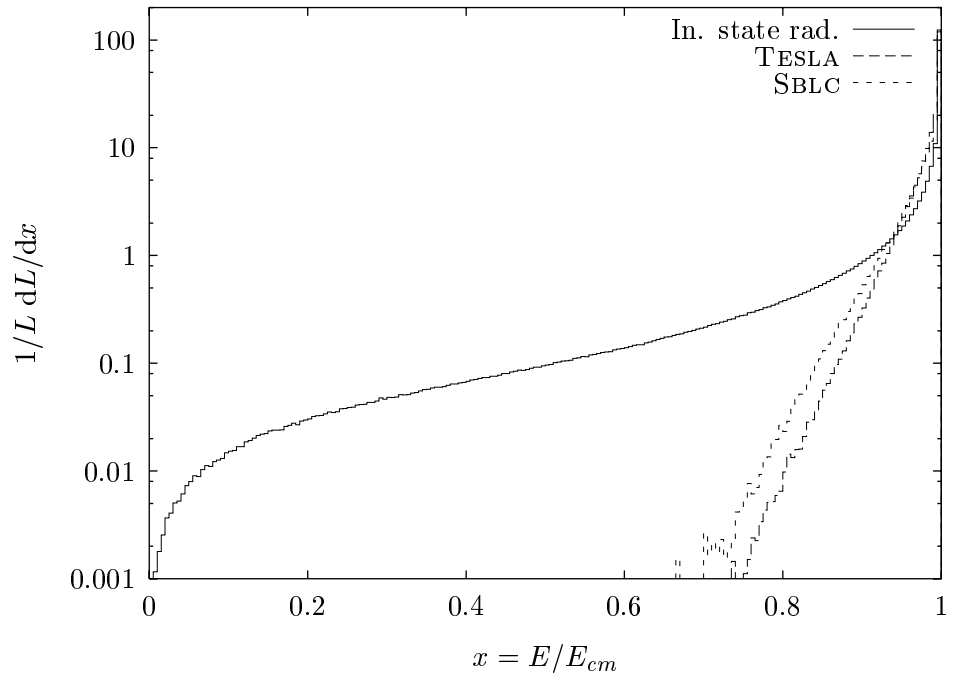

Figure 2.4: The luminosity spectra resulting from initial state radiation and from beamstrahlung alone.

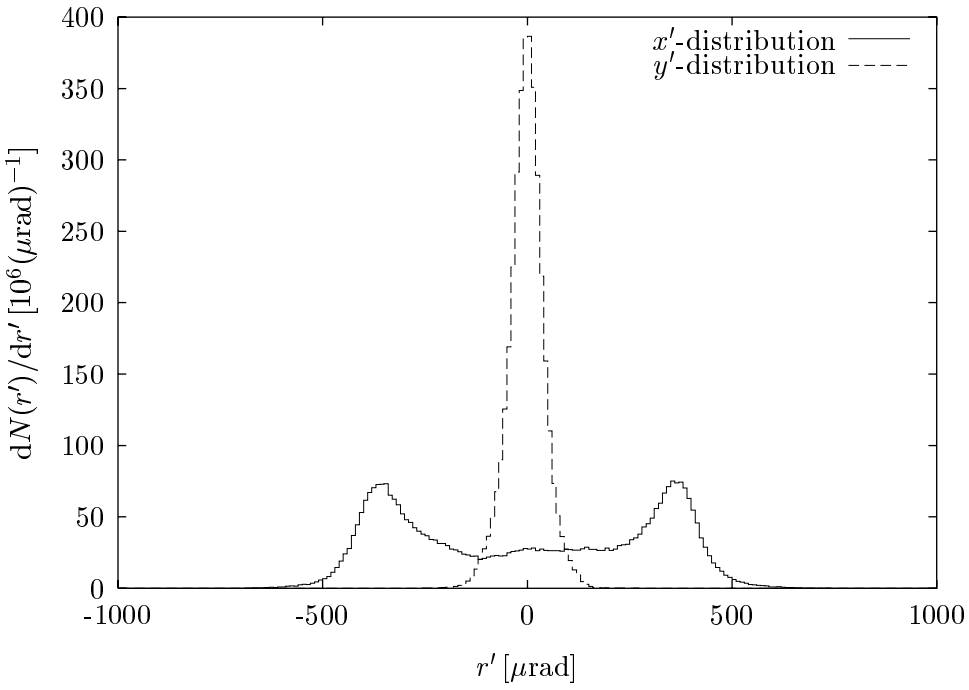

Figure 2.5: The angular distribution of the beam particles for TESLA after the interaction.

Name			JLC-S	JLC-C	JLC-X	JLC-S	JLC-C	JLC-X
E_{cm}	[GeV]		300	300	300	500	500	500
N	$[10^{10}]$		1.56	1.0	0.63	1.3	1.0	0.63
σ_x	[nm]		335	335	335	301	260	260
σ_y	[nm]		3.92	3.92	3.92	3.04	3.04	3.04
σ_z	[μm]		80	80	85	80	80	67
β_x	[mm]		10	10	10	10	10	10
β_y	[mm]		0.1	0.1	0.1	0.1	0.1	0.1
θ_c	[mrad]		11.0	10.4	9.0	7.3	8.0	7.2
L_c	$[10^{29}\mathrm{cm}^{-2}\mathrm{bc}^{-1}]$	A	15.3	6.1	2.4	17.5	10.0	4.7
		GP	15.1	6.0	2.3	16.9	10.0	4.5
δ	[%]	A	7.0	3.5	1.7	9.0	7.0	4.0
		GP	6.5	3.2	1.6	8.5	6.7	3.9

Table 2.1: Comparison of simulation results for the pinch effect from ABEL (A) and GUINEA-PIG (GP). The ABEL results are taken from reference [23].

part of the spectra. The region around $E_{CM} = M_{\mathrm{Z}}$ is dominated by initial state radiation.

A comparison of the results from GUINEA-PIG and ABEL is given in Table 2.1.

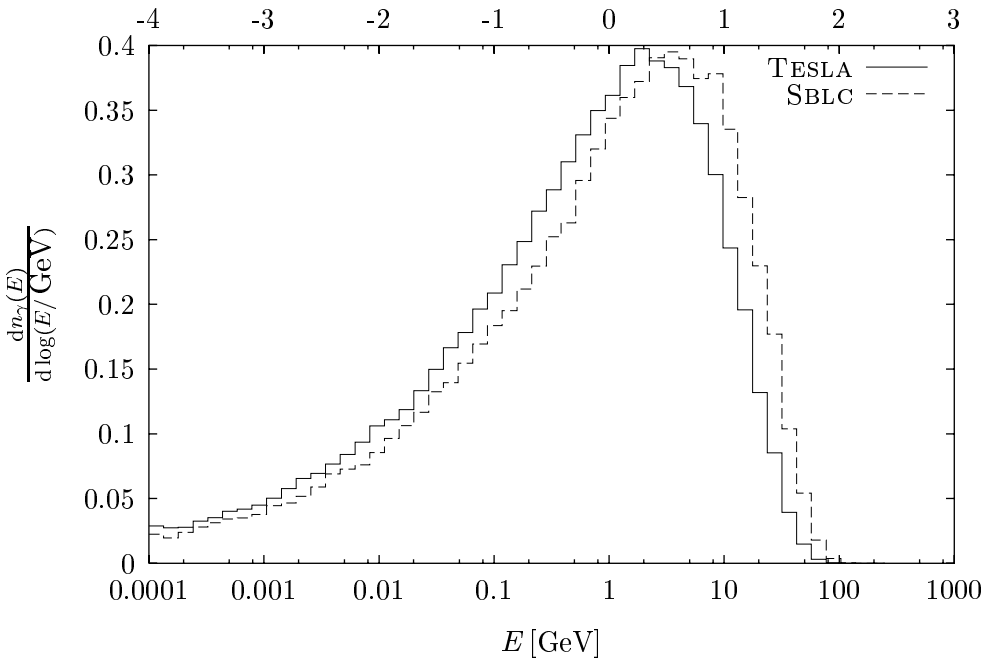

Figure 2.6: The beamstrahlung photon spectrum for TESLA and SBLC. The photon density over the logarithm of the energy is shown. The area below the curve is thus proportional to the number of photons.

The results from ABEL were taken from [23]. The agreement between the two programs is good.

Chapter 3

Beamstrahlung as a Background

The beamstrahlung can cause significant problems for the collider. For TESLA the power of the photons is about 0.2 MW per beam[1]. These photons go into a very small cone with an opening angle of the order of a few hundred micro radian, see Figure 3.1. Since the intensity of the photons is high it is difficult to stop them. In between the beamstrahlung collimators and the detector a septum magnet is necessary to separate the outgoing beam from the incoming beam line. The power deposition in this septum can be reduced by shielding. Detailed calculation were performed by tracking the photons and beam particles produced by GUINEA-PIG with STRUCT in reference [8].

3.1 Possibilities to cope with the beamstrahlung

Three different solutions are possible in principle to cope with the beamstrahlung. The first is to introduce a crossing angle between the two beam lines in the detector. This would allow to extract the photons through the same exit hole as the spent beam and dump them outside. As a second solution one can separate the outgoing photons from the incoming beam by bending the latter close to the detector. The third possibility is to collimate the photons in the beam line.

The first solution is not possible with the present set up, since there is no almost field free region in the superconducting final doublet. The spent beam has therefore to pass through the aperture of the quadrupoles and since it will be very much off axis due the crossing angle it experiences a strong field in the quadrupoles. One can think of using normal conducting quadrupoles. But the field in the detector in the present layout is 3 T. The quadrupoles extend into the detector and their iron will saturate at less 2 T. So it would be necessary to shield the quadrupoles from the outer field by a compensating solenoid. This

[1] This is already an improvement compared with the older TESLA parameters. For these the problem was investigated first, and due to the larger beam power resulted in about 0.5 MW photon power per beam.

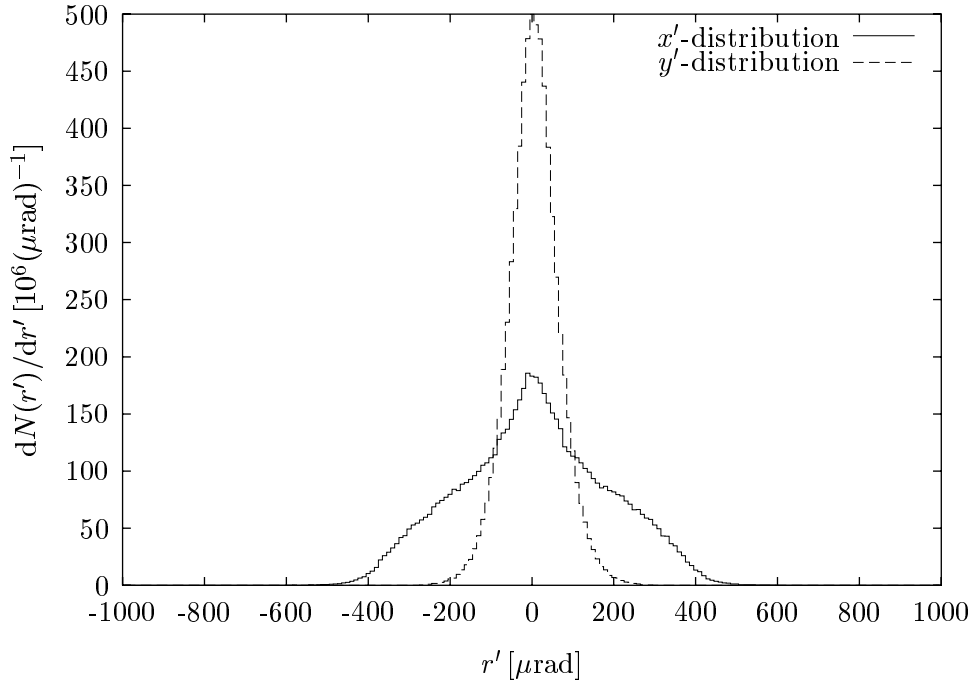

Figure 3.1: The angular distribution of the photons from beamstrahlung for TESLA.

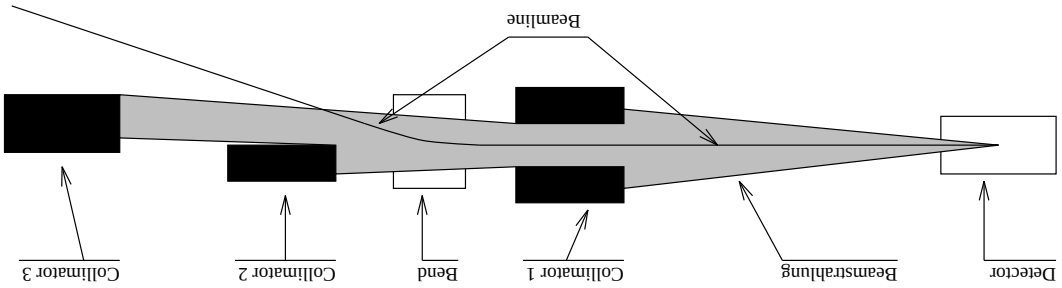

Figure 3.2: Sketch of the collimation of the beamstrahlung.

solenoid will disturb the field inside the detector since it has to bend the field lines from the inner part of the detector to the outside.

With the second solution the incoming beam particles would emit synchrotron radiation in the bend. Since the bend is close to the detector it will be very difficult to collimate this radiation.

The last solution is difficult because of the high intensity of the beamstrahlung. The collimation would have to be done in three steps. The aperture restrictions of the quadrupoles from the second doublet require that the outer cone of the photons is collimated in front of them. The inner core passes through the aperture of the magnets. The second collimator is necessary to shield the optical elements further away from the detector. The innermost cone of the photons is

absorbed in a third stage when the incoming beam line is separated sufficiently from it.

The upper limit for the radius of the first collimator this scheme is about 8 mm. This collimator will be the most critical since it has to intercept most of the power.

Another limit on the maximal radius arises from the requirement that the beamstrahlung collimator should act as a collimator for the synchrotron radiation emitted by the incoming beam in the last bend before the detector. These collimators should not be placed close to the detector to prevent from secondaries hitting the beam pipe in the detector. At a larger distance the required maximal aperture of this collimator however becomes so small that it will be hit by the beamstrahlung on the other side. It is therefore sensible to combine the two collimators.

For the collimators two different designs are considered. The first is a fluid collimator that is a thin beam pipe which is surrounded by water. The second is a solid collimator made from graphite.

3.2 Simulation of the fluid collimator

The collimator consists of a titanium beam pipe with an inner radius of 4 mm and a thickness of 0.5 mm, which should be sufficient to allow for a water flow of 3 m/s [25]. In the simulation the pipe is surrounded by a cylinder of water. The distance to the interaction point is 70 m. A calculation with the detector simulation program GEANT has been done in order to estimate the energy deposition and the stresses in the fluid collimator. A number of photon which were first produced with GUINEA-PIG was tracked through this set up.

The first problem can be the heating of the water. In the simulation the water formes a cylinder around the beam pipe. This cylinder is subdivided a hundred times along the beam axis, twenty times in radial direction and sixteen times in azimuth. For each small cell the deposited energy is calculated. The dependence of the maximal loss per volume on z is shown in Figure 3.3. The maximal power density is approximately 40 W/cm^3. This corresponds to a temperature rise of roughly 10 K per second. Since logitudinall flowing water needs less than 1 s to pass the region of the main energy deposition it will be heated by less than 10 K.

The heating of the beam pipe might be another problem. Figure 3.4 shows the power deposition per unit length in the beam pipe. The second histogram is the power deposition in the one of the sixteen segments of the beam pipe that is heated most multiplied by sixteen. The difference between the two values is not very large so one can conclude that the power is azimuthally almost uniformly distributed in the beam pipe. The longitudinal distribution shows a significant peak close to the end of the collimator pointing towards the detector. This is due to the shower evolution in the titanium since the photons enter almost parallel to

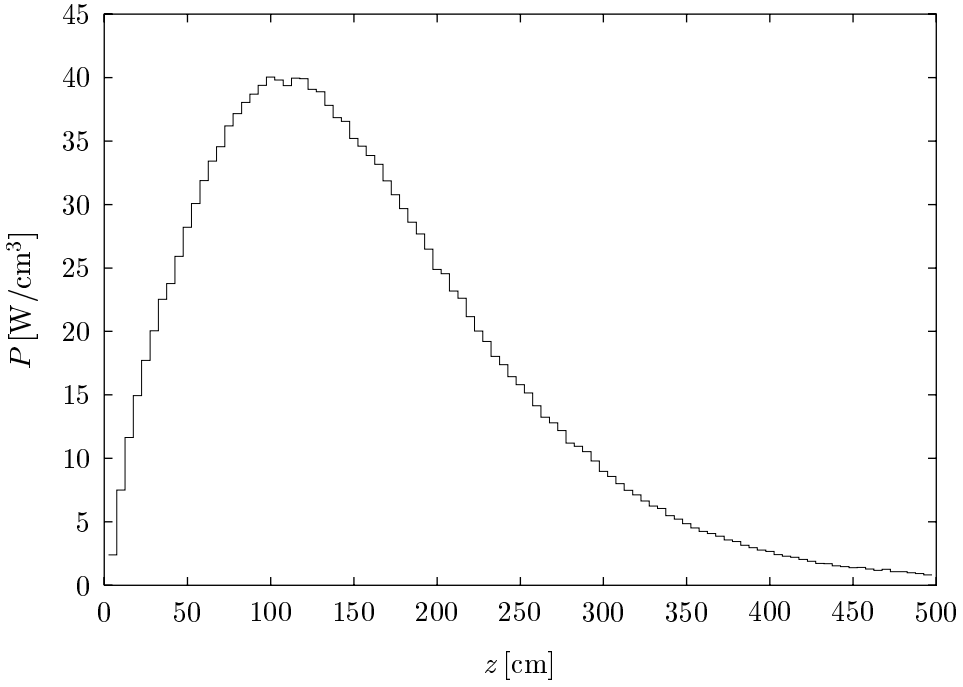

Figure 3.3: Maximal power density in the water of the beamstrahlung collimator.

the axis of the pipe. The sharp peak is followed by a shoulder. This is due to the shower evolution in the water. The showers evolving there feed power into the titanium pipe. The simulation shows that the maximal power per unit length in the beam pipe is expected to be 21 W/cm. The heat capacity per length of the pipe is $C = 0.32\,\mathrm{J/(cmK)}$. The resulting temperature rise is thus about 66 K/s or $\Delta T = 13\,\mathrm{K}$ per bunch train.

The beampipe has to be cooled between the bunch trains. The heat conductivity λ of water is relatively low; $\lambda \approx 0.6\,\mathrm{W/(mK)}$ at room temperature. But the flow of the water increases the heat transport significantly. This increase is given by the Nußelt-parameter Nu. From

$$Nu = \frac{\alpha d}{\lambda} \tag{3.1}$$

where d is the typical length, one can find the heat transport coefficient α.

The Reynolds number Re is given by $Re = \frac{wd}{\nu}$, where w is the speed of the water and ν is the kinematic viscosity. For water of room temperature one finds $\nu = 10^{-6} m^2/s$. In the present case one has to consider turbulent flow since $Re > 2300$ turns out to fulfilled for almost all outer radii.

For a turbulent longitudinal flow in a tube with length l and radius r the

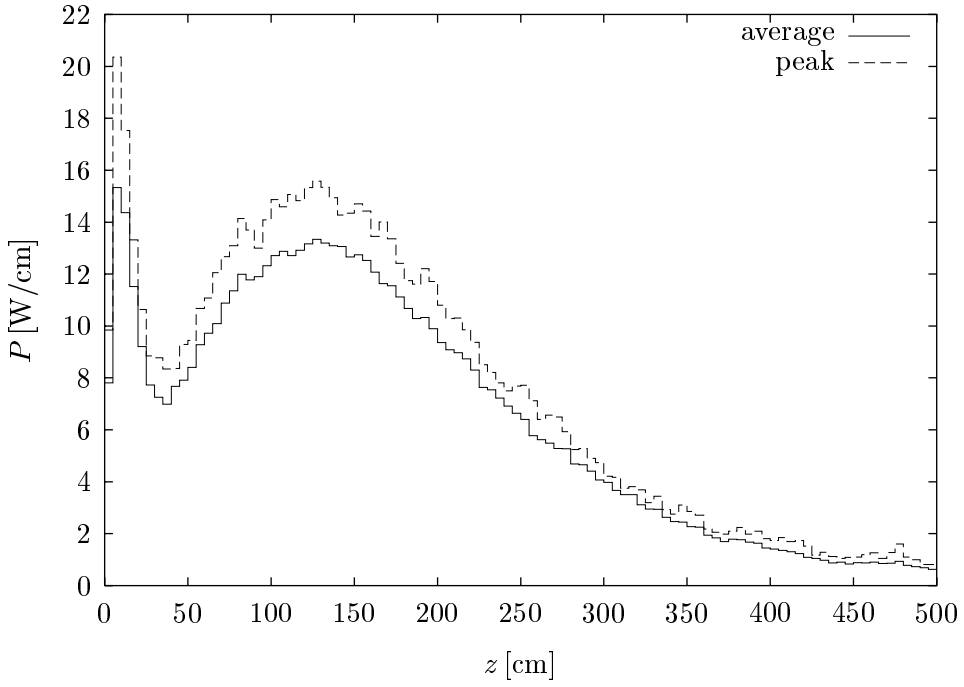

Figure 3.4: Power deposition in the beam pipe. The peak power deposition is the one in the segment with the highest value times the number of segments. This is the value to be used in the calculations.

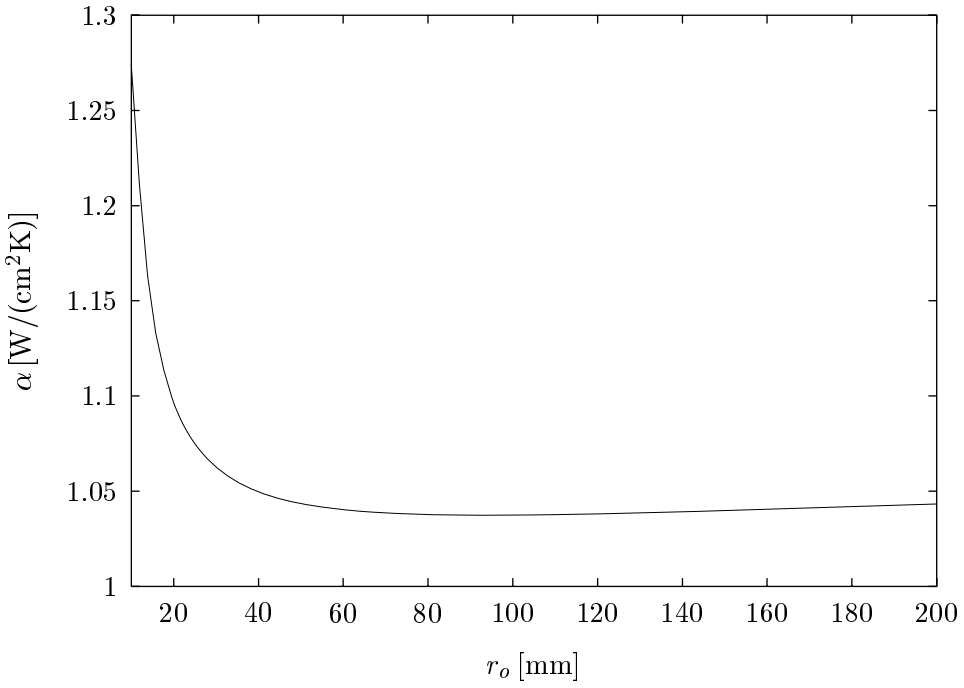

Figure 3.5: The heat transfer coefficient α as a function of the radius of the outer pipe. The inner pipe has a radius of 4.5 mm.

Nußelt parameter can be approximated as [26]

$$Nu \approx \frac{\frac{\zeta}{8}(Re-1000)\,Pr}{1+12.7\sqrt{\frac{\zeta}{8}}\,(Pr^{2/3}-1)}\left(1+\left(\frac{d}{l}\right)^{2/3}\right)\left(\frac{Pr_f}{Pr_w}\right)^{0.11} \tag{3.2}$$

$$\zeta = (1.82\log Re - 1.64)^{-2} \tag{3.3}$$

With the Prandtl number $Pr \approx 7$ for water of room temperature. Pr_f is the Prandtl number at the mean temperature of the fluid and Pr_w that at the temperature of the cylinder. The typical length is $d = 2r$ in the present case. The term $(Pr_f/Pr_w)^{0.11}$ gives a small correction and can therefore be neglected. Since $d \ll l$ the same is true for the term $(1 + (d/l)^{2/3})$. In the case of two concentric tubes with water flowing in between them the diameter d has to be replaced by the difference of inner and outer diameter $d = d_o - d_i$. The Nußelt parameter for the inner tube only, is then given by

$$Nu_i = 0.86\left(\frac{d_o}{d_i}\right)^{0.14} Nu \tag{3.4}$$

Figure 3.5 shows the resulting heat transfer coefficient as a function of the outer radius. From this one can conclude

$$\alpha \approx 1.0 \frac{\mathrm{W}}{\mathrm{cm^2K}} \tag{3.5}$$

If one compares this to the heat transport from the inner to the outer surface of the beam pipe where $\lambda \approx 22\,\mathrm{W/(mK)}$

$$\alpha_{\mathrm{bp}} \approx 4.4 \frac{\mathrm{W}}{\mathrm{cm^2K}}$$

one finds that the heat transport between the water and the beam pipe is the more important problem.

The maximal temperature of the beam pipe can be calculated. In the equilibrium the beam pipe has a temperature T_1 right after the passage of a bunch train ($t = 0$). The temperature drops to T_2 just before the arrival of the next train. The difference between these two temperatures is $T_1 - T_2 = \Delta T \approx 13\,\mathrm{K}$. The mean temperature of the water is T_0. Assuming that the energy flow into the water is proportional to the temperature difference one gets:

$$\frac{d\,E}{d\,t} = C\frac{d\,T}{d\,t} = -K(T - T_0) \tag{3.6}$$

Here $C \approx 0.32\,\mathrm{J/(cmK)}$ is the heat capacity of the beam pipe per unit length as before and $K = \alpha \cdot 2\pi r_{out}$ is the heat flux through the outer surface of the beam pipe. One finds

$$T = (T_1 - T_0)e^{-K/C\,t} + T_0 \tag{3.7}$$

Using $t_2 = \Delta t$ one finally gets

$$T_1 = T_0 + \Delta T \frac{1}{1 - e^{-K/C\,\Delta t}} \tag{3.8}$$

Inserting $\Delta t = 200\,\mathrm{ms}$ and $\Delta T = 13\,\mathrm{K}$ one finds $T_1 \approx T_0 + 1.21 \cdot 13\,\mathrm{K} \approx 16\,\mathrm{K} + T_0$. The temperature difference between titanium and water is thus sufficiently low not to produce vapor.

The temperature differences in the titanium causes stress. For the instantaneous temperature rise this can be approximated by

$$\sigma_I = 1.5 E \alpha_E \Delta T \tag{3.9}$$

E is the elastic modulus, α_E the coefficient of linear expansion, ΔT the temperature rise and σ_I the resulting stress. Using $E = 88 \cdot 10^6\,\mathrm{MPa}$ and $\alpha = 8.5 \cdot 10^{-6}\,\mathrm{K}^{-1}$ one finds $\sigma_I \approx 18\,\mathrm{MPa}$, conservatively including the static temperature rise by using $\Delta T = 15\,\mathrm{K}$. The endurance limit for repeated cycles is $\sigma = 350\,\mathrm{MPa}$ for titanium [27]. The stress induced by the photons will thus be well below this value.

The pressure difference Δp necessary to achieve the flow of $3\,\mathrm{m/s}$ can be calculated using [28]

$$\Delta p = \frac{\lambda_R l}{d} \frac{1}{2} \rho w^2 \tag{3.10}$$

where λ_R is the pipe resistivity and ρ the density of the fluid. For smooth surfaces one can use $\lambda_R = \zeta$. For a radius of the outer pipe of more than $50\,\mathrm{mm}$ the pressure difference per unit length $\Delta p / l = 75\,\mathrm{hPa/m}$ is small.

The dumped photons produce hydrogen in the water at a rate of approximately $0.3\,\mathrm{l/MJ}$. So one has to expect $0.06\,\mathrm{l/s}$ for the $0.2\,\mathrm{MW}$ of photon power. The accumulated hydrogen can of course cause a hazard. This problem can be solved by using a catalytic hydrogen-oxygen recombiner as described in reference [29].

A remaining problem is the radioactivity produced in the collimator. The major product in the water will be $^{15}\mathrm{O}$. Its half life time is about $120\,\mathrm{s}$ only. For longer living products like $^{7}\mathrm{Be}$ a filtering of the water may be necessary.

3.3 Considerations on a solid collimator

Another solution would be the use of a thick tube with an inner radius that is decreased in small steps to spread the energy loss over a length that is sufficient to ensure cooling. The outer surface is cooled as in a beam dump. The length of such a system is determined by the maximal power per unit length that can be transported transversely out of the collimator without exceeding the stress limit of the material.

The outer radius of the tube is assumed to be $b = 20\,\mathrm{cm}$ to ensure that most of the power is stored inside the collimator. The power one can remove through a tube with a temperature difference ΔT is $P = 2\pi l\lambda\Delta T/\ln(b/a)$. Since the dependence on the inner radius a is only logarithmic one can use the smallest $a = 0.4\,\mathrm{cm}$. This leads to $P/l = 0.5\,\mathrm{kW/(mK)}\,\Delta T$. The stress in a thick walled tube can be calculated as [30]

$$\sigma_r(r) = \frac{\alpha E}{1-\nu}\left[\left(1-\frac{a^2}{r^2}\right)\frac{1}{b^2-a^2}\left(f(b)-f(a)\right)-\frac{1}{r^2}\left(f(r)-f(a)\right)\right] \quad (3.11)$$

$$\sigma_\phi(r) = \frac{\alpha E}{1-\nu}\left[\left(1+\frac{a^2}{r^2}\right)\frac{1}{b^2-a^2}\left(f(b)-f(a)\right) + \frac{1}{r^2}\left(f(r)-f(a)\right)-T(r)\right] \quad (3.12)$$

$$\sigma_z(r) = \frac{\alpha E}{1-\nu}\left[\frac{2\nu}{b^2-a^2}\left(f(b)-f(a)\right)-T(r)\right]. \quad (3.13)$$

with ν the Poisson number. One has

$$f(r) = \int (T(r') - T_0) r' \mathrm{d}r'. \quad (3.14)$$

T_0 is the temperature at which the material is stress free. Using $T_0 = T(b)$ one finds

$$T(r) - T_0 = \frac{\ln\frac{r}{b}}{\ln\frac{a}{b}}\Delta T. \quad (3.15)$$

This gives

$$f(r) = r^2\frac{\ln\frac{r}{b}-\frac{1}{2}}{2\ln\frac{a}{b}}\Delta T. \quad (3.16)$$

Figure 3.6 shows the stress in an aluminium tube for a temperature difference of 40 K. The stress is approximately at the limit of the material. This gives a maximal power $\hat{P}/l \approx 20\,\mathrm{kW/m}$. Since the distribution of the power at the inner surface of the tube is not homogeneous and the instantaneous heating of a few K has to be taken into account, a safety factor of two should be allowed. The collimator must therefore already be 20 m long.

A better solution may be the use of graphite. One of the types that can be delivered by industry has a heat conductivity of $\lambda = 107\,\mathrm{W/mK}$. It can stand the same stress as aluminium ($\sigma_{0.2} = 95\,\mathrm{MPa}$) but its thermal expansion coefficient and its elastic modulus are lower ($\alpha_E = 3.8\cdot 10^{-6}\,\mathrm{K}^{-1}$ and $E = 1.2\,\mathrm{GPa}$). The maximal allowed temperature difference is thus given by the sublimation temperature $T_{\mathrm{melt}} \approx 2000\,\mathrm{K}$ rather than the stress limit. The dependence of the properties of the graphite on radiation damage that may be induced by beamstrahlung has to be tested.

The instantaneous temperature rise of the material of a solid collimator can be also estimated using a GEANT simulation. As a very simple model for the

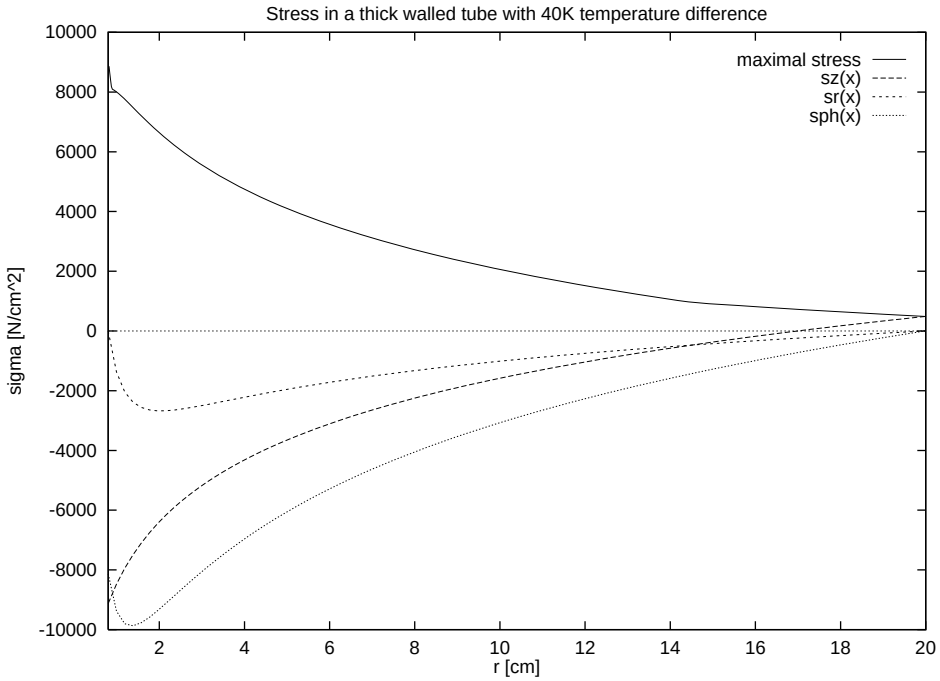

Figure 3.6: Stress in the beamstrahlung collimator.

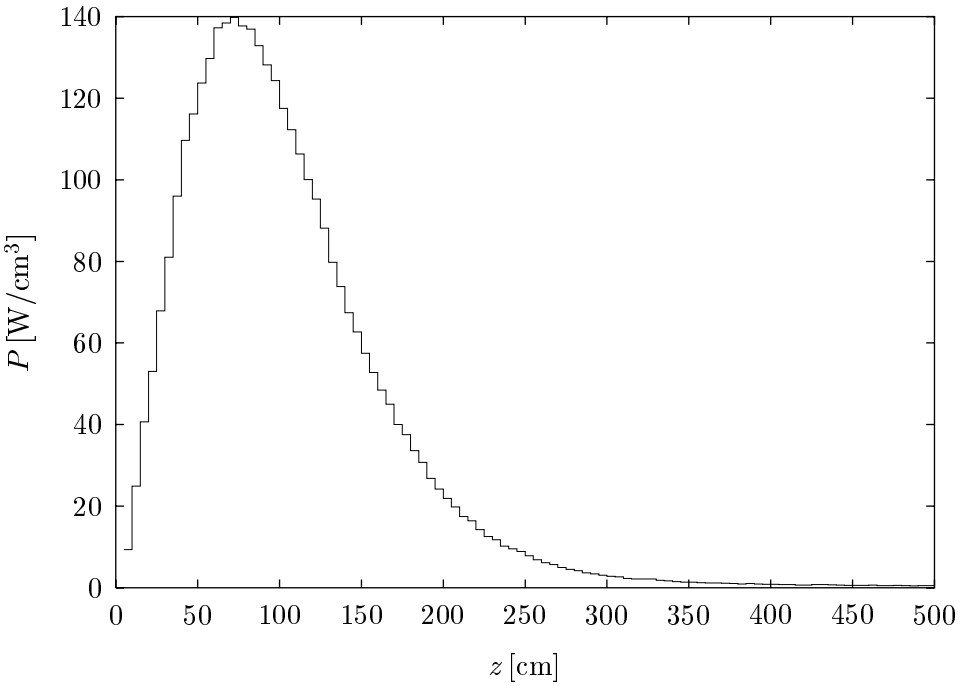

Figure 3.7: Power density of the energy deposition by the beamstrahlung photons in the collimator.

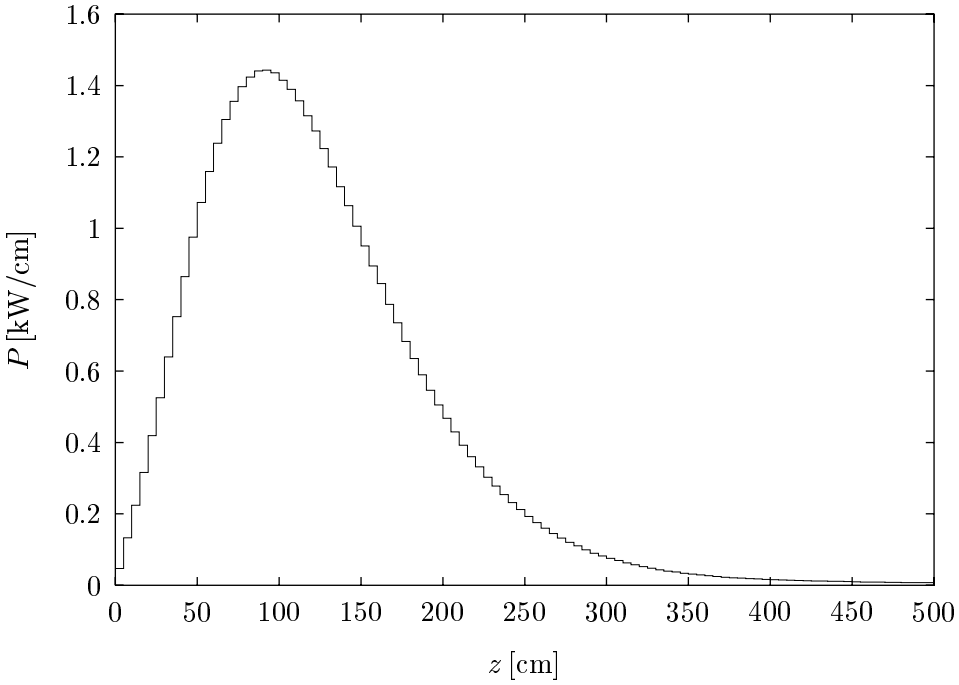

Figure 3.8: Power per length deposited in the collimator assuming one step of collimation only.

collimators a cylinder is used. It is placed in different distances to the interaction point and the energy deposition into the centre is calculated. Figure 3.7 shows the maximum power density in the material for a distance of 70 m between interaction point and collimator. This results in a maximal temperature rise of about 90 K. If the collimation would be done in one step the resulting temperature difference between the inner and outer surface of the collimator would be about 800 K. Using a few steps one can reduce this easily. To avoid the graphite destroying the vacuum and to suppress possible wakefields it seems necessary to have a titanium beam pipe inside which has to be closely connected to the graphite to ensure sufficient heat transport. The endurance limit of titanium $\sigma_{0.2} = 350$ MPa allows for temperature jumps of about 300 K or for a static temperature increase more twice as large. A solid collimator thus seems feasible but much closer to the limit than the fluid one.

Chapter 4

Creation of Pairs and Low Energy Particles

Two possibilities exist for pair creation in the beam-beam interaction. A photon can turn into a virtual electron-positron loop. In a strong field the particles from the loop can be set onto the mass shell. This process is can be deduced from synchrotron radiation if one exchanges the incoming electron and the outgoing photon. This process is called coherent pair creation for obvious reason.

In addition one has to consider the incoherent pair creation. Two colliding real photons from the beamstrahlung can produce an e^+e^--pair. An electron (or positron) is accompanied by a spectrum of virtual photons. These photons can produce pairs with the real or virtual photons of the other beam as well. So one has three incoherent processes in total. In the Breit-Wheeler process $\gamma\gamma \to e^+e^-$ both photons are real, in the Bethe-Heitler process $e\gamma \to e\, e^+e^-$ one is real and one virtual and in the Landau-Lifshitz process $ee \to ee\, e^+e^-$ both photons are virtual. Low energy particles are also produced if a beam particle looses a significant amount of its energy via bremsstrahlung.

4.1 Coherent pair creation

The probability per unit length for a photon with energy $\hbar\omega$ to turn into an $\mathrm{e^+e^-}$ pair in a magnetic field of strength B is given by [31]:

$$\frac{\mathrm{d}w}{\mathrm{d}z} = \frac{\alpha^2}{r_e}\frac{B}{B_c}T(\kappa) \tag{4.1}$$

with $B_c = m^2c^2/(e\hbar)$ and

$$\kappa = \frac{\hbar\omega}{mc^2}\frac{B}{B_c}.$$

The value of B/B_c is related to the beamstrahlung parameter Υ from equation (2.7) via

$$\frac{B}{B_c} = \frac{\Upsilon}{\gamma} = \frac{\hbar\gamma}{mc\rho}. \tag{4.2}$$

$T(\kappa)$ is given by

$$T(\kappa) \approx \frac{4}{25}\frac{1}{\kappa}K^2_{\frac{1}{3}}\left(\frac{4}{3\kappa}\right) \tag{4.3}$$

with the two asymptotic limits

$$T(\kappa) = 0.23\exp(-8/(3\kappa)), \kappa \ll 1$$
$$T(\kappa) = 0.38\kappa^{-1/3}, \kappa \gg 1.$$

The first expression exceeds the value from equation (4.3) for values of κ of the order of 1. An expression that approximates both regimes is given in [10]:

$$T(\kappa) = \frac{0.23e^{-\frac{8}{3\kappa}}}{(1+0.22\kappa)^{-\frac{1}{3}}}$$

The probability for a photon to turn into a pair is very sensitive to the field. Using the average beamstrahlung parameter will thus not be sufficient. For a fixed beamstrahlung parameter the total number of pairs produced can be calculated by folding the Sokolov-Ternov spectrum for this parameter with the probability of the photons to turn into pairs. The integration leads to [10]

$$n = \frac{2\sqrt{3}}{25\pi}\left(\frac{\alpha\sigma_z}{\gamma\lambda_c}\Upsilon\right)^2 G(\Upsilon) \tag{4.4}$$

with the first term being of the order of one and the second:

$$G(\Upsilon) \approx \exp(-16/(3\Upsilon)), \Upsilon \ll 1$$
$$G(\Upsilon) \approx 5.2\Upsilon^{-2/3}\ln\Upsilon, \Upsilon \gg 1$$

In machines with small beamstrahlung parameter the coherent pair creation is thus exponentially suppressed.

The contribution of virtual photons to the coherent pair creation starts to become important compared to the real ones at $\Upsilon \approx 10^3$.

Even if the coherent pair creation is not totally suppressed it does not necessarily create a background. The produced particles move almost along the direction of motion of the photon. Since their spectrum is very hard with a lower limit $\hbar\omega/E_0 \approx 1/(5\Upsilon)$ they leave the detector if the beam crossing angle is large and the deflection angle of the particles in the fields of the beam are small enough. This will be helpful at higher beamstrahlung parameter at higher energies.

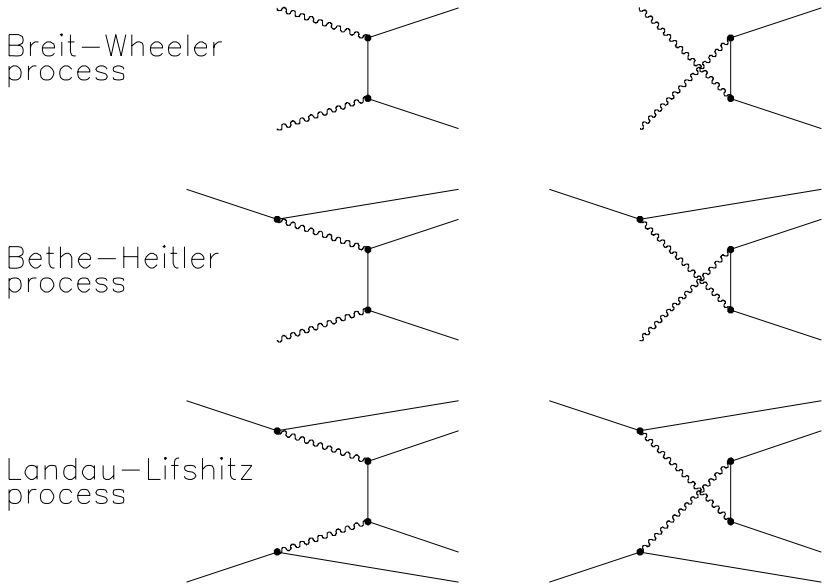

Figure 4.1: The incoherent pair production processes.

4.2 The cross sections for incoherent pair creation

The differential cross section for the Breit-Wheeler process can be found in reference [32]:

$$\begin{aligned}\frac{\mathrm{d}\sigma}{\mathrm{d}t} &= \frac{2\pi r_e^2 m^2}{s^2}\left[\left(\frac{t-m^2}{u-m^2}+\frac{u-m^2}{t-m^2}\right)-4\left(\frac{m^2}{t-m^2}+\frac{m^2}{u-m^2}\right)\right. \\ &\quad \left.-4\left(\frac{m^2}{t-m^2}+\frac{m^2}{u-m^2}\right)^2\right] \qquad (4.5)\end{aligned}$$

where $s=(k_1+k_2)^2$, $t=(k_1-p_1)^2$ and $u=(k_1-p_2)^2$ are the Mandelstam variables; k_i are the four momenta of the incoming photons, p_i those of the outgoing electron and positron. For the production of muon pairs the electron mass has to be replaced by the muon mass exept in the first factor.

The cross section in equation (4.5) can be easily integrated in the centre of mass frame using $t-m^2=-s/2(1-\beta\cos\theta)$ and $u-m^2=-s/2(1+\beta\cos\theta)$. One gets

$$\begin{aligned}\sigma(\beta\cos\theta) = \frac{\pi r_e^2 m^2}{s}&\left[\left(2+\frac{2}{\gamma^2}-\frac{1}{\gamma^4}\right)\ln\frac{1+\beta\cos\theta}{1-\beta\cos\theta}\right. \\ &\left.-\left(2+\frac{2}{\gamma^4}\frac{1}{1-(\beta\cos\theta)^2}\right)\beta\cos\theta\right]. \qquad (4.6)\end{aligned}$$

This gives a total cross section of

$$\sigma_{BW} = \frac{2\pi r_e^2 m^2}{s}\left[\left(2+\frac{2}{\gamma^2}-\frac{1}{\gamma^4}\right)\ln\frac{1+\beta}{1-\beta}-\left(2+\frac{2}{\gamma^2}\right)\beta\right]. \tag{4.7}$$

The total cross section for the Bethe-Heitler process is approximately given by [32] (using $c = 1$):

$$\sigma_{BH} = \frac{28\alpha r_e^2}{9}\left(\ln\frac{s}{m^2}-\frac{109}{42}\right) \tag{4.8}$$

It varies only slowly with the photon energy. For the Landau-Lifshitz process the total cross section is given by [33]:

$$\sigma_{LL} = \frac{\alpha^2 r_e^2}{\pi}\left(\frac{28}{27}\ln^3\frac{s}{m^2}-6.59\ln^2\frac{s}{m^2}-11.8\ln\frac{s}{m^2}+104\right) \tag{4.9}$$

The production of $\mu^+\mu^-$-pairs is suppressed due to the large muon mass. Only at very large transverse momenta, when the particles energy in the centre of mass system exceed their mass significantly the muon contribution is comparable to that of the electron.

4.3 The equivalent photon approximation

The equivalent photon (or Weizäcker-Williams) approximation allows to calculate the Bethe-Heitler and Landau-Lifshitz cross sections easily. In this approach the virtual photons accompanying a charged particle are assumed to be real. Their spectrum is folded with the cross section for the interaction of two real photons.

The virtual photon spectrum is approximately given by [34]

$$\frac{\mathrm{d}^2 n_v(x)}{\mathrm{d}\,x\,\mathrm{d}\,Q^2} = \frac{\alpha}{2\pi}\frac{1+(1-x)^2}{x}\frac{1}{Q^2} \tag{4.10}$$

where $xE = \hbar\omega$ is the photon energy and Q^2 its virtuality squared. Integrating over Q^2 one finds

$$\frac{\mathrm{d}\,n_v(x)}{\mathrm{d}\,x} = \frac{\alpha}{2\pi}\frac{1+(1-x)^2}{x}\ln\frac{\hat{Q}^2}{\check{Q}^2} \tag{4.11}$$

The lower boundary $\check{Q}^2$ can for high $\hat{Q}^2$ be approximated as:

$$\check{Q}^2 = \frac{x^2 m^2}{1-x} \tag{4.12}$$

The upper limit $\hat{Q}^2$ depends on the process which one wants to calculate.

4.4 The beam size effect

In the MD-1 experiment at VEPP-4 the observed bremsstrahlung cross section was smaller for soft photons than expected [35]. This effect could be explained with the beam size effect, see for example reference [36]. In this model one assumes that the virtual photons are not located at the position of the electron but actually are smeared. For a virtual photon with transverse momentum $q_\perp$ the typical impact parameter is $b \approx \hbar/q_\perp$. If the transverse momentum is small this impact parameter can exceed the transverse size of the beam and will thus reduce the cross section. This effect was also observed at HERA [37], see reference [38].

Within the equivalent photon approximation this effect can be described by introducing a lower cutoff for the transverse momentum of the equivalent photons at $\check{q}_\perp = \hbar/\sigma_y$. In the beam-beam simulation this effect can be taken into account by offsetting the virtual photon with the typical impact parameter with respect to the electron position. This may lead to a substancial suppression of the pair production.

4.5 Effect of the field of the oncoming beam

The oncoming beam produces a strong electromagnetic field. Since the particle trajectories are bent by these fields virtual photons with a small angle $\omega_\perp/\omega$ are suppressed [39]. The minimal transverse momentum transfer is in this case given by

$$\check{q}_\perp \approx xmc \left(\frac{\omega_c}{\omega}\right)^{1/3} \tag{4.13}$$

In the low energy part of the equivalent photon spectrum the beam size effect gives a stronger reduction than the external field. Since the mechanism is the same—increasing the minimal transverse momentum of the virtual photons—they do not add up. In an intermediate region of the photon spectrum the external field effect can be more important than the beam size effect. It can lead to a small reduction of the particles with higher transverse momentum.

4.6 Simulation of pair creation

In GUINEA-PIG the photons are not represented by macro photons with different energies, the same way as the beam particles. The pairs from the Breit-Wheeler process are produced in a subroutine that is called for each collision of two macro photons.

If the effect of the external field is switched on, virtual photons with a transverse momentum below the cutoff in equation (4.13) are rejected. The virtual photons are offset with respect to the electron position if the beam size effect is switched on in the simulation. In the subroutine calculating the cross section the

virtuality is taken into account to determine whether the photon contributes to the pair production.

4.7 Comparison to the Vermaseren Monte-Carlo

The above approximation have to be compared to a fully analytic calculation and experimental data. A program to calculate the Landau-Lifshitz cross section was written by Vermaseren [40].[1] It consists of the Monte-Carlo integration routine VEGAS [41] and a function to calculate the differential cross section.

The muon production predicted by this program was compared with data from JADE [42]. The agreement was found to be good. An especially interesting investigation was done at PEP [43]. Here the production of electron-positron pairs was compared to the predictions of the generator and found to be in good agreement. Figure 4.2 shows the dependence of the production rates on the transverse mass $m_t = \sqrt{m^2 + p_\perp^2}$ for the Vermaseren Monte Carlo and the equivalent photon approximation. For the equivalent photon method three different Q scales are used. The first is the mass of the electron, the second the transverse mass of the final state particles and the third half the centre of mass energy of the scattering. The latter two give almost the same result regarding the transverse distribution. The choice $Q^2 = m^2$ significantly underestimates the rate of particles with high transverse momentum. The agreement with the Vermaseren Monte-Carlo is within 50% for the other two choices. A patch factor 1.5 is thus applied in the latter estimate of the effects of this background. The difference is due to events where one of the produced particles has a transverse momentum significantly different from that of the other, something which does not occur in the simplified model.

4.8 Results on pair production

The total number of pair particles produced by the three processes is of the order $1.5 \cdot 10^5$ per bunch crossing for TESLA if one does not take the beam size effect into account, see Table 4.1. They represent a total energy of about $2.7 \cdot 10^5$ GeV $\approx 500 \cdot E_{cm}$. This can pose significant problems for the detector. The number of particles produced per bunch crossing is about 10^5 with a total energy of $1.6 \cdot 10^5$ GeV in the case of TESLA and $2.6 \cdot 10^4$ particles with $5.3 \cdot 10^4$ GeV for SBLC. The numbers for the different processes with and without taking into account the beam-size effect can be found in Table 4.1.

The energy spectra of the produced particles are shown in Figure 4.4 for the calculation with and without the beam size effect. In the Breit-Wheeler process as well as in the Landau-Lifshitz process most particles are produced with low

[1] It should be noted that the Vermaseren Monte Carlo does not contain the beam-size effect.

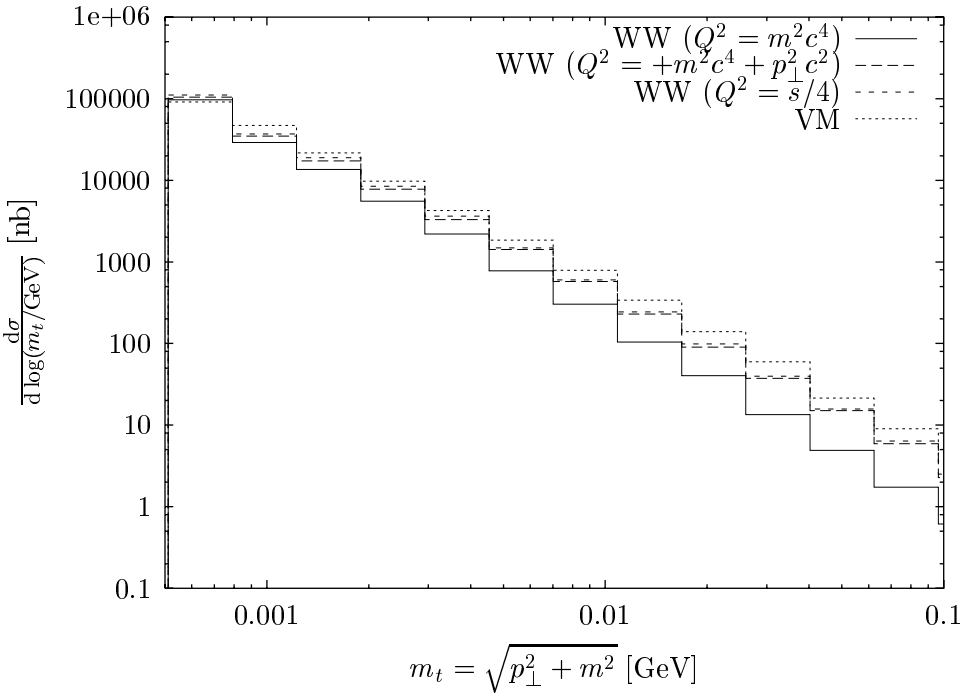

Figure 4.2: The dependence of the pair production cross section on the transverse mass for the equivalent photon approximation (WW) with several different Q^2-scales and the Vermaseren Monte Carlo.

	BW		BH		LL	
	N	E	N	E	N	E
TESLA	3.8	2.0	97	172	48	94
	3.8	2.0	65	97	33.5	61
SBLC	0.6	0.5	25	69	14	28
	0.6	0.5	16	38	9.6	14.5

Table 4.1: The numbers of pair particles per bunch crossing for TESLA and SBLC. All numbers of particles N are in units of 10^3 while all total energies E in units of TeV. For the upper values the beam-size effect is not taken into account.

energies. Taking into account the total number of particles the Landau-Lifshitz process dominates at low energies and at high energies. The spectrum of the Bethe-Heitler process shows a shape completely different from the others. Most of the particles are produced at energies around a few GeV. The shape of the spectrum is comparable to that of the beamstrahlung. Since the real photon spectrum is harder than the equivalent one (except for the high energy tail of the latter) a pair is usually produced by a hard real and a soft virtual photon. The energy of the pair is thus about the energy of the real photon. Since the cross section for the Bethe-Heitler process does not depend very much on the centre

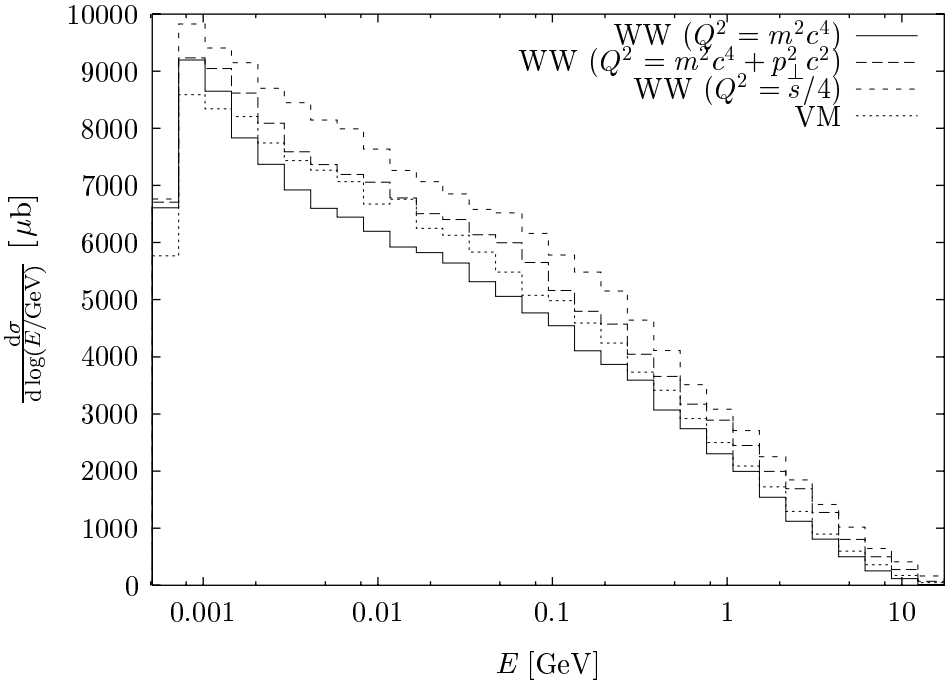

Figure 4.3: The dependence of the pair production cross section on the energy of the produced electron for a centre of mass energy of 35 GeV. Again different Q^2 scales are used for the equivalent photon approximation (WW).

Name		JLC-S	JLC-C	JLC-X	JLC-S	JLC-C	JLC-X
E_{cm}	GeV	300	300	300	500	500	500
N_e	$[10^4]$	6.2	2.0	0.62	7.0	3.9	1.3
		5.8	1.8	0.58	6.4	3.6	1.3
E_e	$[10^4$ GeV$]$	18	6	1.7	58	30	9.1
		14.0	3.4	0.82	31	16.5	4.8

Table 4.2: The total number of particles from pair production calculated with ABEL and GUINEA-PIG. The upper values are taken from reference [23] where the number of particles and their energy is given per beam [24] while the lower are the GUINEA-PIG results. All values are per beam.

of mass energy of the photon and the electron one can conclude that the average energy of the particles produced by this process is about half of the average energy of the beamstrahlung photons.

A comparison between the results of ABEL from reference [23] and GUINEA-PIG shows that the number of particles predicted roughly agrees, see Table 4.2. The total energy of the produced particles however is almost twice as high in ABEL as in GUINEA-PIG.

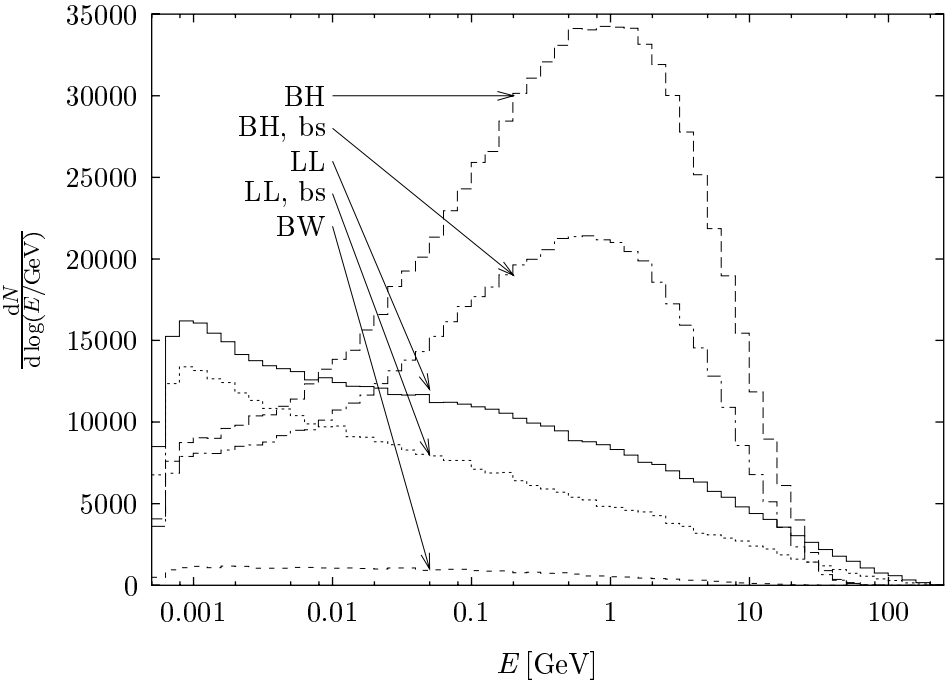

Figure 4.4: The energy spectrum of the particles from pair creation for the three processes with beam-size effect (bs) and without.

A comparison of the spectra of the Landau-Lifshitz process calculated by the two programs is shown in Figure 4.5. In both programs the beam-size effect is switched of. In ABEL no particles below a cutoff energy of 5 MeV are produced. In this program a patch factor is used to achieve the same number of particles as according to equations (4.7) to (4.9) should be expected. Even if the spectrum from ABEL is reduced by a factor to contain only the total number of particles calculated by GUINEA-PIG to have an energy of more than 5 MeV the spectra do not agree, while the Vermaseren Monte-Carlo agrees with GUINEA-PIG at $\sqrt{s} = 35\,\mathrm{GeV}$. Until now the difference between ABEL and GUINEA-PIG is not understood.

The number of muons to be expected is about 3 in TESLA.

4.9 Tracking of the pairs

The produced pairs have a much lower energy than the beam particles. It is necessary to track them through the fields of the beams. At production time most of the particles have a small angle with respect to the beam axis. Contrary to the beam particles in an e^+e^- collider half of the produced particles move into the opposite direction of the beam with the same sign of charge and are therefore

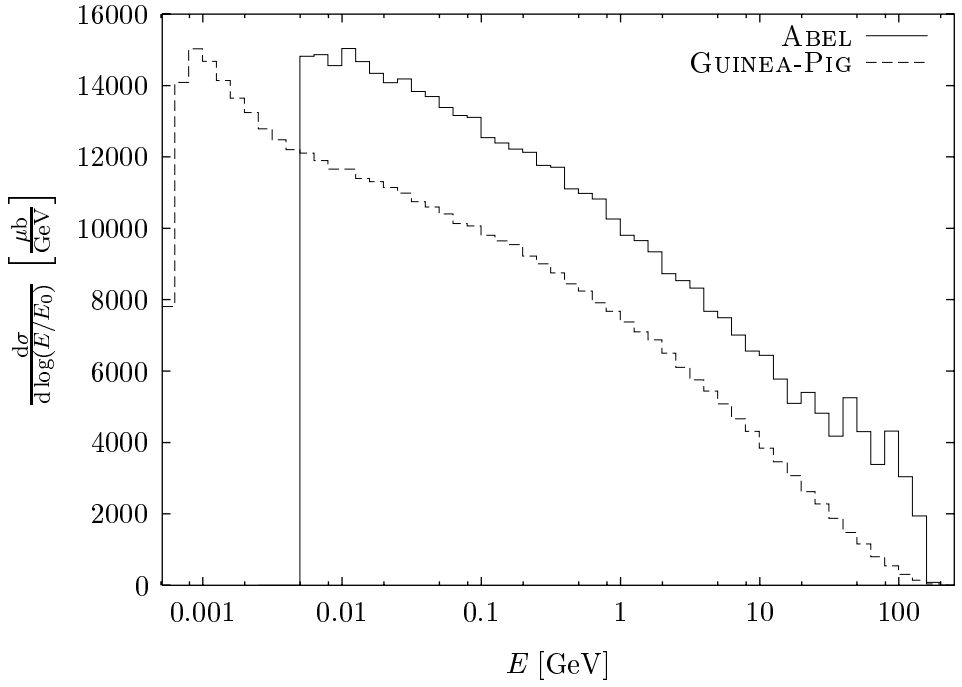

Figure 4.5: The dependence of the cross section for the Landau Lifshitz process on the energy of the secondaries for ABEL was provided by [44] and GUINEA-PIG. The centre of mass energy in this case is 500 GeV.

defocused by this beam[2]. It is thus necessary to calculate the fields outside the normal grid as well. To this end several grids with the same number of cells but different sizes are used. The first of them is only increased in y-direction until the grid is quadratic. The next ones are increased in both dimensions simultaneously. Outside the largest grid the beam is taken to be a line charge. The calculation of the fields takes longer than for the pinch effect. Due to the lower energy of the particles the tracking has to be done in finer time steps than for the beam particles. The particles from pair production do not affect the beams since their total number is smaller by about five orders of magnitude than the number of beam particles. For each time-step the potential produced by the beam is fixed.

The stability of the tracking can be improved by using the so called *leap-frog*-scheme. In this scheme the acceleration and velocity of a particle are calculated for interleaved positions. For electric fields this leads to:

$$\begin{aligned} \vec{v}_{n+\frac{1}{2}} &= \vec{v}_{n-\frac{1}{2}} + \vec{a}_n \Delta t \\ \vec{x}_{n+1} &= \vec{x}_n + v_{n+\frac{1}{2}} \Delta t. \end{aligned}$$

The acceleration $\vec{a}_n$ is given by the electric field at $\vec{x}_n$. If also a magnetic field is

[2]The interaction with the other beam is small as long as the angle stays small.

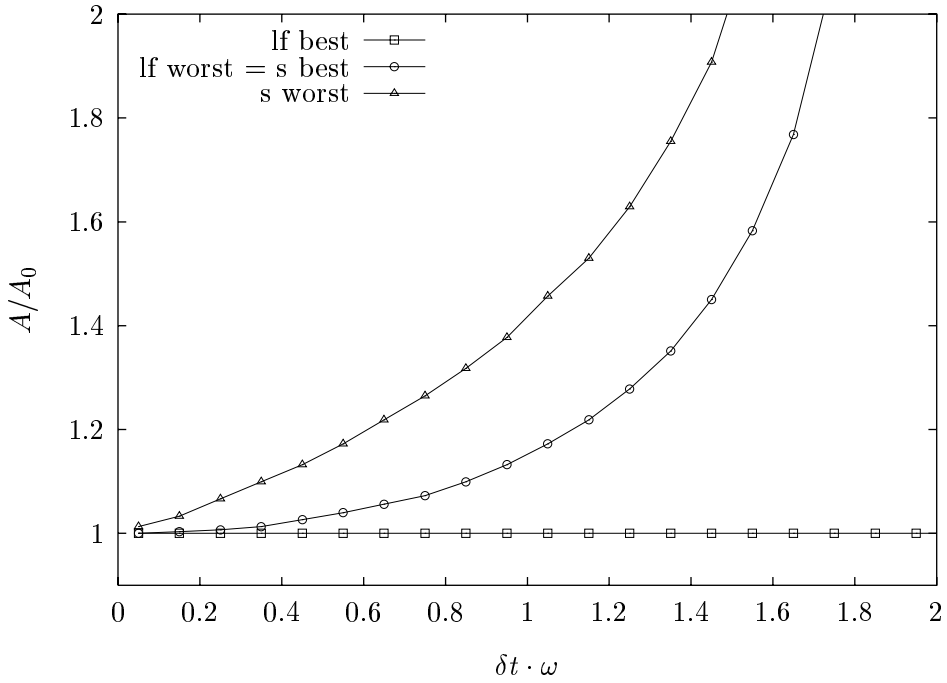

Figure 4.6: The simulated versus the real amplitude for the simple s and leapfrog lf scheme in the case of a harmonic oscillator. The ratio A/A_0 depends on the initial phase.

present more steps are needed:

$$\begin{aligned}
\vec{v}_n &= \vec{v}_{n-\frac{1}{2}} + \frac{1}{2}\vec{a}_n \Delta t \\
\vec{v}'_n &= T_n \vec{v}_n \\
\vec{v}_{n+\frac{1}{2}} &= \vec{v}'_{n-\frac{1}{2}} + \frac{1}{2}\vec{a}_n \Delta t \\
\vec{x}_{n+1} &= \vec{x}_n + v_{n+\frac{1}{2}} \Delta t.
\end{aligned}$$

T_n is the rotation matrix of the velocity vector due to the magnetic field at position $\vec{x}_n$.

The difference between the leap-frog and the simple scheme can be seen in the case of a harmonic oscillator. The maximal amplitude of the particle divided by the analytically calculated is shown for different step sizes and starting phases in Figure 4.6. $\Phi_0 = 0$ stands here for the particle starting at maximal amplitude. For the simple scheme the starting conditions $\Phi_0 = \Phi_1$ and $\Phi_0 = \pi/2 - \Phi_1$ lead to the same amplitude. $\Phi_0 = \pi/4$ gives the largest increase, $\Phi_0 = 0$ the smallest. For the leap frog scheme the error increases from zero for $\Phi_0 = 0$ towards $\Phi = \pi/2$. The worst case $\Phi_0 = \pi/2$ gives the same error as the simple scheme in its best case. If one compares the worst cases of the the two methods and allows for an

error of say ten percent the allowed step size for the leap frog scheme is almost three times larger than for the simple one.

The step size in the figure is given in units of $1/\omega$, where ω is the oscillator frequency. Comparing with equation (2.2) one can conclude that the step size should be of the order $\delta z \approx \sqrt{\epsilon/D}\sigma_z$. In the program the step size is calculated using

$$\delta z = \sqrt{\frac{\epsilon\gamma\sigma_y(\sigma_x+\sigma_y)\Delta z}{4Ar_e\sum_{i,j}N_{i,j}}}$$

where $\Sigma_{i,j}N_{i,j}$ is the total number of particles in the slice with thickness Δz and A can be chosen by the user. In general $A \geq 1$ should be used.

4.10 Particle distribution after deflection by the beams

The result of a simulation of the pair creation for TESLA is shown in Figure 4.7. One can distinguish two different regions. The vast majority of the particles has an upper limit on the angle depending on their energy (this translates into the dependence of the transverse momentum on the angle visible in the plot). The differential cross section is peaked at small angles. The pair particles therefore go usually along the beam axis. If an electron follows the direction of the electron beam it is focused by the positron beam and will make oscillations. If it follows the positron beam it will be deflected by the electron beam. The maximum angle of this deflection depends on the particle energy. For a particle with an energy of ϵE_0 it can be approximated by [45]

$$\theta_m = \sqrt{4\frac{\ln\left(\frac{D'}{\epsilon}+1\right)D'\bar{\sigma}_x^2}{\sqrt{3}\epsilon\sigma_z^2}} \tag{4.14}$$

$D' = Nr_e\sigma_z/(\gamma\bar{\sigma}_x^2)$ is the disruption parameter for a round beam using the average $\bar{\sigma}_x = \langle\sigma_x\rangle$ as resulting from the pinch effect. This formula is valid if the particle angle is in an intermediate range—significantly larger than the angles of the beam particles but smaller than unity.

Some particles happen to be produced with high angles and energy. They can be seen above the edge in the plot. For the total number of pairs the Bethe-Heitler process is most important followed by Landau-Lifshitz process, as stated before. For the high energy and high angle particles the Bethe-Heitler and the Breit-Wheeler processes contribute most.

The particles from pair creation can be trapped by conical masks covering the faces of the final quadrupoles. The opening angle of the masks defines the minimum angle a particle has to have in order to reach the detector. Because of

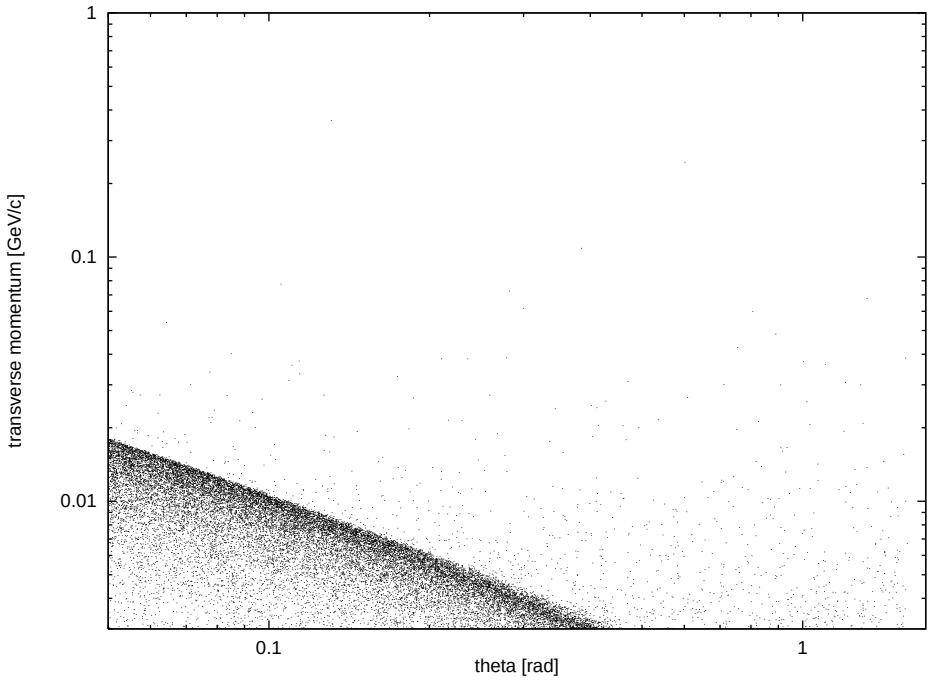

Figure 4.7: The angle theta with respect to the beam axis and the trnasverse momentum of the particles from pair creation for one bunch crossing in TESLA after the tracking through the fields of the beams. Each dot represents one particle.

the longitudinal magnetic field B in the detector, charged particles travel along a helix with a radius of $r_0 \approx 3.33\,\mathrm{mm}\, p_\perp/B\,[\mathrm{T}/(\mathrm{MeV/c})]$. Their distance to the beam axis is

$$r(z) = r_0\sqrt{2(1-\cos\phi(z))} \qquad (4.15)$$
$$\phi(z) = \frac{z}{r_0}\tan\theta_0$$

Hence they need a minimal transverse momentum to reach the detector. The dependence of the half aperture on z, that is required to let pass the particles with a maximum transverse momentum according to equation (4.14) is shown in Figure 4.8. The distance between the interaction point and the mask is 750 mm. The inner opening angle of about 66 mrad gives an aperture of 50 mm at the opening towards the detector. The approximation in Figure 4.8 shows that for a magnetic field of 3 T the required aperture would be significantly smaller.

In TESLA the number of electrons and positrons per bunch crossing that do not enter the mask is about 24 with a total energy of about 6.5 GeV for a magnetic field of 3 T and 52 with a total energy of 10 GeV for a field of 2 T.

Figure 4.10 shows the particle distribution calculated with GUINEA-PIG for the JLC-C parameters. The edge is in good agreement with reference [23].

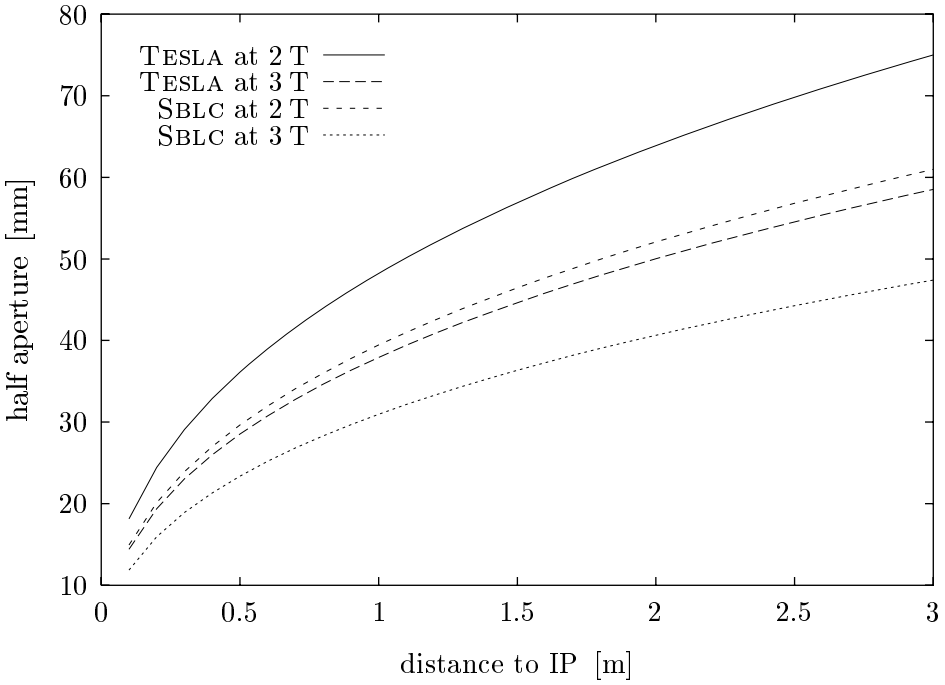

Figure 4.8: The half aperture needed at a certain distance from the interaction point in order to avoid the particles that received their angle from the deflection by the beams.

4.11 Low energy particle due to bremsstrahlung

A beam particle not only interact with the collective field of the particles of the other beam—which leads to beamstrahlung—but also with the field of a single particle. This leads to the emission of a photon. The Feynman graph is shown in Figure 4.11. The differential cross section for the process is given by [32]:

$$\frac{\mathrm{d}\sigma}{\mathrm{d}\omega} = 4\alpha r_e^2 \frac{1}{\omega}\frac{E-\hbar\omega}{E}\left(\frac{E}{E-\hbar\omega}+\frac{E-\hbar\omega}{E}-\frac{2}{3}\right)\left(\ln\frac{4E^2(E-\hbar\omega)}{m^2c^4\hbar\omega}-\frac{1}{2}\right). \tag{4.16}$$

The process can also be regarded as Compton scattering of the electron on a virtual photon and is calculable in the equivalent photon approximation. The cross section for the Compton process is given by [32] (using $c = 1$)

$$\begin{aligned}\frac{\mathrm{d}\sigma}{\mathrm{d}t} &= 8\pi\frac{r_e^2 m^2}{(s-m^2)^2}\left[\left(\frac{m^2}{s-m^2}+\frac{m^2}{u-m^2}\right)^2+\left(\frac{m^2}{s-m^2}+\frac{m^2}{u-m^2}\right)\right.\\ &\quad\left.-\frac{1}{4}\left(\frac{s-m^2}{u-m^2}+\frac{u-m^2}{s-m^2}\right)\right].\end{aligned} \tag{4.17}$$

In the program the cross section is implemented using equation (9.1) on page 119 for the energy of the emitted photon. The bremsstrahlung will also be reduced by

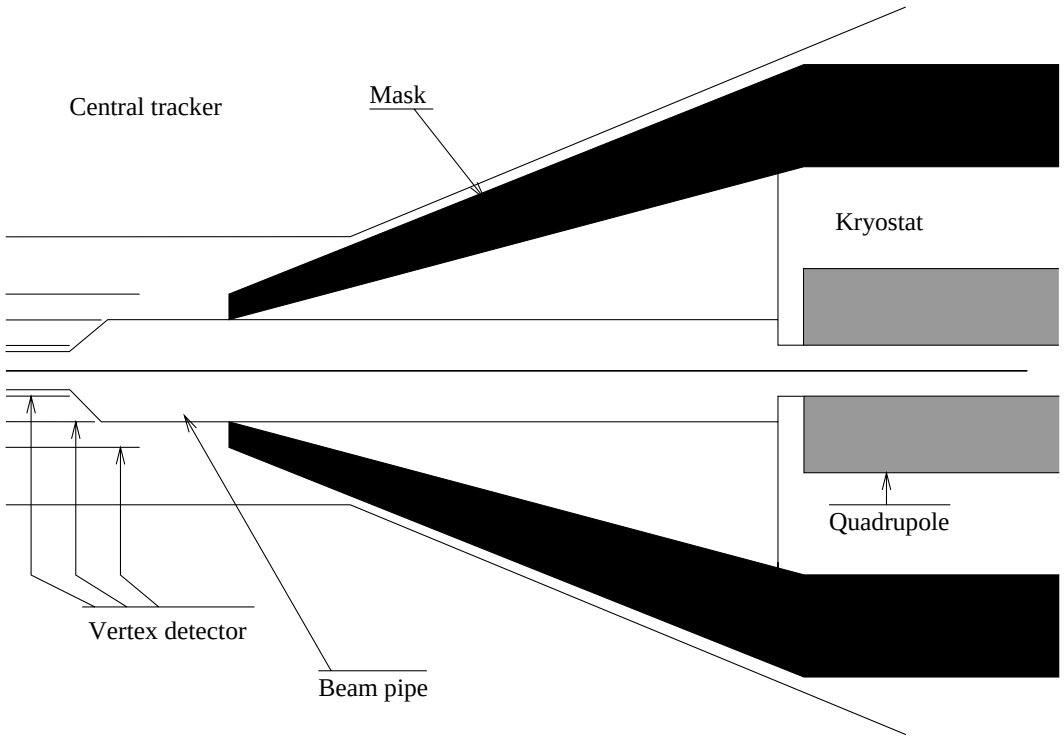

Figure 4.9: The principle layout of the mask to protect the detector from secondaries created by the particles from pair production in the quadrupole.

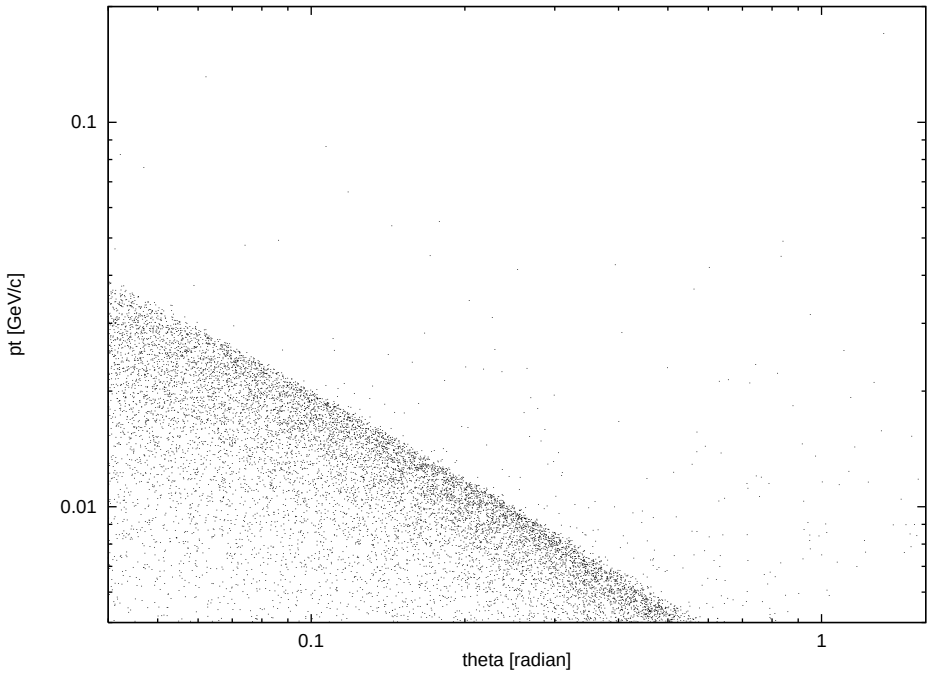

Figure 4.10: The particle distribution in transverse momentum and angle for JLC-C.

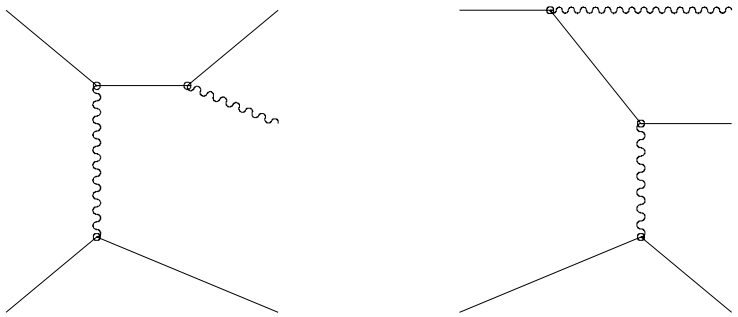

Figure 4.11: The bremsstrahlung process.

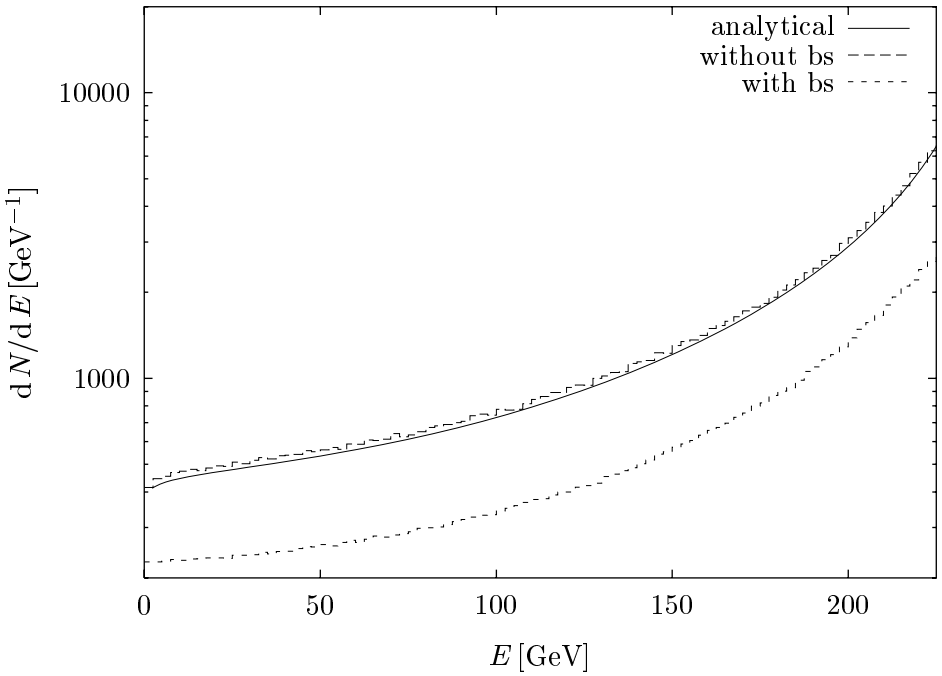

Figure 4.12: Energy spectrum of the beam particles after the interaction due to the emitting of bremsstrahlung. The solid line is the the analytic expression in equation 4.16. The other curves are from the simulation with GUINEA-PIG, the lower curve includes the beam-size effect (bs) the upper does not.

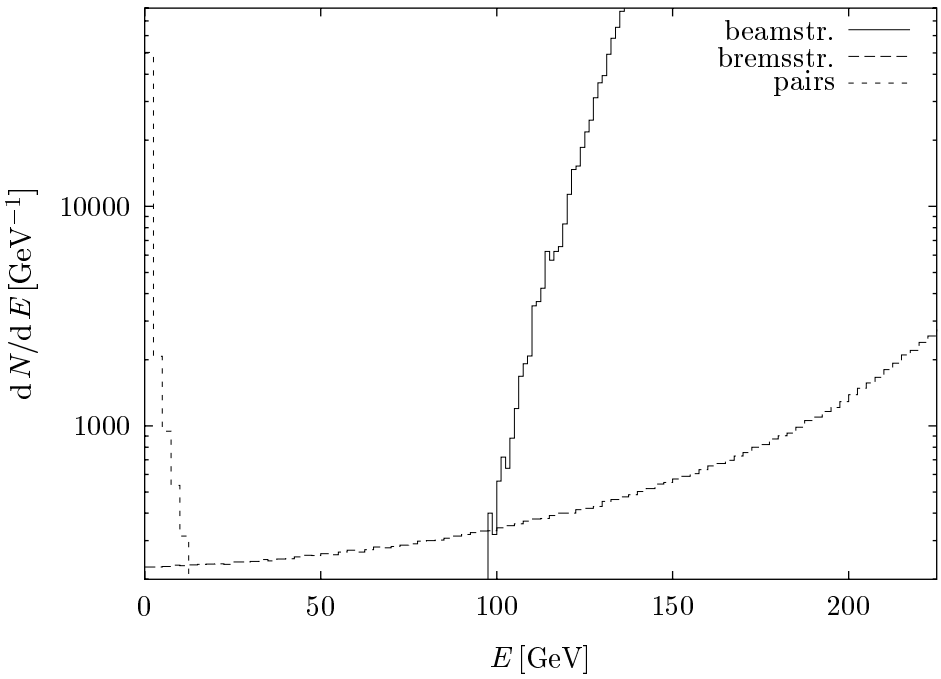

Figure 4.13: The different low energy spectra from pair creation, bremsstrahlung and beamstrahlung.

the beam size effect. This is implemented the same way as for the pair production. Figure 4.12 shows the energy spectrum of beam particles in the spent beams for TESLA at a centre of mass energy of 500 GeV. The analytic formula agrees quite well with the equivalent photon approximation if the beam size effect is not taken into account. This effect reduces the spectrum by an overall factor of about 2. The contribution of the scattering of a beamparticle on real photons from the beamstrahlung is included in the simulation but this contribution is negligible.

Except for the beam-size effect, which varies slowly with the vertical beam size, the number of beam particles that lost a certain amount of energy due to bremsstrahlung is proportional to luminosity. To measure the luminosity the number of beam particles within a certain energy range can be measured. This range has to be chosen as to not contain a significant number of particles from pair creation or beam particles which lost their energy via beamstrahlung, since these processes are not proportional to luminosity. As Figure 4.13 shows, a suitable energy range could be from 20 GeV to 80 GeV. It has however to be investigated if these particles can be separated from the beam particles outside the detector.

Chapter 5

Production of Hadrons

In the collision of two photons not only e^+e^--pairs can be produced but also hadrons. With a certain probability a photon can interact hadronically as a vector meson—mainly a ρ^0. The cross section for process $\gamma\gamma \to$ hadrons has been measured only at low centre of mass energies and can not be calculated with perturbation theory. However there are hard processes that can be calculated this way. They are especially important because they produce jets of relatively high transverse momentum.

5.1 Total cross section

Several models exist for the description of the total cross section. In the vector-meson-dominance model the cross section is parametrised using the ansatz:

$$\sigma_{H,1} = \sigma_{\text{VMD}} + \sigma_{\text{hard}} = A + \frac{B}{\sqrt{s}} + \sigma_{\text{hard}}$$

where s is the centre of mass energy of the two photons squared and A and B are derived from experiment. At TRISTAN jet data was fitted using $A = 240\,\text{nb}$ and $B = 270\,\text{nb} \cdot \text{GeV}$ [46]. σ_{hard} is a hard contribution that can be understood as the minijet contribution described below.

A second parametrisation is based on the assumption that a photon interacts hadronically with a fixed probability. One can then use $\sigma(\gamma\gamma \to X)/\sigma(\gamma p \to X) = \sigma(\gamma p \to X)/\sigma(pp \to X)$. A fit of proton-proton data by Amaldi et al. [47] can be used for σ_{pp}. Photon-proton cross sections are known for centre of mass energies of more than 200 GeV [48]. For the photon-photon cross section one obtains [49]

$$\sigma_{H,2} = \sigma_0 \left[1 + 6.3 \cdot 10^{-3} \ln^{2.1} \frac{s}{\text{GeV}^2} + 1.96 \left(\frac{s}{\text{GeV}^2} \right)^{-0.37} \right] \tag{5.1}$$

with $\sigma_0 \approx 200\,\text{nb}$ from the fit of low energy photon data. The result from ZEUS [50] in reference [48] is $\sigma_{\gamma p} \approx 154\,\mu\text{b}$ for $s = (210\,\text{GeV})^2$, giving $\sigma_0 \approx 230\,\text{nb}$.

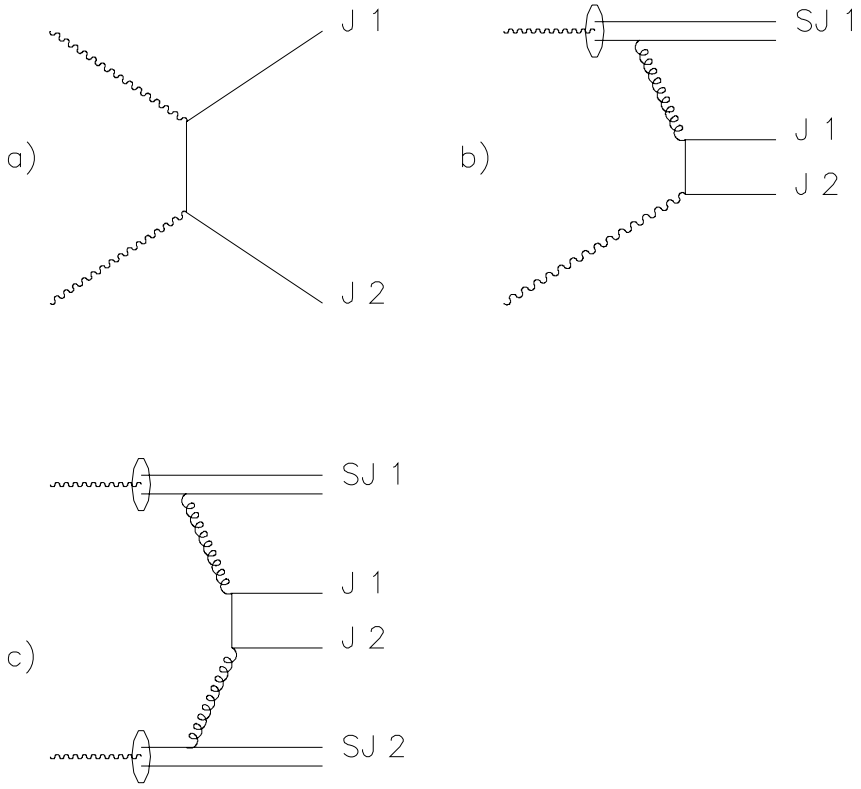

Figure 5.1: Examples for the different processes leading to minijets. The direct process (a) leads to two jets (J1 and J2). In the once resolved processes (b) also a spectator jet (SJ1) is produced from the remnant of the photon; in the twice resolved case (c) two spectator jets are formed.

A third parametrisation is given by [51]

$$\sigma_{H,3} = 211\,\mathrm{nb} \cdot \left(\frac{s}{\mathrm{GeV}}\right)^{\epsilon} + 297\,\mathrm{nb} \cdot \left(\frac{s}{\mathrm{GeV}}\right)^{-\mu} \tag{5.2}$$

with $\epsilon = 0.0808$ and $\mu = 0.4525$. This cross section is used in PYTHIA [52]. It is implemented in GUINEA-PIG.

5.2 Minijets

Most of the secondaries from photon-photon interaction have very small transverse momenta and angles. There is however a small number of hard events in which jets with a large transverse momentum are produced. These are called

minijets since their they are still much less energetic than the jets produced in the reaction $e^+e^- \to Z^*/\gamma^* \to q\bar{q}$. The cross sections can be calculated perturbatively. The first relevant process is $\gamma\gamma \to q\bar{q}$. This is basically the same as the e^+e^--pair production. M. Drees and K. Grassi pointed out that not only the direct contribution of the photons is important [53]; the individual partons of the hadronic part of the photons can scatter as well. So one has to consider three contributions, the direct, the once-resolved and the twice-resolved, see Figure 5.1. In the latter two, one or two of the photons scatter via their partons, respectively. Since one has a remnant part of the resolved photon one gets three jets in the once- and four jets in the twice-resolved case. These additional jets travel along the beam axis and are often called spectator jets.

The main uncertainty in this calculation is the partonic content of the photons. The gluon part turns out to be especially important since gluon-gluon and quark-gluon processes dominate the total cross section for the twice-resolved case.

5.3 Hadronic structure function

The hadronic content of the photon is described by the structure functions $f_{q_i}^{\gamma}(x, Q^2)$ for the quark flavour q_i and $f_g^{\gamma}(x, Q^2)$ for the gluons. Here x is the fraction of the photon energy carried by the parton and Q^2 is the momentum transfer in the interaction. The hadronic content of the photon depends not only on x but also on the typical Q^2 of the interaction. This is because at high Q^2 a probe particle can, for example, resolve a quark anti-quark loop formed by a gluon while this would not be possible at lower Q^2. To find a parametrisation of these functions one can use the results of experiments at a fixed Q^2. The Q^2 dependence is then described by the Altarelli-Parisi equations. The equation for the quark content differs from the normal hadronic case by a term that is due to the point like part of the photon [54]. The part of the structure function produced by this term is the so called anomalous part.

Several parametrisations of the structure functions exist. Two are used here, one derived by M. Drees and K. Grassi [55] the other by M. Glück, E. Reya and A. Vogt [56] (in the following called DG and GRV parametrisation respectively). Up to now these parametrisations are in agreement with the available data [57].

5.4 Minijets and total cross section

The contribution of the minijets to the total cross section is not straightforward to calculate. In the simplest model using the VMD ansatz the total cross section is formed by adding the soft and the hard part $\sigma_{H,0} = \sigma_{\mathrm{VMD}} + \sigma_{\mathrm{MJ}}$. To avoid double counting one requires a minimal transverse momentum p_* for the minijets. Experimentally p_* is in the range from 2.0 GeV to 2.5 GeV [58], [59], [46]. This

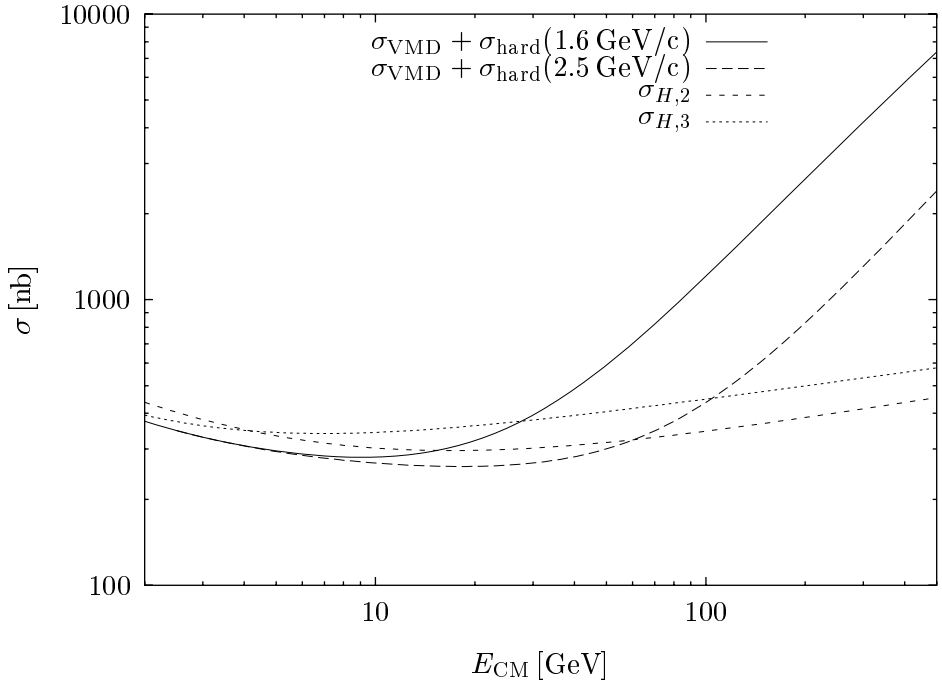

Figure 5.2: The total hadronic $\gamma\gamma$ cross section for different models. The model using the VMD plus minijet approach predicts cross sections much larger than the other two which are in fair agreement. The choice of the transverse momentum cutoff significantly changes the results.

approach however predicts a photon-photon cross section that is rising rapidly with the centre of mass energy due to the fast rise in the minijet cross section.

Other authors claim that this simple model overestimates the total cross section [60]. The problem of the fast rising cross section for parton-parton scattering occurs in two-hadron physics as well. The observed slow increase of the total cross section with increasing centre of mass energy can be explained by introducing an impact parameter distribution of the partons. In this model the total cross section is related to the overlap of the spatial distributions of the partons. The total jet rate is the same as before. If the hadronic discs overlap the probability for individual parton-parton scatterings is so high for large centre of mass energies that often more then one pair of partons scatter. The increasing jet cross section thus does not raise the total cross section drastically but rather the hardness of the events.

The average partonic content of a photon is much smaller than that of a hadron—one could therefore think it necessary to take this effect into account only for very high centre of mass energies, when the photon-photon cross section becomes comparable to the $\mathrm{p\bar{p}}$ (or rather $\rho\rho$) cross section. In an eikonal model one assumes that the photon processes interacts as a hadron with a probability $p_H \approx \sigma(\gamma\gamma)/\sigma(\gamma\pi) \approx 1/300$—the partonic content is enhanced by a factor of

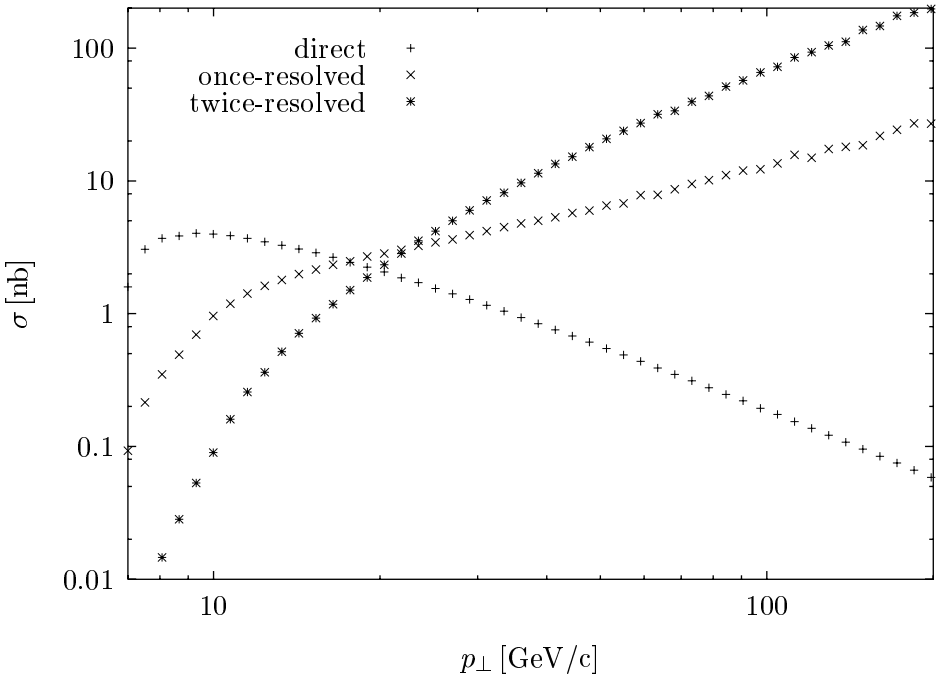

Figure 5.3: The total cross section for minijet production with $p_\perp > 3.2\,\mathrm{GeV/c}$.

about $1/p_H$ in this case (and almost zero otherwise). Thus the same formalism has to be applied for resolved two-photon processes than for two-hadron collision already at small centre of mass energies and cross sections. The situation is nevertheless somewhat different since the photon also contains a so called anomalous contribution to the structure function which arises from its point like part. The correct treatment of the eikonalisation is not clear, since it depends on the assumptions about the distribution of the partons in the hadronic photon.

Figure 5.2 shows the three different cross sections according to equations (5.1) to (5.2). The VMD cross section includes the minijet contribution with two different cutoffs for the hard contribution. The differences are not very large for photon-photon centre-of-mass energies below 30 GeV. Depending on the assumed transverse momentum cutoff the cross section of the simple approach from equation (5.1) rises drastically at higher energies. For the linear colliders under investigation the $\gamma\gamma$ luminosity at these energies is small. Therefore even the simple model does not predict significantly higher rates than those calculated with the other two parametrisations, as will be shown below.

5.5 Calculation of the hadronic cross section

The total number of hadrons produced during one bunch crossing can be calculated approximately using

$$N_{\mathrm{Had}} = L \int\int n_1(x_1, Q^2) n_2(x_2, Q^2) \sigma(\gamma\gamma \to X) dx_1 dx_2 \tag{5.3}$$

where each $n_i(x, Q^2)$ is either the virtual photon spectrum or the average beamstrahlung spectrum (which is of course independent of Q^2). The cross section for the production of minijets can be calculated using

$$\begin{aligned} \sigma_{\mathrm{MJ}} &= \sum_{i,j} \int\int\int\int n_1(x_1, Q^2) n_2(x_2, Q^2) f_i(x_3, Q^2) f_j(x_4, Q^2) \\ &\quad \sigma_{i,j}(x_1 x_3, x_2 x_4, Q^2) dx_1 dx_2 dx_3 dx_4 \end{aligned} \tag{5.4}$$

The functions n_i are the photon spectra and the functions $f_{i,j}$ are the structure functions of the photons giving the content of particle i, j in the photon. For unresolved photons the structure function $f_{i,j}$ is simply replaced by a delta function. The cross section $\sigma_{i.j}$ depends on Q^2 because α_s does:

$$\alpha_s = \frac{12\pi}{(33 - 2n_f) \ln(Q^2/\Lambda^2)}.$$

A first estimate of the rates can be made using an approximation for the average beamstrahlung spectrum derived from fits to simulation results [61]. The total number of photons in the classical limit is given by:

$$n_{\mathrm{cl}} \approx \sqrt{3} \sigma_z \nu_{\mathrm{cl}} \tag{5.5}$$

$$\nu_{\mathrm{cl}} = \frac{5}{2\sqrt{3}} \frac{\alpha^2 \Upsilon}{r_e \gamma} \tag{5.6}$$

In the quantum regime this turns into

$$n_\gamma = n_{\mathrm{cl}} \frac{1}{\sqrt{1 + \Upsilon^{\frac{2}{3}}}}$$

$$\nu_\gamma = \nu_{\mathrm{cl}} \frac{1}{\sqrt{1 + \Upsilon^{\frac{2}{3}}}}.$$

Between the two regimes one can interpolate

$$\langle \nu \rangle = \frac{1}{2} \left((1 + x) \nu_{\mathrm{cl}} + (1 - x) \nu_\gamma \right)$$

The spectrum is now given by:

$$\begin{aligned} n_r(x) &= \frac{1}{\Gamma(1/3)} x_c^{\frac{1}{3}} x^{-\frac{2}{3}} (1-x)^{-\frac{1}{3}} \exp\left(\frac{x}{x_c(1-x)}\right) \\ &\quad \frac{1-w}{g(x)}\left[1 - \frac{1}{g(x)n_\gamma}\left(1-\exp(-g(x)n_\gamma)\right)\right] \\ &\quad + w\left[1 - \frac{1}{n_\gamma}\left(1-\exp(-n_\gamma)\right)\right] \qquad (5.7) \\ g(x) &= 1 - \frac{\langle\nu\rangle}{\nu_\gamma}(1-x)^{\frac{2}{3}} \\ w &= \frac{1}{6}\sqrt{x_c} \end{aligned}$$

$x_c = 3/2\Upsilon$ is the average critical energy divided by the beam energy. In Figure 5.5 the results with this formula and the simulated eγ and $\gamma\gamma$ spectra are compared. While there are significant discrepancies, the overall structure is reproduced. For a very first approach the formula (5.7) should thus be a reasonable choice. For other machines with fewer photons per beam particle the agreement is better.

The beam particles are replaced by the equivalent photon spectra. For the unresolved photons this is:

$$n_v(x, Q^2) = \frac{\alpha}{2\pi}\frac{1+(1-x)^2}{x}\ln\frac{Q^2(1-x)}{x^2 m^2} \qquad (5.8)$$

with $Q^2 = p_\perp^2$ the square of the transverse momentum of the final state particles.

For the resolved case one has to take into account that the partonic content is suppressed for strongly virtual photons. M. Drees and K. Grassi use

$$n_v(x, Q^2) = 0.85\frac{\alpha}{2\pi}\frac{1+(1-x)^2}{x}\ln\frac{Q^2}{m^2} \qquad (5.9)$$

with $Q^2 = s/4$, where s is the centre of mass energy squared of the scattering partons. The factor 0.85 takes care of the above mentioned suppression. This could also be done choosing $Q^2 = \min(m_\rho^2 c^4 \approx 1\,\mathrm{GeV}^2, s/4)$ in equation (5.8).

The parametrisations in equations (5.1) and (5.2) are used for the total cross section. For the minijet contribution eleven cross sections have to be evaluated. The cross section for the direct case is the same as for pair production. Since only events with high transverse momentum are interesting in hard processes, one can assume the three light quarks to be massless. The cross section then is simply

$$\frac{d\sigma}{dt} = \frac{2\pi r_e^2 m^2}{s^2}\frac{3\sum e_{q_i}^4}{e^4}\left(\frac{t}{u}+\frac{u}{t}\right) \qquad (5.10)$$

e_{q_i} is the charge of the quark that is produced. Integrating this requiring $p_\perp = \sqrt{1-\cos^2\theta}\sqrt{s/4} \geq p_*$ leads to

$$\sigma(p_\perp > p_*) = \frac{4\pi r_e^2 m^2}{s}\frac{3\sum e_{q_i}^4}{e^4}\left(\ln\frac{1+c_0}{1-c_0} - c_0\right) \qquad (5.11)$$

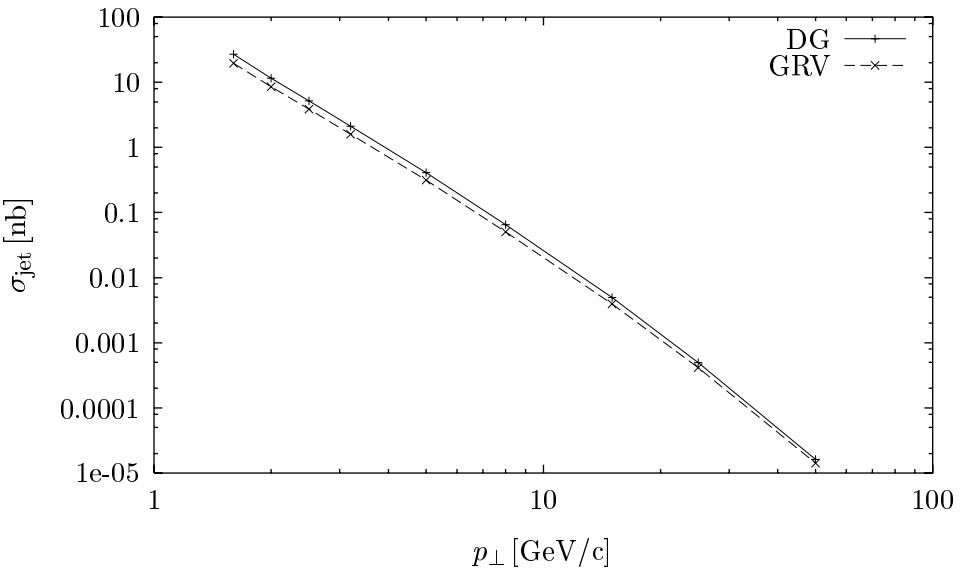

Figure 5.4: A comparison of the twice resolved cross section for TESLA for the DG and GRV parametrisation of the hadronic structure of the photon.

with $c_0 = \sqrt{1 - 4p_*^2/s}$. The cross section depends strongly on the contribution from the c-quark since the charge has to be taken to the fourth power. Therefore the c-quark is included in the program assuming $m_c = 1.6\text{GeV/c}^2$ and using the cross section from equation (4.5).

For the once-resolved case two processes exist, $\gamma q \to gq$ and $\gamma g \to q\bar{q}$. In the calculation all quarks are assumed to be massless. The number of possible quark flavours in the initial as well as final state is chosen according to s. It is three for $s < 80\,\text{GeV}^2$, five for $s > 800\,\text{GeV}^2$ and four in between. The cross section can for example be found in [62] and [63]. For the DG parametrisation $\Lambda_4 = 0.4\,\text{GeV}$ was used since the parametrisation was obtained with this parameter. For the GRV parametrisation $\Lambda_4 = 0.2\,\text{GeV}$ was taken. The parameters Λ_3 and Λ_5 are obtained by matching α_S at the appropriate scales.

The results for the two different parametrisations of the total cross section in equations (5.1) and (5.2) agree within a few percent. For TESLA the total rate of hadronic events with a centre-of-mass energy in excess of 5 GeV is 0.23 per bunch crossing. About 15% ($3.3 \cdot 10^{-2}$) of these are due to the scattering of two virtual photons. $10.8 \cdot 10^{-2}$ and $8.9 \cdot 10^{-2}$ events per bunch crossing contain one or two real photons in the initial state respectively. For SBLC the rate is 0.05 events per bunch crossing.

Figure 5.4 shows the cross sections of the twice resolved case for the two parametrisations for TESLA. The agreement is reasonable.

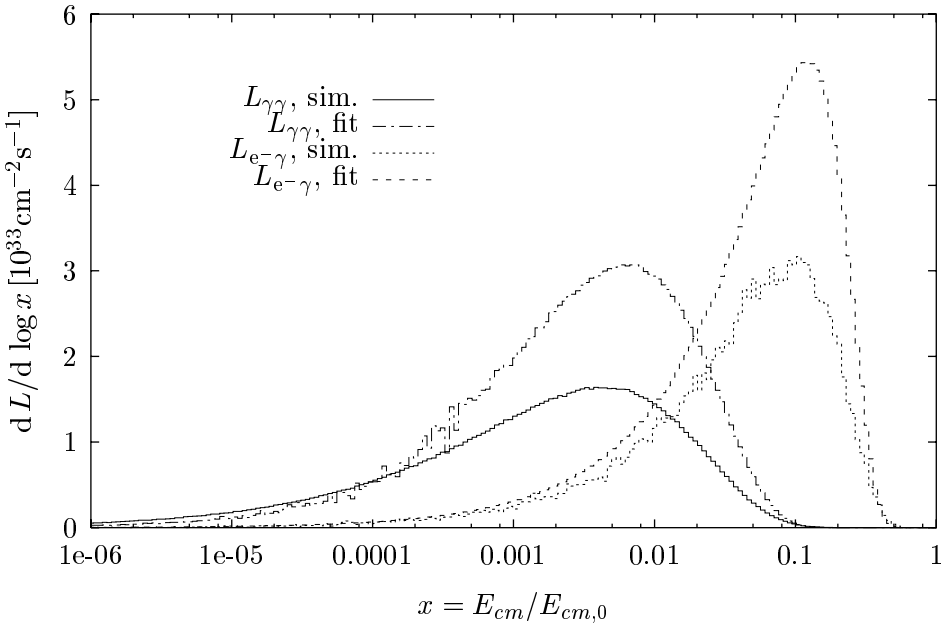

Figure 5.5: Comparison of the electron-photon and photon-photon spectrum using the parametrisation for the real photon spectrum and the simulation with GUINEA-PIG. The TESLA parameters are used.

5.6 Simulation of the hadronic background

The above way of calculating the cross sections depends on the quality of the approximation for the beamstrahlung photon spectrum. The parametrisation is not very good in the case of TESLA as can be seen in Figure 5.5. The calculation of the hadronic event rate is therefore implemented in GUINEA-PIG.

The routines for the hadron production use the parametrisation for the total two-photon cross section of equation (5.2). An electron or positron is replaced by the appropriate number of photons from the equivalent spectrum. The cross sections times the luminosities for each photon-photon scattering are then summed up. Additionally the energies of the photons can be stored in a file according to the cross section. The cross section is thereby enhanced by an appropriate factor to produce more events in order to get better statistics. This allows to simulate the events in more detail afterwards. For TESLA the number of hadronic events with a centre of mass energy of more than 5 GeV is $N_{\mathrm{Hadr}} \approx 0.13$ per bunch crossing, for SBLC $N_{\mathrm{Hadr}} \approx 0.04$. This is significantly different from the calculation using the parametrisation. The rate of hadronic events due to scattering of two virtual photons is $3 \cdot 10^{-3}$ in TESLA. The small difference to the calculation using the parametriation is given by the difference in the estimated luminosities.

5.7 Simulation of the minijet background

For the minijets not only the event rate can be calculated but also the angular distribution of the final state particles. For the direct process the cross section is the same as for e^+e^- pair production except for the different charges. The masses of the lightest three quarks are assumed to be zero, while the c and b quark masses are taken into account.

For the once resolved-processes one has to choose the energy of the parton. A value x_r is chosen in the interval $0 < x_r < 1$ according to a probability distribution $p(x)$. The probability $p(x_r)$ is used as a weight factor for the cross section. The choice of $p(x_r)$ has some influence on the statistical precision of the calculated minijet rate or rather on the total number of evaluations necessary to achieve a certain precision. A distribution $p(x) \propto 1/x$ was found to give good results.

The resolved virtual photons are chosen differently from the ones for the pair and hadron production for the minijets. An equally distributed x was found to give much better statistics due to the rising cross section for higher centre of mass energies.

For each photon-photon scattering thirteen cross sections have to be evaluated. To calculate the four-vectors of the final state the integrals of the cross sections have to be inverted. In contrast to the pair production the secondaries are assumed to be massless since their mass will be small compared to their transverse momentum. The dependence of the cross section on the angle will thus be independent of the centre of mass energy. Only the cutoff angle which gives secondaries with more than the minimal transverse momentum depends on the centre of mass energy. It is therefore possible to compute a table of inverted values before the simulation. From this table bounds can be found for each inversion afterwards. In addition it is possible to linearly interpolate the first guess of the Newton method. This leads to a total reduction in the time for calculating the final cross sections by one order of magnitude depending on the number of precomputed values. The second time-consuming part is the evaluation of the hadronic structure function while the third is the generation of random numbers.

5.8 Results on jet production

It turns out that for TESLA and SBLC the contribution of the minijets to the total cross section is small, see Table 5.1. For the number of hard jets one has to expect, the minijet model is very useful. In reference [49] it is assumed that the twice-resolved contribution is the dominant one and that the once-resolved and the direct case lead only to small corrections. This is justified if one is interested in the rise of the total photon-photon cross section with increasing centre of mass energy. For the number of mini jets in the detector one finds that the sum of the direct and once-resolved processes is larger than the twice-resolved case alone.

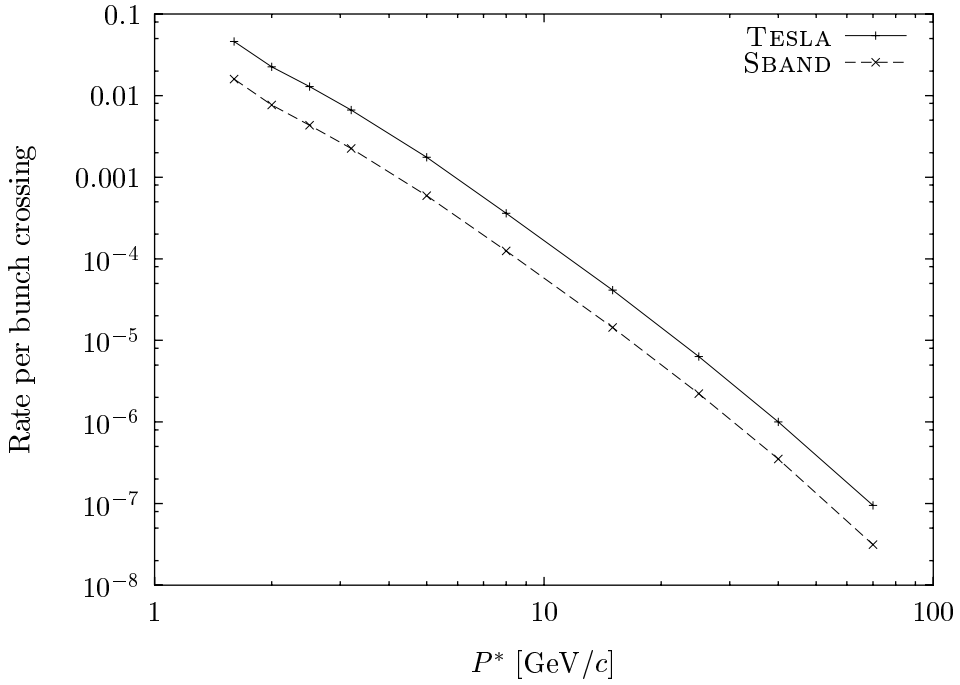

Figure 5.6: The total number of jets produced in one bunch crossing in TESLA and SBLC as a function of the minimal transverse momenta.

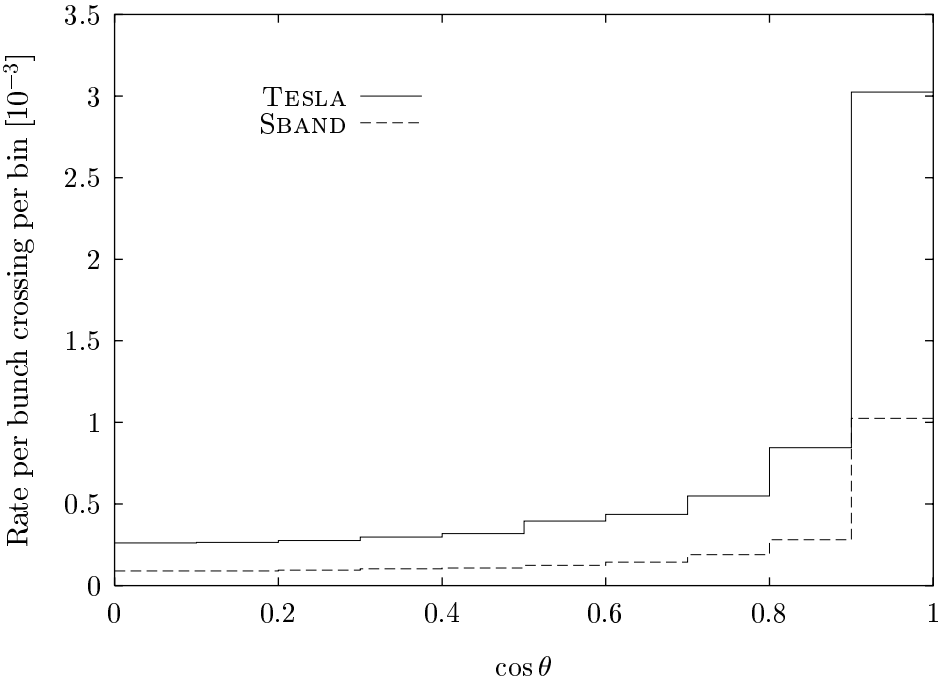

Figure 5.7: The angular distribution of the jets with a transverse momentum of more than 3.2 GeV.

p^* [GeV/c]	unit	c_{max} = 0.9	c_{max} = 0.95	c_{max} = 0.98	c_{max} = 0.995	c_{max} = 1.0
1.6	10^{-2}	3.52/1.18	4.22/1.42	4.99/1.69	5.85/1.99	6.94/2.35
2.0	10^{-2}	1.69/0.56	2.02/0.68	2.39/0.80	2.79/0.94	3.26/1.10
2.5	10^{-2}	0.84/0.28	1.00/0.33	1.18/0.39	1.36/0.46	1.57/0.53
3.2	10^{-3}	3.96/1.34	4.71/1.59	5.50/1.87	6.36/2.16	7.23/2.44
5.0	10^{-3}	1.03/0.35	1.22/0.42	1.41/0.48	1.61/0.55	1.77/0.60
8.0	10^{-4}	2.21/0.79	2.61/0.92	3.01/1.05	3.42/1.17	3.62/1.23
15.0	10^{-4}	0.27/0.10	0.32/0.12	0.37/0.13	0.41/0.14	0.41/0.14
25.0	10^{-5}	0.46/0.17	0.54/0.19	0.61/0.22	0.64/0.22	0.64/0.22
40.0	10^{-6}	0.87/0.31	0.99/0.34	1.05/0.37	1.05/0.37	1.05/0.37
70.0	10^{-7}	0.94/0.29	0.98/0.30	0.98/0.30	0.98/0.30	0.98/0.30

Table 5.1: The fraction of the jets with $|\cos\theta| \leq c_{max}$ for different transverse momenta. The values are for TESLA/SBLC. The DG-parametrisation is used.

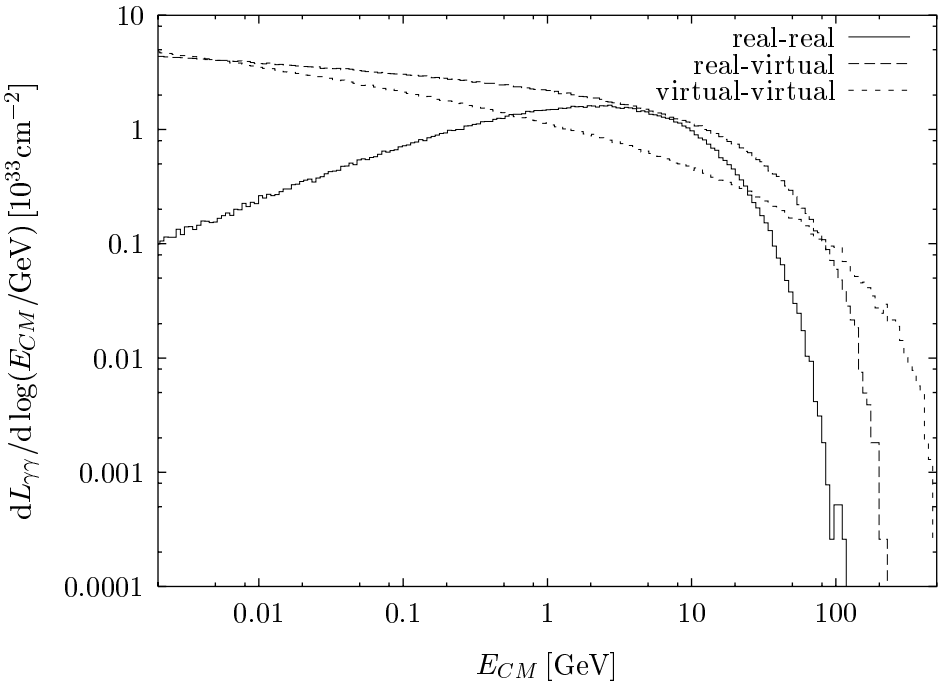

Figure 5.8: The $\gamma\gamma$-luminosity spectra for different combinations of real and virtual photons colliding.

This can easily be understood if one looks at the dependence of the cross sections on the centre of mass energy, see Figure 5.3. It is clear that for small values of s the direct contribution is the most important. The photon-photon luminosity is very high for the region of small centre of mass energies and as can be seen in Figure 5.8 the contribution from the scattering of two real photons is even softer than the one from two virtual photons.

Figure 5.6 shows the expected jet rates per bunch crossing for SBLC and TESLA as calculated with GUINEA-PIG. The number of jets for TESLA will be three times higher than for SBLC but one has to keep in mind that most if not all of the detector components in SBLC will have to integrate the background over several bunch crossings. The total rates are small for both colliders. The angular distribution of the low transverse momentum jets shows a rise towards small angles. Figure 5.7 shows the $\cos\theta$ distribution for jets with $p_\perp > 3.2\,\mathrm{GeV}/c$. Table 5.1 lists the jet rates expected for TESLA and SBLC for different angles and transverse momenta. The overall rates for $p_\perp > 3.2\,\mathrm{GeV/c}$ for all machines can be found in table 1.1 on page 7.

5.9 Fragmentation of the jets

In GUINEA-PIG the minijet production is calculated on the parton level. To study the effect of this background in the detector it is necessary to simulate the fragmentation into hadrons. Two methods are available in GUINEA-PIG. Firstly one can use the information on the parton level for performing the fragmentation. Secondly one can use only the information on the mini jet production cross section by storing the energies of scattering photon pairs according to this cross section. The production of jets is then done with a different program.

In the first method the longitudinal momenta and the transverse momentum of the inner process is stored (and a number to identify the process). The generator uses this information to construct the four-vectors and perform the fragmentation based on the routines in JETSET. For the direct process with only the produced quarks in the final state this is straightforward. The string only consists of a quark anti-quark pair. In the case of the resolved processes the remnant part of the photon has to be taken into account. There is a colour force between the remnant part and the mini jets. If the interacting parton of the photon is a quark the remnant part can be represented in the simulation as a anti-quark and vice versa. If the parton is a gluon the remnant part is a quark anti-quark pair or a gluon. It is not very difficult to perform the fragmentation in the once resolved case. In the final state one always finds a quark anti-quark pair and a gluon. The string is thus formed with the gluon in the centre and the quarks at the ends. In the twice resolved case several possibilities exist for most of the processes to join the final state particles into strings. In addition they have different kinematical properties. The cross sections for the different colour flows can be calculated, see

reference [64]. However, they do not sum up to the original cross section since the interference terms are neglected. In GUINEA-PIG the cross sections from reference [63], which include the interference terms, are used. In GHOST for each event the differential cross sections for each possible colour flow are calculated and used as weight factors according to which one of them is chosen. In this method no multiple interaction is taken into account.

In the second method the generator uses the PYTHIA routines. For each event stored in the file the equivalent process is simulated. Multiple interactions can be switched on which leads to an enhancement of the visible energy produced by a background event. In addition the cross section for high photon-photon centre of mass energies is lower than in the simple model used in GUINEA-PIG. To correct for this the photon-photon events are accepted by GHOST with a probability of

$$p(s,p^*) = \frac{\sigma_{Hadr}(s,p^*)}{\sigma_{\mathrm{MJ}}(s)} \left(1 - \exp\left(-\frac{\sigma_{MJ}(s,p^*)}{\sigma_{\mathrm{Hadr}}(s)}\right)\right). \tag{5.12}$$

This reduces the number of events with large centre of mass energy while for $\sigma_{MJ}(s,p^*)/\sigma_{\mathrm{Hadr}}(s) \ll 1$ the probability tends to become unity.

5.10 Modelling of the hadronic background

Since the rate of minijets is small compared to that of all hadronic events it is necessary to also include the soft part of the hadronic background. PYTHIA now allows to simulate resolved photon-photon interactions. The simplest method to study the impact of the hadronic background is to use GUINEA-PIG to produce a file with the energies of the photons in the initial state. With GHOST the hadronic events can be produced which include the twice resolved minijet contribution.

5.11 Results

To estimate the energy deposited by a minijet event a sample of 7227 events with a transverse momentum cut of 2.5 GeV/c was produced with GUINEA-PIG and fragmented with the help of GHOST. All particles with an angle with respect to the beam axis of less than 100 mrad (or 200 mrad) were removed since they will deposit most of their energy inside the mask. Particles actually hitting the mask can produce secondaries that may contribute to the total power deposition. The magnetic field will bend the trajectories of some of the charged particles strongly enough that they cannot reach the calorimeter. This effect was not taken into account. Figure 5.9 shows the probability distribution for the visible energy of the events. The average deposition is significant and may be a nuisance in the reconstruction of events. For TESLA this will however not be a severe problem since the probability of having an interesting and a minijet event the same time

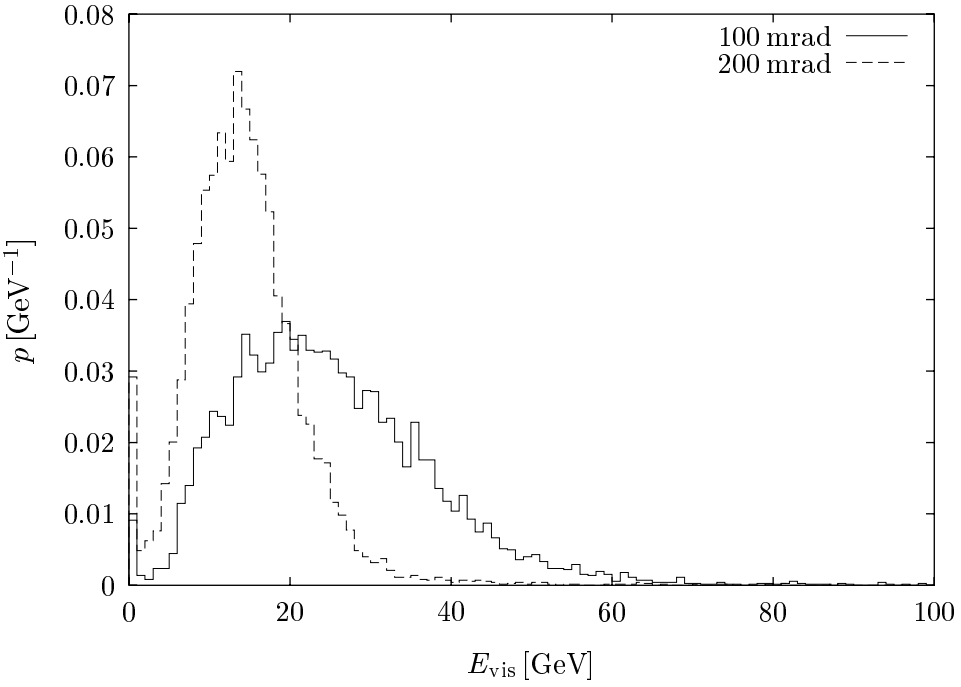

Figure 5.9: The visible energy for the minijet events in TESLA with a minimal transverse momentum of $p_\perp = 2.5\,\mathrm{GeV}$. The simple model is used instead of an eikonal one which would lead to fewer but harder events.

is small. For SBLC the deposited energy per bunch train is about 40 GeV from minijets only. If one does not use detectors that integrate over a few bunch crossings only this will affect the resolution in the forward direction.

However the soft hadronic background may contribute significantly even for TESLA since one event will occur per few bunch crossings. Figure 5.10 shows the visible energy distribution for this process. With the given detector parameters the average visible energy is 10 GeV per event. For SBLC the total energy per bunch train thus is about 133 GeV. The soft hadron background will therefore be important as well.

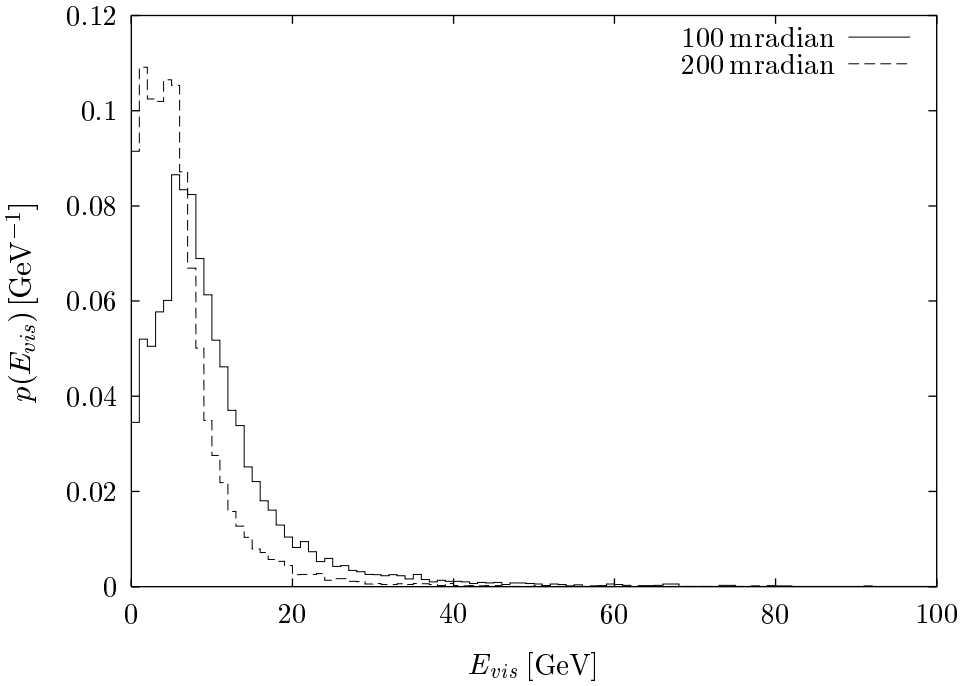

Figure 5.10: The distribution of the visible energy for the hadronic events with a centre of mass energy in excess of 5 GeV in TESLA.

Chapter 6

Principle Layout of the Detector

A detector for a linear collider will most probably be similar to a LEP detector. The main elements are a vertex detector, an intermediate tracker, a central tracker, electromagnetic and hadronic calorimetry, muon chambers and some low angle detectors. A first estimate on the required resolution of the components can be found in Table 6.1 [65].

6.1 Main properties of the detector

The innermost part of the detector has to be different for TESLA and SBLC. Since the distance between the bunches in SBLC is only 6 ns the two beam-lines have to cross at an angle to prevent the incoming bunches from receiving kicks from the outgoing bunches from the previous collisions. For TESLA a crossing angle is not needed since the inter-bunch spacing of about 200 m (equal to 700 ns) is large enough to permit separation of the ingoing and outgoing beam-lines outside the detector.

The final quadrupoles are an integral part of the detector in both cases. The distance between the end of the quadrupole pointing towards the detector and the interaction point is 3 m in the case of TESLA and 2 m in SBLC. The need to have a crossing angle leads to the choice of a normal conducting magnet in SBLC while for the head-on scheme of TESLA a superconducting magnet is appropriate.

In the case with a crossing angle, an exit hole which is almost field free is needed to remove the spent beam from the detector. These holes can be provided by the normal conducting quadrupoles[1]. A superconducting quadrupole can provide a large aperture which can be used to exit the beam. Inside this aperture however one has the main quadrupole field which is very large at increasing distance from the magnet axis and the outgoing bunch would thus experience a

[1]If the crossing angle is large enough it is also possible that the spent beam passes a small magnet on the outside. Such a design using permanent and superconducting magnets is proposed for NLC [66]; it also contains magnets to compress the spent beams.

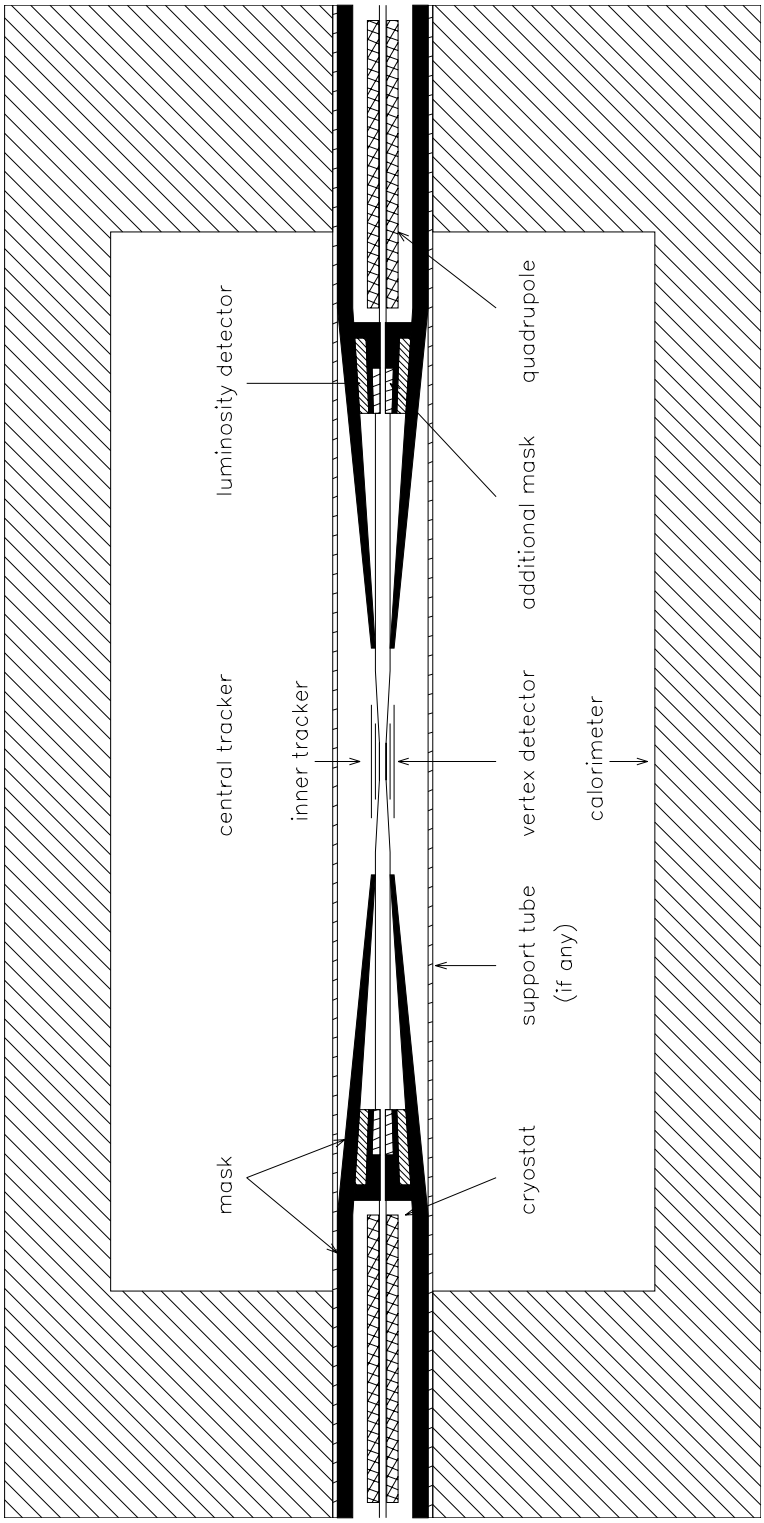

Figure 6.1: Sketch of the detector layout.

strong magnetic field. Since many particles have lost a significant part of their energy they would be strongly deflected. An additional field free hole to avoid this problem would require a special design which may be not feasible.

A normal conducting quadrupole requires an iron yoke to achieve the necessary gradients. Since iron saturates in a magnetic field of less than 2 T it is necessary to shield the quadrupole from the field of the main detector solenoid. This can be done using a compensating solenoid covering the quadrupole. The price one has to pay is a somewhat distorted detector field.

In the case with no crossing angle the large aperture of the superconducting quadrupole can be used to get rid of the spent beam. As a first attempt the use of LHC lattice quadrupoles is assumed [6], which provide an aperture of 48 mm (equal to a radius of 24 mm) and a gradient of 250 T/m. The only difference is that the iron yoke, which is used to slightly increase the field strength in the LHC design, is removed. Without the iron the magnet has an outer radius of less than 100 mm and the outer radius of the cryostat is about 221 mm in a conservative approach. The magnet can operate in an outer field of up to 3 T and thus needs no shielding if the detector field is kept below this level. The field distortion by the quadrupole drops to about 5 mT at a distance of 600 mm from the magnet axis.

A solenoid to provide a field of 3 T is feasible—the magnet planned for CMS has a higher field and more stored energy [67]. Because a higher field reduces the background from pair creation the main focus in the following will be on the option with 3 T.

A tungsten mask covers the face of the quadrupole to suppress the background from pair creation as will be discussed later. Important detector dimensions which are affected by the background are the radii and lengths of the vertex detector layers and of the beam pipe. The other dimensions of the detector are chosen as to achieve the performance given in Table 6.1. The design is not yet fixed because different approaches still compete. The detector solenoid for example could be placed either inside the electromagnetic calorimeter, in between the electromagnetic and hadronic calorimeters or outside of both. The advantages and drawbacks of these different solutions will not be discussed here.

The hermetic coverage of the detector should reach at least $|\cos\theta| \leq 0.98$, corresponding to a blind region with an opening angle of 200 mrad. For TESLA it should be possible to go down to an angle as small as 120 mrad, with the lower limit of the angle given by the size of the cryostat. A more advanced kryostat design could allow for even less than 100 mrad.

The radius of the inner layer of the vertex detector depends on the background and will be discussed in the following sections. The radii of the outer layers depend on the inner layer and the required resolution. The vertex detector is surrounded by an intermediate tracker to link the tracks in the central tracker and the vertex detector.

The inner radius of the support tube would be 321 mm if a mask thickness

Detector	Performance
Vertex detector	$\sigma_d \leq 10\,\mu\text{m} \oplus 50\,\mu\text{m}/(p_\perp \sin^{(1/2)}\theta)$
Tracker	$\sigma_{p_\perp}/p_\perp \leq 2 \cdot 10^{-4}\,\text{c/GeV}\,p_\perp$
EM-calorimetry	$\sigma_E/E \leq 0.1/\sqrt{E/\text{GeV}}$
Hadron-calorimetry	$\sigma_E/E \leq 0.6/\sqrt{E/\text{GeV}}$

Table 6.1: A first estimate of the requirements for the detector.

Detector	Performance
Vertex detector	$\sigma_{x,y} = 10\,\mu\text{m} \oplus 30\,\mu\text{m}/(p_\perp \sin^{(1/2)}\theta)$ $\sigma_z = 20\,\mu\text{m} \oplus 30\,\mu\text{m}/(p_\perp \sin^{(3/2)}\theta)$
Tracker	$\sigma_{p_\perp}/p_\perp = 1 - 2 \cdot 10^{-4}\,\text{c/GeV}\,p_\perp$
EM-calorimetry	$\sigma_E/E = 0.1/\sqrt{E/\text{GeV}} \oplus 0.01$
Hadron-calorimetry	$\sigma_E/E = 0.5/\sqrt{E/\text{GeV}} \oplus 0.04$
Energy flow	$\sigma_E/E = 0.3/\sqrt{E/\text{GeV}}$

Table 6.2: The resolutions currently aimed for in the detector [68].

of 100 mm is assumed. Its size is determined by the outer radius of the mask. Since the masks are very heavy and would require a thick support tube, it is preferable to hold them by different means to minimise material in the detector. The central tracker extends from 350 mm out to 1800 mm. It is surrounded by the calorimetry, the coil of the main solenoid and the muon chambers.

6.2 The vertex detector

Silicon detectors have successfully been used for the reconstruction of vertices in many detectors. They form two or more cylinders around the beam axis. The sensitive medium consists of a layer of silicon which is depleted from free charges by an external electric field. An ionising particle penetrating the depleted layer creates electron-hole pairs that are collected at electrodes. These signals allow the measurement of the particle's coordinates.

6.2.1 Resolution

A usefull quantity the vertex detector can measure is the impact parameter, the minimal distance a track passes from the interaction point. With only two layers in the vertex detector one needs an outer tracker two associate the corresponding hits. With more layers it is possible to find a track without that help. The additional layers of course add to the material inside the detector.

If one considers only the xy-plane the impact parameter $d_{x,y}$ is the minimal possible distance of the track to the beam axis and can be calculated easily in first approximation:

$$d_{xy} = \frac{x_1 y_2 - x_2 y_1}{\sqrt{(x_2 - x_1)^2 + (y_2 - y_1)^2}} \tag{6.1}$$

where x_1, y_1 and x_2, y_2 are the coordinates of the hit in the first and the second layer, respectively. For trajectories which originate close to the interaction point one has

$$d_{xy} = \frac{(\phi_1 - \phi_2) r_1 r_2}{r_2 - r_1} \tag{6.2}$$

where r_1 is the radius of the inner, r_2 the one of the outer layer and ϕ_1 and ϕ_2 are the associated azimuthal angles. The error of this measurement has two sources, the intrinsic precision of the detector and the multiple scattering in the beam pipe and the inner layer. For the first one gets:

$$\sigma_i^2 = \frac{r_1^2 + r_2^2}{(r_2 - r_1)^2} \sigma_{intr}^2 \tag{6.3}$$

This error is only dependent on the intrinsic resolution of the layers and on the ratio r_1/r_2; it can be improved by adding more layers. For the second source, the rms-deflection angle in a plane for multiple scattering is given by

$$\theta_{rms} = \frac{13.6\,\mathrm{MeV}}{p\beta c} \sqrt{D}\,[1 + 0.038 \ln D] \tag{6.4}$$

where D is the thickness of the material in radiation lengths through which a particle of velocity βc with the momentum p travels. Neglecting the logarithmic term, the resulting error is

$$\sigma_{MS} = \frac{13.6\,\mathrm{MeV}}{p\beta c \sin\theta} r_1 \sqrt{\frac{D}{\sin\theta}} \tag{6.5}$$

where D is the combined thickness of the first layer and the beam pipe, if the two are very close. The effective thickness of the material for the particle is then $D/\sin\theta$ with θ being the polar angle of the particle trajectory. The additional term $r_1/\sin\theta$ comes from the extrapolation to the interaction point. If the beam pipe is not close to the detector, one finds

$$\sigma_{MS} = \frac{13.6\,\mathrm{MeV}}{p\beta c \sin\theta} \sqrt{\frac{D_{BP}}{\sin\theta} r_{BP}^2 + \frac{D_1}{\sin\theta} r_1^2} \tag{6.6}$$

This error depends on the absolute dimensions of the detector as well as on the particle momentum and angle. This favours the use of a beam pipe and an inner layer as thin as possible and at the smallest achievable radius. In the rz-plane the errors can be calculated equivalently.

To reach a precision of

$$\sigma^2 = (10\,\mu\mathrm{m})^2 + \left(\frac{50\,\mu\mathrm{m\,GeV/c}}{p}\right)^2 \frac{1}{\sin^3\theta} \tag{6.7}$$

with an intrinsic resolution of $\sigma_{\mathrm{intr}} = 1/\sqrt{12} \cdot 20\,\mu\mathrm{m}$ one requires $r_2 = 2.5 r_1$. With a beryllium beam pipe of $500\,\mu$m thickness and an inner layer of 0.2% radiation lengths, one finds $r_1 \leq 58\,\mathrm{mm}$. If the beam pipe and the inner layer add up to 1.0% of a radiation length, as for example in DELPHI, the requirement is $r_1 \leq 35\,\mathrm{mm}$.

6.2.2 Overview over the different types of vertex detectors

Three different types of silicon vertex detectors are in use. In the first the sensitive region is divided into longitudinal and transverse strips, referred to as xy (or $r\phi$) and z strips. The design is therefore called microstrip detector. In the other two designs the sensitive area is divided into pixels. In one of them charged coupled devices (CCD's) are used in the other each pixel is connected to its own electronics that allows to detect and store a hit.

The typical width between strips of a microstrip detector is 25-100 μm. The thickness of the silicon is of the order of 300 μm, which corresponds to about 0.3 % of a radiation length, for one layer. If the separate xy and z strips are used the total thickness of the detectors inner layer would be twice as high. This can be avoided by using the signal from the electrons and the corresponding holes which are available on the two surfaces of the active layer. On one surface the strips are oriented for an xy one the other for a z readout. The strips are read out in parallel at the ends. The readout time achieved with a pipeline readout system at the H1 vertex detector is below 100 ns, for example. Hence it is fairly easy to read out the detector between bunch crossings in TESLA. In SBLC, however, one would have the integrated signal of at least a few bunch crossings. The lower limit on the readout time is given by the drift velocity of the charge carriers in the external field. For a typical design with 300 μm thickness it is about 8 ns for electrons and 25 ns for holes. For the readout time achieved at H1 the number of integrated bunch crossing would be 16 for SBLC—this could be reduced by faster electronics.

In a CCD the active silicon layer is subdivided into cells with a size of about 20 μm times 20 μm by potential wells [69]. The cells collect the charges set free by a charged particle penetrating the silicon. For readout the rows of these cells

are moved to a special readout line. From there the individual pixels are shifted into an amplifier. The pixel readout frequency is 10 MHz in SLD, but this can be improved[69]. With a typical number of rows of 256 or 512 and the same number of cells per row, the readout time for a chip is of the order of milliseconds. The detector can thus be read out between bunch trains but not between individual bunch crossings. Due to the high number of channels the CCD detector can tolerate a much larger number of hits per readout. Depending on the collider timing it will however accumulate the background from a large number of bunch crossings. The thickness of a CCD detector could be as low as 0.2 % of a radiation length. Together with the small cell size this gives an excellent impact parameter resolution.

The third type of vertex detector is here referred to as the pixel detector to distinguish it from the CCD type. It consists of very small strip-like pixels with a typical size of the order of 50 μm times 500 μm. Each of these pixels is bonded to a micro electronics cell on an additional layer of silicon. This consists of a preamplifier and a discriminator that allows to detect if the charge exceeds a certain threshold. The charge is then passed through a gate into an output latch. The thickness of the sensitive layer including the electronics is of the order of 400 μm and thus somewhat larger than for the other two designs, especially the CCD. The fact that each pixel has its own electronics allows for a variety of interesting readout schemes in the case of TESLA. Three possible options are described in reference [70] here only an example is given.

If a pixel is hit it sends a signal to the readout chip and becomes insensitive to additional hits by closing a gate. If an external trigger requires the information of the vertex detector from a certain bunch crossing only the columns with pixels hit during this very crossing have to be readout. If a hit pixel is not read out during a given delay time it will delete the charge and switch to be sensitive again. Another possibility is that a hit pixel puts its address on a signal bus which connects all pixel in a column. The signal is moved from one pixel to the next to the readout chip which stores hit position and time in a buffer. For LHC a time per step of 25 ns is envisioned, which allows to have the last signal be stored after four bunch crossings (in TESLA) for 100 pixel columns. The rate of colliding signals—where a pixel that holds the address of another is hit—is therefore small. This type of detector can tolerate very high background rates—with all the different readout schemes. The resolution is inferior compared to the CCD due to the thicker layers and the larger cell size.

Each of these detectors can be read out in two different ways. In the first method it is only detected whether the pixel or strip was hit by requiring the charge in this pixel to exceed a certain threshold. The resolution of this so called binary readout is given by $\sigma_{intr} = 1/\sqrt{12}\Delta x$, where Δx is the cell or strip size. An improvement of the resolution is possible by using the analog information. Due to capacitive coupling a particle can deposit charges in neighbouring cells also. Using these it is possible to fit the position of the trajectory with greater

accuracy.

In a microstrip detector one has to find the corresponding hits in the xy and z strips. This can be done using the external tracker. In principle, if a single active layer is used with the electrons and holes read out in different directions, it should be possible to get additional information from the fluctuation of liberated charges from one hit. Comparing the charges collected in the xy strips to those collected in the z strips could assist in correctly associating the hits. This was foreseen in ALEPH but is currently not used.

6.3 The central tracker

Several different designs for the central tracker are possible, for example a drift chamber, a time projection chamber (TPC) or a silicon tracker. While the first two have gas-filled volumes and sample the particle position at a large number of points the latter consists of a few layers of silicon and thus measures a few points only, but these to a much higher precision. A silicon tracker is in general advantageous in high background since it has a better granularity. On the other hand the multiple scattering is worse than in a gas volume and the redundancy needed for track reconstruction is significantly smaller than if a gaseous detector. A gas chamber on the other hand may suffer from the ions which are set free in the avalanches. These ions are removed slowly and can thus change the electric field in the detector, reducing the resolution if the background is too high. An example of a promising detector type which is under development are the so called MICROMEGAS [71]. These offer the advantages of both other designs. They are used in a gas-filled volume and consist of a thin layer of Kapton with anode strips. About 100 μm above this layer lies a mesh, separated from the anodes by quartz fibres. In a few mm distance another mesh is fixed. Between the anode layer and the first mesh a strong field of 100 kV/m is applied, between the two meshes a weaker field of 1 kV/m. A charged particle produces electrons in the gap between the meshes that drift towards the anode. If the electrons pass the mesh close to the anode they induce an avalanche as in a normal gas chamber. The position of hits can be measured to about 30 μm with these detectors. Since they are very thin (10^{-4} of a radiation length) one can use a large number of layers. Because of the small gap between the anodes and the first mesh the ions produced in the avalanche are removed within about 100 ns.

In many detector designs the central tracker is subdivided. The inner part has a better resolution and finer granularity allowing to handle larger background without confusion.

A charged particle in a homogeneous field travels along a helix. The transverse momentum $p_\perp$ can be calculated from the magnetic field B and the radius of the helix R as: $p_\perp\,[\mathrm{GeV/c}] \approx 1/3R\,[\mathrm{m}]B\,[\mathrm{T}]$. The error of this measurement is given

by the error of the curvature $k = 1/R$:

$$\frac{\sigma_{p_\perp}}{p_\perp} = \sigma_k R. \tag{6.8}$$

Two main contributions to the curvature error have to be taken into account, the measurement precision for a single point of the trajectory and the error from multiple scattering. For a detector that samples many (more than ten) points of the trajectory the first contribution can be parametrised as [72]:

$$\sigma_{k_{\mathrm{mes}}} = \frac{\sigma_x}{L^2}\sqrt{\frac{720}{N+4}}. \tag{6.9}$$

Here σ_x is the spatial resolution in the xy-plane for each of the N points measured and L is the length of the trajectory in the same plane. If the trajectory is constraint on one side, with the help of the vertex detector for example, one can replace 720 by 320 in the square root.

The error due to multiple scattering can be approximated as:

$$\sigma_{k_{\mathrm{MS}}} = \frac{13.6\,\mathrm{MeV}}{\beta c p_\perp L}\sqrt{\frac{10}{7}\frac{L}{\sin\theta X_0}}. \tag{6.10}$$

Here θ is the angle with respect to the z-axis and X_0 is the radiation length of the gas.

The total relative precision can thus be written as:

$$\frac{\sigma_{p_\perp}}{p_\perp} = \frac{\mathrm{mT}}{0.3\,\mathrm{GeV/c}B}\left[\frac{\sigma_x}{L^2}\sqrt{\frac{720}{N+4}}p_\perp \oplus \frac{13.6\cdot 10^{-3}\,\mathrm{GeV/c}}{\beta L}\sqrt{\frac{10}{7}\frac{L}{\sin\theta X_0}}\right]. \tag{6.11}$$

where $\oplus$ stands for the for sum in quadrature. With the field of $B = 3\,\mathrm{T}$, a lever arm $L = 1.5\,\mathrm{m}$, a resolution of $\sigma_x = 100\,\mu\mathrm{m}$ and about 50 measurement points and with a radiation length of $X_0 \approx 200\,\mathrm{m}$ one finds

$$\frac{\sigma_{p_\perp}}{p_\perp} = 1.8\cdot 10^{-4} p_\perp/(\mathrm{GeV/c}) \oplus 1.6\cdot 10^{-3}\sin^{-1/2}\theta. \tag{6.12}$$

6.4 The luminosity monitor and low angle tagging

Bhabha scattering can be used to measure the luminosity. The cross section for Bhabha scattering via one photon exchange which dominates at small transverse momentum in the final state is [32][34]:

$$\frac{d\sigma}{dt} = \frac{2\pi m^2 r_e^2}{s^2}\left[\frac{s^2+u^2}{t^2} + \frac{2u^2}{ts} + \frac{u^2+t^2}{s^2}\right] \tag{6.13}$$

Using $t = -\frac{s}{2}(1-\cos\theta)$ and $u = -\frac{s}{2}(1+\cos\theta)$ one can easily find the cross section for a particle to be scattered into an angular range between θ_1 and θ_2 in the centre-of-mass frame

$$\begin{aligned}\sigma(\theta_1 \le \theta \le \theta_2) &= \frac{\pi r_e^2}{4\gamma^2}\left[8\ln\left(\frac{\cos\theta_1 - 1}{\cos\theta_2 - 1}\right)\right. \\ &+ \frac{\cos^4\theta_1 + 2\cos^3\theta_1 + 24\cos^2\theta_1 - 27\cos\theta_1 - 48}{6(\cos\theta_1 - 1)} \\ &\left. - \frac{\cos^4\theta_2 + 2\cos^3\theta_2 + 24\cos^2\theta_2 - 27\cos\theta_2 - 48}{6(\cos\theta_2 - 1)}\right] \quad (6.14)\end{aligned}$$

The cross section is peaked at small angles. In this range the differential cross section is proportional to $1/\theta^4$ and the integrated cross section to $1/\theta^2$. To obtain high counting rates it is necessary to extend the luminosity monitors to the smallest possible angle. So one should place it inside the mask. It has on the other hand to be assured that the background from the pair creation does not interfere with the signal from Bhabha scattering. So the back and inner part of the monitors are protected by a mask. The inner opening angle of the mask is 66 mrad in the design. If one allows the luminosity detector to extend down to 40 mrad one will have approximately 10 events per second.

An additional use of the luminosity monitor is the detection of the remnant electron from photo production. A minimal angle of 40 mrad[73] should be achieved to overlap the measurement with previous LEP experiments. Since one does not have two coincident signals for this tag as for the Bhabha events it will suffer more from background.

One is not only interested in the total luminosity but also in the luminosity spectrum. Especially the top threshold scan requires the knowledge of this spectrum. This can not be measured directly via the centre of mass energy of the particles from the Bhabha scattering since the errors are of the order of percent. The angles of the particles can be measured with a high accuracy of the order of mrad. This can be used to measure the imbalance of the colliding particles. Using the the transformation from the laboratory into the centre of mass system

$$\cos\theta' = \frac{(1+\cos\theta)(1-\beta) - (1-\cos\theta)(1+\beta)}{(1+\cos\theta)(1-\beta) + (1-\cos\theta)(1+\beta)}$$

one finds

$$\frac{E_1^2}{E_2^2} = \frac{(1+\cos\theta_1)(1-\cos\theta_2)}{(1-\cos\theta_1)(1+\cos\theta_2)} \quad (6.15)$$

where θ_1 and θ_2 are measured with respect to the electron and positron beam directions. The unfolding of this distribution needs more input either from measurement or from a model, a possible method is proposed in [74]. The error of the measurement depends on the angle at which one measures as

$$\sigma_{E_1/E_2} \approx \frac{\sqrt{2}}{\sin\theta}\sigma_\theta.$$

One would thus measure in the barrel region and not inside the mask. The resolution of this measurement can then be of the order of a permille.

Chapter 7

Background in the Detector

7.1 Simulation of the detector

To investigate the effect of the background on the experiments a detector simulation program SEAL[1] was written. It is based on GEANT [75] and can read the event-files created by GHOST as well as the four-vectors of the particles from pair production as calculated by GUINEA-PIG. The simulation contains a generic calorimeter, central tracker, vertex detector and luminosity detector or low angle tagger. Also included are the space for a support tube, the beam pipe, the final quadrupoles and the masks. Since tracking the particles produced by beam-beam interaction is time consuming[2] it is necessary to proceed in two steps. In the first the particles are tracked until they either leave the detector or reach some sensitive component. In the latter case they are stored in a file and can be reread in the second step. This will then take only a few minutes. It is possible to overlay events with background.

To suppress the pair background and achieve a better detector performance the solenoid field was chosen to be 3 T as explained in the previous section. In the simulation each layer of the vertex detector consists of a supporting layer of 200 μm beryllium and a sensitive layer of 20 μm silicon.

The beam pipe consists longitudinally of five parts. Closest to the interaction point a 0.5 mm thick beryllium tube. Its inner radius is $r_{BP} = 20$ mm, which is slightly less than that of the inner layer of the vertex detector $r_1 = 25$ mm. The small radius cannot extend to the quadrupoles since particles from the pair background would hit it and emit photons going into the detector. The narrow tube is therefore followed by a conical section on each side, which is also made of beryllium. These cones start at $|z| = 125$ mm and end at $|z| = 240$ mm. They allow an angular coverage of the second layer of the vertex detector of

[1] Simulation of the Experimental Area of a Linac.

[2] For the pair background the tracking of the particles produced in one bunch crossing and of their secondaries takes one day of CPU-time on a work station with a 133 MHz Pentium running `linux`.

$|\cos\theta| < 0.98$. The conical parts are followed by cylindrical aluminium tubes with an inner radius of 48 mm and a wall thickness of 2 mm which extend to the quadrupoles.

Most of the particles from pair production hit the quadrupole at a distance of less than a few centimetres from the beam axis. They produce showers and in the showers soft photons some of which are scattered backwards. The detector has therefore to be protected from these secondaries. This is done by a conical mask. The inner opening angle of this cone is about 66 mrad, the outer 100 mrad. The distance between the interaction point and the opening of the mask is 750 mm. The cone will be mounted to a thick walled cylinder, see Figure 7.2 on page 85. The inner angle of the cone is defined by the space requirement of the cryostat. It may be thus be necessary to increase the angles by about 10 mrad if the outer radius of the cryostat has to 221 mm as in [6], while one could profit from a smaller kryostat if feasible. In the following it turns out to be necessary to introduce an additional mask inside the main part. Figure 7.2 on page 85 shows the layout.

The luminosity monitors are placed inside the inner part of the mask. Their backplane and inner bore are covered with tungsten to suppress the background from pair production.

The main detector field is assumed to be constant with $B_z = 3$ T and $B_{x,y} = 0$ except for the region close to the quadrupoles. At these positions the field is calculated by interpolating values from a table. As a model the normal lattice quadrupole for LHC without the iron yoke is used [76].

7.2 The vertex detector

7.2.1 Acceptable background level

Hits from charged background may confuse the vertex reconstruction. As a rule of thumb one can assume that one hit per mm^2 does not pose a problem for a CCD detector but even rates ten times higher may not be a problem [77]. For the strip detector the occupancy (the number of channels occupied by a signal from the background) may set a limit depending on the strip size. Assuming the total area of a strip[3] to be about $1\,\mathrm{mm}^2$ (eg. 40 mm long and 25 μm wide) a hit density of $10^{-2}\,\mathrm{mm}^{-2}$ leads to an occupancy of about 2% if each hit affects two strips.

An estimate of the number of background hits in a layer that are (wrongly) used in reconstructing a track can be done as follows. The hit density ρ of the background around the position of the real hit is homogeneous. With the outer detector (the central tracker or the outer two layers of the vertex detector for the inner layer) the expected position of the hit is found to be $(r\phi_0, z_0)$. For a uniform

[3]Strip sizes are in the following not the actual sizes of the strips themselfs but of the sensitive areas conntected to a strip.

background hit density ρ the probability to find at least one track closer than Δr to the reconstructed position is given by $1-\exp\left(-\pi\Delta r^2\rho\right)$, where the same error σ is assumed in both directions. Then the probability to find a background hit closer to the expected position than the real hit is

$$P = \int_0^\infty \left(1 - e^{-\pi r^2 \rho}\right) \frac{1}{2\pi\sigma^2} e^{-\frac{r^2}{2\sigma^2}} 2\pi r \mathrm{d}r = 1 - \frac{1}{1+2\pi\sigma^2\rho} \approx 2\pi\sigma^2\rho$$

for $2\pi\sigma^2\rho \ll 1$. If the resolutions are different in the two directions one can replace σ^2 by $\sigma_{r\phi}\sigma_z$.

The precision with which the position of the hit in the inner layer of the vertex detector can be reconstructed is given by the outer two layers. It should be noted that multiple scattering in the inner layer is of no importance since it does not change the position of the hit. While the constant term is of the order of $10\,\mu$m the multiple scattering term is

$$\sigma_{\mathrm{MS,r}\phi} \approx \frac{13.6MeV}{p\beta\sin\theta}\sqrt{\frac{D_2}{\sin\theta}(r_2 - r_1)^2}.$$

in $r\phi$ and

$$\sigma_{\mathrm{MS,z}} \approx \frac{\sigma_{MS,r\phi}}{\sin\theta}$$

in z-direction. The additional $1/\sin\theta$ appears because the error in the rz impact parameter has to be projected onto the cylinder $r = r_1$ to get the error in the z position. Assuming a radius of the inner layer of $r_1 = 25\,\mathrm{mm}$ and of the second $r_2 = 50\,\mathrm{mm}$ with a thickness of $D_2 = 1\%$ one finds

$$\sigma_{\mathrm{MS,z}} \approx \frac{34\,\mu\mathrm{mGeV/c}}{p_\perp\sqrt{\sin^3\theta}}.$$

The situation can be improved by using a detector where the sensitive layers at the end are rotated such that trajectories of particles coming straight from the interaction point will have normal incidence. This would suppress the $1/\sin\theta$ in the effective thickness in the square root and in the case of the longitudinal position the more important $1/\sin\theta$ in the first term. Such a detector may not be easy to build and especially align but the gain of a reduction in the background is a factor $1/\sin^2\theta$ in total. In practice one would most probably choose to have a barrel region of the vertex detector and some end plates perpendicular to the beam axis. With such a layout the maximal angle of incidence can be kept below 45 degrees. This limits the maximal increase in the product $\sigma_{\mathrm{MS,z}}\sigma_{\mathrm{MS,r}\phi}$ at any angle to a factor of two compared to $\theta = \pi/2$.

In the simplest case one could assign the hit that is closest to the expected position of the track. For a track with $p_\perp = 1\,\mathrm{GeV/c}$ the probability of taking a wrong hit would then be 0.73 % for a hit density of 1 hit per mm^2.

For single tracks this probability can be reduced by requiring that the inner layer must have exactly one hit in a certain region around the expected track position. If this region is an ellipse with half axes of $3\sigma_{r,\phi}$ in xy- and $3\sigma_z$ in z-direction, about 1.1% of the true hits will be lost because they are outside this region. For a hit density of $1\,\mathrm{mm}^{-2}$ and the above resolution two hits will be found in this region for about 3% of all tracks with $p_\perp = 1\,\mathrm{GeV/c}$. In these cases no vertex can be reconstructed. The number of wrongly reconstructed vertices will be less than $5 \cdot 10^{-4}$. If the outer layer is a CCD and thus much thinner (D=0.2%) the probability of loosing the vertex is reduced to 0.6% while less than 10^{-4} are wrong.

For a micro strip detector with a background hit density of $10^{-2}\,\mathrm{mm}^{-2}$ the probability to find two hits within a region of $\pm 2.5\sigma_{MS,r\phi}$ is around 7% for a particle with $p_\perp = 1\,\mathrm{GeV/c}$ while the probability that the true hit is not in this region is about 0.1%.

7.2.2 Charged hits in the vertex detector

Pair creation is the main source of charged hits in the vertex detector. The number of particles due to this process that hit the detector directly is shown in Figure 7.1 as a function of the detector radius. In this plot a total angular coverage of $|\cos\theta| \leq 0.98$ was assumed. One can see a drastic rise of the number of particles at radii below 13 mm for $B_z = 3\,\mathrm{T}$. This is the result of the already mentioned deflection of the pair particles by the beams.

The number of actual hits in the vertex detector due to the pairs is estimated using the detector simulation. In a first step only the particles that hit the vertex detector directly are used. The simulation yields about 220 hits in the inner vertex detector layer. Each of the 70 particles thus produces three hits on average.

In a second step all particles with an energy in excess of 1 MeV are used in the simulation. The number of hits per bunch crossing found at a radius of $r_1 = 25\,\mathrm{mm}$ is 1500. This is significantly more than in the previous simulation.

The time dependence of the hit rate is plotted in Figure 7.3. It is easy to see that the majority of the hits is not due to particles directly reaching the vertex detector but to particles or secondaries that are scattered inside the mask in the material of the quadrupole and then are guided backwards into the detector by the main solenoidal field. The distance they have to travel is 6 m and the time after the bunch crossing they need to reach the detector is thus about 20 ns. The combination of the main solenoidal and the quadrupolar field actually leads to a rise of backscattered particles, as can be seen in Figure 7.4. In this plot the positions are shown at which the charged particles cross the planes at $|z| = 3\,\mathrm{m}$, where the ends of the quadrupoles towards the detector are located. The concentration is especially high in the regions where the combined field points towards the aperture of the quadrupole. The number of direct hits per bunch

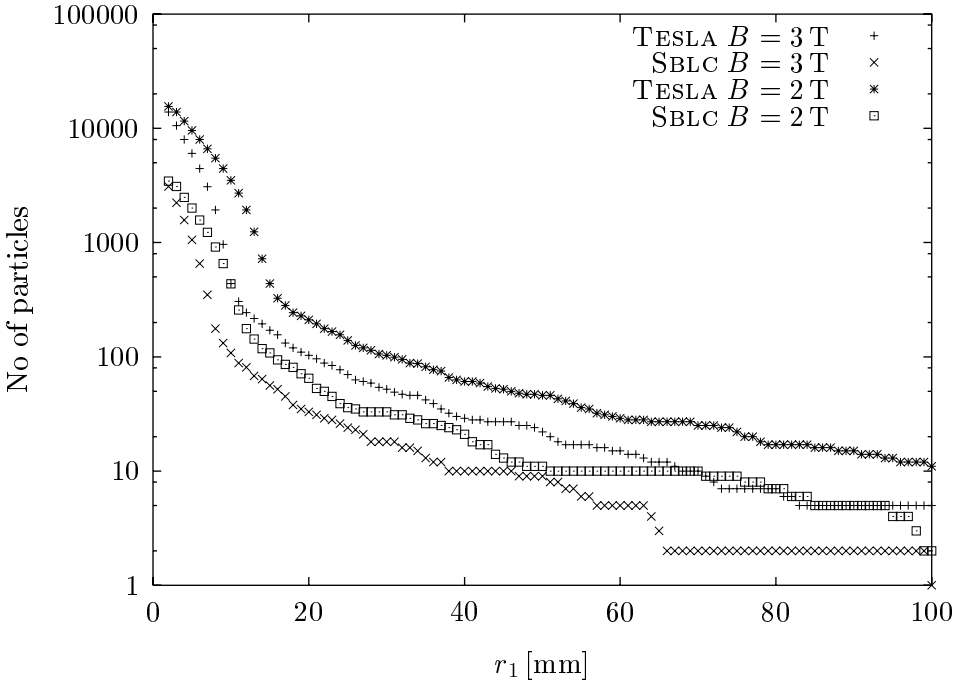

Figure 7.1: Number of particles per bunch crossing from pair creation that hit the innermost layer of the vertex detector. A coverage of $|\cos\theta| \leq 0.98$ is assumed. The luminosity per bunch crossing is smaller in SBLC leading to a smaller background per crossing. With a CCD vertex detector the numbers have to be multiplied by 333 to account for the number of bunches per train for SBLC. For TESLA the factor depends on the specific detector design, see the text. Only particles with an energy at production time of more than 1 MeV are used in this plot.

crossing is about 230 at a radius $r = 25\,\mathrm{mm}$.

7.2.3 Reducing the number of hits

The number of hits can be reduced by increasing the radius of the detector or by using a detector that can be read out very fast. A third method is to suppress the backscattering.

A readout time of 20 ns seems to be very difficult for micro-strip detectors. It could be possible to gate pixel detectors with a resolution of 20 ns [78] but this also is challenging.

Reducing the number of hits has the advantage of not only making the design of the readout easier but also of reducing the radiation damage. Since increasing the radius of the vertex detector compromises the resolution, suppression of the backscattering is advantageous. A possible solution would be to use a cylindrical mask inside the conical part of the main mask, see Figure 7.2. If the radius of the additional mask is smaller than that of the vertex detector it is possible to achieve

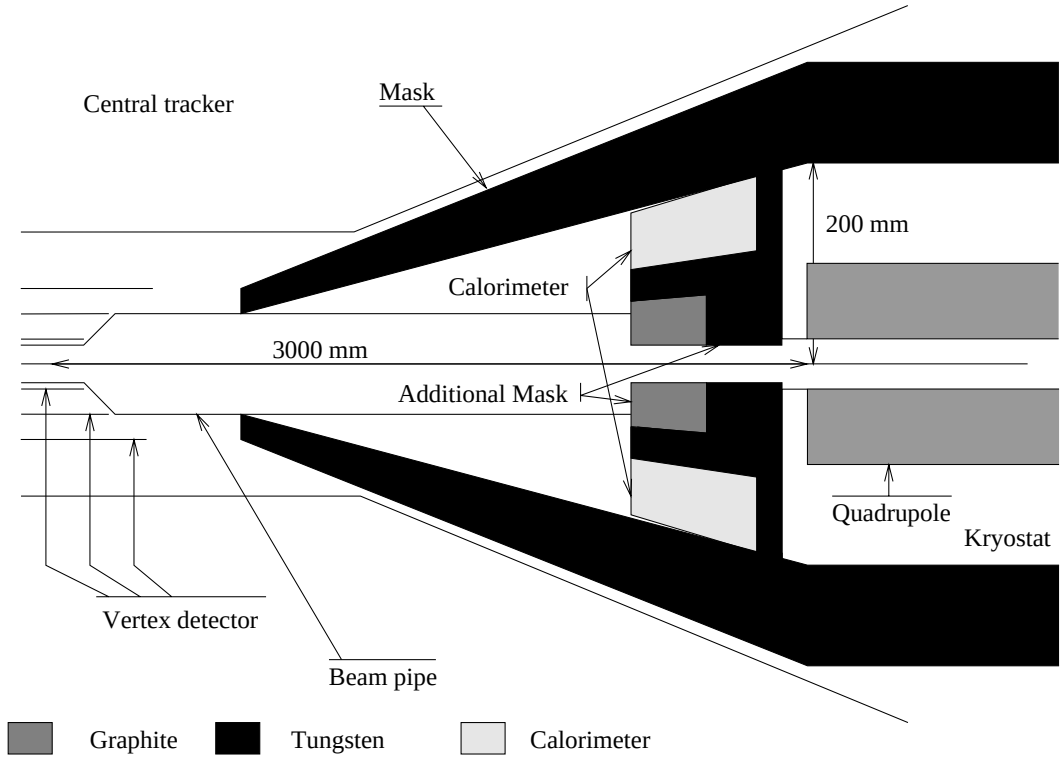

Figure 7.2: Sketch of a possible layout for the mask to suppress the background from the pair creation.

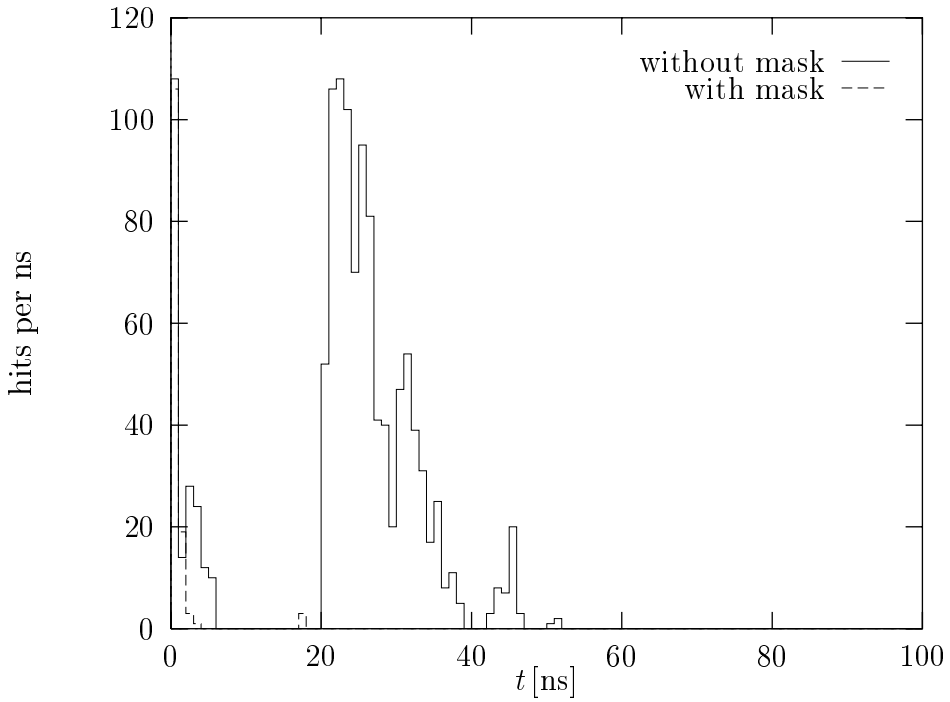

Figure 7.3: The time distribution of the hits in the vertex detector.

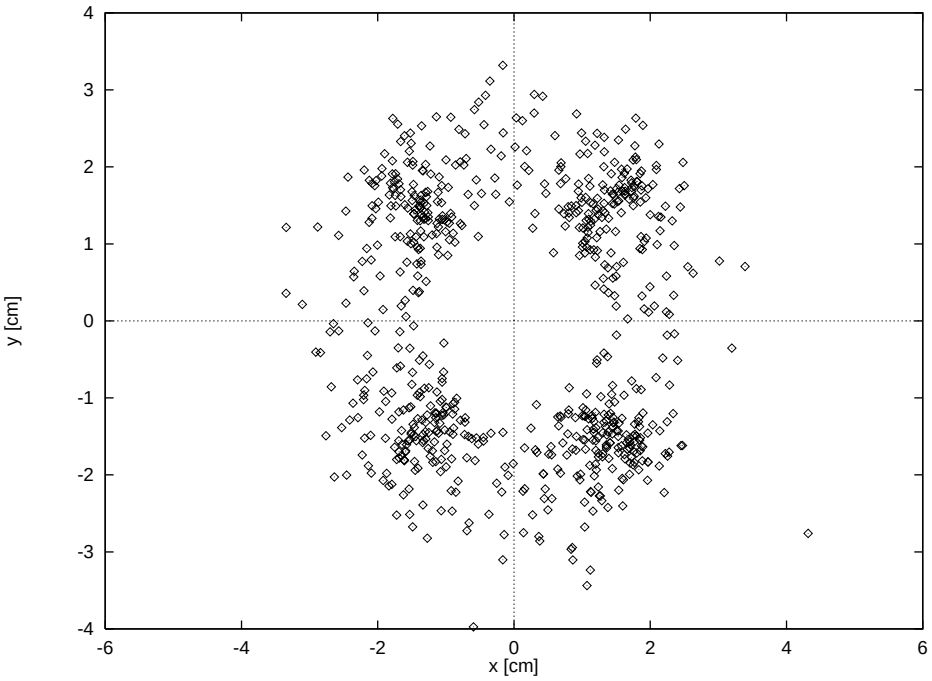

Figure 7.4: Positions where the trajectories of backscattered particles that hit the beam pipe cross the planes $|z| = 3\,\mathrm{m}$. The quadrupoles have their end towards the interaction point at this position.

a reduction of the number of hits. In addition this mask serves as a protection against the neutrons that are produced in the beamstrahlung collimator.

The part of the mask pointing towards the interaction point should be made of a material with a long radiation length. Since in a material with a short radiation length like tungsten low energy electrons tend to be backscattered. A simulation where the additional mask was made only from tungsten showed that the number of hits in the vertex detector was only slightly reduced. The mask however must contain some hard material to stop particles coming from the other side. The solution is to use a front layer of graphite followed by tungsten. The thickness of the mask was chosen to be 300 mm for each layer. This reduces the number of particles that manage to escape through the centre hole back into the detector to a negligible number. The tungsten can be instrumented to be used as a calorimeter comparable to existing luminosity monitors. While it is difficult to identify individual particles (for example from Bhabha scattering) in the background of the pairs, the total energy of the pairs can be well measured.

Figure 7.5 shows the dependence of the hit number per bunch crossing in the inner layer of the vertex detector for different combinations of vertex detector and mask radii. The calculations were done for an older set of TESLA parameters but the principle stays the same. The minimal radius of the additional mask is constrained by the collimation. The parameters in the collimation region are

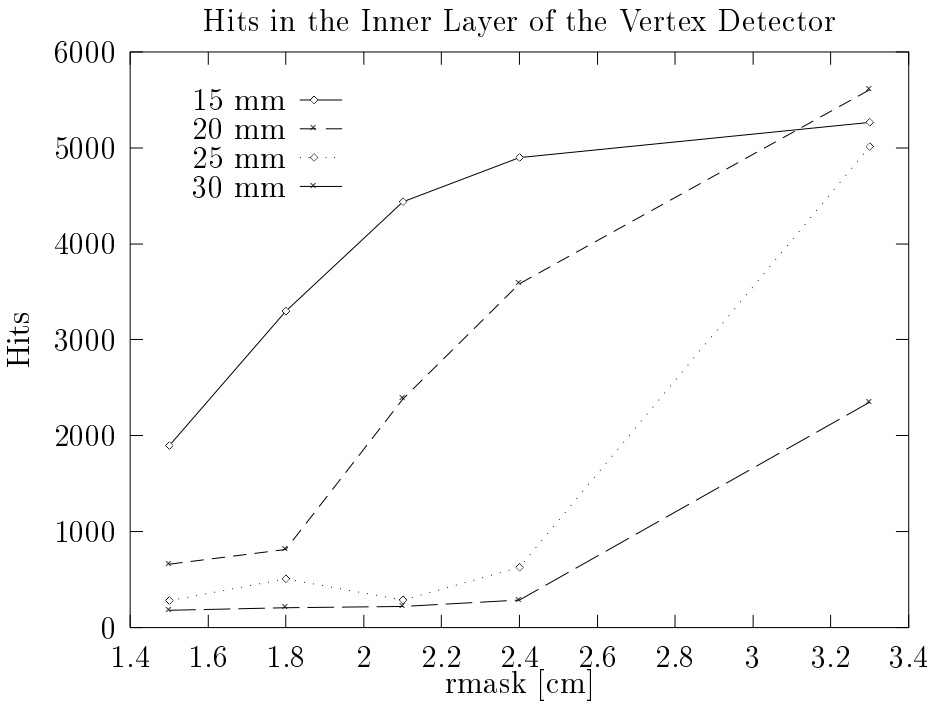

Figure 7.5: The number of hits in the inner layer of the vertex detector for different radii of the mask as well as of the detector. A radius of 33 mm represents no mask. This calculation depends on the detailed layout of the quadrupole, mask etc. and can only just give a hint of the dependencies.

chosen such that none of the remaining particles can emit a synchrotron radiation photon in the final doublet that hits the the quadrupole doublet on the other side. If one does not want to tighten the collimation requirements one therefore has to choose the inner radius r_m of the mask such that it cannot be hit by a photon from synchrotron radiation emitted in the final doublet. This leads to $r_m = 18\,\mathrm{mm}$.

The beam pipe should be larger than this radius in order to avoid the backscattered particles. A reasonable choice is $r_{BP} = 20\,\mathrm{mm}$. This allows the vertex detector to extend to a minimum radius of about 25 mm.

7.2.4 Remaining background

With the additional inner mask the contribution of backscattered particles to the hit density in the vertex detector is reduced to a small fraction of that from direct hits. In Figure 7.6 the number of hits expected for different vertex detector radii in TESLA is shown. The magnetic field is 3 T the angular coverage $|\cos\theta| < 0.98$ and the distance of the inner layer to the beam pipe is 2 mm.

For a geometry with a beam pipe radius of 20 mm, vertex detector layers at $r_1 = 25\,\mathrm{mm}$, $r_2 = 50\,\mathrm{mm}$ and $r_3 = 75\,\mathrm{mm}$ and the same field and angular coverage as before one finds 230 hits per bunch crossing in the inner, 80 in the middle and

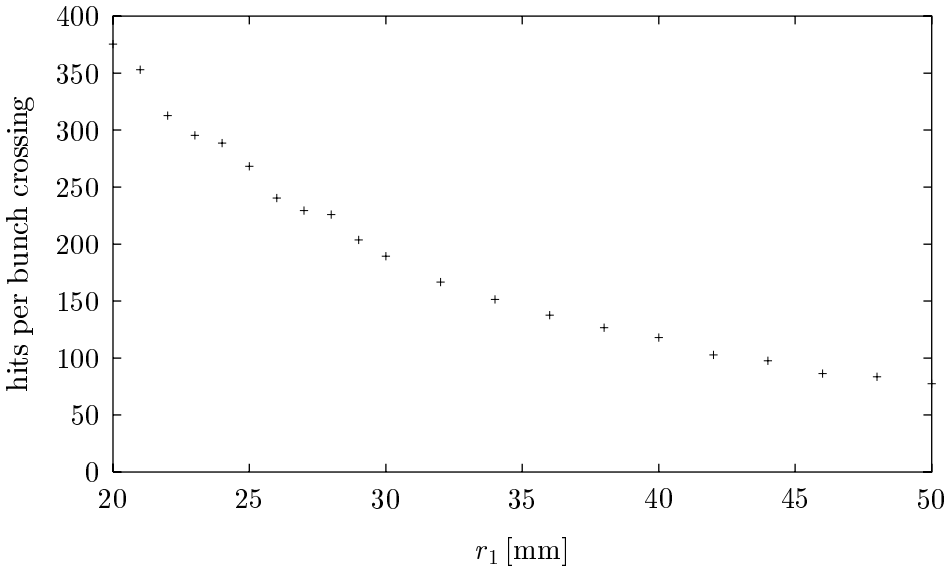

Figure 7.6: The expected number of charged hits in the innermost layer of the vertex detector for different radii. The beam pipe is assumed to have a radius 2 mm smaller than the inner vertex detector layer.

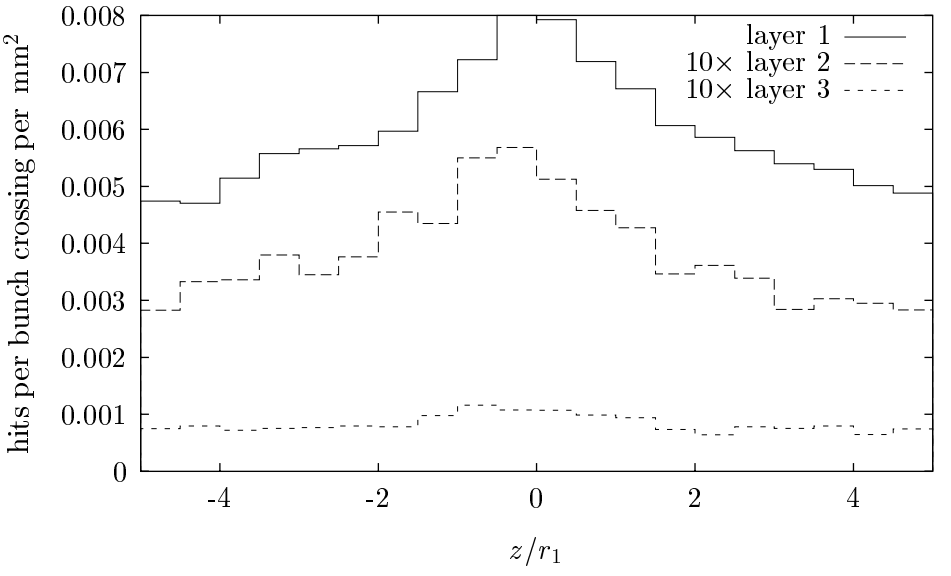

Figure 7.7: The distribution in z of the hit density in the inner layer of the vertex detector at $r_1 = 25$ mm. The density for the second and third layer is multiplied by ten.

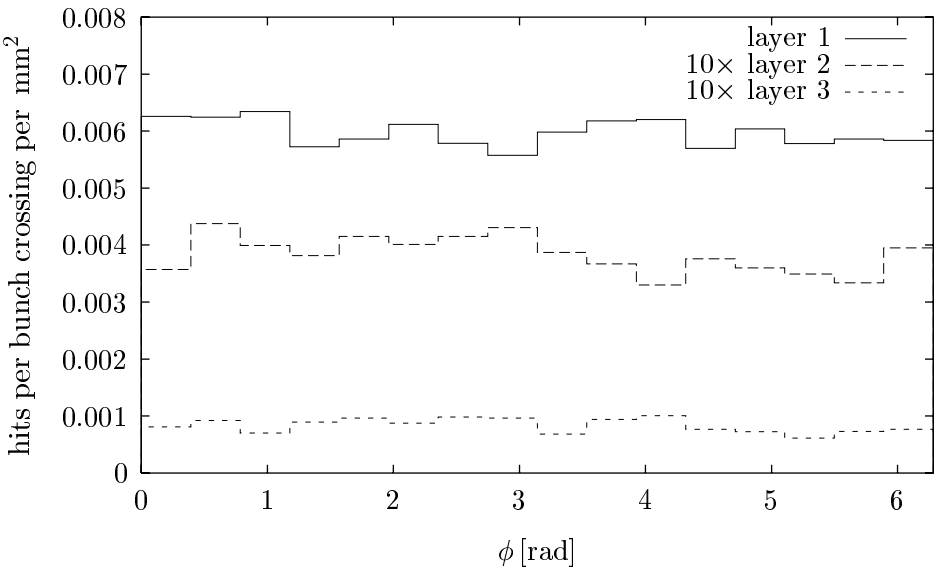

Figure 7.8: The distribution in ϕ of the hit density in the inner layer of the vertex detector at $r_1 = 25\,\mathrm{mm}$.

37 in the outer layer. With a magnetic field of 2 T these rates increase to 470, 120 and 60 respectively. For 4 T one finds 147, 36 and 18 hits.

The dependence of the hit density on the z-position is shown in Figure 7.7 for a field of 3 T. The distribution is relatively uniform with a slight enhancement at $z = 0$. The maximal difference to the medium density is less than 50% at all positions. The angular distribution of the hits is shown in Figure 7.8. It is flat in all layers. This allows to assume a uniform hit distribution in detector in the following calculations.

7.2.5 How to handle the background

In the following some estimates are made how to cope with the background due to charged hits. However it should be kept in mind that the predictions are not compared to measurements to prove that the simulations give correct results. Even for SLC, the existing machine with the highest expected background rate, these are too small to be measurable within the synchrotron radiation background.

In SBLC it will be difficult to profit from the fast readout of micro strip and pixel detectors. Because of the inter-bunch spacing of only 6 ns, a few bunch crossings occur during one readout. A possible solution is a CCD based vertex detector.

In the case of TESLA one can in principle try to use any of the three types of vertex detectors. A minimal radius of $r_1 = 25\,\mathrm{mm}$ for the inner layer is chosen to stay safely away from backscattered charged particles as well as from neutrons originating from the beamstrahlung collimators. The expected number of hits

per bunch crossing is about 230 at this radius assuming an angular coverage of $|\cos\theta| < 0.98$. Including the patch factor 1.5 to take into account the difference to the Vermaseren Monte-Carlo this number is about 350. The active layer at $r_1 = 25\,\mathrm{mm}$ is roughly $4 \cdot 10^4\,\mathrm{mm}^2$. The hit density thus is about $1 \cdot 10^{-2}\,\mathrm{mm}^{-2}$.

Micro strip detector For a micro strip detector the sensitive area per strip is taken to be about $1\,\mathrm{mm}^2$. This is somewhat less than in ALEPH. At $r_1 = 25\,\mathrm{mm}$ the occupancy is therefore 2% if each hit affects two strips. If the second layer with a thickness of 0.3% of a radiation length is located at $r_2 = 50\,\mathrm{mm}$ the probability of loosing the vertex of a track with $p_\perp = 1\,\mathrm{GeV/c}$ because a background hit falls into the $\pm 2.5\sigma$ region around the expected hit position is 4%. These numbers seem a bit too high.

Reducing the size of the strips can of course reduce the problem but will gradially turn the detector into a pixel device. At a radius of $r = 40\,\mathrm{mm}$ however the number of hits will be about 120 per bunch crossing, so that with the safety factor an occupancy of about 0.4% seems to be feasible.

Pixel detector The pixel detector can handle background with the help of external triggers. Each pixel that is hit stores the charge measured and reports that and when it was hit to the readout chip [70]. It will switch to being insensitive for further hits. If after some time no request was received to send the data to the readout chip, clear the memory is cleared and the pixel becomes sensitive again. Since after a trigger only cells that where hit during the specific bunch crossing have to be read out this procedure can be done relatively fast. An occupancy of less than 1% can be achieved. Assuming cells with dimensions of $30\,\mu\mathrm{m} \times 500\,\mu\mathrm{m}$ and that each hit occupies two cells, about one out of 3300 will become insensitive per bunch crossing. The time until it is allowed to clear the signal should thus be below $23\,\mu\mathrm{s}$—which is very long compared to the trigger latency of $2\,\mu\mathrm{s}$ that is foreseen in ATLAS, for example.

The hit density at $r = 25\,\mathrm{mm}$ is low enough to avoid confusion of background and real hits. Assuming a second layer at $r_2 = 50\,\mathrm{mm}$ with a thickness of 0.4% of a radiation length leads to the loss of less than 0.25% of the true hits with $p_\perp > 0.5\,\mathrm{GeV/c}$ due to background hits. It is assumed, that a hit prohibits also the use of neighboring cells in one of the z-directions.

CCD detector For SBLC a CCD detector is a good choice. Its inner layer can be read out in between the bunch trains. The total hit density at a radius of 25 mm to be expected for one bunch train is $333 \cdot 3.5 \cdot 10^{-3}\,\mathrm{mm}^{-2}$. This barely exceeds the rule of thumb limit mentioned before. With the simple calculation one finds that only 0.6% of the tracks with $p_\perp = 0.5\,\mathrm{GeV/c}$ are reconstructed incorrectly.

If in the case of TESLA the CCD detector is read out in the usual way between the bunch trains, it integrates the background signal of more than thousand bunch crossings. At small radii the number of hits will thus become very large and exceed the limit of one hit per square millimetre by more than an order of magnitude. Increasing the radius helps but even at $r = 50\,\mathrm{mm}$ the number of hits per bunch crossing is about 80. This leads to about one hit per mm^2 including the patch factor.

One can on the other hand think of improving the readout scheme. A possibility would be to use a fast-trigger fast-clear scheme. While the readout time of a CCD is of the order of ms the time necessary to clear it is only about $1\,\mu\mathrm{s}$. Assuming that the time to generate the trigger signal and the clear time are smaller than the time between the bunch crossings one could simply clear the CCD's after waiting for the trigger latency after each crossing. If the signal is given, the detector is not cleared the remaining bunches are shot into the detector with an offset with respect to the other beam thus avoiding further luminosity and background. The detector can be read out before the next bunch train arrives.

This method has the disadvantage that one reduces the luminosity. The size of this reduction depends on the cross section of the trigger. At a centre of mass energy of 500 GeV the s-channel cross section is about 18 pb. Assuming that for each of these events half a bunch train is lost the total luminosity reduction would be about 1%. The trigger cross section will most probably be somewhat higher since some t-channel processes like $\mathrm{e^+e^-} \to \mathrm{W^+W^-}$ may contribute to it as well as some hard hadronic background events. Comparing with Table 5.1 the rate of minijets with a transverse momentum of more than $25\,\mathrm{GeV/c}$ is about 10^{-2} per bunch train. Assuming these will trigger as well the total luminosity loss will be increased to 1.5 %. The feasibility of such a trigger for all interesting events has to be studied in detail.

With the bunch spacing of 700 ns, a possible—but ambitious—trigger latency of 500 ns and a clear time of about 1000 ns this simple scheme cannot be applied. One can on one side try to reduce the clear time as well as the latency by technical means. An alternative is increasing the bunch distance (and the bunch charge to keep the smae charge per bunch train). This will lead to higher wakefield effects in the linac but since they are well under control this seems not to be prohibitive. A simple method to apply the fast-trigger fast-clear scheme is to clear the detector every few—say n—bunch crossings. If after the last of these crossings no trigger signal is given, the detector is cleared. For bunch crossings that occur during the clearing time the inner layer of the vertex detector cannot be used but the rest of the detector can. The background in this scheme is n times that of a single bunch crossing and for $1/n$ or $2/n$ of the bunches the inner layer of the vertex detector cannot be used. Choosing $n = 30$ for example leads to a hit density of $0.3\,\mathrm{mm}^{-2}$. Depending on the actual time needed for the trigger and clearing, for 3% or more of the events the innermost vertex detector layer cannot be used.

With some effort it should also be possible to divide the bunch train into smaller sections. The distance between the bunches in a section would be smaller than the current 700 ns while that between the first and the last bunch of different sections would be larger. This allows to clear between the sections so that the inner layer can be used for all bunches. The gain however seems to be small.

While the CCDs would provide excellent resolution and little material it is not clear that this outweighs the effort necessary to operate them in the inner layer of the vertex detector.

7.2.6 Radiation damage

The performance of the vertex detector is degraded by radiation. This is a problem especially for the innermost layer. In a micro-strip or a pixel detector the electronics tends to be more sensitive than the active silicon. In the case of the H1 vertex detector a limit of 1.5 kGy was found for electronics which was not radiation hard [79]. With radiation hardening however 10 kGy should be possible. CCD's with a radiation hardness of up to 0.5 kGy are available and a hardness of 10 kGy should be possible in the near future [80].

At a radius of $r_1 = 25$ mm one finds a rate of the order of 40 Gy per year from the unavoidable direct hits alone, taking into account the safety factor. This would allow to operate even a normal CCD for several years while the other possible detectors would be less sensitive.

7.3 Background in the low angle tagger

To estimate the energy deposition in the low angle calorimetry all particles entering it are stopped. The total energy deposited depends on the details of the masking system. The number of particles from pair creation that directly hit the detector is small. The main contribution to the energy in the detector comes from secondary photons. Two important sources for them exist. The first are the showers the electrons and positrons produce in the quadrupoles or the inner mask. The inner mask actually gives a significant rise to this type of background since it leads to showers close to the taggers while the showers in the quadrupole will mainly deposit energy in the forward and sideways direction. The second source is formed by bremsstrahlung photons that are emitted by the electrons and positrons when they penetrate the beam pipe. The particles themselves will be confined by the main solenoidal field. In the simulation a tube made out of aluminium with a thickness of 2 mm and an outer radius of 50 mm was used. The tube thus fills the aperture provided by the mask and is straight inside the mask. The simulation with inner mask and beam pipe leads to about 24 GeV total energy per bunch crossing in the two taggers. Removing the inner mask leads to an energy deposition of 15 GeV. For a detector field of 2 T the energy

deposition in presence of the inner mask would rise to 250 GeV.

A Bhabha event produces two coincident signals with opposite angles in ϕ. The energy of the particles is close to the nominal beam energy. It should therefore be possible even in the most pessimistic scenario to identify these events. If one assumes a perfect efficiency it would take about 15 minutes to give a statistical error of the counting rate of less than 1%.

In one out of about 100 bunch crossings a particle from pair creation with an energy in excess of 10 GeV hits the tagger. A particle with more than 20 GeV hits the tagger once per 600 crossings only.

The hadronic background in the low angle taggers requires some thought since the energy per event is substantial. The centre of mass system of the event is boosted, hence a single event is thus not able to produce a false double tag. In addition the jets will contain significant hadronic energy which produces a small signal in the electro magnetic calorimeter.

7.4 Background in the central tracker

The different background sources will lead to charged tracks in the central tracker. For pair creation a rough approximation can be made using formula 5.7 for beamstrahlung. The number of electrons per bunch crossing with a transverse momentum higher than a given limit is shown in Figure 7.9. A transverse momentum of 0.1 GeV leads in a field of 3 T to a maximal distance of 220 mm from the beam axis. For TESLA one can expect to have about three electrons or positrons per crossing with such a transverse momentum and an angle with respect to the beam axis of more than 200 mrad and about five with an angle larger than 100 mrad.

To calculate the number of charged tracks in the central tracker due to a photon-photon hadronic event a number of these events was produced with GUINEA-PIG according to the parametrisation in equation (5.2). The energies are used in GHOST to produce the secondaries. The total number of events with a photon-photon centre of mass energy of more than 5 GeV was 13116 corresponding to 10^5 bunch crossings. Figure 7.10 shows the number of charged particles per event above a transverse momentum cutoff. The number of charge track due to minijet events is shown in Figure 7.11.

A third source of charged tracks are the secondaries from the soft photons. This background depends very much on the type of tracker used. One has to distinguish two contributions to these photons, those from the interaction point and those which penetrate the mask and thus have an energy that leads to a very small cross section in matter. The number of photons expected in the central tracker is about 400 per bunch crossing for a mask thickness of 100 mm. For a 50 mm thick mask the number increases to about 3000. An additional contribution to the background can be expected from neutrons.

The background in the central tracker seem not to pose a problem for TESLA

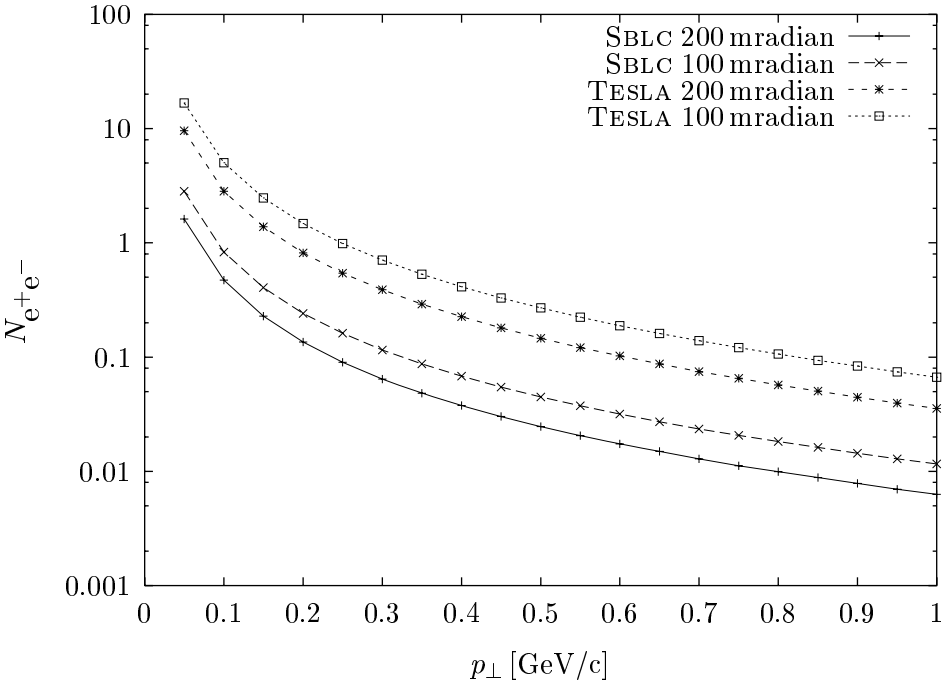

Figure 7.9: Number of electron and positron trajectories per bunch crossing in the central tracker.

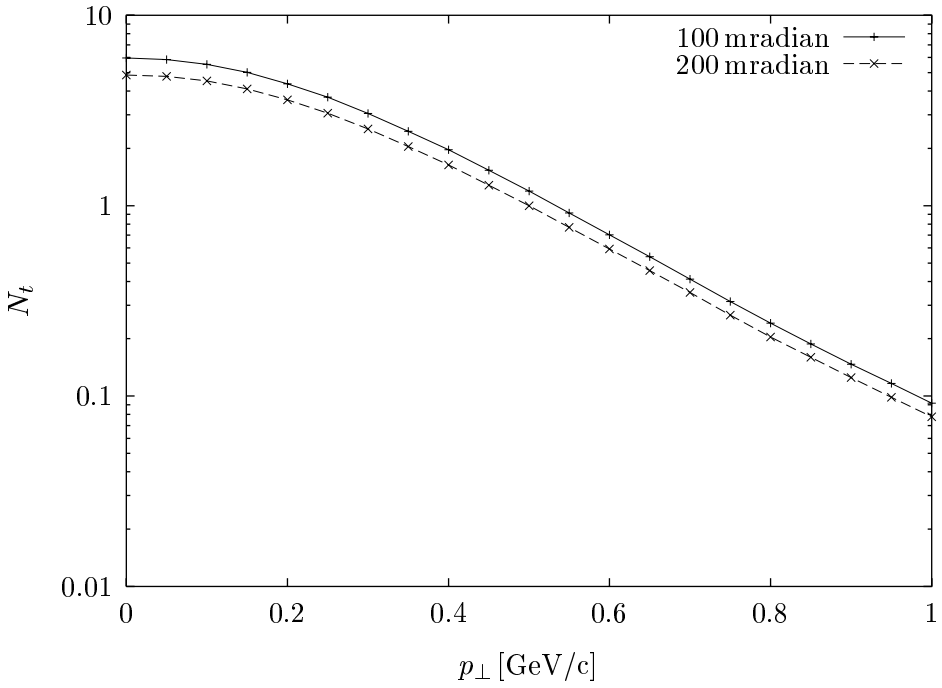

Figure 7.10: Average number of tracks in the central tracker for all hadronic event with at least 5 GeV photon-photon centre of mass energy.

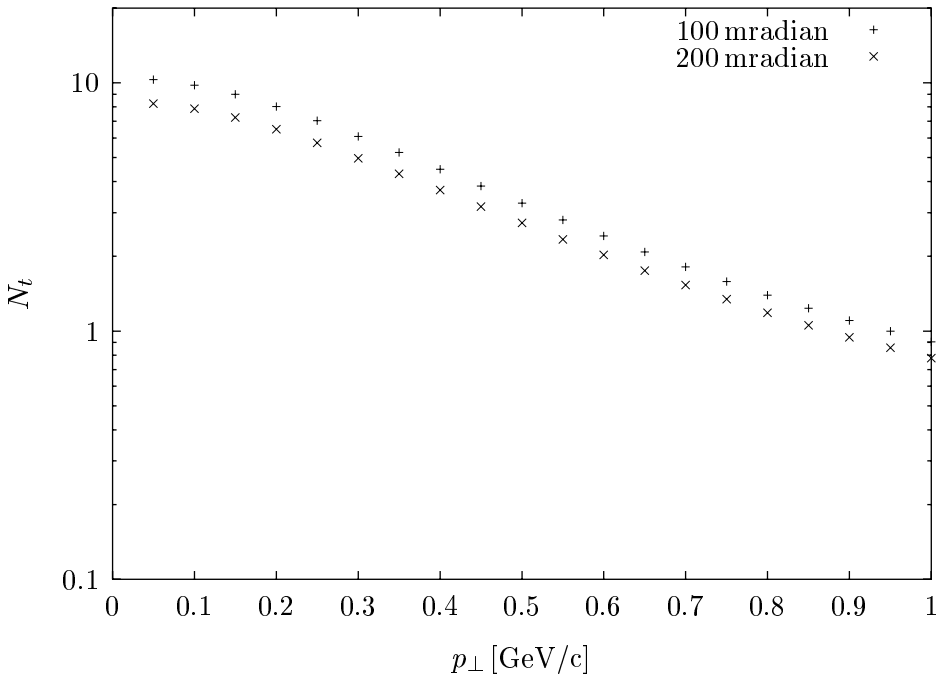

Figure 7.11: Average number of tracks in the central tracker for each minijet event with $p_\perp > 2.5\,\mathrm{GeV/c}$.

if the ions are removed fast. This is for example possible with a multi-wire drift chamber or micromegas. For SBLC a careful design of the tracker is needed. A reduction of the background can be achieved by using a fast tracker that does not integrate over the bunch train, by increasing the inner radius of the tracker and by reducing the angular coverage.

7.5 Production of secondary photons and thickness of the mask

Besides the background produced by electrons and positrons from pair production there is also some contribution from secondary photons. It can be divided into four parts. The first is due to the photons produced by the few charged particles that do not enter the mask. They usually hit the mask on the outside and produce secondary photons. The second contribution originates from photons produced by the charged particles in the vertex detector and beam pipe that do enter the mask. The third comes from photons leaking out of the opening of mask. The fourth is due to photons which penetrate the mask.

The third source contributes little to the total photon flux in the central tracker, since the number of photons escaping through the opening of the mask

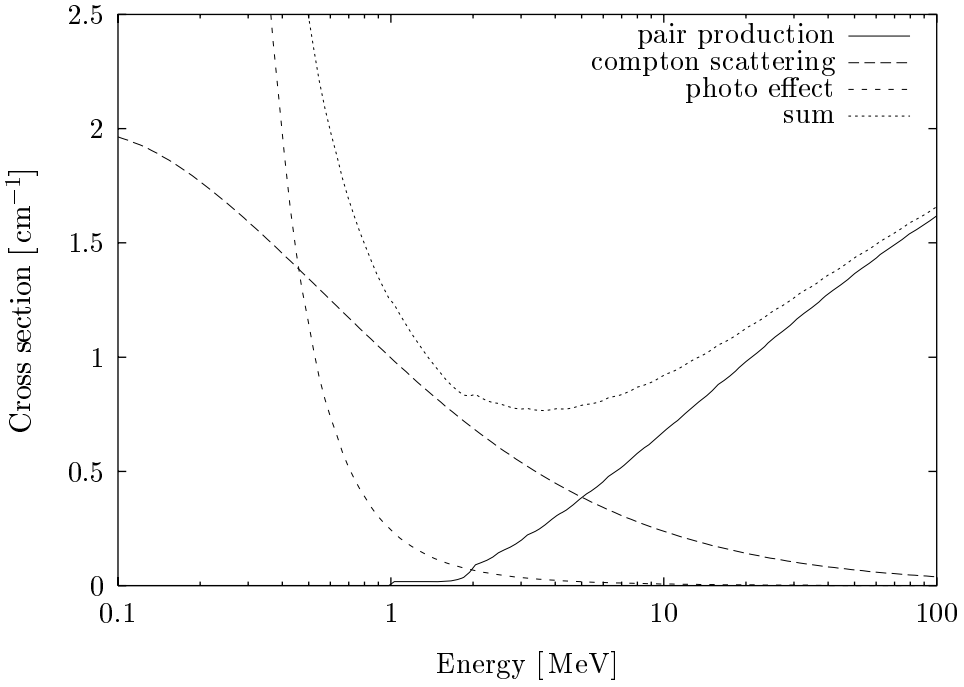

Figure 7.12: The cross sections of photons in tungsten for the important region around 3 MeV.

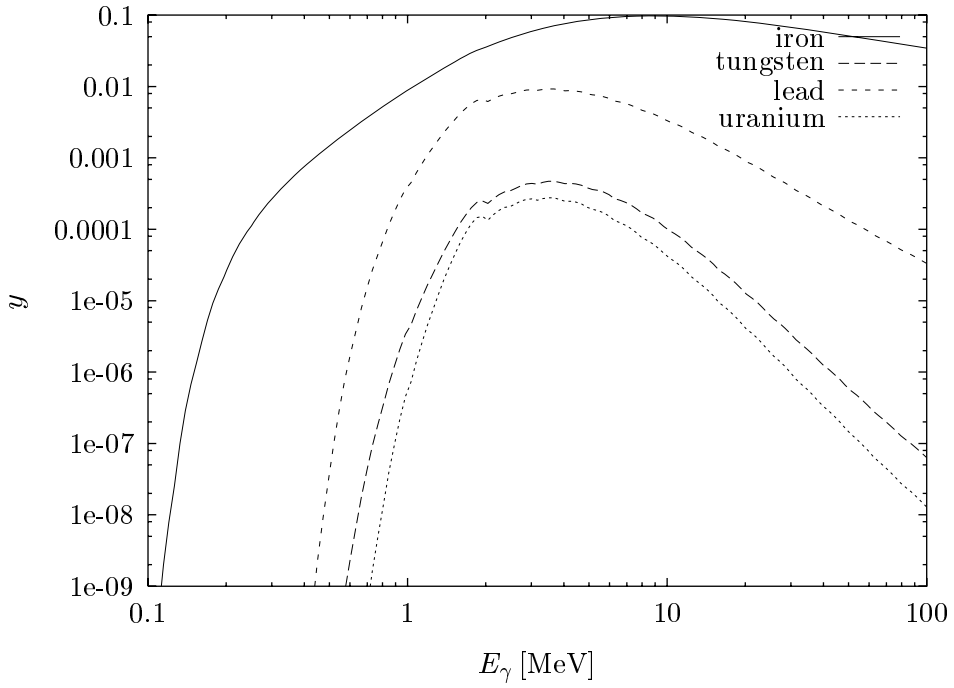

Figure 7.13: Comparison of the suppression factors for different materials, for a mask of the same thickness of 100 mm. If the same weights were used the lead mask would become comparable to the tungsten mask.

d [mm]	$\|z\| < 3.5\,\mathrm{m}$ [GeV]	$3.5\,\mathrm{m} < \|z\| < 4\,\mathrm{m}$ [GeV]	$4\,\mathrm{m} < \|z\| < 4.5\,\mathrm{m}$ [GeV]	$4.5\,\mathrm{m} < \|z\| < 5\,\mathrm{m}$ [GeV]	$5\,\mathrm{m} < \|z\|$ [GeV]
25	23.0/0.65	107/10.0	66/46.5	40/97.5	60/365.0
50	3.9/0.05	14.4/1.5	8.6/7.2	5.2/13.5	5.8/43
75	0.85/—	2.4/0.25	1.15/1.0	0.69/2.05	0.76/6.2
100	0.41/—	0.67/0.02	0.17/0.2	0.1/0.3	0.13/0.9

Table 7.1: Energy deposition in the different detector regions for different mask thicknesses d. The numbers are for the secondaries of the pair/bremsstrahlung particles respectively.

is small and concentrated at small angles. The first and the second source leads to about 300 photons in the central tracker per bunch crossing. The total energy deposited in the calorimeter is about 1.3 GeV. The number of photons depends on the radius and thickness of the beam pipe and the vertex detector. Increasing the thicknesses of both by a factor two the number of photons increases to 350— depositing a total energy of 1.4 GeV in the calorimeter.

The last contribution will be considered in more detail. The attenuation of photons in matter is dominated by three processes: Compton scattering, photo absorption and pair production. The energy dependence of all the cross sections as used in GEANT can be seen if Figure 7.12 for tungsten. A comparison of iron, tungsten, lead and uranium is shown in Figure 7.13.

The major part of the particles that are scattered transversely out of the quadrupole are photons in the energy range of a few hundred keV. Figure 7.14 shows the spectrum of these secondaries produced in an iron target, calculated with GEANT. If these photon are shielded by a 25 mm layer of tungsten the low energy part of the spectrum is strongly suppressed due to photo absorption.

Sandwich layers are used frequently to enhance the effectiveness of a mask for low energy photons. Due to the discrete binding energies the photo absorption cross section is not monotonous rising towards lower energies but shows maxima at these binding energies. The material is therefore more transparent for photons with certain energies. Using a layer of another material, with the maxima of the cross sections at energies different from the first material, can suppress the remaining photons.

Sandwich layers do not help in the present case since the main contribution to the penetrating particles comes from an energy region where the cross section of all materials is dominated by Compton scattering and thus is about proportional to the density. The low energy photons are suppressed stronger.

In the TESLA detector most of the energy of the pairs will be deposited in the quadrupoles or the masks. It is therefore necessary to shield the detector not only from backscattered but also from transversely scattered particles. This

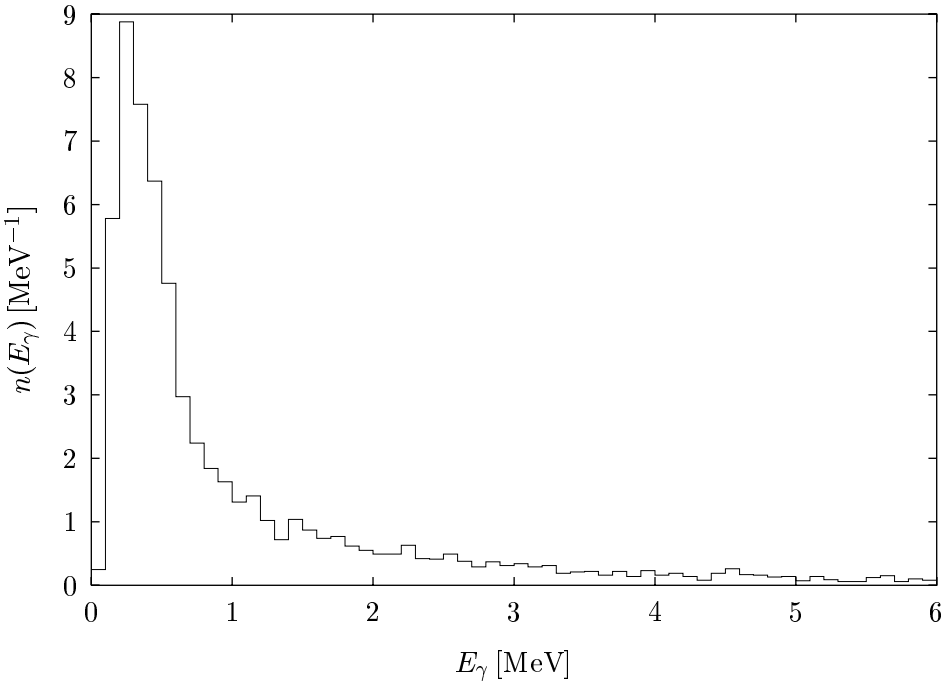

Figure 7.14: Energy spectrum of soft photons produced by an electron of 1 GeV in a cylindrical iron target with a radius of 100 mm.

can be achieved with a tungsten cylinder connected to the conical mask, which suppresses the backscattered particles. To reduce the cost one may like to replace tungsten with a cheaper material, which would require to increase the thickness of the mask to achieve the same suppression factor. The energy deposited in the calorimeter was calculated for different thicknesses d of the mask. In addition to the secondary photons from the pairs there is also a contribution from particles which lost energy due to bremsstrahlung and are thus are deflected strongly in the quadrupoles, see Table 7.1. The 25 mm and 50 mm thick masks lead to a significant power in the innermost layer of the end-cap calorimeter, while the other two give small background. The choice between 75 mm and 100 mm is a question of optimisation which needs input from the detector requirements and from cost estimates.

7.6 Neutron production

Photons with an energy around 10 MeV travelling through matter can excite the nuclei via a process called the giant resonance. The nuclei emit in turn low energy neutrons almost isotropically. Their spectrum is peaked at energies around 1 MeV where the peak energy $\hat{E}$ depends on the material. For incoming electron with an energy in excess of 100 MeV the neutron yield depends only weakly on their

energy—it is then simply proportional to the total energy of the showers. Two main sources of these neutrons exist in the interaction region. The first is formed by the beamstrahlung collimators and the second by the quadrupoles inside the detector. The neutrons are of concern since they can cause radiation damage and their secondaries can also produce background signals in the detector components.

The number of neutrons produced in water by the photons of electromagnetic showers is about $2 \cdot 10^8$ per watt of incident electron power, see reference [81]. The total beamstrahlung power is about 0.4 MW for both sides added. This leads to a production of $0.8 \cdot 10^{14}$ neutrons per second in the beamstrahlung collimators. If one assumes the collimator to be a point source and neglects the (self-) shielding, the neutron flux at the position of the detector is $7.9 \cdot 10^4$ neutrons $\mathrm{s}^{-1}\mathrm{cm}^{-2}$ or about 14 neutrons cm^{-2} per bunch crossing. Assuming the accelerator is operated 10^7 seconds per year the total flux is $8 \cdot 10^{11}$ neutrons cm^{-2} per year. For comparison the total flux of of particles expected in the ATLAS experiment at the LHC in the inner layer of the vertex detector at a radius of about 11 cm is equivalent to about $6 \cdot 10^{13}$ neutrons with a kinetic energy of 1 MeV [70]. Such a high level of radiation requires a special design for this detector.

The detector should be shielded against this radiation. The low energy neutron flux Φ behind a concrete shielding with thickness d can be expressed as

$$\Phi(d) = \Phi_0 e^{-d/\lambda}$$

with $\lambda \approx 18$ cm, see reference [82]. To be on the safe side the value of λ for high energy neutrons $\lambda \approx 45$ cm can be used. As will be shown later the neutron flux from inside the detector will be of the order of $5 \cdot 10^{-2}$ neutrons cm^{-2} per bunch crossing. To keep the background level of neutron from the beamstrahlung collimators to that from inside the detector the reduction due to the shielding should be a factor of more than 400. This requires a thickness of more than roughly 2.7 m. The dose rate H expected from the neutron flux is given by $H = A\Phi$, with $A \approx 0.4$ nSv cm^2 for neutrons with an energy of 1 MeV. To achieve less than 1 μSv/h requires a shielding thickness of 12 attenuation lengths of concrete or $d \approx 5.5$ m. For a detailed layout of this region the possibility of neutron backscattering should be kept in mind.

The shield has to have a hole for the beam pipe. Therefore the neutron flux in the innermost region of the detector can not be reduced. Since a silicon vertex detector is sensitive to neutrons it should be used only in the shadow of some shield. The radius of the inner layer of the vertex detector is thus limited by the minimal possible radius of this shield. The additional mask in the detector that is used to suppress the pair background can also serve as such a shield. The number of neutrons that hit the vertex detector nevertheless has to be calculated.

If one wants to decrease the radius of the vertex detector further such that it can not be shielded, one can still profit from the development of radiation hard detectors necessary for ATLAS.

The pairs will induce showers in the quadrupoles inside the mask that lead to the production of neutrons. For the $1.6 \cdot 10^5$ GeV per bunch crossing about $2.5 \cdot 10^4$ neutrons would be produced, if the target material is copper—see reference [81]. The energy deposition of the particles from bremsstrahlung is about $2 \cdot 10^5$ GeV per bunch crossing producing about the same number. The total rate is thus about $6 \cdot 10^4$ neutrons per bunch crossing. If the inner radius of the calorimetry in the barrel is 1.5 m the flux at this position can be estimated as about 0.2 neutrons per cm^2.

In reference [23] the average energy deposition of these neutrons is estimated to be 0.1 MeV with a detection efficiency of 0.5 in a lead-scintillator electromagnetic and an iron-scintillator hadronic calorimeter. The resulting energy deposition per 120 mm × 120 mm hadron calorimeter tower would thus be 1.5 MeV. If all the energy was deposited in the end-cap tower closest to the mask the average energy deposition would be less than 100 MeV per tower.

The energy of the neutrons is about 1.5 MeV on average [23] and their total energy 90 GeV per bunch crossing. It is thus important to ensure that the calorimetry in the end-caps is not sensitive to neutrons. The signal they produce in the calorimeter depends very much on the type used. Especially materials containing hydrogen can suffer from low energy neutrons since recoiling protons from hydrogen-neutron scattering are heavily ionising and therefore deposit their energy in a very short range. In calorimeters containing scintillator this may become a problem in contrast to those using liquid argon instead.

The longitudinal distribution of the energy loss and thus the neutron production distribution is shown in Figure 7.15. Assuming that all neutrons are produced in 3 m distance to the interaction point the flux per bunch crossing at the position of the vertex detector is of the order of 0.05 neutrons per cm^2. The resulting rate of about $3 \cdot 10^9$ neutrons per cm^2 and year would lead to a lifetime of the CCD of about one year only[4]. An improvement of the radiation hardness by a factor of ten seems possible [77]. However careful studies are necessary to predict the CCD lifetime. If it is found to be too small the use of pixel detectors is advisable.

To get a first impression of the order of magnitude of fluxes to be expected in the detector, a simple simulation can be performed. GEANT allows to use a modified version of MICAP [83] for this purpose, a program to simulate the transport of low energy neutrons. The calorimeter in the detector simulation is assumed to be made of 80% lead and 20% scintillator. It starts at $|z| = 3000$ mm instead of $|z| = 3500$ mm.

The neutrons from the beamstrahlung collimators are assumed to illuminate an area of 100 mm × 100 mm around the beam axis and to have an angle of up to 1 mrad. The suppression of these neutrons is shown in Figure 7.16—it is

[4]The precise lifetime depends also on the spectrum, here all neutrons are assumed to have 1 MeV.

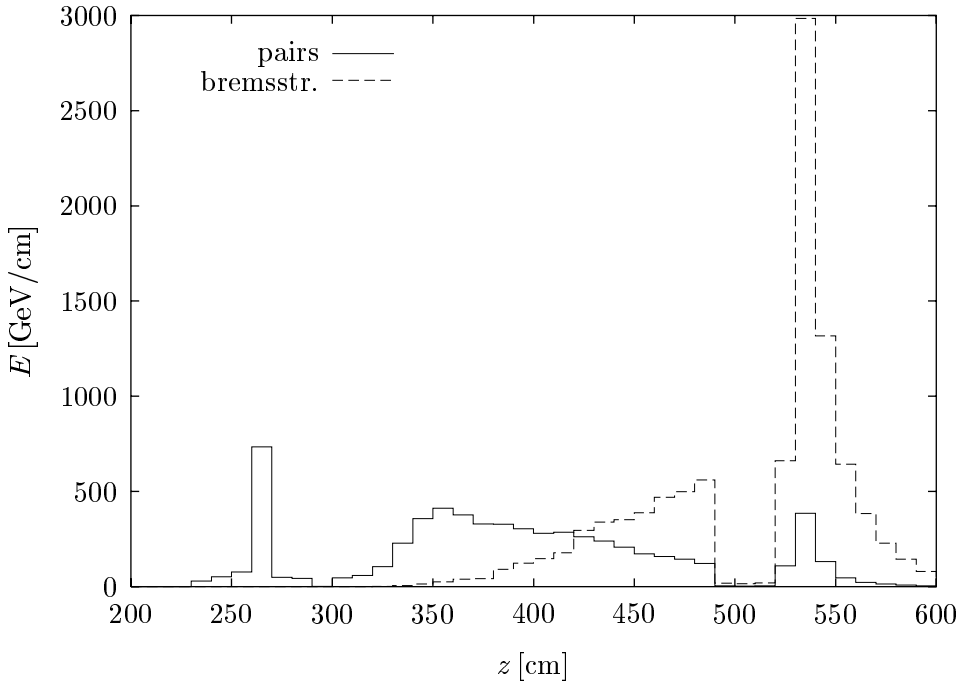

Figure 7.15: Longitudinal distribution of the energy deposition inside the detector.

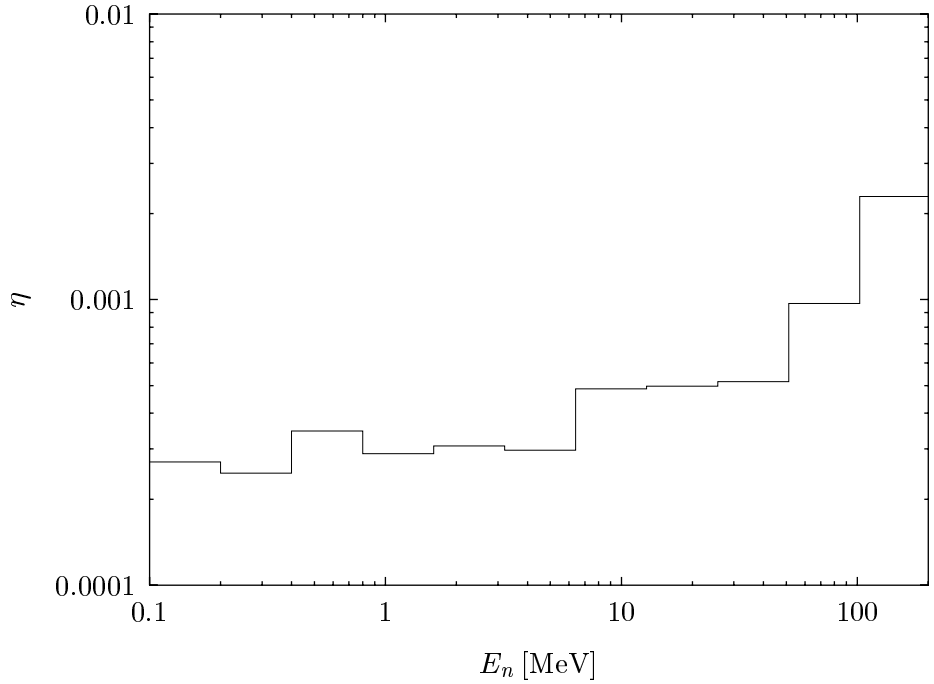

Figure 7.16: The suppresssion of neutrons from the beamstrahlung collimators in different energy regions. η is the flux per incoming particle relative to the one expected without shielding.

sufficient. The GHEISHA libray of GEANT, which is not optimised for low energy neutrons, yields a much smaller suppression at low energies; in the range from 0.1 MeV to 0.2 MeV it calculates the reduction to be only about 0.02.

The second source are the neutrons from within the detector. Since the production of secondary neutrons from photons is not implemented in GEANT their spatial and energy distribution has to be calculated first. The number of neutrons produced in a shower is proportional to the deposited power if the initial electron energy exceeds about 100 MeV. In the tungsten of the additional mask the neutron yield is enhanced compared to the copper and steel of the quadrupoles [84] [85]. In the detector simulation it is assumed that for all photons with an energy in between 10 MeV and 30 MeV the cross section for producing a neutron is the same—and zero for the others. The cross section is chosen to yield the appropriate number of neutron in each material. The low energy part of the neutron energy spectrum $n(E)$ is given by

$$n(E) = \frac{E}{\hat{E}^2} \exp \frac{-E}{\hat{E}} \tag{7.1}$$

where the peak energy $\hat{E}$ lies in the range from 0.5 to 2 MeV. In the present rough simulation $\hat{E} = 1$ MeV is used for all materials.

The flux in the inner layer of the end-cap calorimetry is found to be about 1.5 neutrons per cm^2 and bunch crossing or equal to $\Phi \approx 10^{11}\,\mathrm{cm}^{-2}\mathrm{y}^{-1}$, which is comparable to that in the ZEUS vertex detector [86].

The average neutron flux in the tracker is about $0.02(0.1)\,\mathrm{cm}^{-2}$ per bunch crossing or $0.2 \cdot (1.0)10^{10}\,\mathrm{cm}^{-2}\mathrm{y}^{-1}$ for a calorimeter out of lead and scintillator (out of lead only). In the region of the vertex detector the flux is $\Phi \approx= 0.5(2) \cdot 10^9\,\mathrm{cm}^{-2}\mathrm{y}^{-1}$.

The track length of all photons in the central tracker produced by neutrons in one bunch crossing is about 150(800) m, which is comparable to the total track length of the secondary photons produced directly by electromagnetic showers. The total track length of charged particles in the tracker is about 1.5(20) m mainly due to interactions of the photons. If the gas contains hydrogen scattering of the neutrons on the protons causes charged tracks directly. The protons are heavily ionising due to their small velocity. They increase therefore the number of ions significantly but do not contribute very significantly to the total charged track length.

If the detector design starts to become more specific, a precise calculation of the neutron background is necessary. The numbers can depend very sensitivly on the materials used—even small amounts of some materials can change the results significantly, see [87]. Also details of the layout as for example the position of the calorimeter (starting at $|z| = 3000$ mm or at $|z| = 3500$ mm) are of importance. It is then also necessary to use a program to generate the neutrons in the showers in a less handwaving fashion—FLUKA should be suited for this purpose.

Chapter 8

Measurement of Beam Properties at the Interaction Point

For the operation of the collider a measurement of the dimensions of the bunches at the interaction point is essential. The ground motion in the final focus system for example will lead to a vertical offset of the two beams in the interaction point of the order of σ_y within one second in the case of TESLA [88]. After about thousand seconds the vertical beam spot will double in size for the same reason. The methods used to measure the beam properties in the interaction point can be divided into two classes; those that can be applied during luminosity runs and those that need dedicated beam time. Three strong signals are produced in the interaction point. The beam beam kicks received by the bunches can be detected with beam position monitors downstream. The second is the distribution of the pairs inside the mask. The third is the beamstrahlung.

The bunch charge can be measured with wall current monitors with sufficient accuracy. Since the bunch length is not expected to change significantly it can also be measured outside the detector.

For measuring the bunch transverse dimensions without collision a so called laser wire can be used for the horizontal plane. This is essentially a wire scanner where the wire is replaced by a laser beam—the backscattered photons are used as a signal to estimate the beam density at the laser beam position. For the vertical dimension a Shintake monitor can be used [89]. In this monitor a standing wave pattern is produced with two laser beams. The distance between the intensity maxima of the pattern depends on the laser wavelength. If a beam is shot through this pattern it produces hard photon via Compton scattering which can be measured downstream. If the beam is moved in steps over the pattern one can calculate the beamsize from the modulation of the photon rate.

A very important difference exists between TESLA and SBLC concerning the timing. In SBLC all beam-beam based measurements can be performed once per bunch train. It is difficult to sample the crossings of individual bunches. The sampling frequency is 50 Hz. In TESLA the large bunch spacing allows to measure

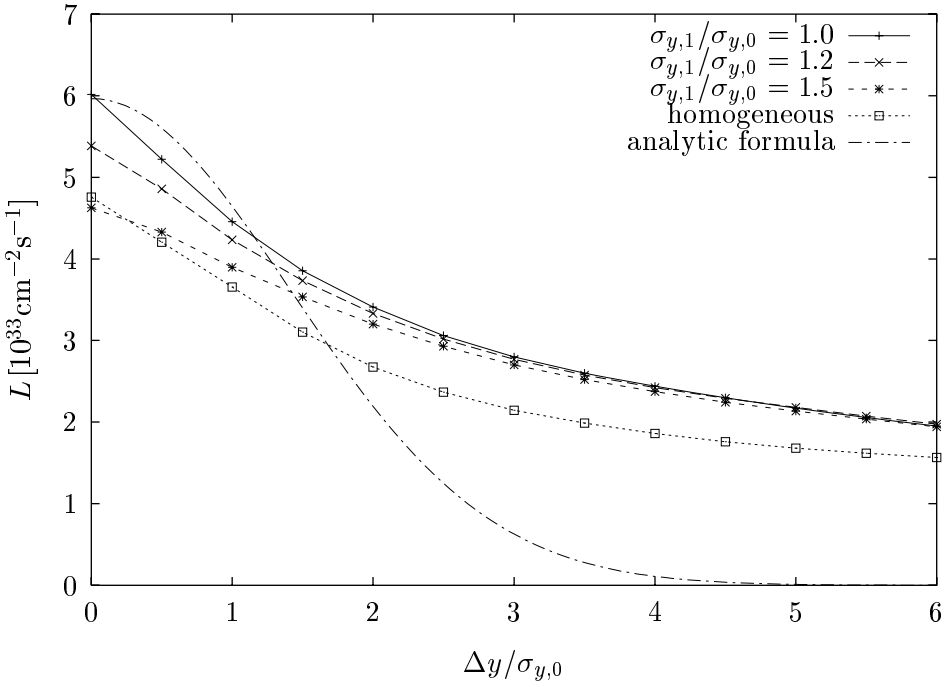

Figure 8.1: The dependence of the luminosity on the vertical offset for different beams.

individual bunch crossings and to use them for a feedback with a rate of 1.4 MHz.

8.1 Luminosity with beam offsets

The dependence of the luminosity on the transverse offsets Δ_x and Δ_y is shown in Figure 8.1. For negligible disruption the luminosity can be calculated as:

$$L = L_0 \exp\left(-\frac{\Delta_x^2}{4\sigma_x^2} - \frac{\Delta_y^2}{4\sigma_y^2}\right) \tag{8.1}$$

With pinch effect the dependence of the luminosity on the offset is completely different. For small offsets the luminosity drops somewhat faster but for larger offsets it is much higher than expected from formula (8.1). If one of the two beams is vertically enlarged the luminosity without offset is lower but for increasing offsets it is almost the same as in the standard case.

For comparison a longitudinally uniform distribution with the same RMS-value, that is $\sigma_z = l/\sqrt{12}$ was used, where l is the bunch length. In this case the luminosity is lower than for bunches with a Gaussian distribution in longitudinal direction. The relative dependence of the luminosity on the offset is the same.

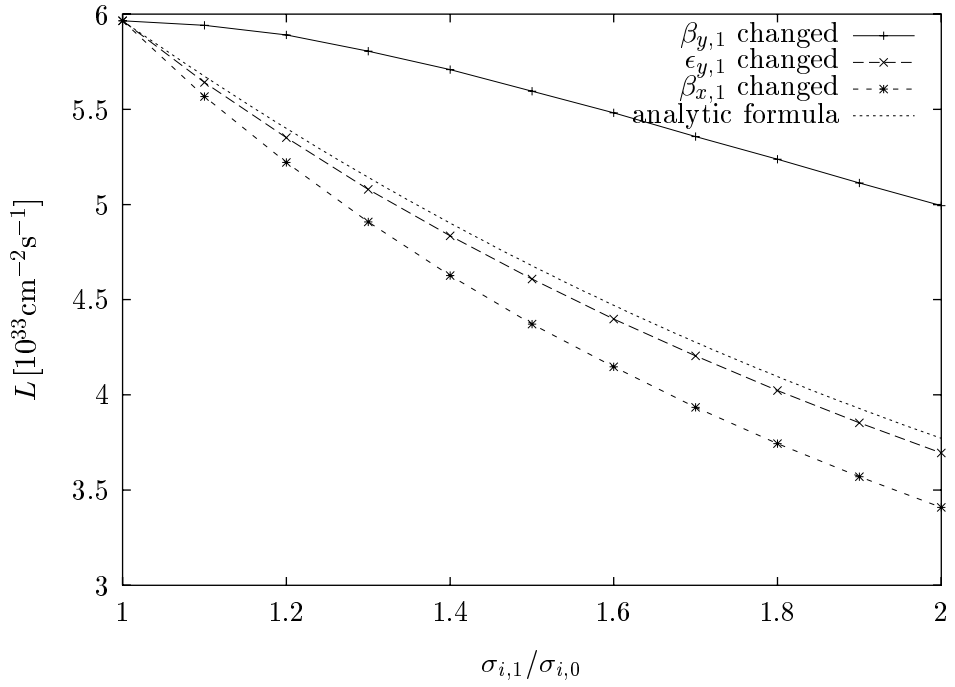

Figure 8.2: The dependence of the luminosity on the vertical and horizontal bunch size.

8.2 Luminosity losses for beams with unequal transverse dimensions

Figure 8.2 shows how the vertical and horizontal spot sizes affect the luminosity. Without pinch effect the luminosity for unequal beams ($\sigma_{r,1} \neq \sigma_{r,0}$) can be expressed as

$$L = L_0 \sqrt{\frac{2\sigma_{r,0}^2}{\sigma_{r,1}^2 + \sigma_{r,2}^2}}. \tag{8.2}$$

where $\sigma_{r,1}$ and $\sigma_{r,2}$ are the r-dimensions of the two beams and $\sigma_{r,0}$ is the nominal size. In the figure this is referred to as the analytic formula. The bunch size is changed either via the beta function or the emittance. For the vertical bunch size $\sigma_y = \sqrt{\epsilon_y \beta_y}$ a change in the beta function β_y is very different from a change in ϵ_y. The first affects the luminosity only slightly whereas in the second case the simulation is almost in agreement with the analytic formula. This can be understood by keeping in mind that an increased beta function leads to a smaller hourglass effect and that the pinching can be more effective if the angular spread, which is proportional to ϵ_y/β_y, is smaller. The difference between the analytic formula and the case with increased vertical emittance can be explained by the decreased vertical disruption parameter.

An increased horizontal size of one bunch leads to a lower luminosity than

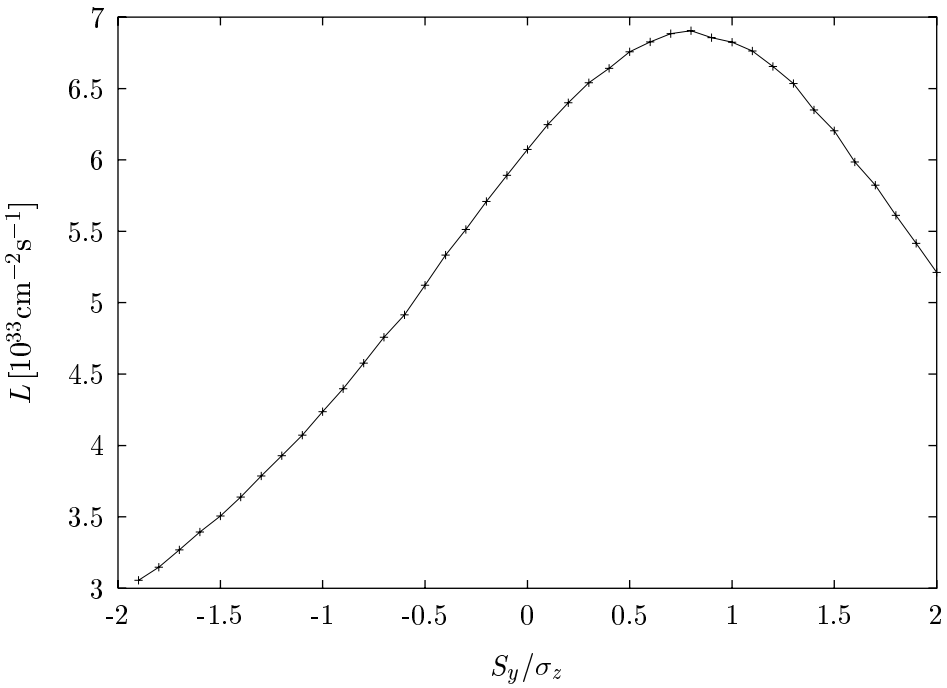

Figure 8.3: The expected luminosity for symmetrically shifted vertical waists. A positive value of the waist shift indicates that the vertical focal point lies before the position where the centres of the bunches collide if one is looking into the direction of motion of the beam.

expected from the analytic formula because both the disruption parameters are decreased.

8.3 Waist shift

In practice, waist shifts turn out to be one of the main reasons for a reduced luminosity[90]. In this case the focal point is longitudinally shifted from the position where the centres of the bunches collide. The luminosities expected for symmetrically shifted vertical waists is shown in figure 8.3. The highest luminosity is achieved if the bunches reach their smallest vertical dimension slightly before the centre of the collision. This is due to the focussing by the vertical pinching.

8.4 Beam-beam deflection

The beam-beam kick can be measured using beam position monitors. These monitors allow to determine the centre of a bunch with an accuracy of about $1\,\mu$m. Since the beams receive the kicks in the interaction point the best position

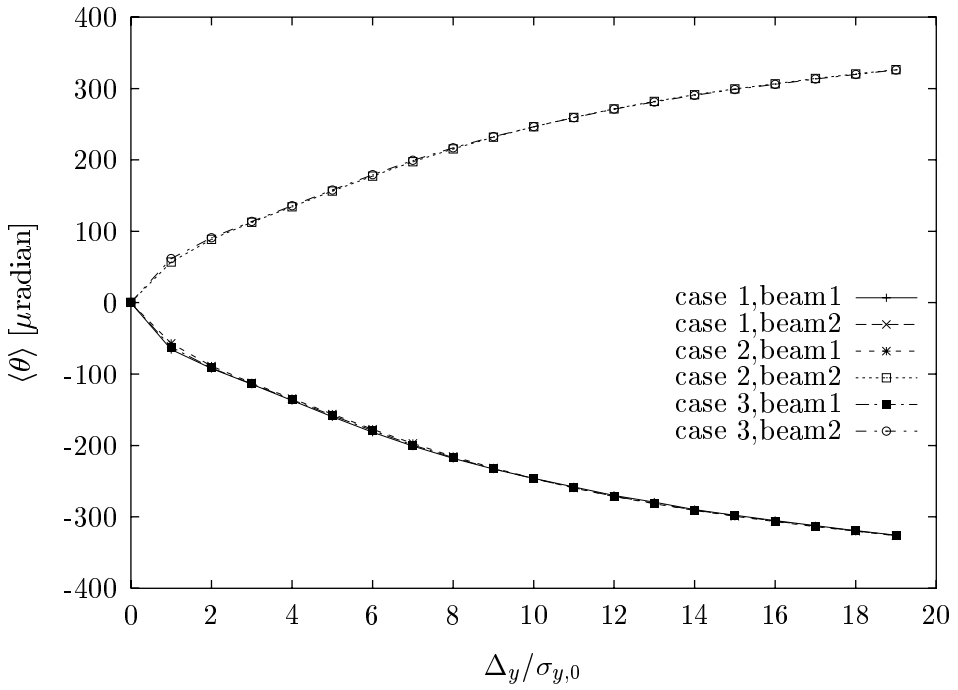

Figure 8.4: The vertical kick angle of the bunch receives as a function of the vertical offset. The vertical size of the first bunch was changed by changing the vertical emittance. The curves are very similar for the different bunch heights. Case 1 has nominal bunch dimensions, while in case 2 both beams have a vertical emittance twice as high but the same beta-function. In case 3 only the first beam has an emittance twice as high as the nominal one.

of the monitors is at a betatron phase advance of about $\pi/2$ from this point. First the trajectory of the bunch without the interacting beam is measured. If the second beam is switched on the first beam will be deflected depending on the relative offsets between the two beams at the interaction point. If the two beams collide head on the new trajectory will not change with respect to the reference trajectory. If they have an offset their particles receive an average angle which translates into an offset with respect to the reference trajectory at the beam position monitor. This allows to correct the offset for the next crossing. This method is already used at SLC. Neglecting disruption the kick angle the centre of the bunch receives for an offset $(\Delta x, \Delta y)$ is given by[91]:

$$\begin{aligned}\Delta x' - i\Delta y' &= \frac{2Nr_e}{\gamma}\frac{i\sqrt{\pi}}{\sqrt{4(\sigma_x^2-\sigma_y^2)}}\left[\mathrm{erf}\left(\frac{\Delta x + i\Delta y}{2\sqrt{\sigma_x^2-\sigma_y^2}}\right)\right. \\ &\left. - \exp\left(-\frac{\Delta x^2}{4\sigma_x^2} - \frac{\Delta y^2}{4\sigma_y^2}\right)\mathrm{erf}\left(\frac{\Delta x\sigma_y/\sigma_x + i\Delta y\sigma_x/\sigma_y}{2\sqrt{\sigma_x^2-\sigma_y^2}}\right)\right]\end{aligned}$$

The beam-beam deflection can be used to measure the transverse beam size.

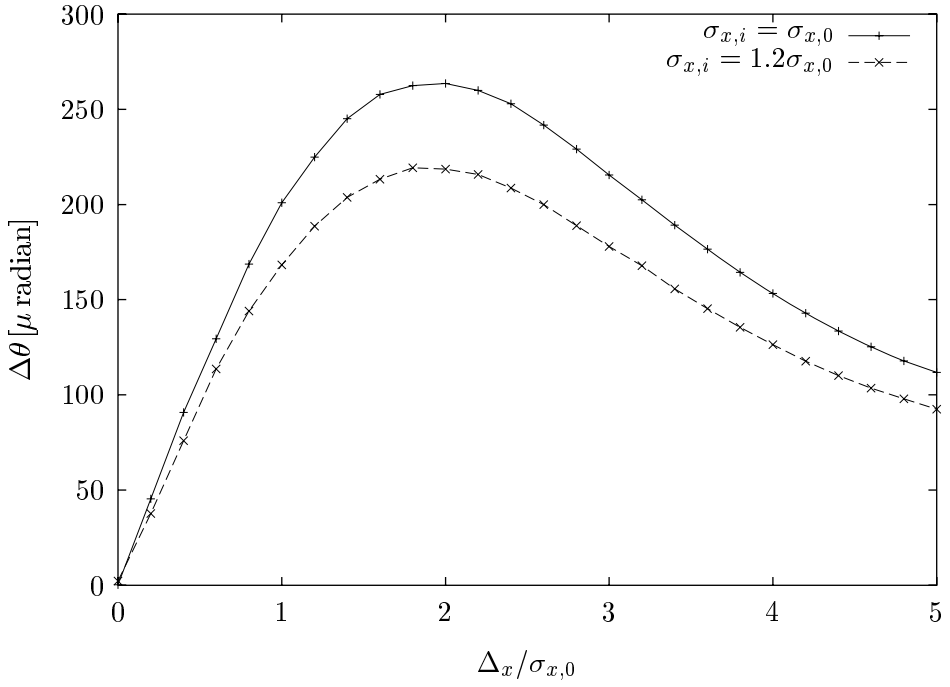

Figure 8.5: Dependence of the angular kick on the offset for the horizontal beam-beam scan.

One of the beams is moved in steps transversely from a negative to a positive offset. From the dependence of the deflection on the position the spot size can be fitted. This is done routinely at SLC. The drawback of this method is that a single bunch cannot be measured and that the measurement cannot be done during luminosity accumulation.

The horizontal scan can be used in TESLA as in SLC, see Figure 8.5. For the vertical scan the correction due to the pinch effect is important. Figure 8.4 shows the dependence of the kick angle on the relative offsets for the nominal case and enlarged vertical bunch sizes. It is obvious that the vertical beam size does not have a significant effect. The vertical scan measuring the kick angles can thus not be applied in TESLA without increasing the horizontal beamsize first.

As an alternative one can use the average energy loss of the beam particles. Figure 8.6 shows its dependence on the vertical offset for different beam sizes. It is even possible to distinguish between an increase of $\sigma_{y,1}$ and $\sigma_{y,2}$. For a head-on collision a simultaneous increase in both vertical bunch sizes does not give a significant signal. The dependence on the vertical offset is however different.

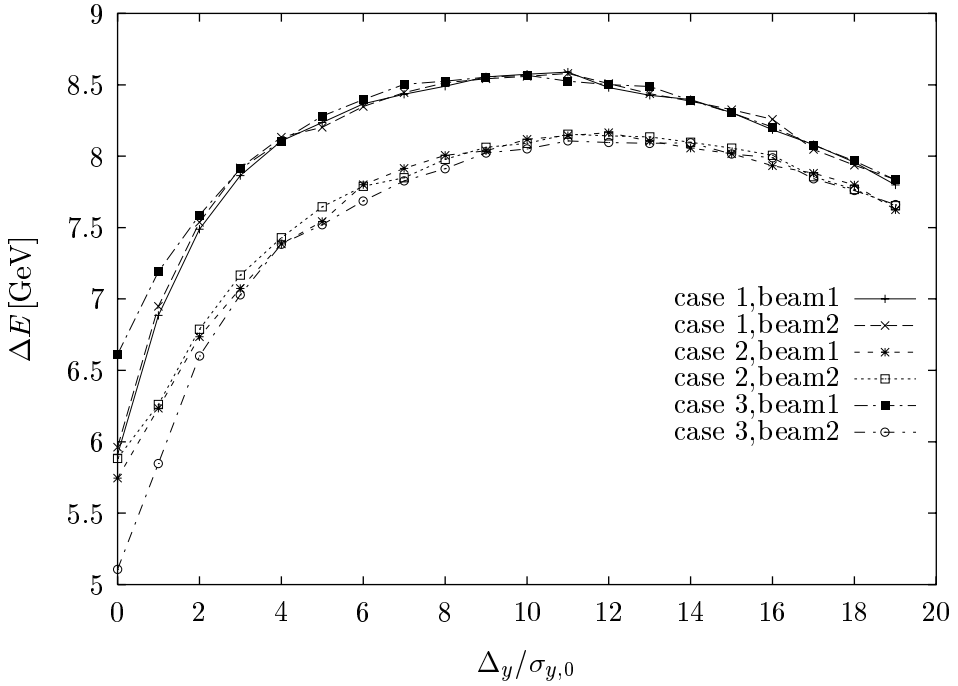

Figure 8.6: The average energy loss per beam particle as a function of the vertical offset for different vertical bunch sizes.

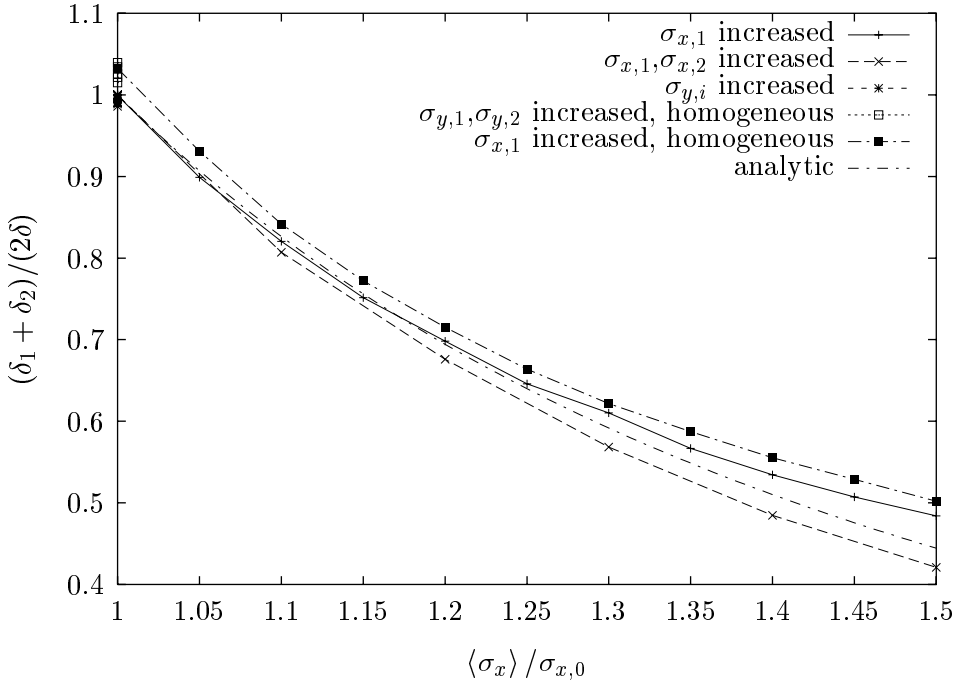

Figure 8.7: The total energy loss due to beamstrahlung for different beam parameters compared to the expected loss for nominal parameters.

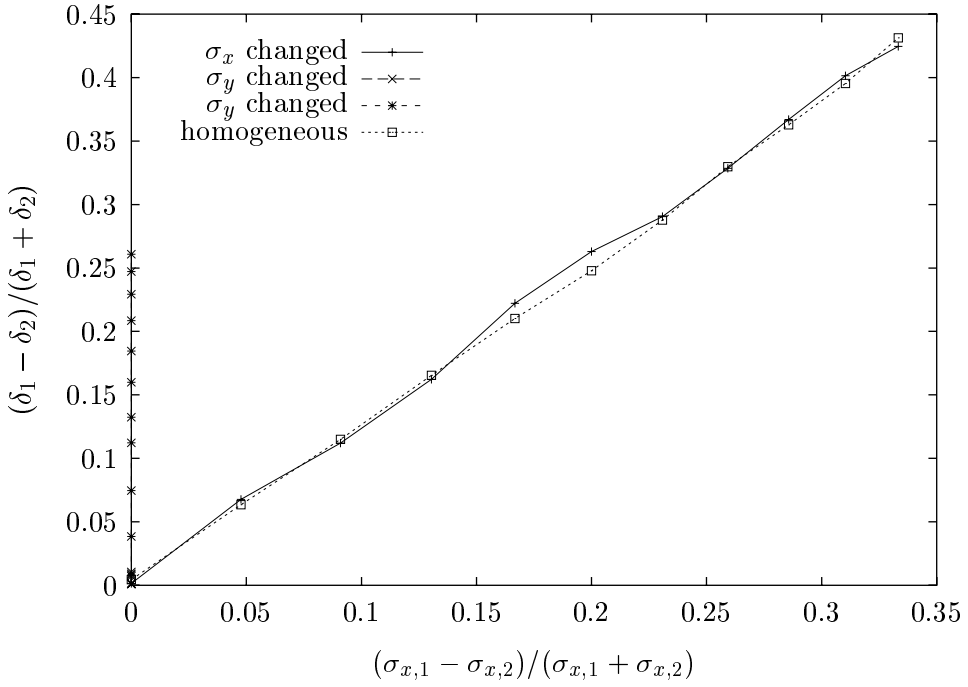

Figure 8.8: The forward backward imbalance of the total beamstrahlung energy for different horizontal beam dimensions.

8.5 Measuring the mean σ_x

If the lengths of the bunches as well as their charges are known the average transverse spot size $\langle\sigma_x\rangle = 1/2(\sigma_{x_1} + \sigma_{x_2})$ can be calculated using the average energy losses δ_1 and δ_2 of the two beams. Assuming $N_1 = N_2$ and $\sigma_{z_1} = \sigma_{z_2}$ one gets:

$$\langle\sigma_x\rangle \approx \sigma_x \sqrt{\frac{2\delta}{\delta_1 + \delta_2}} \tag{8.3}$$

where δ is the energy loss for nominal parameters. In Figure 8.7 the normalised sum of the two losses is plotted as a function of $\langle\sigma_x\rangle$. A change in the horizontal bunch dimensions leads to a significant change of the total energy loss. A change of the vertical spot sizes on the other hand does not yield a significant change in this loss. The agreement with formula (8.3) is good. It is interesting to note that the measurement is not changed significantly if the longitudinal charge distribution is uniform.

8.6 Forward backward asymmetry

The difference $\delta_1 - \delta_2$ of the two average energy losses also holds information. Figure 8.8 shows this difference as a function of the horizontal beam size. An

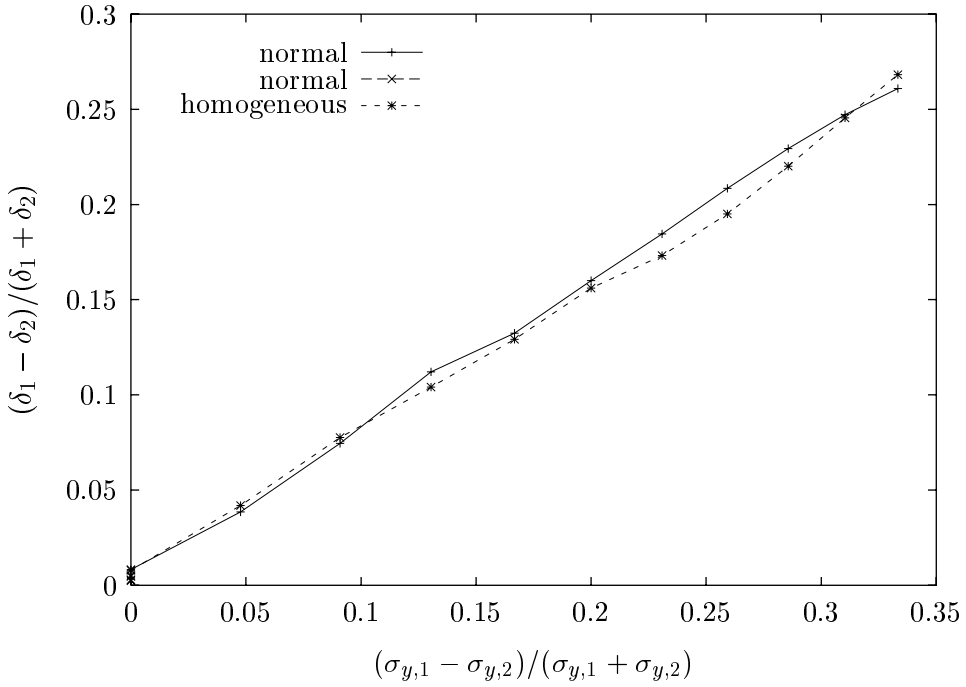

Figure 8.9: The forward backward imbalance of the total beamstrahlung energy for different vertical dimensions of the beams.

almost linear relationship is observed

$$\frac{\sigma_{x,1} - \sigma_{x,2}}{\sigma_{x,1} + \sigma_{x,2}} = A_x \frac{\delta_1 - \delta_2}{\delta_1 + \delta_2} \tag{8.4}$$

The results for a longitudinally uniform charge distribution are almost identical to those from the normal distribution. The imbalance in the energy loss depends also on the vertical bunch size. The relationship in this case is again about linear

$$\frac{\sigma_{y,1} - \sigma_{y,2}}{\sigma_{y,1} + \sigma_{y,2}} = A_y \frac{\delta_1 - \delta_2}{\delta_1 + \delta_2} \tag{8.5}$$

with a constant A_y different from A_x in equation 8.4. If the vertical beam sizes were known it would now be possible to calculate the horizontal. Unfortunately the vertical sizes are more difficult to measure. Even for known horizontal spot sizes only a difference in the vertical could be detected. A simultaneous change in $\sigma_{y,i}$ however does not give any signal.

If not only the information from a single bunch crossing is used but the average beam sizes shall be measured one can get some information due to the independent change of the parameters of the two beams. If the horizontal bunch sizes are not stable the sum of the energy losses will vary whereas if they are stable the sum will stay constant. After getting an idea of how σ_x behaves, it is possible to estimate the variability of σ_y by now looking at the spread in the differences of the two losses.

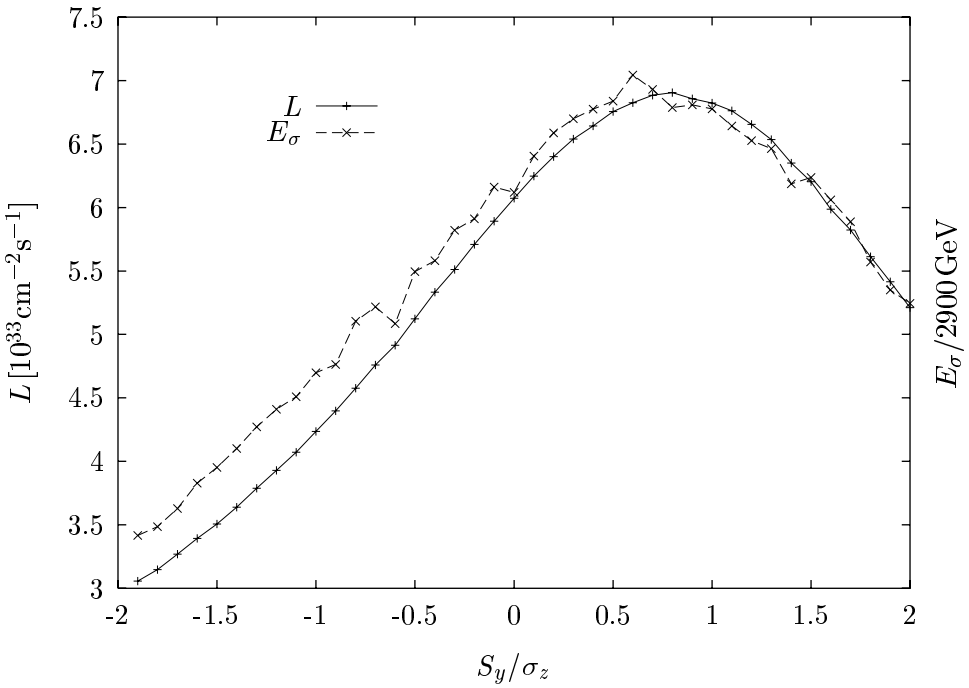

Figure 8.10: Luminosity and energy stored by the pairs in the additional mask E_σ for two symmetrically shifted waists.

8.7 Tuning the vertical spot size using e^+e^- pairs

The number of e^+e^- pair particles N_e produced depends on the average number of photons emitted per beam particle and on the luminosity. The deflection of the particles depends mainly one their energy and the bunch length and charge. If all beam parameters except the vertical bunch size are kept constant the number of produced particles is proportional to $1/\sigma_y$. Since the deflection is almost independent of σ_y the total energy of the particles outside a given angle with respect to the beam axis is also proportional to $1/\sigma_y$. If the other beam parameters are known this can be used to determine the bunch height. To this end a tungsten calorimeter can be implemented into the first centimetres of the tungsten of the additional mask. With these calorimeters the total energy deposition of the pairs in this part of the mask can be measured. For nominal beam parameters this is 8900 GeV per bunch crossing and side. Increasing the size of both beams vertically by a factor 1.2 (1.4) reduces this to 7500 GeV (6400 GeV) as expected.

For a symetric waist shift the energy deposited by the pairs is about proportional to the luminosity as can be seen in Figure 8.10. If both waist still are on top of each other but are shifted with respect to the collision point one also obtains an almost proportional signal, see Figure 8.11

Ideas how to use the number of pairs and their angular distribution for measuring the beam properties can be found in reference [92].

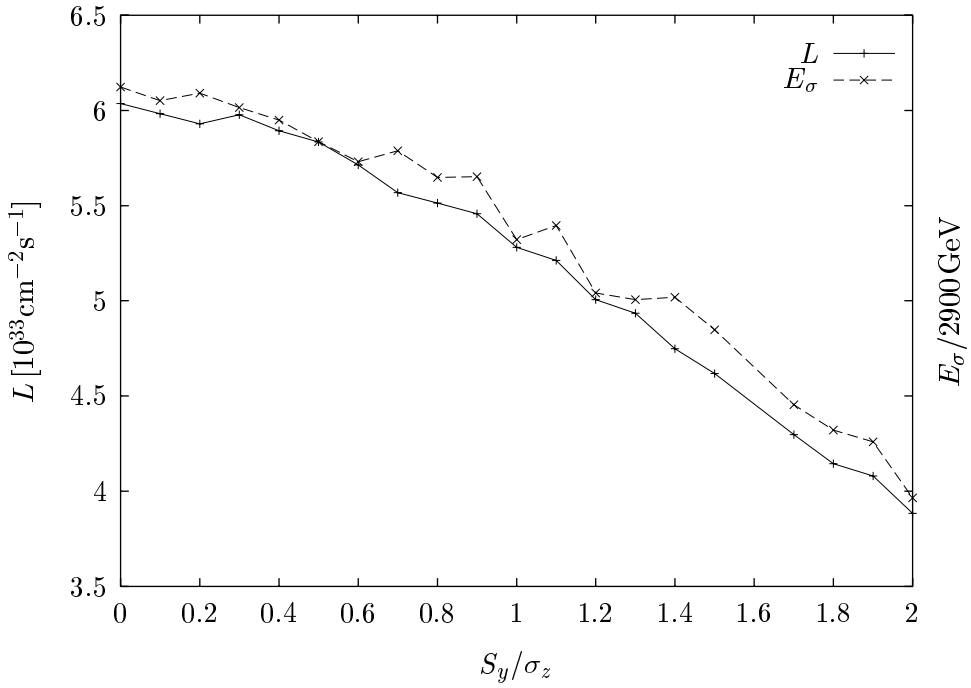

Figure 8.11: Luminosity and energy stored by the pairs in the additional mask E_σ if the two waist are at the same position but are shifted with respect to the collision point.

Chapter 9

Additional Options

9.1 Parameters for different energies

An increase of the collider energy may be required especially for the investigation of possible supersymmetric leptons. Due to the decreasing s-channel cross sections the luminosity has to be higher than for the 500 GeV machine. If on the other hand the vertical emittance and the average energy loss are kept constant the power has to grow linearly with the energy just to keep the same luminosity. By the time one might be upgrading to higher energies one will have gained experience with the lower energy design. It is therefore reasonable to assume that it will be possible to produce and transport a smaller vertical emittance at that time. Allowing for a larger beamstrahlung energy loss can also increase the luminosity but would degrade the conditions for the experiment.

A proposed upgrading strategy is to exchange the cavities of the 500 GeV machine which have a gradient of 25 MV/m with improved ones reaching 40 MV/m. This allows for an adiabatic upgrade to 800 GeV centre of mass in the same tunnel. It is assumed that during the same time the normalised emittance can be reduced to $0.1 \cdot 10^{-6}$m. A further increase in energy requires a longer tunnel. A possible step could be using twice the length, leading to 1600 GeV centre of mass energy. Luminosities and background estimates for these options can be found in Table 9.1.

For investigation of the top quark at threshold a collider centre of mass energy of 350 GeV is required. Two possible parameter sets are considered in Table 9.1. The first leads to higher luminosity and more beamstrahlung than the second.

9.2 e^-e^--option

It was suggested to run the machine in an e^-e^--mode for some experiments. In contrast to the e^+e^- case the beams will not focus but rather blow up each other at the interaction point. The luminosity will thus be smaller than geometrically

Parameter	unit	TESLA	TESLA	TESLA	TESLA	SBLC	SBLC	SBLC	SBLC
E_{cm}	[GeV]	350	350	800	1600	350	350	725	1000
L_0	$[10^{33}\mathrm{cm}^{-2}\mathrm{s}^{-1}]$	1.83	2.61	5.62	12.7	1.55	2.22	3.64	7.23
f_r	[Hz]	5	5	3	3	50	50	50	50
N_b		1135	1135	1135	2825	333	333	125	125
t_b	[ns]	705	705	705	283	6	6	4	4
N	$[10^{10}]$	3.63	3.63	3.63	1.8	1.1	1.1	1.2	1.69
$\gamma\epsilon_x$	$[10^{-6}\mathrm{m}]$	14.0	14.0	14.0	14.0	5.0	5.0	5.0	5.0
$\gamma\epsilon_y$	$[10^{-6}\mathrm{m}]$	0.25	0.25	0.1	0.03	0.25	0.25	0.1	0.1
β_x	[mm]	25.0	25.0	25.0	25.0	15.7	11.0	13.0	25.0
β_y	[mm]	0.7	0.7	0.7	0.7	0.63	0.45	0.3	0.3
σ_x	[nm]	1207	1001	669	473	479	400	303	357
σ_y	[nm]	27.0	22.6	9.5	3.66	21.6	18.0	6.5	5.5
σ_z	[μm]	700	700	700	500	300	300	300	300
P_B	[MW]	5.8	5.8	7.9	19.8	5.1	5.1	8.6	17.2
L	$[10^{33}\mathrm{cm}^{-2}\mathrm{s}^{-1}]$	3.1	4.1	9.3	23.0	2.7	3.6	5.4	10.5
L_C	$[10^{29}\mathrm{cm}^{-2}]$	5.5	7.3	28.3	27.1	1.6	2.2	8.7	16.9
δ	[%]	0.86	1.3	5.3	5.2	0.9	1.5	4.9	7.6
n_γ		1.3	1.7	2.5	1.6	1.0	1.2	1.7	2.0
E_γ	[GeV]	1.12	1.35	8.5	26	1.8	2.1	10.2	19.3
$L_{e\gamma}$	$[10^{33}\mathrm{cm}^{-2}\mathrm{s}^{-1}]$	1.6	2.4	7.2	12.1	1.2	1.8	3.4	7.7
$L_{\gamma\gamma}$	$[10^{33}\mathrm{cm}^{-2}\mathrm{s}^{-1}]$	0.9	1.7	7.4	8.1	0.6	1.1	2.6	6.7
N_P	$[10^3]$	44	64	278	190	11	17	73	157
E_P	$[10^3\,\mathrm{GeV}]$	37	57	1000	1800	13	19	297	1125
$N_\perp$		14.6	21.4	72.1	41.8	3.4	5.0	18.0	34.2
N_{Hadr}		0.026	0.044	0.73	0.64	0.01	0.015	0.17	0.50
$(E_{CM} > 5\mathrm{GeV})$									
$1/2 \cdot N_{MJ}$	$[10^{-2}]$	0.06/0.07	0.09/0.11	2.4/3.2	5.1/7.0	0.02/0.02	0.03/0.04	0.62/0.79	2.7/3.6
$(p_\perp > 3.2\mathrm{GeV})$									

Table 9.1: Parameters for the different centre of mass energies in TESLA.

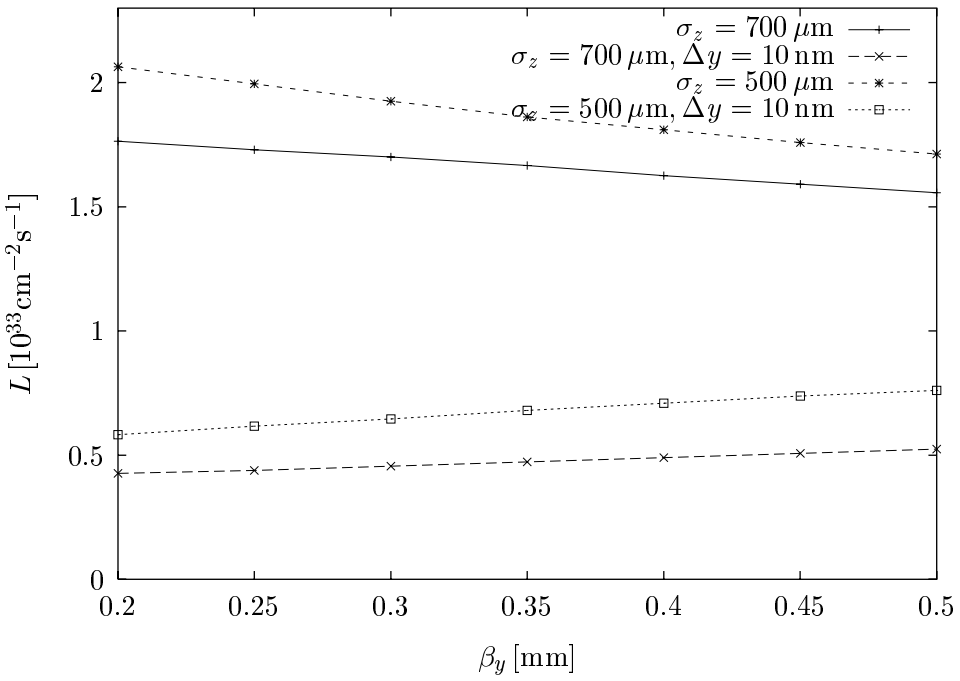

Figure 9.1: Dependence of the luminosity on the vertical beta function.

calculated.

9.2.1 Choice of parameters

The bunch length σ_z for the e^-e^- machine will be the same as for the e^+e^- machine. This is also true for the emittances and most probably for the timing and thus the bunch charge. Changing these parameters would significantly affect the damping rings, the bunch compressor and the rest of the machine. Assuming that the average energy loss per beam particle should be below about 3% as for the e^+e^- case one first has to find an appropriate horizontal beam size. Since in this case the beam-beam forces will lead to effective beamsizes larger than the nominal ones it is possible to decrease the horizontal beam size compared to the e^+e^- parameters. For the fixed horizontal beam size the vertical beam size yielding the maximal luminosity can now be found with a lower bound of $\beta_y \approx 0.2\,$mm due to the Oide limit [93]. One here expects the best choice of the beta function will also be a value smaller than for the e^+e^- case.

The simulations are done using GUINEA-PIG with only the direction of the forces inverted. They show that a reasonable choice is $\beta_x = 15\,$mm giving $\sigma_x \approx 655\,$nm. The expected energy loss is about $\delta \approx 2.6\%$ for this case. The dependence of the luminosity on β_y is shown in Figure 9.1. The best choice is $\beta_y = 0.2\,$mm, but the differences are small. The resulting luminosity is

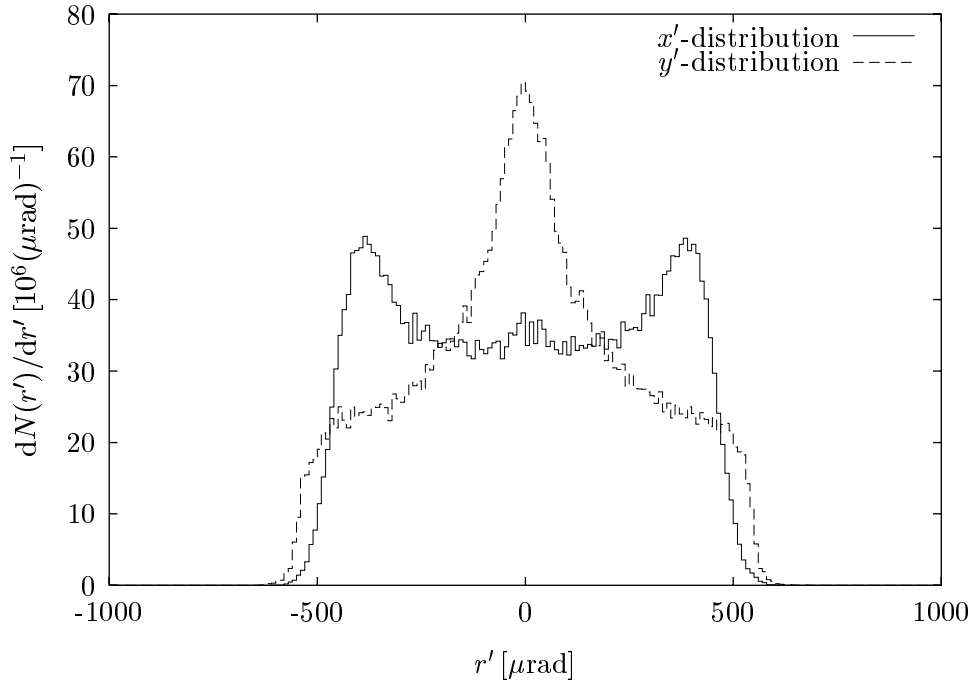

Figure 9.2: Angular distribution of the beams after the interaction. The field was assumed to be symmetric.

$L = 1.7 \cdot 10^{33}\,\mathrm{cm}^{-2}$. One should keep in mind that an $\mathrm{e}^-\mathrm{e}^-$ machine is much more sensitive to offsets than a $\mathrm{e}^+\mathrm{e}^-$ type since the luminosity decreases faster than in the case with no pinch effect. Figure 9.4 shows the decrease of the luminosity with the offset. Even the small fluctuations in the distribution of the macroparticles give rise to luminosity losses. The simulation was done once forcing the potentials to be up-down symmetric and compared to the normal case. Since the difference is of the order of 5% the results should still be reasonable as long as the real bunch shape does not differ much from the normal distribution used in the model.

A shorter bunch length leads to a higher luminosity as can be seen in Figure 9.1. For a bunch length of $\sigma_z = 500\,\mu\mathrm{m}$ the horizontal beta function was chosen $\beta_x = 20\,\mathrm{mm}$ to lead to the same energy loss as before. These parameters yield a higher luminosity and also reduce the sensitivity to offsets.

9.2.2 Background

The hadronic background for the option with $\sigma_z = 700\,\mu\mathrm{m}$ leads to about 0.045 events per bunch crossing with a centre of mass energy of more than 5 GeV while the minijet rate is about $0.42 \cdot 10^{-2}$ jet pairs with a transverse momentum of more than 2 GeV. The total number of electrons and positrons from pair creation per bunch crossing is $3.7 \cdot 10^4$ with a total energy of $4.8 \cdot 10^4\,\mathrm{GeV}$. Compared to

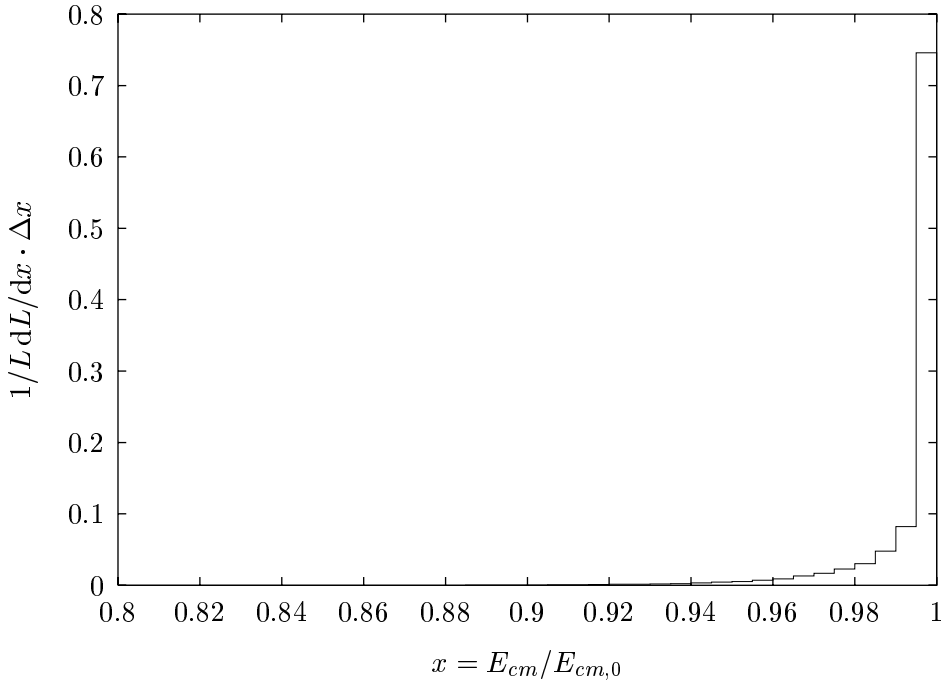

Figure 9.3: Luminosity spectrum of the collider in e^-e^- mode. The fields where not assumed to be symmetric thus numerical fluctuations within bunch are present which show that small fluctuations in the real machine do not affect the results very much.

the e^+e^- design the direct background from beam-beam interaction will thus be smaller as expected from the smaller luminosity.

9.3 Photon-photon collider

An interesting option could be to use the linear accelerator as a photon-photon collider. In an e^+e^- or e^-e^- machine gamma-gamma collisions are available of course. The main contribution to these at high centre of mass energies are due to two virtual photons. The real photons from beamstrahlung will enhance the spectrum only at intermediate energies, see Figure 5.8. The total gamma-gamma luminosity with gamma-gamma centre of mass energies above 300 GeV will be about $L_{\gamma\gamma} \approx 5 \cdot 10^{-4} L_{e^+e^-} = 3 \cdot 10^{30}\,\mathrm{cm}^{-2}\mathrm{s}^{-1}$ for TESLA. An efficient method to produce the required hard photons is to use Compton scattering. For this method one uses electron beams on both sides since electrons are easier to produce than the positrons. The beams are focused as for the e^-e^- option. A short distance away from the interaction point one lets them collide with a laser photon beam. The backscattered photons move in the direction of the incident electron and take most of their energy. A detailed review of the principles of photon colliders can be found in reference [31].

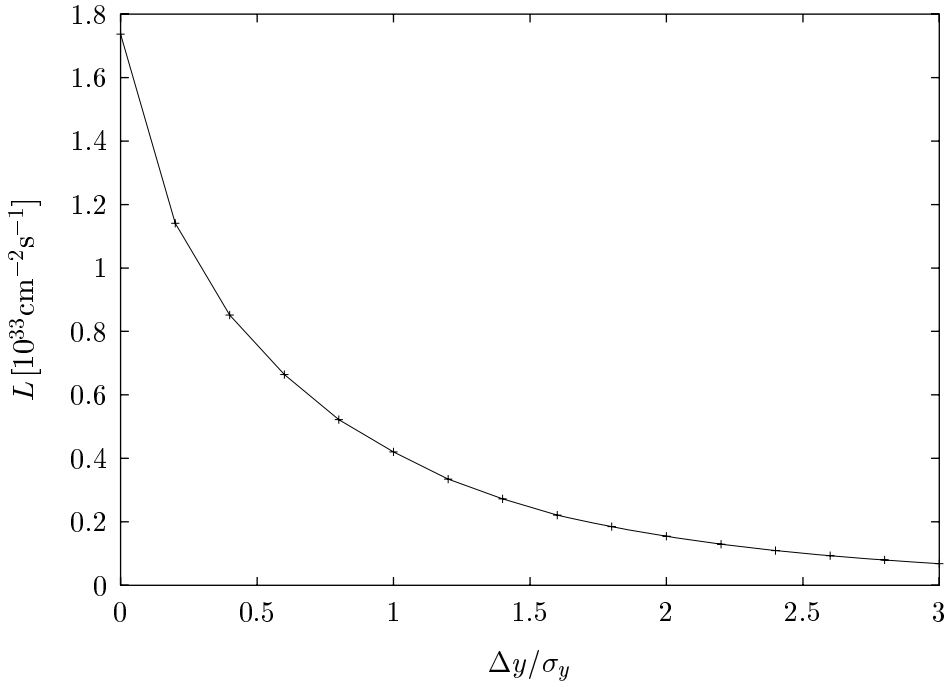

Figure 9.4: The dependence of the luminosity on the vertical offset for the e^-e^- option.

9.3.1 The produced photon spectrum

The differential cross section for the Compton scattering of a photon on an electron is given by:

$$\frac{\mathrm{d}\sigma_c}{\mathrm{d}y} = \frac{2\pi r_e^2}{x}\left[\frac{1}{1-y} + 1 - y - 4r(1-r) + 2\lambda P r x(1-2r)(2-y)\right]. \qquad (9.1)$$

$yE_0 = \hbar\omega$ is the energy of the backscattered photon, $(x+1)(mc^2)^2 = s$ is the square of the centre of mass energy. The quantity $r = y/(x(1-y))$ is introduced for convenience as well as the classical electron radius r_e. λ is the helicity of the electron and P the polarisation of the initial photon. Figure 9.5 shows the spectrum of the scattered photons for different initial polarisations of the electron and the photon. It is obvious that polarised laser and electron beams result in a much sharper spectrum. In order to achieve a high probability for electron Compton scattering close the density of the soft photon beam has to be much larger than that of the electron beam.

The maximal energy of the scattered photons is given by $\hat{E}_\gamma = y_m E_0$ with $y_m = x/(x+1)$. The initial photon energy should thus be as high as possible. On the other hand the backscattered photons can scatter on the laser photons. Therefore the centre of mass energy of the hardest backscattered and the laser photons should be below the threshold for e^+e^- pair production. The cross section

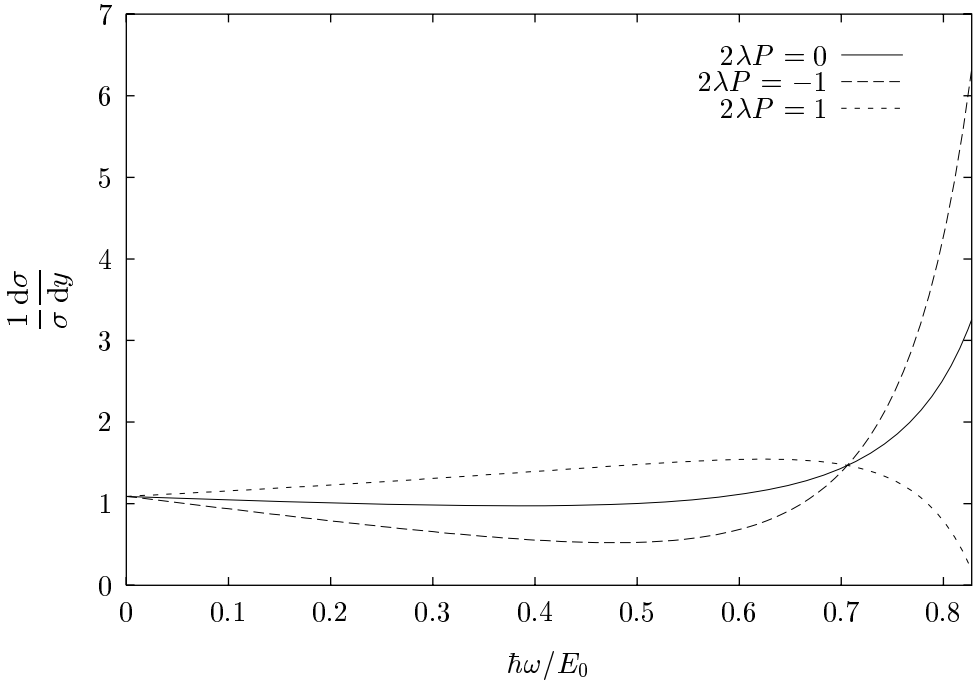

Figure 9.5: The normalised spectrum of the backscattered photons for different polarisations of the incoming particles.

for this process is comparable to that of Compton scattering. It would thus turn many of the already produced hard photons into pairs. The upper limit for x therefore is:

$$xy_m < 4 \rightarrow x < 2\left(1+\sqrt{2}\right) \approx 4.8$$

In the following discussion $x = 4.8$ will be used. This results in $y_m \approx 0.83$. The required energy of the incoming photon can be calculated using:

$$x = \frac{4E_0\hbar\omega_0}{(mc^2)^2}\cos^2\frac{\alpha}{2}.$$

where α is the angle between the incoming laser photon direction and the beam direction, since it is very small it will be neglected in the further discussion. For $E_0 = 250\,\mathrm{GeV}$ the required photon energy thus is about $\hbar\omega_0 \approx 1.25\,\mathrm{eV}$.

9.3.2 Conversion efficiency

Not all of the electrons will scatter in the photon beam. Assuming the laser beam to be transversely homogenous one can describe the probability by using the conversion efficiency k or by using a target thickness k_L. The first parameter simply gives the number of electrons that scatter at least once. The second expresses the thickness of the photon beam in terms of conversion lengths. The

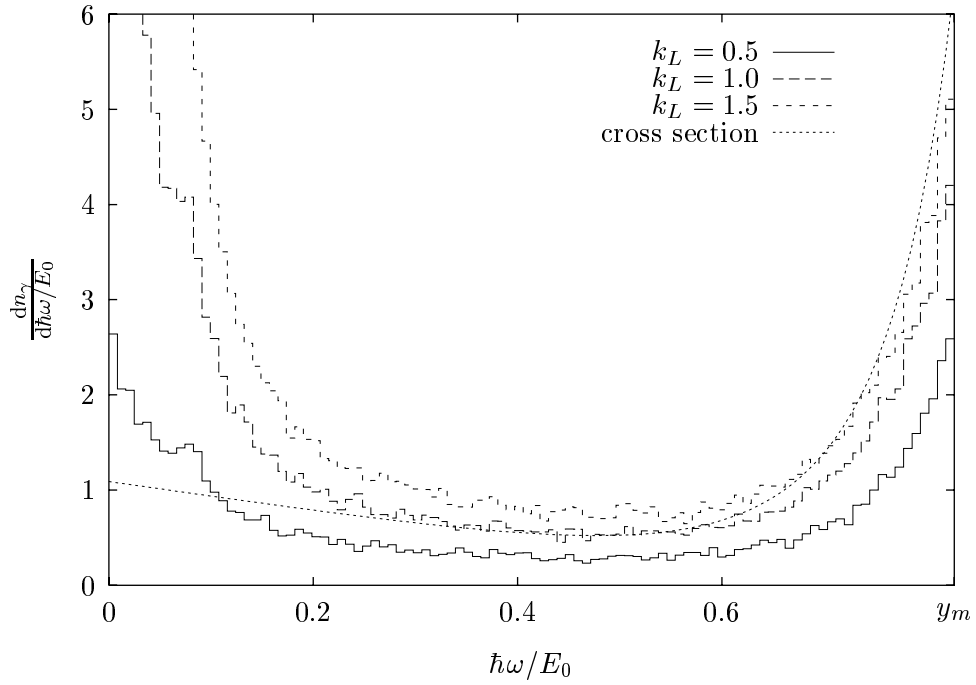

Figure 9.6: The energy spectrum of backscattered photons for different lengths of the photon target. The spectrum labelled cross section is the spectrum one would gain if all electrons would scatter exactly once.

two parameters are correlated via $k = 1 - \exp(-k_L)$. A thick laser target leads to a high number of hard photons. Since the electrons can scatter more than once the photon beam has a more pronounced enhancement at low energy than expected from the cross section alone, see Figure 9.6. If the thickness of the target is small the number of hard photons will be smaller but the low energy tail will be suppressed even more. A compromise has to be found depending on the requirement for the total luminosity and for a sharply peaked luminosity spectrum. The spectrum in Figure 9.6 was calculated with a program using macroparticles. The produced photons as well as the scattered electrons can be stored in a file and later be fed into GUINEA-PIG. The energy distribution of the secondaries was calculated by using the integral of the differential cross section in equation (9.1) and the Newton method of inversion as described before. The program uses the beam parameters at the interaction point, transports the particles back to the conversion region and after conversion brings them to the interaction point again. No magnetic field is assumed in between these two points.

9.3.3 Monochromatisation of the spectrum

The backscattered photons have small angles with respect to the direction of the initial electron. These angles are of the order of $1/\gamma$ and depend on the energy

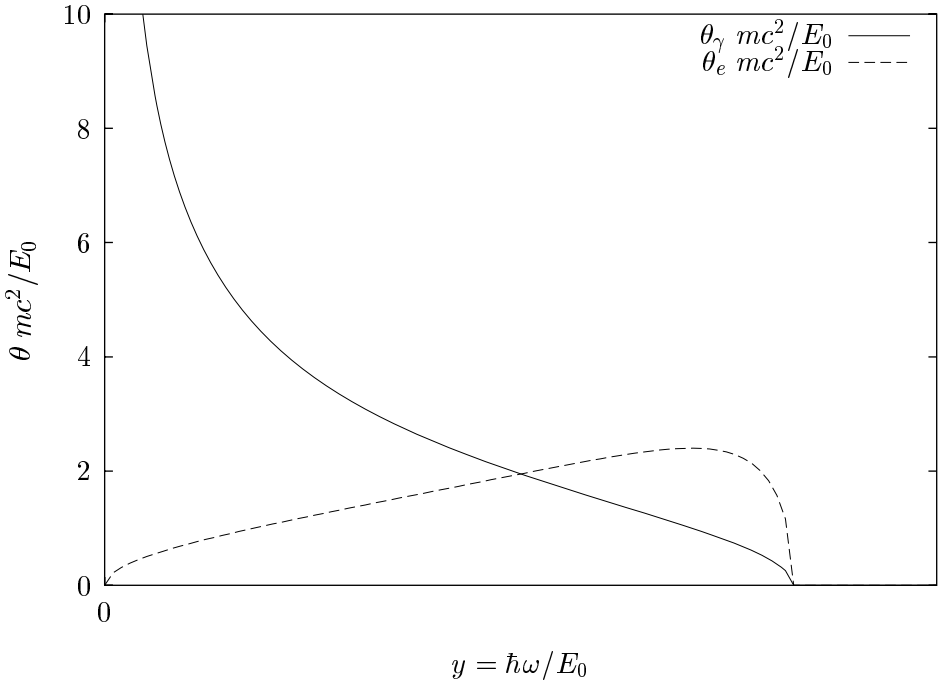

Figure 9.7: The dependence of the angle of the backscattered photons with respect to the direction of motion of the electron on the photon energy.

of the backscattered photon:

$$\theta_\gamma(y) = \frac{mc^2}{E_0}\sqrt{\frac{x-(x+1)y}{y}}, \qquad \theta_e(y) = \frac{mc^2}{E_0}\sqrt{\frac{y(x(1-y)-y)}{(1-y)^2}}.$$

See Figure 9.7. Without this angle the photon-photon luminosity would be simply $L_{\gamma\gamma} = L_0 n_\gamma^2$. L_0 is the geometrical luminosity, excluding the pinch effect, and n_γ is the average number of photons per incoming electron. Due to the scattering angle the photon-photon luminosity will depend on the distance d between the interaction point and the conversion region. Since the low energy photons have larger angles than the hard ones their contribution to luminosity decreases faster with the distance. A convenient dimensionless parameter to describe the distance is $\rho = d/(\gamma\sigma_y^*)$. Figure 9.8 shows the dependence of the absolute luminosity spectrum for a target thickness of one conversion length and several distances[1]. Here again one has to make a tradeoff between total luminosity and sharpness of the spectrum.

[1]The parameters for the collider in this case are discussed below.

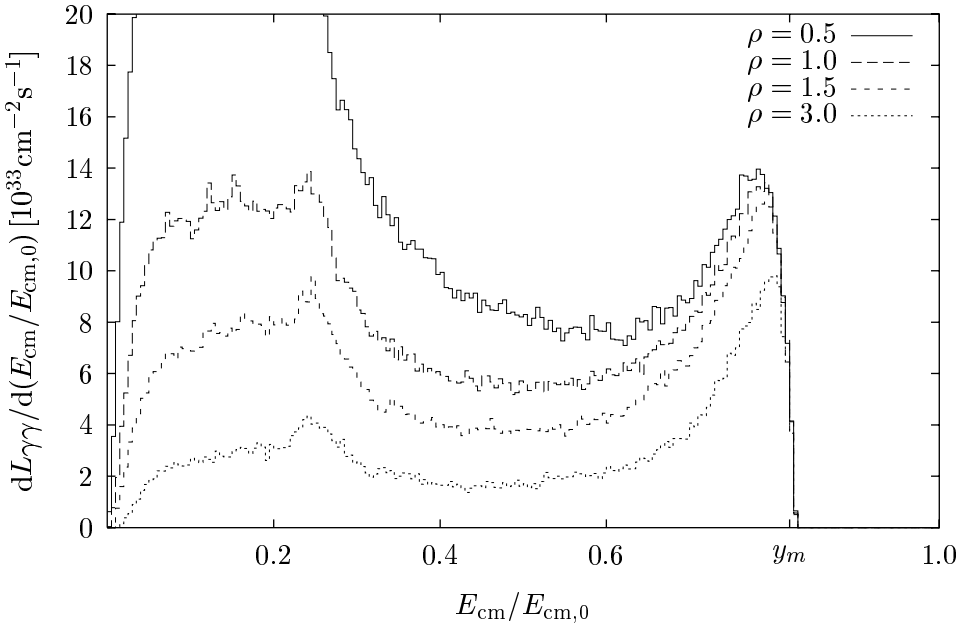

Figure 9.8: The luminosity spectra for a laser photon target thickness of $k_L = 1$ and several distances between the conversion and the interaction region.

9.3.4 Luminosity optimisation

To find an appropriate parameter set for the photon-photon option one has to keep in mind that the photon-photon luminosity is proportional to the geometrical luminosity with a proportionality factor depending on the required spectrum. To increase the geometrical luminosity one can in principle reduce either the vertical or the horizontal beam size or increase the bunch charge. The vertical spot size is given by $\sigma_y^* = \sqrt{\epsilon_y \beta_y^*}$. A decrease of the vertical emittance meets the same difficulties as for the $\mathrm{e^+e^-}$ option. One could reduce the vertical beta function that means focus the bunch stronger. If the beta function becomes significantly smaller than the bunch length this will lead to luminosity loss due to the hourglass effect. Using shorter bunches avoids this effect but requires a more efficient bunch compressor. In an $\mathrm{e^+e^-}$ machine shortening the bunch length requires to increase the horizontal bunch size to keep the average energy loss due to beamstrahlung the same—the resulting luminosity is here about the same as with the longer bunch. For the $\gamma\gamma$ option, in contrast, the horizontal bunch size has not to be changed. The wakefield effects in the linac will change with the bunch length, partly becoming worse partly improving. If the total increase of the vertical emittance due wakefields increases for the shorter bunch length has to be calculated. In any case a lower limit of $\sigma_y^* \approx 10\,\mathrm{nm}$ for the vertical beam size exists due to the Oide limit.

The horizontal beam size is given by $\sigma_x^* = \sqrt{\epsilon_x \beta_x^*}$. In the case of the $\mathrm{e^+e^-}$

option this size has a lower limit since one wants to keep the average energy loss due to beamstrahlung below 3%. This limit does not exist for the $\gamma\gamma$ option. By simply changing the horizontal beta function one could reduce the horizontal beam size to about 400 nm[94]. In addition it should be possible to reduce the horizontal emittance, something that is not important for the e^+e^- machine.

If the bunch charge is increased and the transverse dimensions are kept constant the geometrical luminosity also will be enhanced. This is not possible for the e^+e^- option since to avoid an larger average energy loss the horizontal beam size has to be increased as well. A higher bunch charge N however leads to a larger growth of the vertical emittance due to wakefields $\Delta\epsilon_y/\epsilon_y \propto N^2$. Since this increase is very low for the e^+e^- machine one could consider to allow it to be larger. It seems nevertheless to be safer to be able to compare the simulations for this effect with measurements first.

As a first approach it is assumed that the normalised horizontal emittance can be reduced to $7 \cdot 10^{-6}$ m. While the vertical bunch size, its length and charge are kept constant the horizontal bunch size will be decreased to $\sigma_x = 200$ nm. The longitudinal polarisation of the beam is 80% while that of the laser is 100%. No method of beam separation is used. The resulting spectra for the photon-photon, electron-photon and electron-electron luminosity are shown in Figure 9.9. The total gamma-gamma luminosity is found to be $L_{\gamma\gamma} = 9.1 \cdot 10^{33}\,\mathrm{cm^{-2}s^{-1}}$ of which $1.6 \cdot 10^{33}\,\mathrm{cm^{-2}s^{-1}}$ has a centre-of-mass energy of more than 300 GeV. One further finds $L_{e^-e^-} = 1.3 \cdot 10^{33}\,\mathrm{cm^{-2}s^{-1}}$ and $L_{\gamma e^-} = L_{e^-\gamma} = 4.7 \cdot 10^{33}\,\mathrm{cm^{-2}s^{-1}}$.

9.3.5 Background

The background can be subdivided into three main parts. The first is the background from the interaction point, the second that produced in the conversion region and the third is induced by the spent beam leaving the detector.

The background from the interaction point depends on the beam separation scheme. If one uses a magnet for separation the background will be due to photon-photon interactions only. The photons are either the hard ones from the Compton scattering or softer ones from the synchrotron radiation emitted in the separating magnet. Another possibility is to simply let the beams collide after the conversion. As in the e^-e^- design they will deflect each other and since in addition they are scattered in the conversion region the total e^-e^- luminosity should be low. This method seems to be the simplest as far as the region close to the interaction point is concerned. It will be considered here.

The photon-photon luminosity spectrum including the colliding electron beams is shown in Figure 9.9. While the hard part of the spectrum remains unchanged the soft tail is significantly increased. This is due to the beamstrahlung by the interacting electron beams. In addition there are collisions between the real photons from Compton scattering and beamstrahlung with the virtual photons of the electrons. While in collisions with a high centre of mass energy the photons

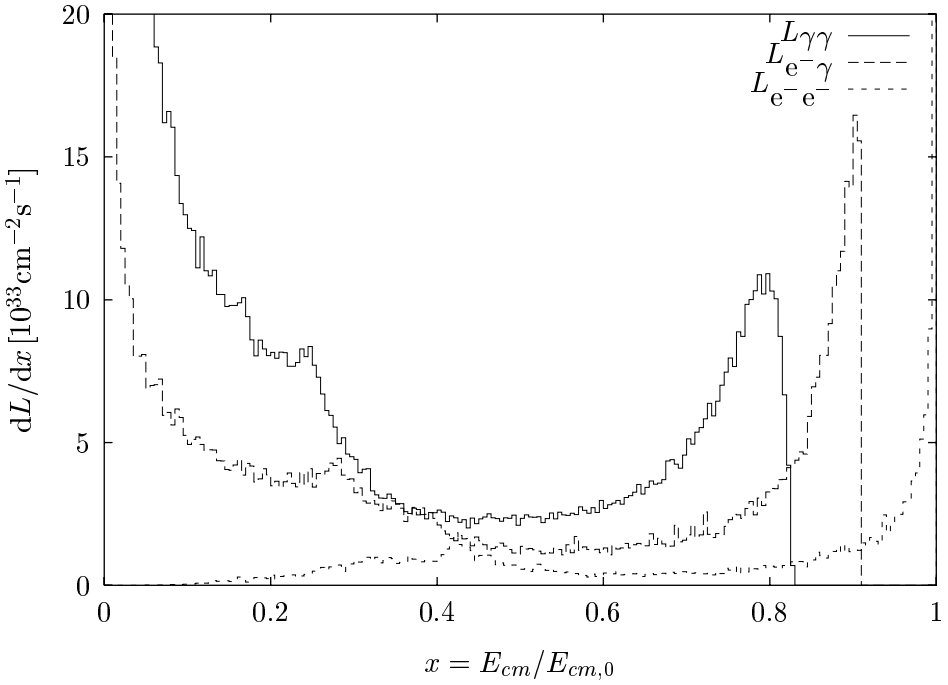

Figure 9.9: The photon-photon luminosity spectrum for the case with colliding spent beams.

tend to be polarised they are not for the low centre of mass energies at which the pair production processes are important. For the calculation of this background the polarisation is therefore ignored. The dependence of the hadronic structure function of the photon on its polarisation is till now not known. The simple cross section for the twice resolved process leads to results much larger than the eikonal models.

The total number of electrons and positrons produced per bunch crossing is about $N_{e^+e^-} = 87 \cdot 10^3$ with a total energy of about $E_{e^+e^-} = 3.2 \cdot 10^6\,\mathrm{GeV}$. While the number of pairs is lower than in the e^+e^- version their total energy is significantly higher. There are $N_H \approx 0.62$ hadronic events per bunch crossing with a centre of mass energy above 5 GeV and the average number of minijet pairs is $N_{MJ}(p_\perp > 10\,\mathrm{GeV/c}) \approx 5.4 \cdot 10^{-3}$. This background seems to be manageable even though it is higher than for the e^+e^- option. A significant additional source however can be the spent beams. Figure 9.10 shows their angular distribution. A number of particles have lost a significant amount of energy especially if they scattered more than once. They will thus be strongly deflected by the other beam. It is obvious that the spent beams would deposit a large power in the final quadrupoles of the e^+e^- layout. This problem can be solved by introducing a crossing angle between the two beam-lines. This angle has to be rather large in order to avoid that the quadrupoles are hit by the tails. It will be necessary to make a detailed study of the detector layout to ensure this background is

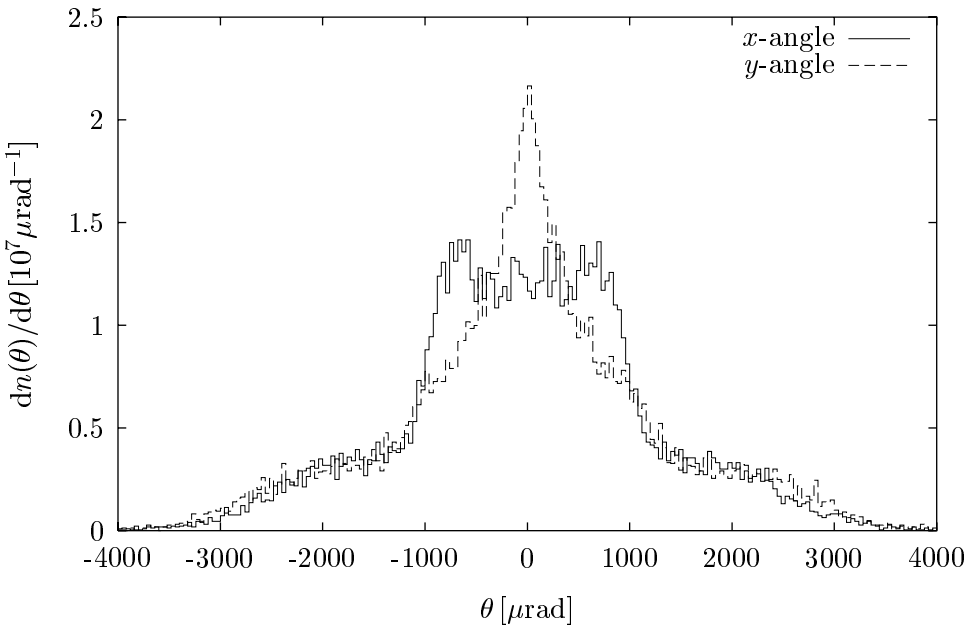

Figure 9.10: The angular distributions of the particles in the spent beam. No method of separating the beams was applied.

small enough. If everything else fails one can compromise the gamma-gamma luminosity to reduce the deflection.

Chapter 10

Investigation of the Top Quark at Threshold

The top quark can be investigated either at centre of mass energies that exceed twice the top mass significantly or at threshold. At high energies the top quark mass is measured via the invariant mass of its decay products. In contrast to the lighter quarks the top decays weakly into a W and a b-quark before the $t\bar{t}$ system can fragment into hadrons. This allows to calculate the decay reliably in contrast to resonances of lighter quarks. The top production cross section at threshold depends on several parameters, the most important ones are the top mass, the strong coupling α_S and the Higgs mass. To calculate the cross section one has to assume a potential for the $t\bar{t}$-system at threshold. It is then necessary to find the solution of the Schrödinger equation (in coordinate space) or of the Lippmann-Schwinger equation (in momentum space) for this potential. The top momentum distribution can be calculated from these wave functions. Different programs exist to perform this calculation which are in reasonable agreement with each other [95]. Measuring the energy dependence of the top production cross section around threshold allows to determine the top mass and other parameters as for example the strong coupling by fitting the predicted cross sections onto the measured. This method does not require to really reconstruct the top quark but only to decide whether an event was a top event or not. Measuring the momentum distribution for a given centre of mass energy can further constrain the physics parameters. For this purpose it is of course necessary to reconstruct the top.

10.1 Principle of the threshold scan

The shape of the cross section around the top production threshold depends the top mass m_t, the strong coupling α_S and the width of the top Γ_t. While α_S and the top mass are input values for the Standard Model the top width

can be calculated. In the following it is assumed that the top has a mass of $m_{\mathrm{t}} = 175\,\mathrm{GeV/c^2}$ and that the strong coupling has a value of $\alpha_{\mathrm{S}}(m_{\mathrm{Z^0}}) = 0.12$[1]. If the Higgs boson exists also its mass m_{h} and the coupling to the top are important. Figure 10.1 shows the threshold behaviour of the cross section for different values of the strong coupling, calculated with TOPPIK [96].

The centre of mass energy is not well defined due to initial state radiation, beamstrahlung and the energy spread of the particles in the beam. These effects modify the energy dependence of the top production cross section significantly. Figure 10.2 shows the effective cross sections. If the luminosity spectrum can be well measured the physical parameters can still be extracted from the scan but the resolution is degraded.

The scan can be done measuring the cross section at ten different centre of mass energies starting with $E_{\mathrm{cm}} = 345\,\mathrm{GeV}$. For the following points E_{cm} is increased in steps of 1 GeV. To measure the background an additional point well below threshold is needed. This measurement has a rather small systematic error—mainly from the uncertainty of the detector acceptance—if one uses the counting rates and thus the total cross section only.

10.2 Choice of beam parameters

The beam parameters in the interaction point can be changed to achieve less beamstrahlung at the price of a reduced luminosity. Therefore two possible options are used to construct beam parameters for 350 GeV from those proposed for 500 GeV. In the first the beta functions are kept constant which leads to an increase of the transverse beam dimensions proportional to $\sqrt{1/E_{cm}}$. In the second the angular divergence $\sigma' = \sqrt{\epsilon/\beta}$ is kept constant leading to an increase of the transverse dimensions proportional to $1/E_{cm}$. The resulting luminosities for TESLA and SBLC can be found in Table 9.1 on page 115.

In the following it is assumed that the luminosity spectrum can be measured with sufficient accuracy to not contribute significantly to the systematic error. In reference [74] the authors propose a method to measure the luminosity spectrum using Bhabha scattering. Since the lepton energies can be measured with a precision in the percent range only, one can in addition use the acolinearity of the final state particles which can be measured with a precision of the order of a mrad. The acolinearity is a measure for the ratio of the energies of the two initial particles E_1/E_2. With the help of a model this distribution is unfolded into two beam energy spectra which can in turn be folded to get the luminosity spectrum. The effect of final state radiation should be well under control since the emitted photon has a very small angle with respect to the electron and thus does not change its direction signifcantly. The precision of this procedure has

[1] From this value the strong coupling can be calculated for the required scales.

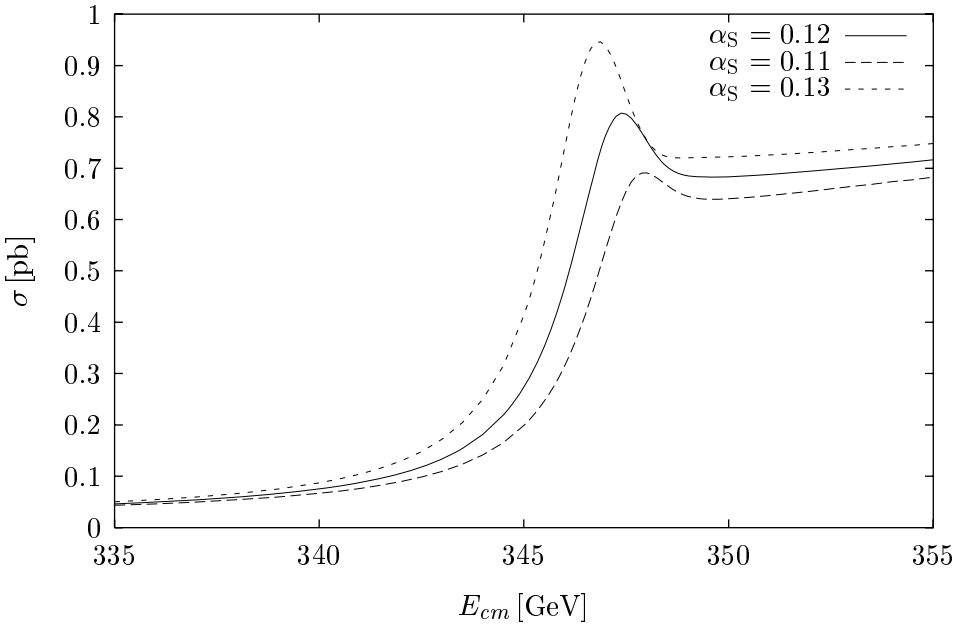

Figure 10.1: Top production cross section at the threshold for different values of α_S. A change in the top mass would lead to horizontal shifts of the cross sections graphs. The cross section is for sharp centre of mass energies.

not yet been investigated with a Monte-Carlo simulation. Of the three sources for the luminosity spectrum the initial state radiation can be calculated, even though a measurement would be preferable. The energy spread can be measured with a spectrometer. There is some uncertainty left how to fold the two energy spectra since there may be a correlation between particle energy and position in the bunch. Since the effect of the energy spread for TESLA turns out to be small anyway this should not be a severe problem. While these two sources of the luminosity spectrum seem to be well under control, the beamstrahlung depends strongly on the beam parameters and can therefore not be calculated with the necessary precision. It is in addition only present together with initial state radiation and the energy spread. One therefore has to measure the overall luminosity spectrum. If the precision of the measurement turns out to be inadequate it will necessary to reduce beamstrahlung by increasing the horizontal beam size—at the cost of a reduced luminosity.

10.2.1 Simulation of detector effects

In the following calculations the detector effects are included in a simplified way. In this simple model the experimental setup consists of a vertex detector, a central tracker, an electromagnetic and a hadronic calorimeter and a muon detector. The simulation includes the effect of a magnetic field for the position of hits in the

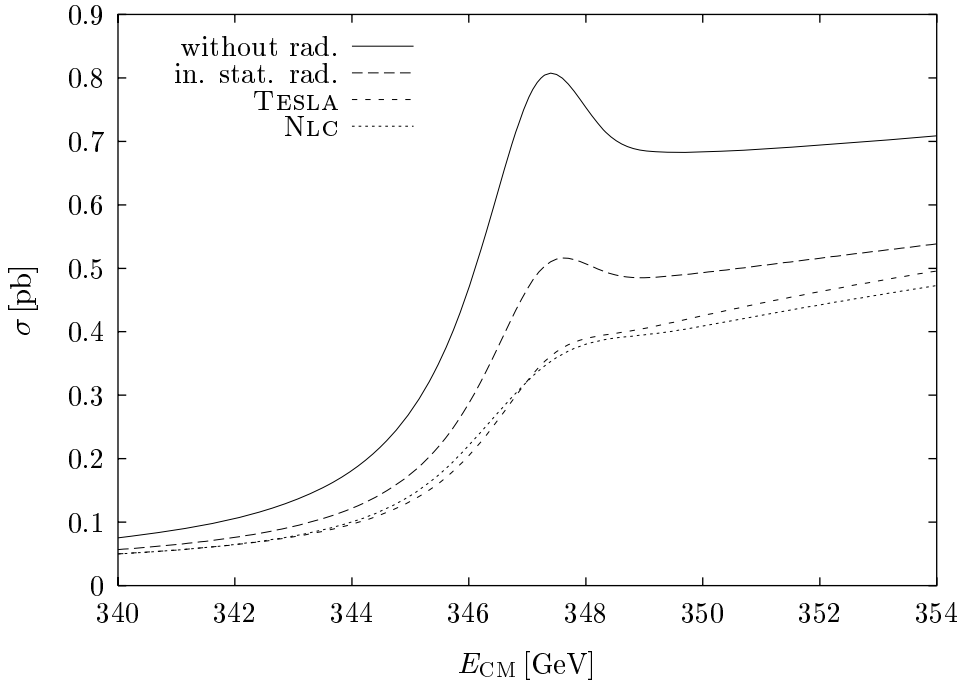

Figure 10.2: Effective top production cross section for different luminosity spectra. In the curves for TESLA and NLC beamstrahlung, energy spread and initial state radiation are taken into account.

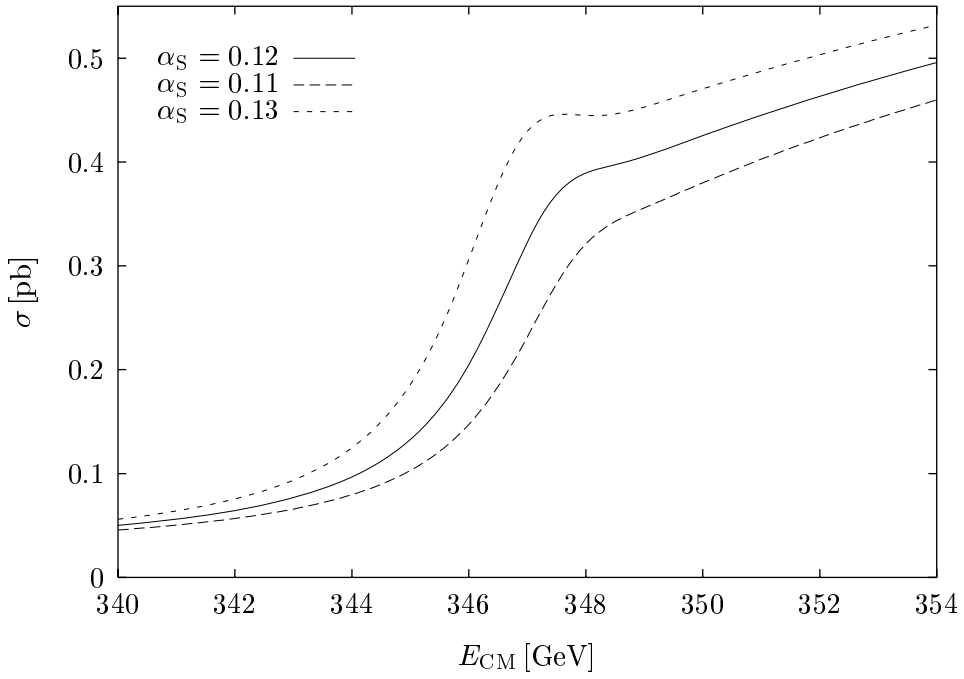

Figure 10.3: Top production cross section at the threshold for different values of α_S taking the luminosity spectrum into account.

calorimetry. Particles which make a full turn in the detector are assumed to be not measurable. For the calorimeter this is certainly true since they hit the masks. The magnetic field is assumed to be 3 T and the inner radius of the calorimeter 2 m.

- The vertex detector measures the impact parameter in $r\phi$ only. Its resolution is parametrised as $\sigma_{\mathrm{V}} = A_{\mathrm{V}} \oplus B_{\mathrm{V}}/(\sin^{1/2}\theta p_{\perp})$, with $A_{\mathrm{V}} = 10\,\mu$m and $B_{\mathrm{V}} = 50\,\mu\mathrm{m\,GeV/c}$. The reconstruction efficiency for vertices is $\eta_{\mathrm{V}} = 0.95$. With a probability $\zeta = 0.01$ the reconstructed vertex is incorrect, in which case it is randomly chosen in the interval $0\,\mathrm{mm} \leq d \leq 10\,\mathrm{mm}$.

- The resolution for transverse momenta of the central tracker is given by $\sigma_{\mathrm{D}} = A_{\mathrm{D}} \cdot p_{\perp} \oplus B_{\mathrm{D}} \cdot p_{\perp}^2$, with $A_{\mathrm{D}} = 2 \cdot 10^{-3}$ and $B_{\mathrm{D}} = 4 \cdot 10^{-4}\,(\mathrm{GeV/c})^{-1}$. The angular resolution is parametrised as $\Delta\theta_D = 2\,\mathrm{mrad}$ and $\Delta\phi_D = 1\,\mathrm{mrad}$. If the angle between the beam axis and the particle trajectory is small this resolution is degraded. If a particles leaves the central tracker through the end-caps and not the barrel the lever arm is shorter and the number of sampling points smaller than for tracks with large angles. The transverse momentum resolution is then calculated according to $\sigma_{\mathrm{D}} = A_{\mathrm{D}} \cdot p_{\perp} \oplus B_{\mathrm{D}} \cdot p_{\perp}^2 g^{5/2}$, with $g = \max(1, \tan\theta_0/\tan\theta)$. θ_0 is the smallest angle at which a particle still hits the barrel of the tracker. For the simulation $\tan\theta_0 = 0.7$ is used. The efficiency of the tracker is $\eta_{\mathrm{D}} = 0.99$.

- The resolution of the electromagnetic and hadronic calorimetry is given by $\sigma_{\mathrm{E}} = A_{\mathrm{E}}E \oplus B_{\mathrm{E}}\sqrt{E}$ and $\sigma_{\mathrm{H}} = A_{\mathrm{H}}E \oplus B_{\mathrm{H}}\sqrt{E}$ respectively, with $A_{\mathrm{E}} = 0.01$, $B_{\mathrm{E}} = 0.15$, $A_{\mathrm{H}} = 0.02$ and $B_{\mathrm{H}} = 0.6$. The position of the hit is calculated using the magnetic field and radius of the central tracker. The angular resolution for an isolated hit is given by $\Delta\theta_{\mathrm{E}} = \Delta\phi_{\mathrm{E}} = 2 \cdot 10^{-3}$ and $\Delta\theta_{\mathrm{H}} = \Delta\phi_{\mathrm{H}} = 10 \cdot 10^{-3}$. If the distance between two hits in the hadron calorimeter is smaller than $l_{\mathrm{H}} = 30\,\mathrm{cm}$ they are joined into one cluster.

- Isolated electrons and muons are assumed to be identified with an efficiency of 99%. All hadronic charged particles are assumed to be pions and are also identified with 99% efficiency. A misidentified electron is reconstructed either as a muon or as a pion with equal probability. In the same way a misidentified muon is reconstructed as a pion or an electron and a pion as a muon or an electron. If a charged track is closer than l_{H} to a track that contributes to a hadronic cluster the identification efficiency for electrons and muons is reduced to 80%. In the remaining 20% they are reconstructed as pions.

The reconstruction of the particles is done in a very simple way. For all isolated particles the detector component giving the best resolution is used. For charged particles the measured angles from the central tracker are used. Electrons

and muons which are connected to a hadronic cluster are reconstructed next. If the total energy of all remaining charged particles whose trajectories point towards a hadronic cluster is consistent with the energy of the cluster within one standard deviation it is assumed that the cluster contains the energy of the charged particles only, which can be measured with better resolution in the tracker. If the energy of the charged particles exceeds the cluster energy the cluster is also no longer used. This is based on the assumption that one or more of the charged particles must be an electron or muon, which were wrongly reconstructed as a pion, and can thus not be seen in the hadron calorimeter. If the cluster energy exceeds the charged particles energy the difference is assumed to be due to a neutral particle (a K_L^0).

To check that the described smearing method is reasonable a test run was performed. The different detector resolutions were set to the ALEPH [97] values. As input Z^0 events at a centre-of-mass energy of 91.87 GeV were used. The total energy resolution was found to be $\sigma_E \approx 6.5\,\mathrm{GeV}$. This is comparable with the actually measured resolution of 6.2 GeV. The energy flow resolution is thus about $0.65/\sqrt{E}$.

10.2.2 b-tagging

For the top threshold scan as well as for the search of Higgs particles with a mass close to the Z^0 mass the possibility to tag b-jets will be useful. As a simple method the number of high impact parameter tracks in a jet can be used. A track will be assigned a high impact parameter if it causes two hits in the vertex detector and if the two dimensional impact parameter exceeds 2.5 times the resolution of the detector for the given angle and particle momentum. The impact parameter has in addition to be smaller than 10 mm. No additional methods are used to increase the purity of the tagging.

The tagging efficiency was calculated using $e^+e^- \to Z^0$ events with $E_{CM} = M_{Z^0}$. If one requires two high impact parameter tracks per jet to accept it as a b-jet the efficiency is about 63%. With the same cut 25% of the c-jets are accepted as well as 3% of the s-jets. The amount of c-jets can be reduced by using sharper cuts but this will also reduce the efficiency for b-jets. Using three dimensional impact parameters increases the efficiency, up to 78% are expected for a CCD design [23].

10.3 Efficiency of tagging top events

Since the width of the top is large ($\Gamma_t \approx 1.4\,\mathrm{GeV}$ for $m_t = 175\,\mathrm{GeV/c^2}$ and $\alpha_S = 0.12$) its decay time is so small that the quarks in the top-anti-top system decay weakly into bottom quarks before they are able to fragment into hadrons. The top quark decays into a bottom quark and a W^+, the anti-top quark into a anti-

C_W [GeV/c^2]	C_t [GeV/c^2]	N_b	N'_b	N_W	ϵ [%]	σ_B [fb]	σ'_B [fb]
10	50	0	0	∞	16.1	7.5	13.5
20	50	0	0	∞	18.0	11.5	18.0
30	50	0	0	∞	18.3	13.0	19.5
50	50	0	0	∞	18.3	13.0	20.0
10	50	2	0	∞	5.4	0.0	0.1
20	50	2	2	∞	7.1	0.0	0.2
30	50	2	2	∞	7.8	0.2	0.3
50	50	2	2	∞	8.5	0.4	0.4
10	50	0	2	∞	13.7	0.7	1.5
20	50	0	2	∞	16.2	1.4	2.5
30	50	0	2	∞	17.0	1.9	3.0
50	50	0	2	∞	17.3	2.3	3.5

Table 10.1: Efficiencies ϵ and effective background cross section σ_B for tagging top events with one of the W-bosons decaying semi-letonically using different cuts. The numbers are given with higher precision than the statistical error— since they where obtained using the same sample the differences between the different cuts can still indicate which one is better.

C_W [GeV/c^2]	C'_W [GeV/c^2]	C_t [GeV/c^2]	N_b	N'_b	N_W	ϵ [%]	σ_B [fb]	σ'_B [fb]
50	50	60	0	0	∞	33.3	22.5	37.0
30	30	60	0	0	∞	32.8	21.5	35.0
10	10	60	0	0	∞	23.4	12.5	16.0
50	30	60	0	0	∞	33.3	22.5	37.0
50	10	60	0	0	∞	32.3	21.0	34.0
30	10	60	0	0	∞	31.8	20.0	32.0
50	30	60	2	2	∞	18.9	2.2	4.4
30	10	60	2	2	∞	14.0	1.1	1.9
50	30	60	2	2	3	18.4	2.1	4.1
20	10	50	0	2	∞	23.1	4.7	6.5
50	20	60	0	2	∞	29.4	10.0	15.0
30	10	60	0	2	∞	27.1	7.0	11.0

Table 10.2: Efficiencies and background for tagging top six jets events using different cuts.

bottom quark and a W^-. The W bosons decay hadronically with a probability of about 70% resulting in two jets each. With a probability of araound 10% for each family they can also decay into a lepton and a neutrino.

In about 46% of all $t\bar{t}$-events one thus finds six jets in the final state. In 44% one of the W bosons decays semi-leptonically leading to four jets and a hard lepton in the detector. If this is a τ lepton, one can of course also find five jets. In the remaining 10% both bosons decay into a lepton and a neutrino and one finds two jets and two hard leptons.

Different numbers can be found in literature for the efficiency with which top events can be tagged at the threshold. For a top mass of $m_t = 150\,\mathrm{GeV}$ reference [98] finds 29.5% including the branching ratios for all decay channels. Reference [99] finds an efficiency of 29.5% for the six-jet decays alone. Excluding the branching ratio this corresponds to an efficiency of 63%. The author claims that about the same could be achieved for the other two decay channels[2].

Because of this disagreement the efficiency is estimated in the following, using PYTHIA as a generator for the top and background events. This generator is not optimised for the production of top quarks at the threshold—it is for example not possible to produce top quarks below the threshold. The results could thus differ to some extend from those of a dedicated generator which was unfortunately not available. All events are smeared using the method given above.

As background processes $e^+e^- \to q\bar{q}$, $e^+e^- \to W^+W^-$ and $e^+e^- \to Z^0Z^0$ are taken into account.

The first analysis makes use of the events where one W decays leptonically. To this end a jet analysis with the JADE algorithm is performed using a cut parameter $y_{\mathrm{cut}} = 0.005$. Events with less than five jets are rejected. The remaining ones are analysed with another jet algorithm from the PYTHIA library to yield exactly five jets. As a distance measure the quantity [52]

$$d_{i,j} = \frac{2p_ip_j \sin\frac{\theta_{i,j}}{2}}{p_i + p_j}$$

is used, which gives a better momentum reconstruction than the standard JADE algorithm. The events are required to contain one isolated lepton with an energy of at least 20 GeV. The criterion for isolation is that the jet which contains the lepton does not exceed the lepton energy by more than ten percent, this accepts leptons which emitted final state radiation. Two of the remaining four jets are required to have an invariant mass that is consistent with the W mass:

$$C_{\mathrm{W}} \geq |m_{2j} - m_{\mathrm{W}}|$$

Together with one of the remaining two jets the invariant mass has to be close to half the centre of mass energy:

$$C_{\mathrm{t}} \geq \left| m_{3j} - \frac{1}{2}E_{\mathrm{cm}} \right|$$

[2] In the paper they conservatively ignore these contributions.

The efficiencies achieved with different values can be found in Table 10.1. For $C_{\mathrm{W}} = 20\,\mathrm{GeV/c^2}$ and $C_{\mathrm{t}} = 50\,\mathrm{GeV/c^2}$ one finds an efficiency $\epsilon \approx 18\%$ including the branching ratio. The total effective background cross section is about $\sigma_B = 13\,\mathrm{fb}$. This results in a signal-to-background ratio of about 7.5 to 1.

The background can be significantly suppressed by using b-tagging. In addition to the cuts mentioned before one requires that the two jets which originate from the $\mathrm{b\bar{b}}$-system must have at least N_{b} ($N_{\mathrm{b}} = 0, 2, 3$) high impact parameter tracks while the jets associated with the W must not have more than N_{W} ($N_{\mathrm{W}} = 2, 3, ..\infty$) tracks. This reduces the background by an order of magnitude while the efficiency is only reduced by a factor of two. The values can also be found in Table 10.1. A good compromise between purity and efficiency is to require only one tagged b-jet. One therefore requires at least one of the jets to contain N'_{b} high impact parameter tracks.

Also the six-jet decays of the top-pair can be used. A preselection of events that are not accepted by the first reconstruction is done by requiring a visible energy in between $0.65E_{\mathrm{cm}} < E_{\mathrm{vis}} < 1.05E_{\mathrm{cm}}$. This is mainly to get rid of events with a radiative return to the Z^0 peak[3]. Furthermore cuts are applied on the thrust value $T < 0.85$, on the thrust axis $|\cos\theta_{\mathrm{T}}| < 0.95$ and on the charged multiplicity $m > 20$. An analysis with the JADE jet algorithm is performed using $y_{\mathrm{cut}} = 0.005$ and events with less than six jets are rejected. The cut parameter is then varied to yield exactly six jets. Combinations among these jets are searched, where two jet pairs which have an invariant mass consistent with the W boson. For one of the pairs an agreement $C'_{\mathrm{W}} > |m_{2\mathrm{j}} - m_{\mathrm{W}}|$ is required, while for both $C_{\mathrm{W}} > |m_{2\mathrm{j}} - m_{\mathrm{W}}|$ must be fulfilled. To each of the jet pairs, which is assumed to originate from a W boson, one of the remaining jets is added requiring an invariant mass close to half the centre of mass energy $C_{\mathrm{t}} > |m_{3\mathrm{j}} - 1/2E_{\mathrm{cm}}|$.

The resulting efficiencies can be found in Table 10.2. They are around 30% with an effective background cross section of about 20 fb. The signal to background ratio is 7 to 1. With tighter mass cuts this ratio can be improved at the cost of reduced efficiency. A significant improvement can be achieved using b-tagging as for the semi-leptonic decay. The efficiencies is reduced to around 18% with an effective background cross section of about 2 fb leading to a signal to background ratio of 40 to 1. Tagging of one b-jet only does not compromise the efficiency significantly but the gain in purity is smaller than for the semi-leptonic case.

The combined efficiency for both channels can thus reach about 52% for an effective background cross section of 35 fb or cleaner samples could be selected with 47% (36%) efficiency and $\sigma_B \approx 12.3\,\mathrm{fb}$ (4.1 fb) requiring one b-jet to be tagged in the semi leptonic decay and one (two) in the hadronic decay.

[3]Due to the large cross section at $E_{\mathrm{CM}} = m_{\mathrm{Z}^0}$ there will be a significant rate of events at this centre of mass energy where the initial state particles emitted initial state radiation.

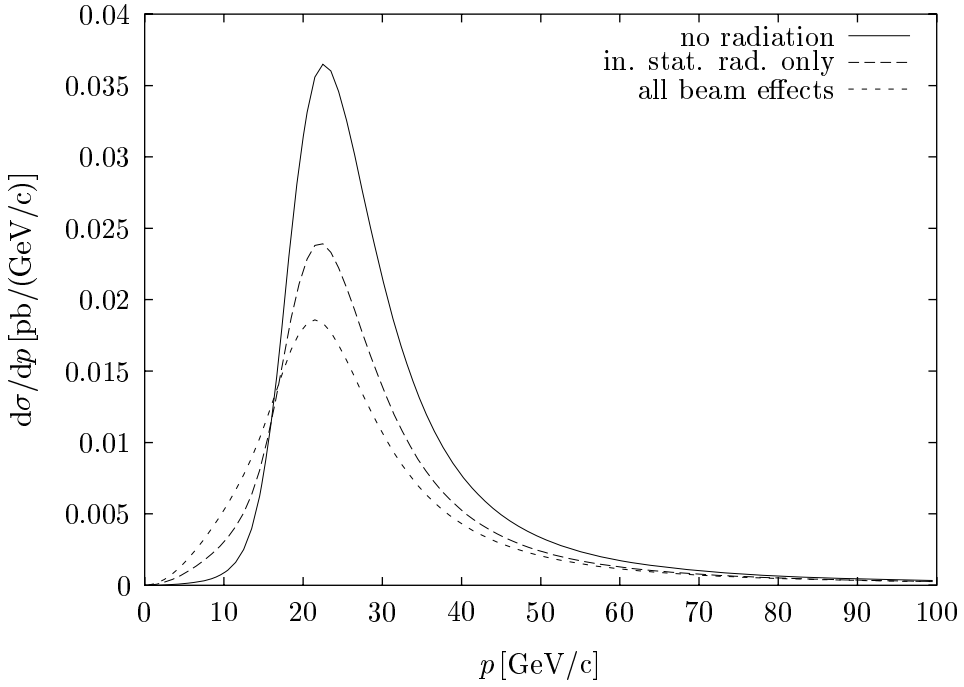

Figure 10.4: The momentum distribution of the top quark at a centre of mass energy of 351 GeV without and with initial state radiation and with the luminosity spectrum of TESLA.

10.4 The momentum distribution of top quarks

The momentum distribution of the top quarks produced at the threshold can be used to improve the measurement. The distribution is influenced by the initial state radiation, the beamstrahlung and the energy spread, see Figure 10.4. These influence the height and width of the distribution while the peak position stays about constant.

The momentum distribution is mainly sensitive to the difference between the centre of mass energy and twice the top mass. This information can therefore help to reduce the correlation between α_S and the top mass. Figure 10.5 shows the momentum distribution as calculated with TOPPIK [96] for different top masses, Figure 10.6 for different values of the strong coupling.

The dependence of the momentum peak position on the centre of mass energy for different physical parameters is shown in Figure 10.7.

10.5 Measuring the top momentum

The simplest channel that can be used to measure the top (or anti-top) momentum is that in which one W decays into a lepton and a neutrino and the other

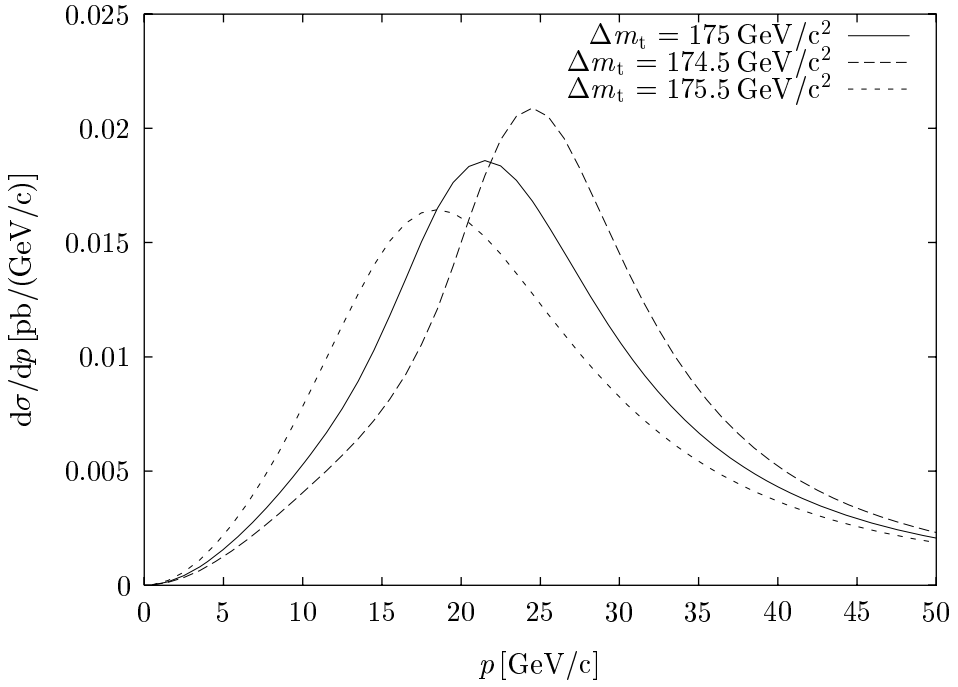

Figure 10.5: The momentum distribution of the top quarks at a centre of mass energy of 351 GeV for slightly different top masses. The luminosity spectrum is taken into account. The position of the peak shows is shifted with the top mass.

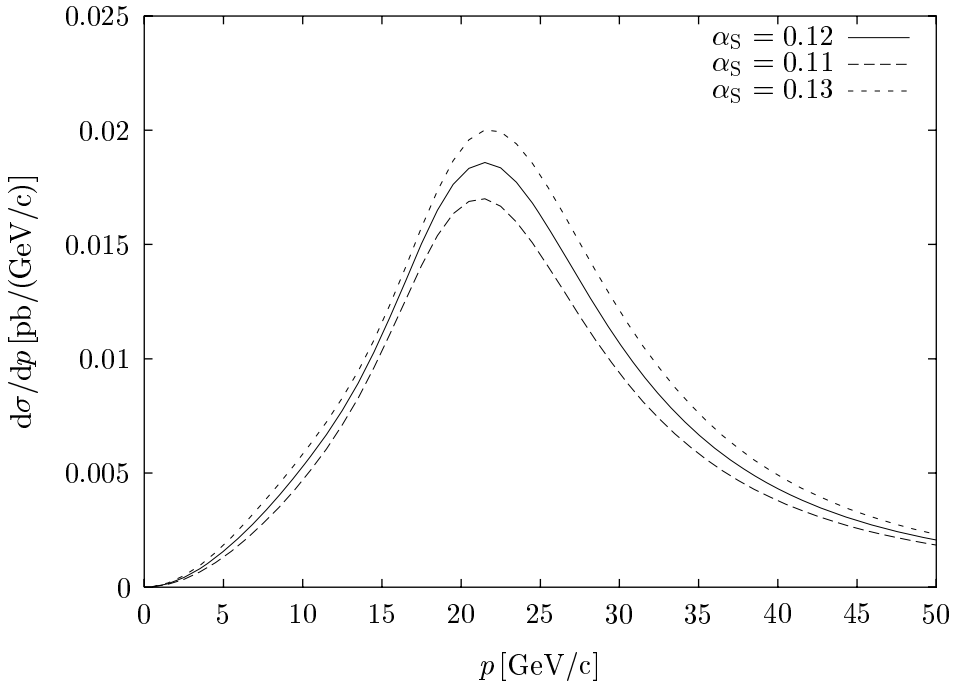

Figure 10.6: The momentum distribution of the top quarks for different values of the strong coupling at a centre of mass energy of 351 GeV. The position of the peak is almost unchanged.

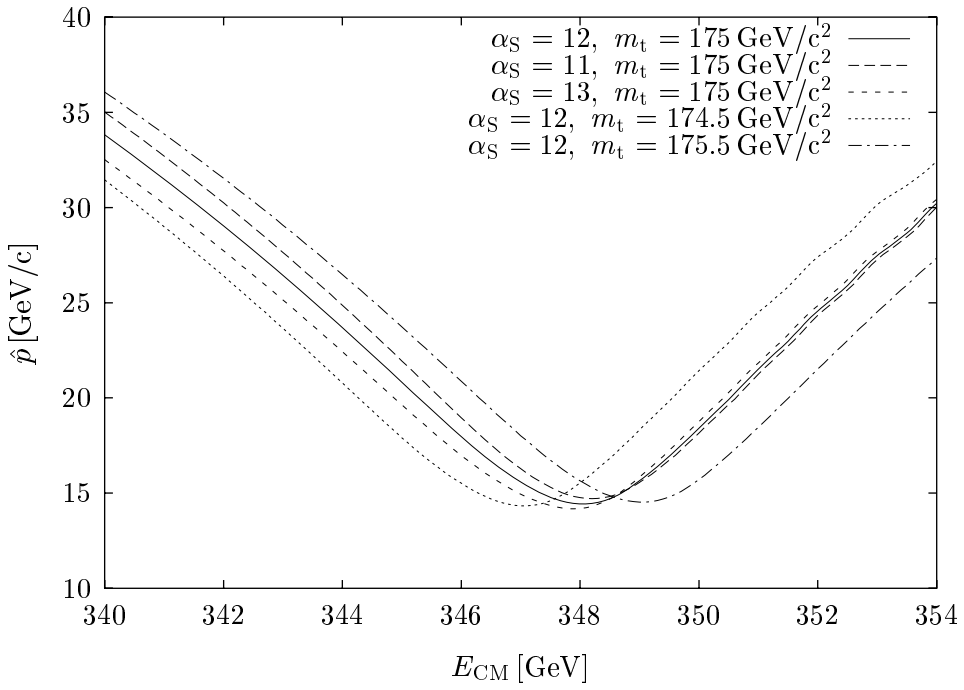

Figure 10.7: The dependence of the peak momentum on the centre of mass energy for different parameters. Initial state radiation and beam effects are taken into account.

hadronically. The final state has four hadronic jets and a hard lepton. This reduces the combinatorics in comparison with the six-jet final states.

The analysis is performed the same way as above except that a different cut for the reconstructed top mass is used, $C_t = 25\,\mathrm{GeV/c^2}$. This suppresses events where the top quarks loose significant energy into neutrinos. A very sharp cut is however not appropriate since if the top quarks have a sizeable momentum only one of them can be on mass shell. If more than one interpretation of the jets in an event passes the cuts that resulting in a top mass closest to the expected top mass is used. If two interpretations lead to the same top mass the one in better agreement with the W-mass is used.

Figure 10.8 shows the momentum distribution of the reconstructed top for loose mass cuts ($C_W = 20\,\mathrm{GeV}$ and $C_t = 25\,\mathrm{GeV}$) and Figure 10.9 for tight mass cuts ($C_W = 3\,\mathrm{GeV}$ and $C_t = 10\,\mathrm{GeV}$). Efficiencies can be found in Table 10.3. After the reconstruction it is checked that two b-jets actually receive most of their energy from the $b\bar{b}$-system and the two W-jets from the W-system. With the loose mass cuts the number of events where the jets are not correctly attributed to the W or the $b\bar{b}$ system is quite large. This method is thus not well suited for them momentum reconstruction. The distribution of the events with correct assignment however reproduces the actual momentum distribution reasonably well. With tighter mass cuts the reconstruction leads to the correct momentum

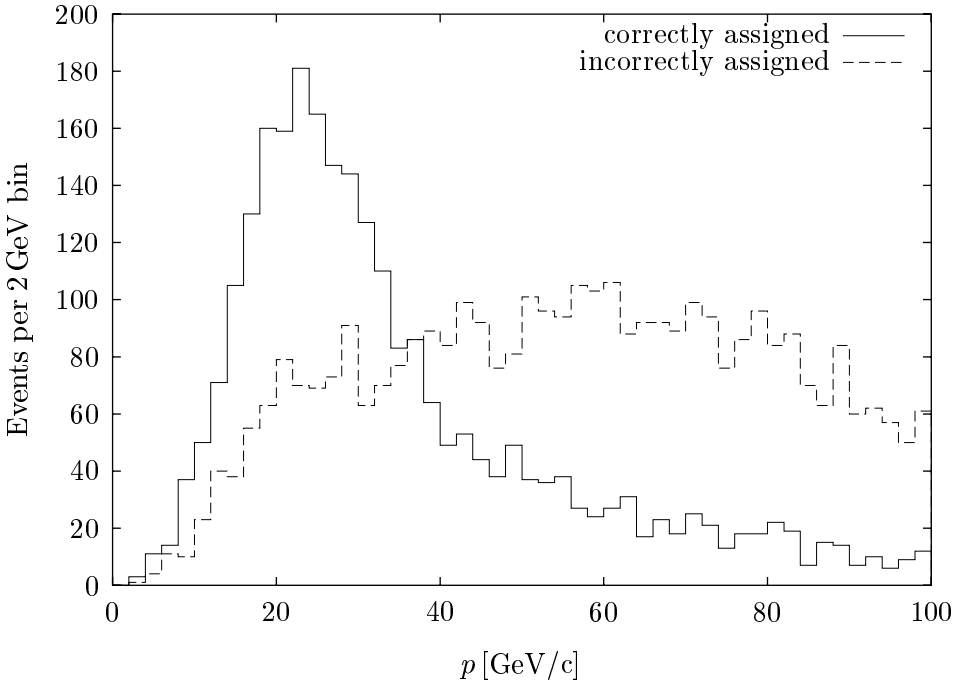

Figure 10.8: Momentum distribution of the reconstructed top quarks for loose mass cuts $C_W = 20\,\mathrm{GeV/c^2}$ and $C_t = 25\,\mathrm{GeV/c^2}$. The event is assumed to be correctly reconstructed if the jets reconstructed as b-jets actually received the majority of their energy from the $b\bar{b}$ system and the jets assigned to the W-boson from the decay products of the W-system. No b-tagging was used.

with increased probability such that the measurement can be used. On the other hand the efficiency decreases significantly.

The benefit of a vertex detector can be seen in Figure 10.10 where the loose mass cuts are used and a b-tag is required for each of the two b-jets ($N_b = 2$). In addition an anti-b-tag $N_W = 3$ can be used without compromising the efficiency while reducing the number of wrong combinations by about 20%. The efficiency is larger than for the tight mass cuts while the absolute background level is reduced. A further improvement in the cleanliness can be achieved by using even sharper cuts but this would compromise the efficiency.

Using the vertex detector improves the reconstruction significantly for reasonable detector resolutions and is superior to using sharp mass cuts. If one assumes better detector resolutions the methods using mass cuts only improve, but even if one does not take into account any detector effects except for the vertex detector they can only almost match the method using the vertex detector.

The efficiencies for different cuts are given in Table 10.3 It is clear from this simulation that a good vertex detector is essential for this measurement. Even very tight mass cuts achieve less purity of the sample than simple b-tagging.

As a reasonable compromise between purity and efficiency the loose mass

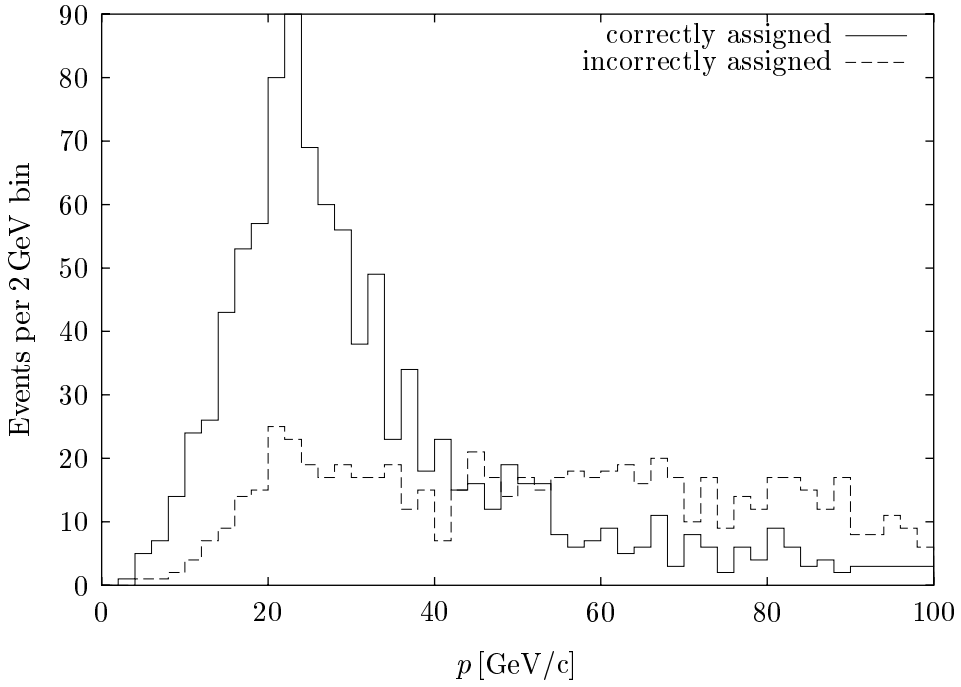

Figure 10.9: Momentum spectrum using sharper mass cuts $C_{\mathrm{W}} = 3\,\mathrm{GeV/c^2}$ and $C_{\mathrm{t}} = 10\,\mathrm{GeV/c^2}$.

cuts with b-tagging for the two b-jets is used in the following. The efficiency for finding events is about 6.5%.

TOPPIK calculates the differential cross section in the centre of mass system. One has thus either to include the boosts when folding this cross section with the luminosity spectrum or one has to reconstruct the centre of mass system from the event. This can be done by finding the momentum of the neutrino (the missing sixth jet) using the fact that the sum over all transverse momenta must be zero as well as that the invariant mass of the neutrino and the lepton must be the W mass.

To estimate the effects of the detector and the reconstruction the difference between generated and measured top momentum is investigated. The distribution of these residuals in the centre of mass system is shown in Figure 10.11. The peak has a width of about 12 GeV/c and can be reasonably well approximated by a Gaussian distribution with $\sigma = 6\,\mathrm{GeV/c}$. There is a systematic shift of the measured momenta compared to the generated ones. This shift is smallest in the region of $p_{\mathrm{t}} > 30\,\mathrm{GeV/c}$ and is neglected in the further calculations. About 15% of the reconstructed events are not contained in the Gaussian distribution. The width of the residual distribution in the laboratory system is about 4.8 GeV/c. It is smaller than in the centre of mass system since the measurement error for the lepton as well as for the fourth jet do not contribute to this error.

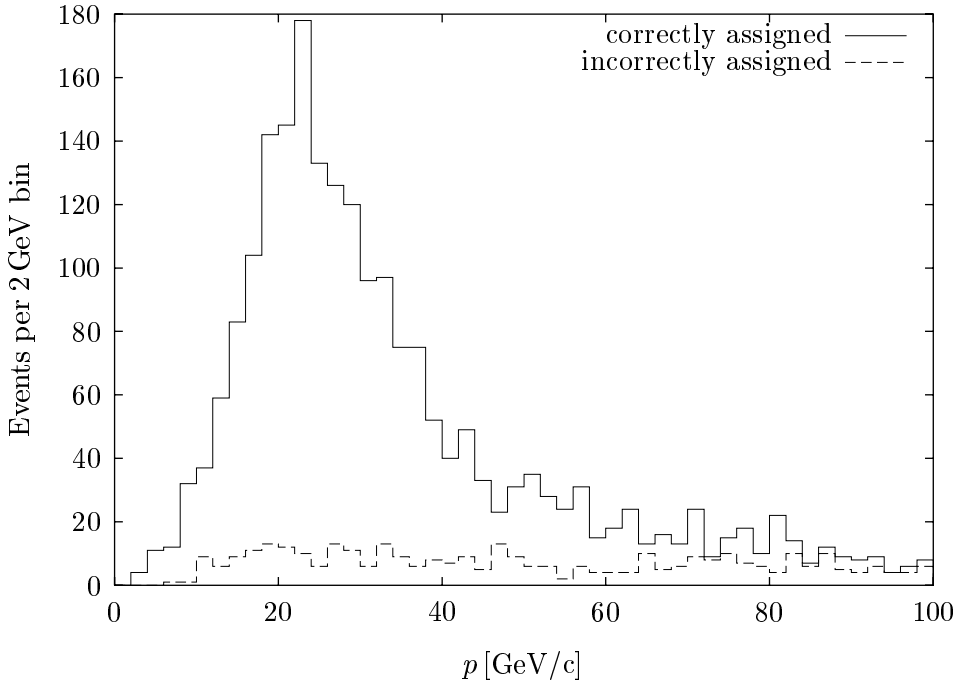

Figure 10.10: The momentum spectrum reconstructed using b-tagging. Loose mass cuts $C_W = 20\,\mathrm{GeV/c^2}$ and $C_t = 25\,\mathrm{GeV/c^2}$ are applied. In addition the b-jets are required to have two high impact parameter tracks ($N_t = 2$) while no cut was used for the W-jets ($N_W = \infty$.) One can see the improvement compared to the cuts in the previous graphs.

10.6 Comparison of the momentum distributions

To compare the momentum distributions for different physics parameters a simplified approach is chosen. First the momentum distribution is folded with the initial state radiation, the beamstrahlung and the energy spread. The result is then folded with a Gaussian with $\sigma = 6\,\mathrm{GeV/c}$ resulting in a distribution $f^*(p)$ which represents the momentum distribution of the correctly reconstructed events. A fraction η of the events are wrongly reconstructed, the measured momenta of these are assumed to be uniformly distributed in the interval from 0 to 100 GeV. The momentum distribution f is calculated as

$$f(p) = (1-\eta)f^*(p) + \frac{\eta}{100\ \mathrm{GeV/c}}$$

For the loose mass cuts and b-tagging $\eta = 0.15$ is used.

The difference between two distributions can be calculated by either using the difference of the peak or the median momenta. To calculate the median, only events with a momentum below $50\,\mathrm{GeV/c}$ are used. The error for the median

C_{W} [GeV]	C_{t} [GeV]	N_{b}	N_{W}	ϵ_t %	ϵ_f %	ϵ_{t+f} %
20	25	0	∞	6.5	8.8	15.3
5	10	0	∞	3.7	2.4	6.1
3	10	0	∞	2.5	1.7	4.2
3	25	0	∞	3.4	3.3	6.7
20	10	0	∞	4.8	5.8	10.6
20	25	2	∞	5.4	1.1	6.5
10	25	2	∞	4.4	0.6	5.0
5	25	2	∞	2.0	0.4	3.3
20	25	3	∞	2.7	0.4	3.1
10	25	3	∞	2.1	0.12	2.3
5	25	3	∞	1.3	0.1	1.4
20	25	2	3	5.5	0.8	6.3
10	25	2	3	4.5	0.5	5.0
5	25	2	3	2.9	0.2	3.1
20	25	2	2	5.0	0.6	5.6
10	25	2	2	4.0	0.3	4.3
5	25	2	2	2.7	0.2	2.8

Table 10.3: The efficiencies ϵ for the different mass cuts and b-tagging methods. ϵ_t is the efficiency for accepting an event, ϵ_f is the part of the wrongly reconstructed events and ϵ_{t+f} the total efficiency for reconstructing events correctly.

can be approximated as

$$\sigma_m \approx \frac{1}{2f(p_m)}\frac{1}{\sqrt{N}}$$

For the peak momentum it is assumed that the error of the peak value is given by $\sigma_{\hat{p}} = 5/3\sigma/\sqrt{N}$, where σ and N are taken from a Gaussian distribution having the same full width half maximum and the same number of particles in this range.

The difference between the two distributions f_1 and f_2 can also be calculated using $\Delta\chi^2$

$$\Delta\chi^2 \approx \int_0^{p_{\max}} \frac{(f_1(p) - f_2(p))^2}{f_1(p)}\mathrm{d}p \tag{10.1}$$

It may be difficult to extract the peak momentum from a small sample, especially in the presence of background. The median however should give a stable value that can be used even for relatively small statistics. Using $\Delta\chi^2$ gives better precision but again the small sample behaviour may be difficult to handle.

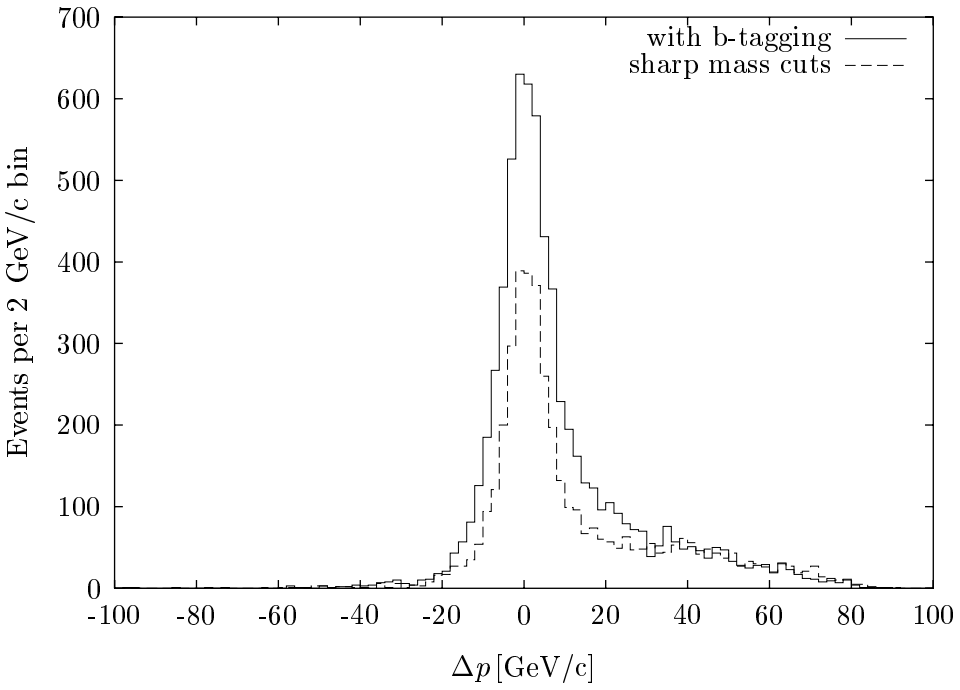

Figure 10.11: The distribution of the residual (difference between measured and actual momentum) of the top momentum. The solid line shows the results for loose mass cuts and b-tagging while the dashed line that of sharp mass cuts without b-tagging.

10.7 Sensitivity to hadronic backgrounds

The reconstruction of the top events relies mainly on overall event shapes. The tracks from the hadronic background could reduce the resolution since the suppression of events as $e^+e^- \to q\bar{q}$, $e^+e^- \to W^+W^-$ and $e^+e^- \to Z^0Z^0$ by the reconstruction algorithm has to be of the order of 10^{-3}. The effect of the hadronic background can be estimated by adding one soft hadronic event to each of the above events. The resulting effective background cross sections are shown in Tables 10.1 and 10.2. In all the cases with enough statistics the increase is less than a factor of two. Since the GUINEA-PIG calculation predicts that a hadronic background event will occur only in less than one out of twenty bunch crossings, the background cross section will be increased only by a few percent.

10.8 Resolution for α_S and top mass

A scan can be performed with eleven steps one of which is to measure the background. The difference in the centre of mass energy between the ten main points is 1 GeV. The starting point is at $\Delta E = -5$ GeV. The machine is run at each

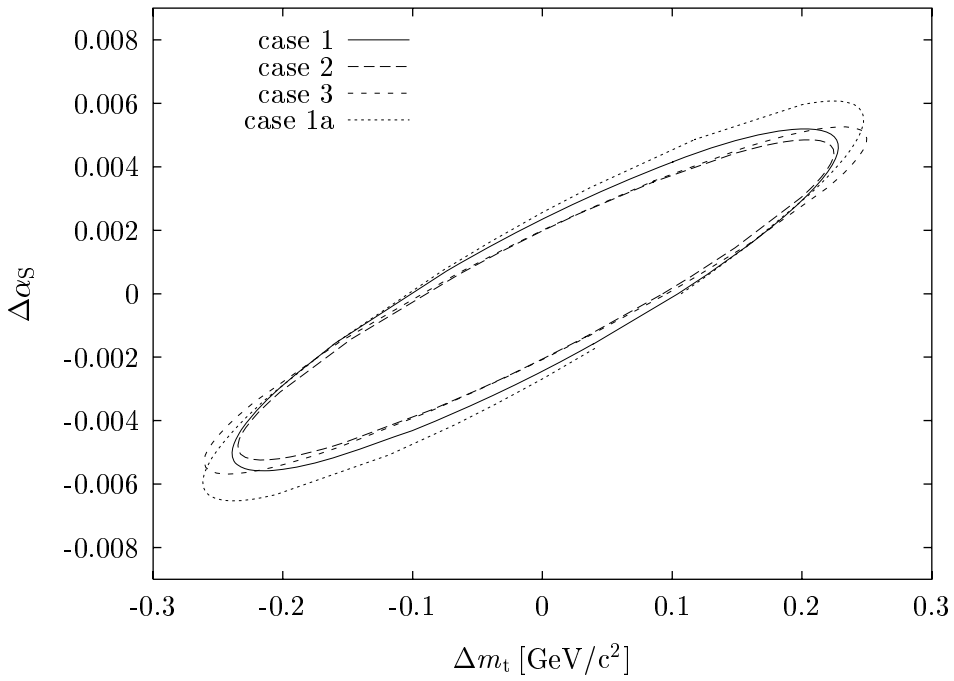

Figure 10.12: The $\Delta\chi^2 = 1$ contour for the usage of different cuts. A ten point scan with a running time of $2 \cdot 10^5$ s per point and an additional point to measure the background is assumed. Case 1 has an efficiency of $\epsilon = 51.6\,\%$ and an effective background cross section of $\sigma_B = 35.5$ fb, case 2 has $\epsilon = 46.7\,\%$ and $\sigma = 12.3$ fb and case 3 has $\epsilon = 35.9\,\%$ and $\sigma_B = 4.1$ fb. In case 1a a systematic error of 3 % is included for the cross section.

point for $2 \cdot 10^5$ s and the parameter set with higher luminosity is used.

Figure 10.12 shows the $\Delta\chi^2 = 1$ contour for this scan for different cuts of the reconstruction. A strong correlation between the top mass and α_S is visible. It can be concluded that the event reconstruction without b-tagging is superior to the one with b-tagging that results in a cleaner but smaller sample. A systematic error of 3 % was assumed for the cross section in the last curve—the uncertainty of the detector acceptance.

The additional information from reconstructing the peak momentum improves the resolution as can be seen in Figure 10.13. For the momentum distribution a systematic error of 4 % is assumed. The effective resolution enhancement due the momentum peak is small. Use of the momentum peak position alone would leave α_S almost unconstrained.

In the planned experiment ATLAS at LHC one may achieve a resolution for the top mass of $\Delta m_t \approx 2$ GeV [70]. In a linear collider the statistical error for the direct reconstruction of the top mass at energies well above threshold can be reduced well below 100 MeV but the systematic errors are important [98].

In Figure 10.14 the contour is shown for different running times.

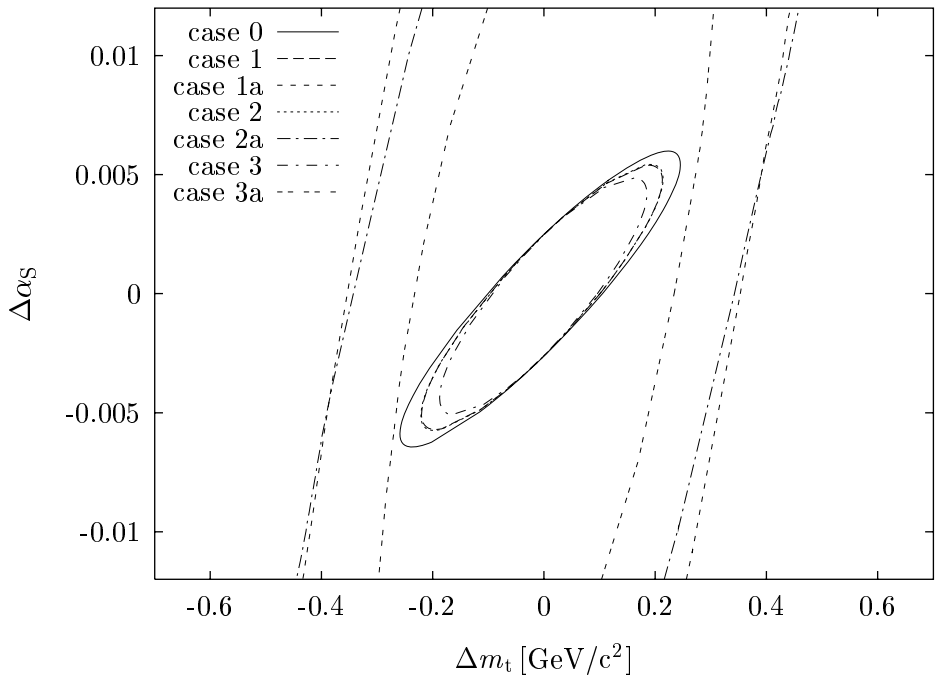

Figure 10.13: The $\Delta\chi^2 = 1$ contour for the usage of different measurements. Case 0 is the contour if only the cross section is used. Cases 1–3 (the outer curves) are the contours if the only the momentum distribution is used, while cases 1a-3a (the inner curves) are the resulting errors for the combination of cross section and momentum measurement. In case 1 the position of the peak is used and in case 2 that of the median. Case 3 makes use of the integral in equation (10.1).

10.9 Comparison of different colliders

The influence of the beamstrahlung on the effective cross section differs significantly for the collider designs. This may affect the precision that can be reached with the threshold scan. NLC is taken as an instructive example for a machine with a small number of beamstrahlung photons. The luminosity spectrum for this machine peaks significantly more pronounced at the nominal centre of mass energy if one takes only the beamstrahlung into account. However this machine has a larger energy spread of 0.8% full width in the beams. In the simulation the distribution is assumed to be constant within this range while in reality there are two peaks at lowest and highest energy where the probability density is about twice as high as on average. Figure 10.15 shows a comparison of the precision that can be achieved using the total cross section at the threshold only for TESLA, SBLC and NLC. A flat energy spread with an RMS value of 0.1%, 0.3% and 0.25% is assumed for the designs respectively. For all machines the parameter set with the higher beamstrahlung give a slightly better resolution. The differences between the machines are not very large. One can conclude that all of them

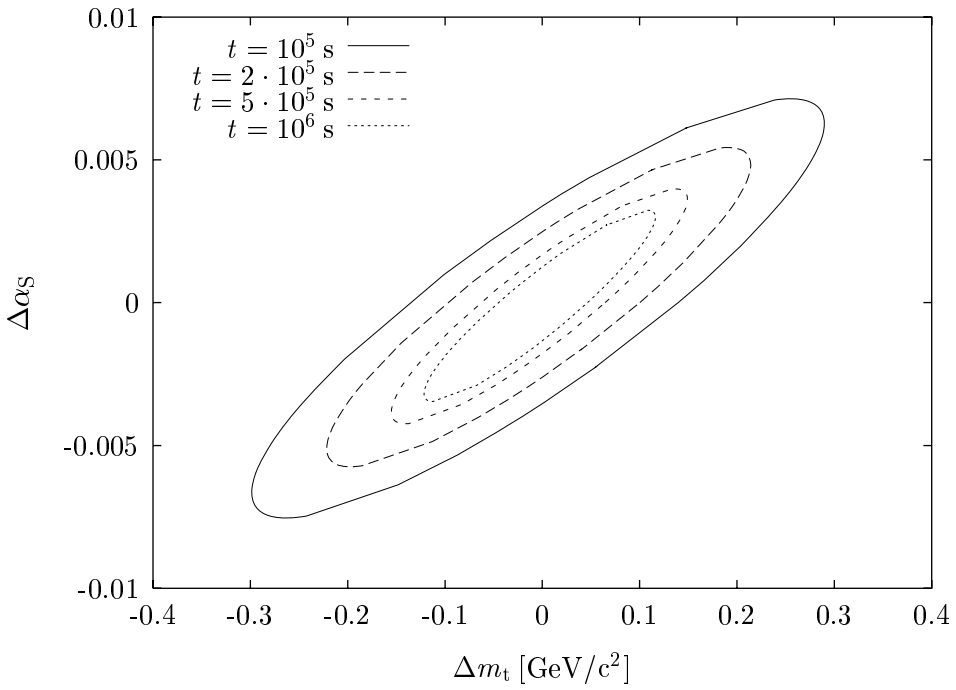

Figure 10.14: The resolution of the top threshold scan for different running times.

are about equally well suited for this measurement. However it still has to be checked if the reconstruction of the luminosity spectrum works equally well for all of them.

10.10 Fit of the top width

The top width can also be estimated from the threshold scan. It can be calculated within the frame of the standard model. Measuring it would thus provide an interesting check about the assumptions of the model. If one assumes that the strong coupling is known from a different source one can apply a two dimensional fit. Figure 10.16 shows the contour for this measurement. The time per scan point is 10^6 s and thus longer than for the previous scan. The spectrum of TESLA is used. In addition a lower starting energy is advantageous. The top width can be extracted with a relative error of about 7%. The correlation between the mass and the width is very small compared to the one between the strong coupling and the mass. The relative error for the top mass is only 50 MeV/c^2, simply because α_S was fixed.

If one assumes the strong coupling to be totally unconstrained one can apply a three dimensional fit. Figure 10.17 shows the projections of the resulting three dimensional contour into the m_t, Γ_t-plane. The $\Delta\chi^2 = 1$ contour is given by an ellipsis that contains all projected curves. The resolution for the width is

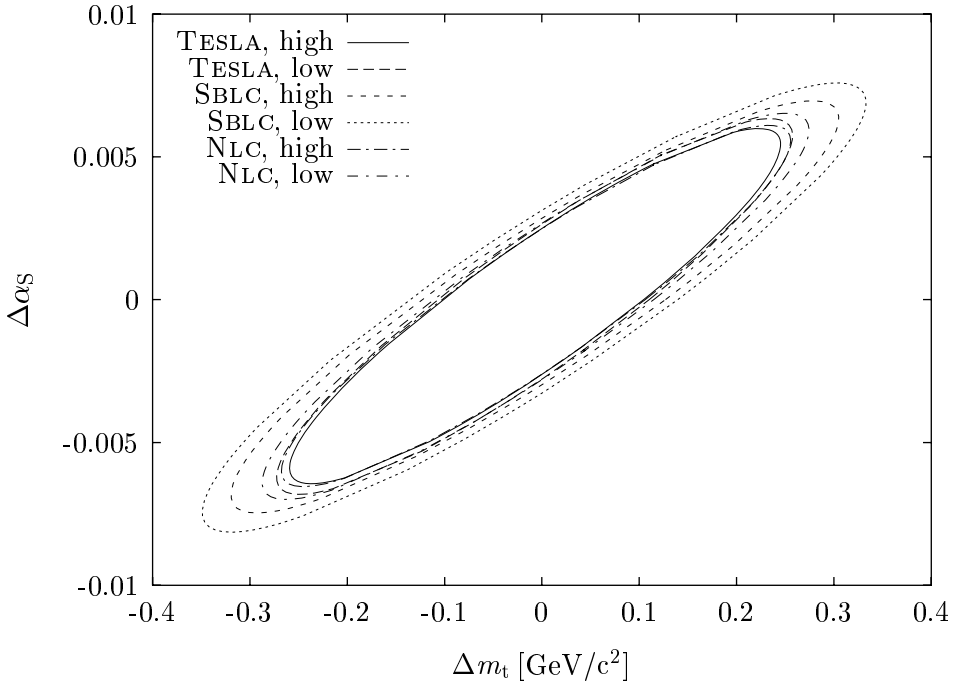

Figure 10.15: The $\Delta\chi^2 = 1$ contour for α_S and m_t. It was assumed that the Standard Model width of the top is correct and that the Higgs has a mass of 1000 GeV/c^2 in order to minimise its effect on the measurement—even so the expected value is smaller. High referes to the paramter set giving more, low to the one giving less beamstrahlung.

decreased to about 9%. For the top mass the resolution is about 150 MeV/c^2 while for α_S one finds an error of about 0.004.

A top width not in agreement with the Standard Model would however mean that most probably the detector acceptance changes. Therefore each possible reason has to be considered seperately to include all effects.

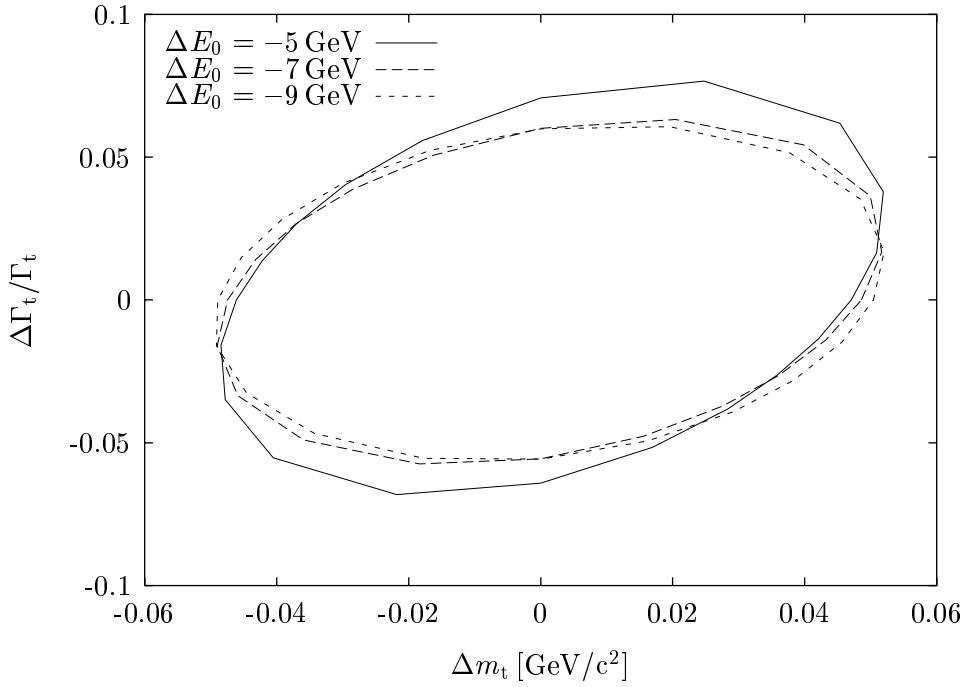

Figure 10.16: Contour of the threshold scan for unknown top mass and top width. It was assumed that α_s is know from another source to infinite precision.

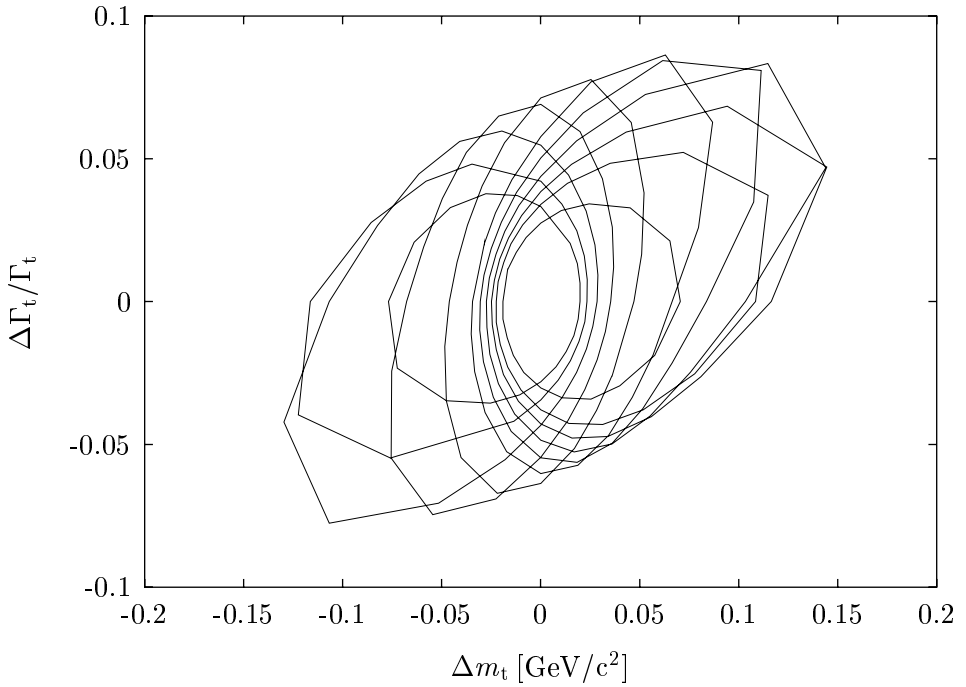

Figure 10.17: Contour of the threshold scan for unknown α_s, m_t and Γ_t projected into two dimensions.

Chapter 11

Conclusions

Beam-beam effects are important for future linear colliders. They force the beam particles to emit beamstrahlung. The resulting energy loss smears the luminosity spectrum. With the presented program GUINEA-PIG the results of another program—ABEL—could be confirmed.

The emitted beamstrahlung has a significant power (about 200 kW per beam in TESLA). This radiation can be a hazard to the collider. With the collimators described, the photons can be safely removed from the beam-line.

The beamstrahlung also increases the background in the detector due to two-photon processes. The main contribution will be the production of e^+e^- pairs in the interaction point. Per bunch crossing about 10^5 of these particles with a total energy of $1.6 \cdot 10^5$ GeV will be created in TESLA. A significant difference was found between ABEL and GUINEA-PIG regarding the energy spectrum of the produced particles. The Vermaseren Monte-Carlo, which can calculate one of the main processes and which was successfully compared to data, agrees with GUINEA-PIG.

The produced particles are be deflected by the fields of the beams. ABEL and GUINEA-PIG allow to simulate this effect. The dependence of deflection angle on particle energy calculated by the two programs was tested for one of the JLC designs and was found to be in good agreement.

A mask at the final quadrupoles together with the detector field can trap most of these particles and prevent secondaries from hitting the detector. This mask has to surround the quadrupole with a thickness of 5–10 cm.

The vertex detector can suffer from background due to charged particles backscattered at the quadrupoles. The proposed mask can suppress this background almost completely. The minimal possible radius of the inner layer of the vertex detector is found to be 25 mm if one wants to avoid the backscattered particles. A further reduction of this radius will have a significant impact on the machine design.

A number of particles produced with large angles and transverse momenta will hit the vertex detector despite the mask. An appropriate vertex detector

design seems feasible. Some promising approaches as the CCD with fast clear option need further investigation.

The number of hadronic background events due to two-photon processes is low enough to not affect the measurements significantly.

The impact of the neutrons produced in the showers induced by the pair and bremsstrahlung background have to be investigated in detail.

Measuring the kick angles during a beam beam scan is a method used at SLC to measure the vertical bunch size. Because of the strong beam beam interaction this is not applicable in TESLA. The beamstrahlung power (or the particle energy loss) can be used instead. This signal also allows to measure some of the beam properties during the luminosity run.

Simulations of a possible photon-photon option for TESLA predict a high $\gamma\gamma$ luminosity. The background from the interaction point is higher than for the e^+e^- version but does not seem to be prohibitive. The spent beams will have an angular spread much larger than in the e^+e^- or e^-e^- option. To prevent the particles from hitting the final quadrupoles it will be necessary to introduce a large crossing angle. However careful analysis of the background due to the spent beam remains to be done.

The change of the luminosity spectrum due to beamstrahlung will have an impact on the top threshold scan. The achievable resolution for the strong coupling constant and the top mass is investigated for different beam parameters. One can conclude that if the luminosity spectrum is well measured a reduction of the beamstrahlung is not worthwhile. The different linear collider designs allow for comparable resolutions for the top mass and the strong coupling. Compared to the ATLAS experiment at LHC the top mass resolution is better by almost order of magnitude.

Appendix A

GUINEA-PIG

A call to GUINEA-PIG is done with three command line arguments. The first is the name of the accelerator, the second the name of a computational parameter set and the third is the output file name. The parameters for the accelerator and the computational parameters are searched in a data file "acc.dat".

A.1 Format of `acc.dat`

This file contains the definitions of the accelerators and the computational parameter sets.

An entry for an accelerator is defined as

```
$ACCELERATOR:: name
{var1=value1;var2=value2*value3;...}
```

Where the definitions in the braces can extend over several lines. The variables can be of different types. The `INT` and `DOUBLE` contain single integer and double precision values. The `INT_2` and `DOUBLE_2` type variables contain two integer or double precision elements each. The elements can be accessed by appending `.1` or `.2` onto the name of the variable, as for example `sigma_x.1=1.0;`. Both elements can set simultaneously to the same value via `sigma_x=1.0;`, but `sigma_x` can not be used in the definition of a value as in `test=sigma_x;`. One has then to use `test=sigma_x.1`. The last types of numerical values are `INT_MIRROR` and `DOUBLE_MIRROR`. They can be used as the `INT_2` and `DOUBLE_2` except that `offset_x=1.0;` will be equal to `offset_x.1=1.0; offset_x.2=-1.0;`. Using a wrong name for a variable will cause the program to write an error message and to stop. The values attributed to a variable can be simple expressions containing brackets, multiplication , division, addition and subtraction. Instead of constants also the names of existing variables may be used.

`particles` (`DOUBLE_2`) The number of particles per bunch in units of $[10^{10}]$.

`energy` (`DOUBLE_2`) The energy of the particles in GeV.

`espread` (`DOUBLE_2`) The RMS value of the relative energy spread of the beam particles. The shape of the distribution is set via `which_espread`.

`which_espread` (`INT_2`) The energy distribution of the beam particles. If `which_espread` is 0 no energy spread, if it is 1 a flat distribution, for 2 two peaks and for 3 a Gaussian distribution is assumed.

`charge_sign` (`DOUBLE`) The relative sign of charge of the two beams—is -1 for an e^+e^- collider and 1 for e^-e^-. If it is set to zero no beam-beam force is assumed.

`sigma_x` (`DOUBLE_2`) The horizontal beamsize in nm.

`sigma_y` (`DOUBLE_2`) The vertical beamsize in nm.

`sigma_z` (`DOUBLE_2`) The longitudinal beamsize in μm, the RMS value should be used in case of distributions different from the Gaussian.

`f_rep` (`DOUBLE`) The repetition frequency of the collider, that is the number of bunch trains per second. This value is currently not used since all results are per bunch crossing.

`n_b` (`INT`) The number of bunches per bunch train. This value is currently not used.

`dist_z` (`INT_2`) The longitudinal charge distribution, for `dist_z`=0 a normal for `dist_z`=1 a homogeneous distribution is used. Default is 0.

`trav_focus` (`INT`) For a value not equal to zero the beams are assumed to have a travelling focus.

`emitt_x` (`DOUBLE_2`) The normalised horizontal emittance in 10^{-6}m rad.

`emitt_y` (`DOUBLE_2`) The normalised vertical emittance in 10^{-6}m rad.

`beta_x` (`DOUBLE_2`) The horizontal beta function in mm.

`beta_y` (`DOUBLE_2`) The vertical beta function in mm.

`offset_x` (`DOUBLE_MIRROR`) The horizontal offset in nm, default is 0.0.

`offset_y` (`DOUBLE_MIRROR`) The vertical offset in nm, default is 0.0.

`waist_x` (`DOUBLE_MIRROR`) The shift in μm of the horizontal waist with respect to the plane of collision.

`waist_y` (`DOUBLE_MIRROR`) The shift of the vertical waist.

`angle_x` (`DOUBLE_2`) The horizontal angle in rad, default is 0.0. Keep in mind that the system of beam 2 is lefthanded. To simulate an angle θ_0 between the two beams (not compensated with the crab crossing scheme) one simply has to set `angle_x=0.5`θ_0`;`. It is important to note that the user is responsible for choosing a grid that is sufficiently large to contain the beams.

`angle_y` (`DOUBLE_2`) The vertical angle in rad, default is 0.0.

`angle_phi` (`DOUBLE_2`) The transverse tilt angle of the bunch, default is 0.0.

It is only necessary to define two variables out of the combination of emittance, beta function and beam size. If all three are defined a check for agreement is performed.

Equivalently one has for the computational parameter set

```
$PARAMETERS:: name
{var1=value1;var2=value2;...}
```

In this declaration all the parameters from the definition of the accelerator can be addressed and in addition the following:

`n_x` (`INT`) The number of cells in horizontal direction.

`n_y` (`INT`) The number of cells in vertical direction.

`n_z` (`INT`) The number of cells in longitudinal direction.

`n_t` (`INT`) The number of timesteps used to move a slice to the next slice of the other bunch.

`n_m` (`INT_2`) The number of macroparticles used.

`cut_x` (`DOUBLE`) Size of the grid in horizontal direction in nm. If less than zero $3 \cdot \max($`sigma_x.1`$,$ `sigma_x.2`$)$ will be used.

`cut_y` (`DOUBLE`) The same as `cut_x` but for the vertical direction

`cut_z` (`DOUBLE`) Size of the grid longitudinally in μm.

`integration_method` Selects direct (=1), fast Fourier (=2) or iterative method (=3) the second is advised (it is necessary to use powers of two for `n_x` and `n_y` in this case)

`force_symmetric` (`INT`) If this value is not equal 0 the beams are assumed to be up-down and left-right symmetric.

`rndm_save` (`INT`) If not equal 0 the status of the random number generators is stored in the file `rndm.save`.

`rndm_load` (`INT`) If not equal 0 the file `rndm.save` with the status of the random number generators is loaded. If the file does not exist the generators are initialised with the standard values.

`do_lumi` (`INT`) If not zero a file containing the energies for electron-positron scattering is produced. This file serves as an input file for the event generator GHOST.

`num_lumi` (`INT`) The maximal number of scatters stored in the file mentioned above. The actual number will be at least half of this except for a value of `lumi_p` which is too low. The default value is 0.

`lumi_p` (`DOUBLE`) The initial scaling factor for the storage of particles into the luminosity file. The value will be adjusted to stay within the allowed maximum number of entries. If `lumi_p` is to small the number of entries in the file will be less than than half the allowed number. If the value is very high a small overhead is caused at the start of the program till it is adjusted to a sensible value.

`store_beam` (`INT`) If not equal zero the spent beams will be stored in the files `beam1.dat` and `beam2.dat` respectively. The files are in ASCII the first of the three values per line is the energy of the particle in GeV, the second and the third are the angles with respect to the beam axis for the horizontal and vertical direction. Default is 0.

`electron_ratio` (`DOUBLE`) Part of the electrons to be used for luminosity spectrum and background calculations. It has to be within $[0 : 1]$. If it set to a value smaller than 10^{-6} these calculations are completely suppressed except for the total luminosity. The choice of this parameter effects the precision (and time consumption) of the calculations but not the results (except for statistical reasons).

`do_photons` (`INT`) If not zero store the photons (needed for background calculations).

`photon_ratio` (`DOUBLE`) Part of the photons to be used for background calculations. The same considerations apply as for `electron_ratio` except that for setting `photon_ratio` to a value below 10^{-6} (the same as setting `do_photons=0;`) no photon-electron or photon-photon luminosity will be calculated.

`gg_cut` (`DOUBLE`) The photon-photon luminosity is calculated for all photon-photon centre of mass energies and separately for the part exceeding `gg_cut`.

`do_hadrons` (`INT`) If not zero calculate hadrons

`store_hadrons` (`INT`) If not zero the energies of the initial photons of the hadronic interactions during one bunch crossing are stored in the file `hadron.dat`.

`hadron_ratio` (`DOUBLE`) The weight factor with which the cross section of the hadronic interaction is scaled for the storage in the file.

`do_jets` (`INT`) If not zero calculate minijets.

`store_jets` (`INT`) If not zero the final states of the minijets are stored in the file `minijet.dat`.

`jet_ptmin` (`DOUBLE`) Minimal transverse momentum of the jets in GeV/c.

`jet_ratio` (`DOUBLE`) Factor with which the probability of jet production is enhanced (needed for producing a file of these jets).

`jet_log` (`INT`) If not zero uses different way to select the energy of the parton in a resolved photon. The default which gives better results is 1.

`do_pairs` (`INT`) If not zero calculate pairs

`pair_ratio` Probability of a produced pair to be stored (used to reduce the total number of particles to be tracked. This value has to be in $[0:1]$.

`pair_q2` (`INT`) Selects the Q^2 scale for the pair production, if 0 $Q^2 = m^2$, if 1 $Q^2 = m^2 + p_t^2$, if 2 $Q^2 = \hat{s}/4$. This value is preset to 2.

`track_pairs` (`INT`) If not zero the pairs are tracked through the fields of the beams. In order to get reasonable results it is necessary to chose an appropriate value of `grids`.

`grids` (`INT`) The number of grids used for the tracking of the pairs should be seven if they are tracked zero otherwise.

`pair_ecut` (`DOUBLE`) Minimal energy in GeV the particles from pair creation need to have to be stored

`pair_step` (`DOUBLE`) Scaling factor for the step size of the pairs; if the value is increased the step size is decreased.

`beam_size` (`INT`) If not zero the beam size effect is switched on. For `beam_size`=1 the impact parameter is calculated as $b = \hbar/q_\perp$, for `beam_size`=2 this is used as the width of a Gaussian distribution from which the impact parameter is selected. The preset and recommended choice is 1.

`ext_field` (`INT`) If not zero the program takes into account the effect of the external magnetic field for the equivalent photon approximation.

`do_eloss` (`INT`) If not zero the beam particles loose energy due to beamstrahlung. The default is 1.

`do_espread` (`INT`) If not zero the beam particles energy spread is taken into account. The energy of the particles is chosen for each collision.

`do_isr` (`INT`) If not zero the initial state radiation is taken into account.

`do_compt` (`INT`) If not zero the program produces soft particles via the bremsstrahlung process.

`load_beam` (`INT`) If not zero the initial beams are loaded from the file `beam.ini`.

`load_photons` (`INT`) If not zero the initial photon beams are loaded from the file `photon.ini`. This is useful for the $e^-\gamma$ and $\gamma\gamma$ options.

`store_photons` (`INT`) If not zero the photons of the spent beams are stored in the file `photon.dat`.

`do_prod` (`INT`) If not zero soft particles with a fixed energy `prod_e` are produced during the beam-beam interaction. The cross section is assumed to be constantly `prod_scal`.

`prod_e` (`DOUBLE`) Energy (in GeV) of the particles produced with the switch `do_prod`.

`prod_scal` (`DOUBLE`) The cross section for the production of particles with the switch `do_prod`.

`do_cross` (`INT`) If not zero the file `cross.ini` is loaded and the contained cross section is folded with the luminosity spectrum.

A.2 The input files

A.2.1 `electron.ini`

If the switch `load_beam` is set the initial distribution of electrons and positrons is load from the file `electron.ini`. On each line this file contains seven parameters

describing one particle. The first value gives the particles energy in GeV—if it is negative its absolute value is used and the particle is attributed to beam 2 instead of beam 1. The second value gives the degree of longitudinal polarisation of the particle ranging from -1 to 1. The third and forth value contain the angles in x and y the particle has in radian. The last three give the position of the particle in the bunch. The first two give the x and y position in nm when the particle crosses the plane $z = 0$. The last value gives the longitudinal position in μm within the bunch—negative values indicate that the particles are in the head of the bunch.

The number of particles for bunch j in the file may not exceed the number `n_m.j`, but it can be less. The weight of the macro particles is calculated using `particles.j/n_m.j`. The particles within each bunch have to be sorted according to their z-position.

A.2.2 `photon.ini`

This file is comparable to `electron.ini`. It is used when the switch `load_photons` is used. Each line of the file contains the seven parameters of one photon. They have the same meaning as in the file `electron.ini`—the second value is the degree of circular polarisation. The number of photons is not restricted nor need they to be ordered.

A.2.3 `rndm.save`

This file can be read with the switch `rndm_load`. If it does not exist the standard initialisation of the random number generators is used. The file can be created using the switch `rndm_save`. Since it is binary it cannot be transported from one machine to another.

A.2.4 `cross.ini`

This file contains in the first line the number of energies at which the cross section is defined `n` and the number of cross-sections per energy `n_val`. The next two values on this line define how the axis are threated in the moment they should be simply zero. The following (`n`) lines each contain the energy at which the cross section is evaluated and the apropriate `n_val` cross sections. If all cross sections are evaluated simultaneously or if only the first is defined by a flag inside the program: `MCROSS`. This part of the program is likely to change and comments and suggestions are welcome (as for the rest).

A.3 The Main Output File

The output file contains the settings of the variables in almost the same form as the input file. In addition it of course contains the results. The view program `gpv` allows to write the results onto the screen (very bad layout) and to produce data files from the histograms stored in the file. They are prepared to be used with `GNUPLOT` with `set data style lines`.

The variables in the output file containing the results are

`lumi_fine` The luminosity in m^{-2} per bunch crossing as calculated from the charge densities.

`lumi_ee` The luminosity in m^{-2} per bunch crossing as calculated from the colliding beam particles. This value is zero if `electron_ratio=0.0;` is used.

`lumi_eg` The eγ-luminosity in m^{-2} per bunch crossing. The value is calculated only if `electron_ratio` and `photon_ratio` are not equal zero.

`lumi_ge` The γe-luminosity in m^{-2} per bunch crossing.

`lumi_gg` The $\gamma\gamma$-luminosity in m^{-2} per bunch crossing.

`lumi_gg_high` The $\gamma\gamma$-luminosity with a centre of mass energy of more than `gg_cut` in m^{-2} per bunch crossing.

`upsmax` Maximal value of Υ that occurred during the interaction.

`miss` The relative amount of interacting particles that were outside the grid during one timestep. Should be small compared to 1.

`ephot` The average photon energy of the photons of beam 1 or 2.

`bpm_vx` The average angle in x in μrad of the particles of each beam after the interaction.

`bpm_sig_vx` The RMS angular spread in x of the spent beams.

`bpm_vy` The same as `bpm_vx` only for the y direction.

`bpm_sig_vy` The same as `bpm_sig_vx` only for the y direction.

`hadron_cut` The minimal photon-photon centre of mass energies for hadronic events.

`hadron_ee` The number of hadronic events per bunch crossing due to the virtual photons in ee collisions.

`hadron_eg`	The number of hadronic events per bunch crossing due to eγ collisions.
`hadron_ge`	The number of hadronic events per bunch crossing due to γe collisions.
`hadron_gg`	The number of hadronic events per bunch crossing due to $\gamma\gamma$ collisions.
`jets0`	The number of minijet events per bunch crossing due to the direct process.
`jets1`	The number of minijet events per bunch crossing due to the once resolved process.
`jets2`	The number of minijet events per bunch crossing due to the twice resolved process.
`n_pairs`	Total number of pair particles produced per bunch crossing.
`e_pairs`	Total energy of these particles.
`n_BW`	The number of particles due to the Breit-Wheeler process.
`e_BW`	The total energy of the particles due to the Breit-Wheeler process.
`n_BH`	The number of particles due to the Bethe-Heitler process.
`e_BH`	The total energy of the particles due to the Bethe-Heitler process.
`n_LL`	The number of particles due to the Landau-Lifshitz process.
`e_LL`	The total energy of the particles due to the Landau-Lifshitz process.
`high_BW`	The number of particles due to the Breit-Wheeler process with a transverse momentum of more than 20 MeV and an angle with respect to the beam axis of more than 150 mrad.
`high_BH`	The same as `high_BW` for the Bethe-Heitler process.
`high_LL`	The same as `high_BW` for the Landau-Lifshitz process.
`high_tot`	The total number of these particles.
`high_e`	Their total energy.
`de`	The average energy loss of the beam particles in GeV.
`cross`	The results of the cross-section calculation.
`cross_var`	The errors of the cross section calculation.

A.4 The Output Files

There are several additional output files which can usually be produced with the switches. So the particles from pair pair creation will be stored in `pairs.dat`.

A.4.1 `pairs.dat`

This file is an ASCII file. Each lines contains one particle. The first value in a line is the particles energy in GeV. If it is negative the particle is a positron otherwise an electron. The next three values are the velocities in x- y and z-direction divided by the speed of light.

A.4.2 `hadron.dat`

This file contains the energies of colliding photons that produced a hadronic event. Since the number of these events is small per bunch crossing the number will be enhanced by the factor `hadron_ratio`. The file is an ASCII file. Each line contains the energy of the photon from beam 1 and the one from beam 2 in GeV.

A.4.3 `minijet.dat`

This file contains the four vectors of the partons before fragmentation on each line. The first two values are the energies of the photon remnant in GeV. They are negative for non-existing remnants. The next two values contain the longitudinal momenta of the two hard jets in GeV. A positive value points into direction of beam 1. The next value is the tranverse momentum of the final state partons in GeV. In this model it is the same for both jets. The last value is an integer giving the process responsible for the jets.

A.4.4 `lumi.dat`

Each lines of this file contains the energies of two colliding particles in GeV.

A.4.5 `beam.dat`

Actually two files `beam1.dat` and `beam2.dat` are produced containing the particles of the first or second beam, respectively. Each line contains the energy of the particle and the angles in x and y in radian. It is possible to customise the program to also store the z-position within the bunch as well as the (x, y)-position at the intersection plane[1].

[1]The particles position is extrapolated back to this plane after the interaction, the real position was of course different.

A.4.6 `photon.dat`

This file contains the photons after the interaction, each line gives the photon energy (if negative the photon is from the second beam) and angles in x and y.

A.4.7 `rndm.save`

This file is automatically created if the switch `rndm_save` is set. It is a binary file and cannot be transported from one machine to another. With the switch `rndm_load` it can be reread in the next run.

Bibliography

[1] G. A. Low, private communication. Numbers are updated values (September 1996) for the International Linear Collider Technical Review Commitee Report, SLAC-PUB-R-95-471 (1995).

[2] The TESLA and SBLC Collaborations. Conceptual design of a 500 GeV electron positron collider with integrated x-ray laser facility. To be published December 1996.

[3] D. Burke for the FFTB Collaboration. Results from the final focus test beam. London, 1994.

[4] R. Brinkmann, A. Drozhdin, D. Schulte, and M. Seidel. The TESLA beam collimation system. TESLA 95-25 (1995).

[5] O. Napoly, 1995. Talk given in Gran Sasso.

[6] O. Napoly, E. Klein, and J. M. Rifflet. TESLA final focus system with superconducting magnets in the interaction region: Optics, tolerances and magnet design. TESLA 94-31 (1994).

[7] M. Sachwitz and J. Schreiber. Muon background in a 500 GeV TESLA linear collider. TESLA 94-27 (1994).

[8] A. Drozhdin. Extraction of the spent beam into the TESLA beam capture section. TESLA 94-29 (1994).

[9] K. Hirata, K. Oide, and B. Zotter. Synchrotron radiation limit of the luminosity in TeV linear colliders. CERN-LEP-TH/89-34 (89).

[10] P. Chen. Beamstrahlung and the QED, QCD backgrounds in linear colliders. SLAC-PUB-5914 (1992).

[11] V. G. Bagrov, N. I. Fedosov, and I. M. Ternov. Radiation of relativistic electrons moving in an arc of a circle. Phys. Rev. D, **28** (1983) 2464.

[12] R. Blankenbecler and S. D. Drell. Quantum treatment of beamstrahlung. Phys. Rev. D, **36** (1987) 277.

[13] P. Schmüser. Vorlesungsskript Beschleunigerphysik.

[14] A. A. Sokolov and I. M. Ternov. *Synchrotron Radiation*. Pergamon Press, 1968.

[15] V. D. Shiltsev. TESLA damping ring impedances: Preliminary design consideration. TESLA 96-02 (1996).

[16] K. Floettmann and J. Roßbach. Lattice studies for a large dogbone damping ring for TESLA. In *Proc. of the European Particle Acceleraotr Conf.*, London, 1994.

[17] O. Napoly. The luminosity for beam distributions with error and wakefield effects in linear colliders. Part. Accel., **40** (1993) 181-203.

[18] J. M. Dawson. Particle simulation of plasmas. Rev. Mod. Phys., **55** (1983) 403.

[19] R. W. Hockney. The potential calculation and some applications. Methods of Computational Physics, **9** (1970).

[20] W. H. Press, S. A. Teukolsky, W. T. Vetterling, and B. P. Flannery. *Numerical Recipes*. 1992.

[21] K. Yokoya. A computer simulation code for the beam-beam interaction in linear colliders. KEK-Report 85-9 (1985).

[22] E. A. Kuraev and V. S. Fadin. On radiative corrections to e^+e^- single photon annihilation at high energy. Sov. J. Nucl. Phys., **41** (1985) 466.

[23] The JLC Group. JLC-I. KEK Report 92-16 (1992).

[24] T. Tauchi,private communication.

[25] D. R. Walz. Private communication.

[26] Verein Deutscher Ingenieure, editor. *VDI-Wärmeatlas*. VDI Verlag, 1994.

[27] C. J. Smithells. *Metals Reference Book*. 1967.

[28] W. Beitz and K.-H. Kütter, editors. *Taschenbuch für den Maschienenbau*. Springer Verlag, 1981.

[29] D. R. Walz and L. R. Lucas. The sphere dump. SLAC-PUB-555 (1969).

[30] K. Teutenberg, P. Sievers, and W. C. Middlekoop. Absorber blocks for internal and external beam dumping at the SPS. CERN-LAB II/BT/74-4 (1974).

[31] V. Telnov. Principles of photon colliders. Nucl. Instr. Meth. A, **355** (1995) 3–18.

[32] W. B. Berestetzky, E. M. Lifshitz, and L. P. Pitajewski. *Lehrbuch der Theoretischen Physik. Band 4.* 1986.

[33] V. N. Baier, V. S. Fadin, V. A. Khoze, and E. A. Kuraev. Inelastic processes in high energy quantum electrodynamics. Phys. Rep., **78** (1981) 293.

[34] F. Halzen and A. D. Martin. *Quarks & Leptons.* Wiley & Sons, 1990.

[35] A. E. Blinov et al. Phys. Lett. B, **113** (1982) 423.

[36] G. L. Kotkin, V. G. Serbo, and A. Schiller. Processes with large impact parameters at colliding beams. Int. J. Mod Phys. A, **7** (1992) 4707–4745.

[37] J. L. Augneres et al. HERA. A Proposal for a large Electron-Positron Colliding Beam Facility at DESY. DESY HERA 81/10 (1981).

[38] K. Piotrzkowski. Observation of the beam-size effect at HERA. DESY 95-051 (1995).

[39] V. N. Baier and V. M. Katkov. Production of bremsstrahlung during collisions of high-energy particles in a magnetic field. Sov. Phys. Dokl., **17** (1973) 1068.

[40] I would like to thank J.-E. Olsson for providing me with a version used at PETRA.

[41] G. P. Lepage. A new algorithm for adaptive multidimensional integration. J. Comp. Phys., **27** (1978) 192–203.

[42] The MARK J Collaboration. Physics with high energy electron-positron colliding beams with the MARK J detector. Physics Reports, **63** (1980) 337.

[43] R. P. Johnson. *Measurements of Charged Two-Particle Exclusive States in Photon-Photon Interactions.* PhD thesis, 1986.

[44] T. Tauchi was so kind to provide the spectrum calculated with ABEL.

[45] D. Schulte. Simulation des Untergrundes durch inkohärente Paarerzeugung in Linearbeschleunigern. TESLA 93-39 (1993).

[46] The TOPAZ Collaboration. Measurement of the inclusive cross section of jets in $\gamma\gamma$ interactions at TRISTAN. Phys. Lett. B, **314** (1993).

[47] U. Amaldi, G. Cocconi, A. N. Diddens, R. W. Dobinson, J. Dorenbosch, W. Duinker, D. Gustavson, J. Meyer, K. Potter, and A. M. Wetherell. The real part of the forward proton proton scattering amplitude measured at the CERN intersection storage rings. Phys. Lett. B, **66** (1977) 390.

[48] The ZEUS Collaboration. A measurement of $\sigma_{tot}(\gamma p)$ at $\sqrt{s} = 210\,\mathrm{GeV}$. DESY 92-127 (1992).

[49] P. Chen and M. E. Peskin. Hadron production in $\gamma\gamma$ collisions as a background for e^+e^- linear colliders. SLAC-PUB-5873 (1992).

[50] The ZEUS Collaboration. The ZEUS detector: Technical proposal. DESY-HERA-ZEUS-1 (1986).

[51] T. Sjoestrand. What is a photon and how should it diffract? Talk given at Photon 95.

[52] T. Sjöstrand. High-energy physics event generation with PYTHIA5.7 and JETSET7.4. Computer Physics Commun., **82** (1994) 74–90.

[53] M. Drees and R. M. Godbole. Aspects of two photon physics at linear e^+e^- colliders. DESY 92-044 (1992).

[54] M. Dress and F. Halzen. Hadron structure of high-energy photons. Phys. Rev. Lett., **61** (1988) 275.

[55] M. Drees and K. Grassie. Parametrisations of the photon structure and applications to supersymmetric particle production at HERA. Z. Phys. C, **28** (1985) 451–462.

[56] M. Glück, E. Reya, and A. Vogt. Photonic parton distributions. Physical Review D, **46** (1992) 1973.

[57] J. M. Butterworth. Photon structure as seen at HERA. DESY 95-043 (1995).

[58] The H1 Collaboration. Total photoproduction cross section measurement at HERA energies. DESY 92-160 (1992).

[59] M. Erdmann et al. New results from the H1 experiment at HERA on photoproduction, deep ineleastic scattering and searches for new particles. DESY 93-77 (1993).

[60] J. R. Forshaw and J. K. Storrow. Minijets and the total inelastic photoproduction cross section. Phys. Lett.B, **268** (1991) 116–121.

[61] P. Chen. Differential luminosity under multi-photon beamstrahlung. Phys. Rev. D, **46** (1992) 1186.

[62] D. W. Duke and J. F. Owens. Quantum-chromodynamic corrections to deep-inelastic compton scattering. Phys. Rev. D, **26** (1982) 7.

[63] B. L. Combridge, J. Kripfganz, and J. Ranft. Hadron production at large transverse momentum and QCD. Phys. Lett. B, **70** (1977) 234.

[64] H.-U. Bengtsson. The Lund Monte Carlo for hight-p_{T} physics. Physics Communications, **31** (1984) 323–355.

[65] R. Settles, private communication.

[66] The NLC ZDR Design Group. Zeroth order design report for the next linear collider. (1996).

[67] P. Colas, 1994. Talk at Orsay, March 1994.

[68] R. Settles. Minutes of the Third Workshop of the ECFA/DESY Study on Physics and Detectors for Linear Colliders, September 1996.

[69] C. K. Browdery and C. J. S. Damerell. Progress report on a CCD-based vertex detector design, and some observations on the microsstrip detector option. In *Workshop on Physics and Experiments with linear* $\mathrm{e^+e^-}$ *Colliders*, Hawaii, 1993.

[70] ATLAS Collaboration. Technical proposal for a general-pupose pp experiment at the large hadron collider at CERN. CERN/LHCC/94-43 (1994).

[71] Y. Giomataris, Ph. Rebourgeard, and J. P. Robert. MICROMEGAS: a high-granularity position-sensitive gaseous detector for high particle-flux environments. CERN/LHC/96-04 (1996).

[72] Particle Data Group. Review of particle properties. Phys. Rev. D, **50** (1994) 1264.

[73] D. J. Miller, B. W. Kennedy, J. J. Ward, and J. R. Forshaw. Deep inelastic $\mathrm{e}\gamma$ scattering, with beamstrahlung. In *Workshop on Physics and Experiments with Linear* $\mathrm{e^+e^-}$ *Colliders*, Hawaii, 1993.

[74] M. N. Frary and D. J. Miller. Monitoring the luminosity spectrum. DESY 92-123-A (1992).

[75] Application Software Group. GEANT *Detector Description and Simulation Tool.* 1993.

[76] A. Koski was so kind to provide a field map calculated with OPERA.

[77] C. J. S. Damerell. Private communication.

[78] J. Bürger. Private communication.

[79] The H1 Collaboration. Technical proposal to build silicon tracking detectors for H1. H1 06/92-226 (1992).

[80] C. J. S. Damerell. CCD vertex detectors in particle physics. Nucl. Instr. Meth. A, **342** (1994) 78–82.

[81] A. H. Sullivan. *A guide to radiation and radioactivity levels near high energy particle accelerators.* 1992.

[82] K. Tesch. Shielding against high energy neutrons from electron accelerators — a review. Radiation Protection Dosimetry, **22** (1988) 27-32.

[83] J. O. Johnson and T. A. Gabriel. A user's guide to MICAP: A Monte-Calo Ionization Chamber Analysis Package. ORNL-TM-10340 (1988).

[84] R. M. Barnett et al. Review of particle physics. Phys. Rev. D, **54** (1996) 1-720.

[85] M. Barbier. *Induced radioactivity.* 1969.

[86] The ZEUS Collaboration. The ZEUS detector. Status report 1993. (1993).

[87] C. Zeitnitz and T. A. Gabriel. The GEANT CALOR interface user's guide. 1994.

[88] O. Napoly and A. Sery. Influence of ground motion on the time evolution of beams in linear colliders. TESLA 95-19 (1995).

[89] T. Shintake. Proposal of a nanometer beam size monitor for e^+e^- linear colliders. Nucl. Instr. Meth. A, **311** (1992) 453-464.

[90] N. Walker, private communication.

[91] O. Napoly and B. Zotter. Kink instability for small crossing angles. CLIC-Note-289 (1995).

[92] T. Tauchi and K. Yokoya. Nanometer-beam-size measurement during collisions at linear colliders. Phys. Rev. E, **51** (1995) 6119–6126.

[93] R. Brinkmann. Private communication.

[94] O. Napoly, private communication.

[95] P. Igo-Kemenes, M. Martinez, R. Miquel, and S. Orteu. Top measurement at threshold. In *Physics and Experiments with Linear* e^+e^- *Colliders*, Hawaii, 1993.

[96] I would like to thank R. Miguel for providing me with a copy of TOPPIK.

[97] The ALEPH Collaboration. Performance of the ALEPH detector at LEP. (1994). To be submitted to Nucl. Instr. Meth. A.

[98] G. Bagliesi et al. Top quark physics, experimental aspects. DESY 92-123A (1992).

[99] K. Fujii, T. Matsui, and Y. Sumino. Physics at t anti-t threshold in e^+e^- collisions. Phys. Rev. D, **50** (1994) 4341–4362.